Tubular solar receiver with dense particle suspension upward flow

Hadrien Benoit

Collège Doctoral du Languedoc-Roussillon

THÈSE

Pour obtenir le grade de

Docteur

Délivré par

UNIVERSITE DE PERPIGNAN VIA DOMITIA

Préparée au sein de l'école doctorale
Energie et Environnement

Et de l'unité de recherche
Procédés, Matériaux et Énergie Solaire
(PROMES-CNRS, UPR 8521)

Spécialité :
Sciences de l'ingénieur

Présentée par
Hadrien BENOIT

RECEPTEUR SOLAIRE TUBULAIRE A SUSPENSION DENSE DE PARTICULES EN ECOULEMENT ASCENDANT

Soutenue le 16/12/2015 devant le jury composé de

M. Robert PITZ-PAAL, Professeur d'Université, Institute of Solar Research, DLR	Rapporteur
M. Manuel ROMERO, Directeur de Recherche, Instituto IMDEA Energía	Rapporteur
M. Jan BAEYENS, Professeur d'Université, University of Warwick	Examinateur
M. Daniel GAUTHIER, Ingénieur de Recherche, PROMES-CNRS	Examinateur
M. Mehrdji HEMATI, Professeur d'Université, LGC, INPT	Examinateur
M. Olivier POULIQUEN, Directeur de Recherche, IUSTI	Examinateur
M. Frédéric SIROS, Ingénieur de Recherche, EDF R&D	Invité
M. Renaud ANSART, Maître de Conférences, LGC, INPT	Co-Directeur
M. Gilles FLAMANT, Directeur de Recherche, PROMES-CNRS	Directeur

UNIVERSITÉ PERPIGNAN VIA DOMITIA

Remerciements

Cette thèse a été réalisée au sein du laboratoire Procédés, Matériaux et Energie Solaire du Centre National de la Recherche Scientifique (PROMES-CNRS), à Font-Romeu Odeillo. Elle n'aurait pas été possible sans la participation de nombreuses personnes auxquelles je souhaite faire part de ma gratitude.

Je remercie Gilles Flamant, Directeur de Recherche au CNRS et directeur de cette thèse. Sa vision est à l'origine de ce projet. Il a toujours été capable de me guider dans la bonne direction et j'ai beaucoup appris grâce à lui.

Renaud Ansart, Maître de Conférences et co-directeur de la thèse, m'a accompagné pour la réalisation du travail de simulation numérique. Malgré la distance qui sépare Toulouse et Odeillo, il a toujours été disponible pour répondre à mes questions et m'indiquer le chemin à suivre. Je lui exprime toute ma gratitude.

Je suis très reconnaissant envers Daniel Gauthier, Ingénieur de recherche au CNRS, qui a lui aussi encadré mon travail. Son expérience s'est prouvée nécessaire à plusieurs reprises tant pour les expérimentations que pour les travaux théoriques.

J'ai une pensée particulière pour Inmaculada Pérez López, Ingénieur d'étude au CNRS et membre de l'équipe de ce projet. Son travail assidu a été indispensable au bon avancement de notre recherche.

J'adresse un grand merci à Jean-Louis Sans, Ingénieur de recherche au CNRS et responsable du Grand Four Solaire d'Odeillo où toutes les expériences ont été réalisées. Son savoir et son expérience ont largement contribué à la réussite du projet.

Je remercie également Emmanuel Guillot, Ingénieur de recherche au CNRS, qui a pu nous consacrer du temps à la fois pour la réalisation des mesures de flux et pour son aide dans la mise au point du système d'acquisition du pilote multi-tubulaire. J'inclus aussi dans ces remerciements les membres de l'équipe SISIA Nicolas Boullet et Régis Olives qui ont a un moment où un notre contribué à notre travail.

Je suis reconnaissant envers Cyril Caliot, Chargé de recherche au CNRS, de m'avoir appris l'utilisation du logiciel Solfast-4D et de m'avoir épaulé dans la réalisation du modèle de rayonnement.

Merci à Michael Tessonneaud pour son aide dans les expérimentations sur le pilote multi-tubulaire et pour sa bonne humeur.

Merci aux partenaires du projet, en particulier l'entreprise COMESSA qui a réalisé un travail de qualité dans la réalisation du pilote multi-tubulaire.

Ma reconnaissance va également à l'ensemble des techniciens du laboratoire PROMES sans qui rien n'aurait été possible. Roger Garcia qui a en grande partie mis au point et assemblé le pilote mono-tubulaire. Marc Garrabos et Olivier Prevost qui nous ont secouru chaque fois qu'un problème nécessitait une solution technique. Jean-Marc Bienfait et Olivier Berthelot, les électriciens qui ont raccordé nos équipements.

Je remercie aussi les informaticiens Laurent Lestrade et George Pichelin qui ont rendu possible mes travaux numériques.

Je remercie plus généralement tous les membres du laboratoire PROMES pour les trois années fantastiques que j'ai passé à Odeillo. Ce fut un grand plaisir de tous vous rencontrer.

Enfin, merci aux rapporteurs de cette thèse, Robert Pitz-Paal et Manuel Romero, aux membres du jury de soutenance, Jan Baeyens, Mehrdji Hemati et Frédéric Siros, ainsi qu'à Olivier Pouliquen qui l'a présidé. Leurs remarques constructives ont permis d'améliorer mon manuscrit, de souligner les éléments de mon travail qui devront être approfondis et leurs questions pertinentes ont mis en évidence certains axes de recherche qui restent à explorer.

Contents

Résumé

Introduction

Cette thèse porte sur l'étude d'un nouveau procédé de récepteur solaire utilisant une suspension dense de particules (en Anglais : Dense Particle Suspension = DPS) en circulation ascendante dans des tubes verticaux comme fluide caloporteur. Elle a été réalisée dans le cadre du projet européen "Concentrated Solar Power in Particles" (CSP2) (FP7, Project No. 282 932) [1]. Le terme suspension dense de particules désigne un mélange fluidisé de particule et de gaz, avec une fraction volumique de particules de l'ordre de 30 %, et de faibles vitesses de circulation (quelques cm/s). L'intérêt d'utiliser des particules à la place des fluides de caloporteurs solaires classiques est qu'elles ne sont pas limitées en température, si ce n'est par leur température de frittage. Dans le cas du carbure de silicium qui a été utilisé au cours des études présentées ici, cette température est d'environ 1600 °C. Ainsi, les particules permettent d'atteindre les températures nécessaires à l'utilisation des cycles de conversion thermodynamiques à haut rendement tels que le cycle de Brayton ou les cycles combinés. L'amélioration des performances des centrales solaires thermodynamiques par la mise en œuvre de tels cycles est en effet l'un des objectifs principaux de la recherche actuelle dans ce domaine. D'autre part, les particules peuvent aussi servir de milieu de stockage de chaleur direct, sans passer par des échangeurs de chaleur. Le stockage thermique étant l'un des points forts du solaire thermodynamique, puisqu'il permet la production continue d'électricité, c'est un autre avantage de l'utilisation des particules.

Introduction générale

Dans ce document, une introduction générale présente rapidement la technologie solaire thermodynamique. Les différentes formes de récepteurs sont abordées et un intérêt particulier est accordé aux récepteurs centraux pour les centrales à tour puisque le récepteur à suspension dense de particules appartient à cette catégorie. Les centrales à tour sont aujourd'hui en plein développement car elles permettent d'obtenir les meilleurs rendements de conversion solaire-électricité et un stockage thermique efficace. Un historique de la recherche sur l'utilisation des particules dans les récepteurs solaires depuis les années 80 est ensuite présenté. Plusieurs concepts ont été étudiés : rideau de particules, lit fluidisé, récepteur rotatif, récepteur centrifuge. Le fonctionnement général d'une centrale à tour utilisant un récepteur à particules est illustré par la Figure 1. Les particules venant du stockage froid sont transportées jusqu'au récepteur, en haut de la tour, où elles absorbent le rayonnement solaire. Elles circulent ensuite jusqu'au stockage chaud puis sont dirigés vers le système de conversion d'énergie. Celui-ci comprend un échangeur de chaleur dans lequel les particules transmettent l'énergie emmagasinée à un fluide de travail, par exemple de l'eau qui se transforme en vapeur. Le fluide de travail est ensuite détendu dans une turbine où la chaleur est transformée en énergie mécanique, puis en électricité par un alternateur.

Chapitre 1 : Etude des cycles thermodynamiques à haut rendement et des fluides caloporteurs solaires classiques

Le Chapitre 1 passe en revue les différents cycles thermodynamiques à haut rendement qui justifient l'étude de fluides caloporteurs supportant des hautes températures. Il s'agit en

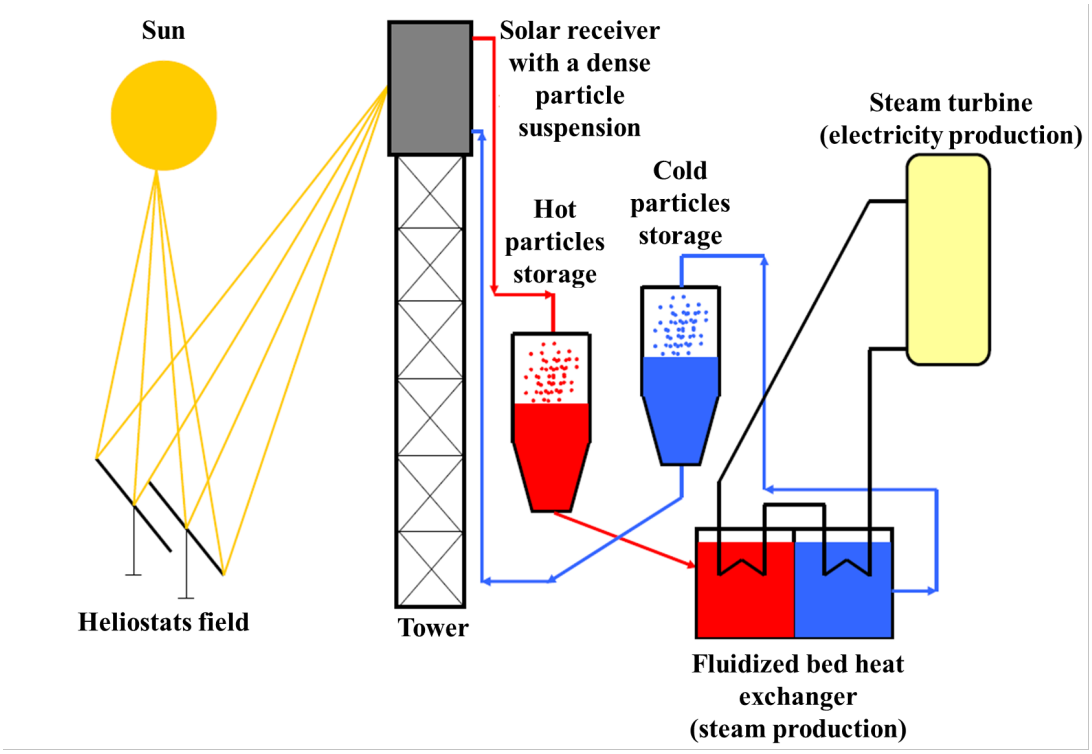

Figure 1: Schéma de fonctionnement d'une centrale solaire à tour avec récepteur à particules.

particulier des cycles de Brayton et des cycles combinés, leurs principes sont expliqués par les schémas des Figures 2 et 3 respectivement.

Dans le cycle de Brayton à recompression, le gaz froid (1) est comprimé une première fois (C1). De l'état (2) à l'état (3), il est refroidi dans un échangeur de chaleur (HEX) ce qui permet une deuxième compression plus efficace (C2). Le gaz à sa pression la plus haute (4) est alors préchauffé dans le régénérateur pour atteindre l'état (5). Il entre alors soit directement dans le récepteur solaire, soit dans un échangeur où il récupère la chaleur du fluide caloporteur solaire. Le gaz à haute température et haute pression (6) est enfin détendu dans la turbine jusqu'à basse pression (7). Une partie de la chaleur restante est utilisée dans le régénérateur pour préchauffer le côté froid du cycle. Finalement, le gaz retourne à son état initial en passant par un échangeur de chaleur.

Le principe du cycle combiné est d'utiliser la chaleur restante après le passage dans la turbine à gaz afin d'alimenter un second cycle fonctionnant à plus basse température. Dans le schéma de la Figure 3, ce cycle bas est un cycle de Rankine organique qui peut fonctionner à plus basse température qu'un cycle de Rankine à vapeur.

Une analyse combinant les cycles thermodynamiques avec un récepteur solaire [2] a montré que le rendement de conversion solaire-mécanique d'un cycle de Brayton à recompression fonctionnant avec du CO2 supercritique pouvait atteindre 42,9 % à 746 °C avec un système refroidissement à eau et 39,1 % à 766 °C avec un refroidissement à air. Les cycles combinés utilisant un cycle de Rankine à vapeur comme cycle basse température peuvent atteindre 60 % de rendement quand la température d'entrée de la turbine est 1300 °C [3].

Le Chapitre 1 considère aussi les différents fluides caloporteurs solaires :

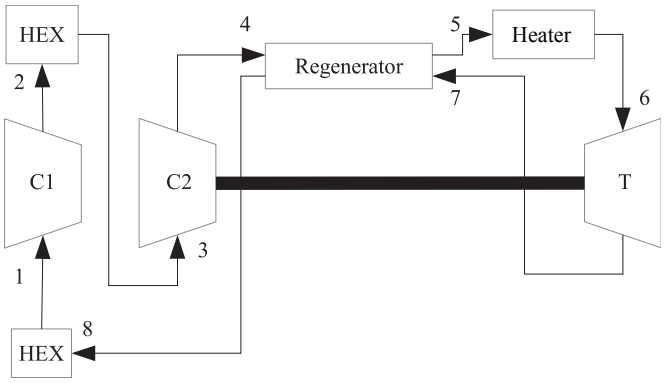

Figure 2: Schéma de fonctionnement du cycle de Brayton [2].

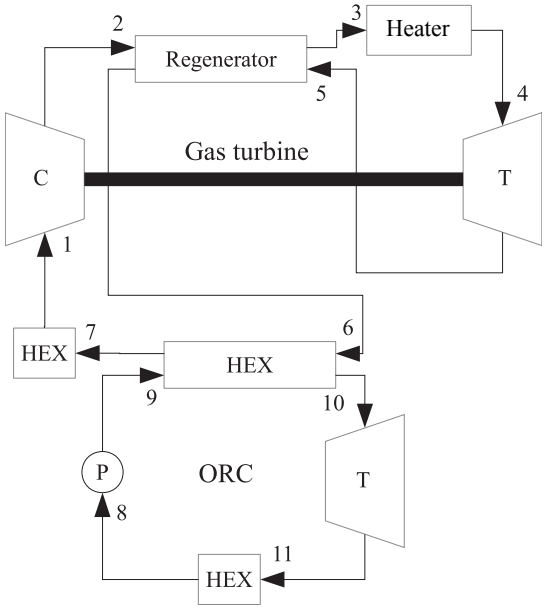

Figure 3: Schéma de fonctionnement d'un cycle combiné [2].

- Liquides :
  - Huiles thermiques : Therminol VP-1®, Dowtherm®, etc.
  - Sels Fondus : Solar salt, Hitec®, Hitec XL®, etc.
  - Métaux liquides : sodium (Na), alliage plomb-bismuth (LBE), etc.
- Fluides gazeux :
  - Gaz pressurisés : Air, CO_2, He, H_2.
  - Fluides supercritiques : s-CO_2, s-H_2O.
- Eau/Vapeur.
- Suspension de particules utilisée comme fluide de transfert.

Leurs températures de fonctionnement limitées par leur stabilité thermique sont résumées sur la Figure 4. On voit que les fluides actuellement utilisés sont beaucoup plus limités que les nouveaux fluides en développement tels que les métaux liquides et les suspensions de particules.

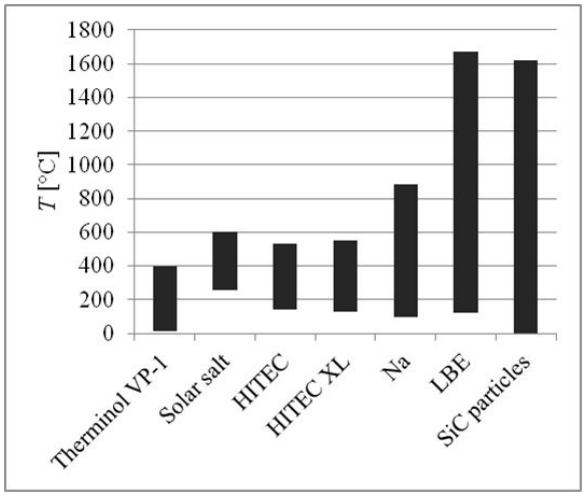

Figure 4: Domaines de températures des fluides caloporteurs solaires.

Les coefficients d'échange de chaleur des fluides caloporteurs avec une paroi solide sont étudiés. En effet c'est ce paramètre qui fixe la densité de flux maximum que peut supporter un absorbeur solaire. Pour une même densité de flux solaire, plus le coefficient d'échange est élevé, moins la température de paroi de l'absorbeur est élevée.

Le calcul du coefficient d'échange de chaleur se fait par l'intermédiaire de corrélations sur le nombre de Nusselt Nu. Une étude bibliographique a été effectuée afin de rassembler les corrélations existantes pour déterminer lesquelles étaient les plus appropriées au calcul du coefficient d'échange de chaque fluide. Il ressort que la corrélation de Gnielinski [4] est largement applicable mais que pour certains fluides, il existe des corrélations plus précises. Ainsi, pour les sels fondus il existe la corrélation de Wu et al. [5], et pour les métaux liquides il vaut mieux utiliser celle de Cheng et Tak [6].

Pour pouvoir appliquer les corrélations préalablement citées, il faut connaître les propriétés des fluides qui ont donc été compilées et rassemblées dans un tableau sous forme d'équations

polynomiales. La plupart sont applicables dans toute la gamme d'utilisation des fluides de transfert.

L'utilisation des corrélations sur le nombre de Nusselt avec les équations des propriétés a donc permis le calcul des coefficients d'échange de chaleur des différents fluides dans une configuration d'écoulement bien définie : écoulement dans un tube de diamètre 0.025 m, à vitesse constante (2 m/s pour les liquides, 15 m/s pour les fluides), sur toute la gamme de température supportée par chaque fluide.

Les résultats montrent que les fluides avec le meilleur coefficient d'échange sont les métaux liquides et en particulier le sodium. Ils sont prometteurs pour l'utilisation dans des centrales à haute température et haute concentration solaire mais ne peuvent pas être utilisés comme milieu de stockage de chaleur (capacité thermique trop faible et coût trop élevé). L'eau présente aussi un très bon coefficient. Pour les gaz, la vapeur à haute pression présente un bon coefficient d'échange. L'hydrogène présente un coefficient de transfert plutôt élevé tandis que l'air a le coefficient le plus faible. Il nécessite donc des configurations particulières développées pour améliorer le coefficient de transfert.

Ce chapitre montre que des rendements de conversion chaleur-mécanique de plus de 50 % peuvent être atteints avec des fluides caloporteurs supportant 700 °C ou au-delà. Plusieurs candidats existent.

Chapitre 2 : Etude d'un récepteur solaire expérimental mono-tubulaire utilisant une suspension dense de particules en écoulement ascendant comme fluide caloporteur

Dans ce chapitre, le cœur du sujet est abordé dans la configuration la plus simple. Un récepteur solaire expérimental mono-tubulaire utilisant une suspension dense de particules en écoulement ascendant comme fluide caloporteur a été testé au grand four solaire du CNRS, à Odeillo. Les résultats sont ici présentés et analysés.

La Figure 5 présente un schéma de l'expérimentation. Le réservoir de stockage alimente le lit fluidisé nourrice où les particules sont fluidisées par injection d'un courant d'air à la base du caisson à travers une plaque poreuse en acier inoxydable fritté. La suspension dense de particules circule verticalement vers le haut grâce à la différence de pression imposée entre le lit fluidisé nourrice et le lit fluidisé collecteur. Le tube absorbeur (36 mm de diamètre intérieur et 4.2 mm d'épaisseur) est exposé au rayonnement solaire concentré sur une hauteur de 0,5 m dans la cavité ce qui permet de chauffer les particules en circulation. La balance à la sortie permet de calculer le débit de solide en circulation.

Les gammes de paramètres opératoires explorées aux cours des 2 campagnes expérimentales sont indiquées dans le Tableau 1. Lors des essais, la température de sortie des particules a atteint 750 °C en régime stable, ce qui a validé le procédé d'utilisation d'une suspension dense de particules comme fluide caloporteur haute température, puisque cette température est de 200 °C supérieure à celle des sels fondus. Ce résultat est illustré par la Figure 6.

Table 1: Gamme de paramètres opératoires

Flux massique de solide $[kg.m^{-2}.s^{-1}]$	Aération $[Nm^3/m^2.s]$	Densité de flux solaire $[kW/m^2]$	Température du lit fluidisé nourrice [K]	Température des particules en sortie [K]
		1^{re} campagne expérimentale		
9,5-21,7	0,011-0,109	144-248	6,5-65	241-351
		2^{me} campagne expérimentale		
10,2-45,1	0,021-0,042	213-393	229-503	446-723

Par ailleurs, la répartition des températures entre entrée, sortie, proche de la paroi et centre du tube a permis la mise en évidence d'un mode de circulation particulier consistant en une redescente des particules en proche paroi et une ascension au centre. Ce résultat a été confirmé par des simulations numériques 3D et par la détermination du profil de vitesse des particules dans le tube grâce à un traçage par émission de positron (méthode PEPT) réalisée par les partenaires du projet européen CSP2. Le schéma de la Figure 7 explique cette recirculation.

Les mesures du débit de particules et des températures ont permis de calculer la puissance absorbée par la suspension dense pendant son passage dans la cavité réceptrice. Du fait de la recirculation, les températures à considérer dans un bilan enthalpique entre l'entrée et la sortie ne sont pas la moyenne des températures en entrée et en sortie (2 mesures : proche paroi et centre du tube). Idéalement, il faudrait connaitre parfaitement les profils de vitesse et de température, mais comme ce n'est pas le cas, nous avons utilisé la température dans le lit fluidisé émetteur et la température au centre du tube en sortie de cavité. La puissance absorbée par la suspension dense de particules au cours de son chauffage dans les 0,5 m de tube absorbeur chauffé varie de 2,5 à 9 kW (moyennes sur des périodes stables) en fonction des paramètres opératoires.

Le coefficient d'échange de chaleur global entre la partie irradiée du tube et la suspension dense de particules (h_{tube}) a été calculé en considérant comme différence de température entre la paroi et la suspension la différence de température logarithmique moyenne. La surface d'échange considérée est la surface interne de la partie irradiée. Le coefficient d'échange varie de 400 à 1100 $W.m^{-2}.K^{-1}$. L'ensemble des données obtenues est représenté sur la Figure 8. Les paramètres influençant h_{tube} ont été étudiés. Plus le flux de solide est important, plus h_{tube} est élevé. Au contraire, plus l'aération est importante, plus h_{tube} est faible. La température a aussi une influence positive due à l'augmentation des échanges par rayonnement et à l'augmentation de la conductivité de l'air.

L'ensemble des valeurs de h_{tube} obtenues ont permis l'établissement d'une corrélation sur le nombre de Nusselt. Pour cela, la viscosité et la conductivité de la suspension dense de particules ont été calculées à partir de modèles donnant des valeurs équivalentes pour un mélange de phase et les nombres de Reynolds et de Prandtl de la suspension dense ont pu être calculés. La corrélation obtenue est : $Nu_{DPS} = 4.5 + 35.4 Re_{DPS}^{0.61} Pr_{DPS}^{0.94}$. Le graphe de la Figure 9 compare la corrélation et les valeurs expérimentales. La correspondance est bonne avec un coefficient de détermination $R^2 = 0,95$ et des erreurs relatives maximum et moyennes de 14,7 % and 5,5 % respectivement. Grâce à cette corrélation, la valeur du coefficient d'échange peut être prévue dans n'importe quelle condition appartenant aux gammes de paramètres testés, ce qui est très utile pour dimensionner un récepteur à échelle industrielle ou pour piloter une centrale utilisant ce procédé.

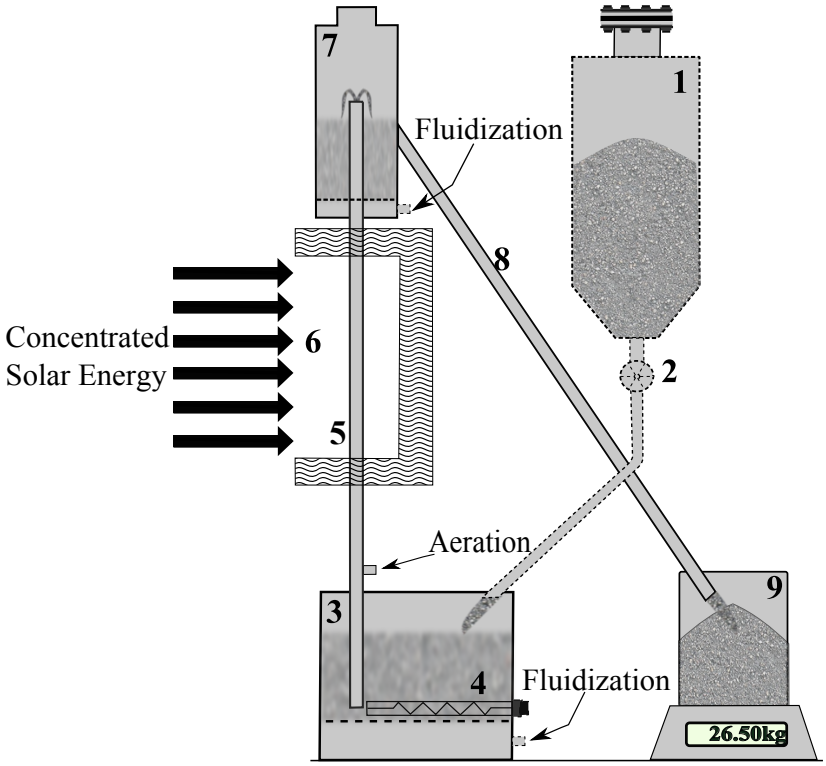

Figure 5: Schéma du récepteur expérimental mono tubulaire : 1. Réservoir de stockage de solide, 2. Vanne rotative d'alimentation, 3. Lit fluidisé nourrice, 4. Résistances électriques, 5. Tube absorbeur solaire métallique, 6. Cavité solaire réceptrice, 7. Lit fluidisé collecteur, 8. Tube d'évacuation, 9. Balance.

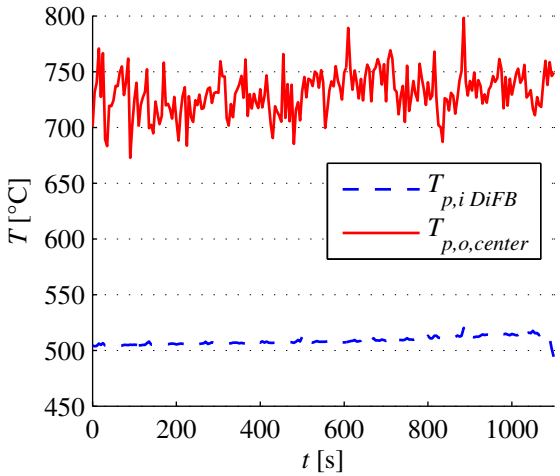

Figure 6: Température des particules en fonction du temps ($T_{p,iDiFB}$: température dans le lit fluidisé nourrice, à l'entrée du tube; $T_{p,o,center}$: température en sortie de la cavité, au centre du tube).

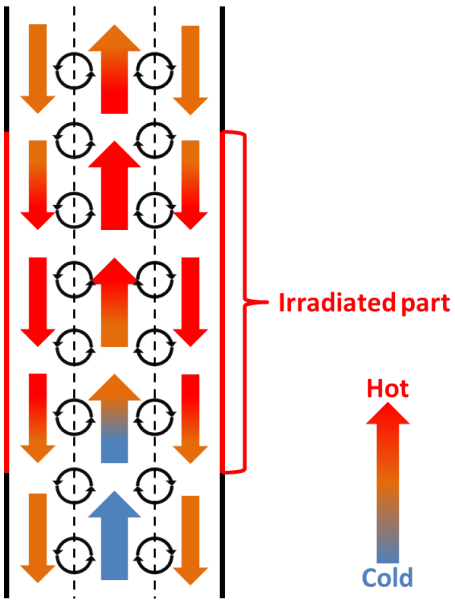

Figure 7: Schéma de la circulation et recirculation dans le tube absorbeur.

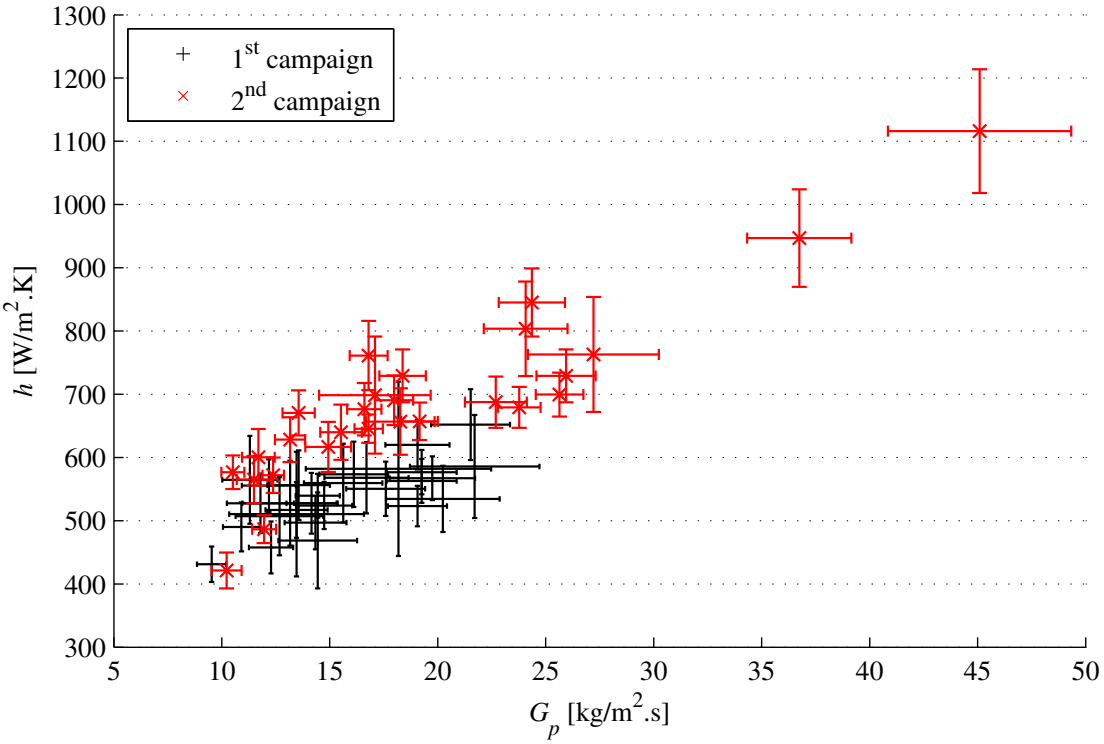

Figure 8: Coefficient d'échange de chaleur global en fonction du flux de solide avec les intervalles de confiance à 95 %.

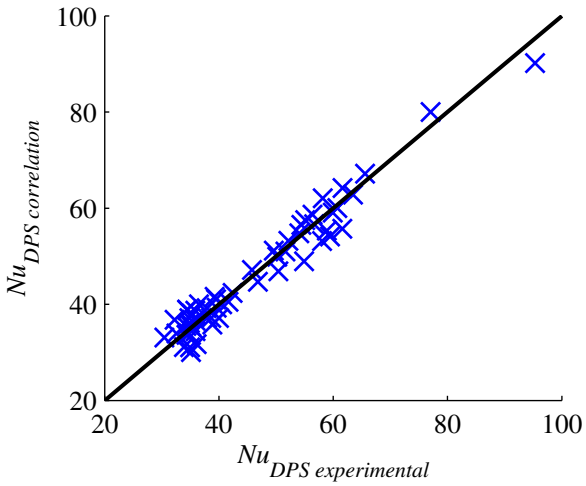

Figure 9: Nu_{DPS} corrélation en fonction de Nu_{DPS} expérimental.

Cette étude a donc montré qu'un de récepteur à suspension dense de particules peut atteindre des températures de particules en sortie de 750 °C, ce qui rend possible l'utilisation de cycles de conversion à haut rendement, et que le coefficient d'échange de chaleur paroi du tube-suspension était compris entre 400 et 1100 W.m-2.K-1 dans les conditions testées. Il est à noter que des flux de solide plus de 10 fois supérieurs ont déjà été obtenus par d'autres chercheurs [7] avec des suspensions denses et que cela devrait mener à une augmentation du coefficient d'échange. La corrélation sur le nombre de Nusselt qui a été établie sera utile pour le dimensionnement et le pilotage de futures centrales utilisant ce procédé.

Chapitre 3 : Simulation numérique 3D de la circulation d'une suspension dense de particules en circulation dans un tube sous chauffage uniforme

Afin de mieux comprendre l'écoulement des particules dans le tube et d'étudier les phénomènes d'échange de chaleur entre la paroi et le centre du tube, des simulations numériques ont été réalisées à partir d'une approche eulérienne n-fluides pour les écoulements fluide-particules turbulents polydisperses, développée et implantée dans le code NEPTUNE_CFD par l'IMFT (Institut de Mécanique des Fluides de Toulouse). Ce code, volumes finis, non structuré et parallèle, est développé dans le cadre du projet NEPTUNE, financé par le consortium Commissariat à l'Énergie Atomique (CEA), Électricité de France (EDF), Institut de Radioprotection et de Sûreté Nucléaire (IRSN) et AREVA.

L'approche eulérienne multiphasique est effectuée à partir des densités de probabilités jointes fluide-particules permettant d'obtenir les équations sur les moments de la vitesse des particules. Dans l'approche de modélisation multiphasique euler-euler utilisée, les équations de transport moyennées (masse, quantité de mouvement et énergie cinétique fluctuante) sont résolues pour chaque phase et couplées au travers de termes de transfert à l'interface. Les transferts d'énergie par convection et diffusion entre la phase gazeuse et la phase particulaire sont pris en compte, ainsi que le rayonnement entre particules selon l'approximation de Rosseland.

La géométrie simulée correspond au récepteur mono-tubulaire expérimental testé à Odeillo.

Le lit fluidisé nourrice et le tube sont représentés. Le diamètre intérieur du tube a été modifié (0,034 m au lieu de 0,036 m) pour correspondre au pilote froid testé au LGC sur lequel des simulations ont déjà été effectuées. Le système comprend 3 entrées : air de fluidisation, alimentation solide, air d'aération. Il y a 2 sorties libres : sortie caisson, sortie tube. Une perte de charge est imposée à la sortie du caisson pour reproduire numériquement le comportement de la vanne de régulation de la pression du ciel du lit utilisée pendant les expériences. Le maillage comprend environ 1 700 000 cellules hexaédriques (base ˜1,2 mm × 1,2 mm ; hauteur ˜1, 5 mm).

La Figure 10 est une photo prise au microscope électronique à balayage des particules de carbure de silicium utilisées. On voit que leurs formes sont très irrégulières avec une grande dispersion de taille. Leur diamètre de Sauter moyen est de 63,9 μm (diamètre d'une sphère ayant le même rapport volume sur surface). Du fait des formes très irrégulières des particules, l'expansion du lit était sous-estimée. Ce résultat est illustré par la Figure 11 qui montre l'évolution de la porosité du lit en fonction de la taille de particule, pour une vitesse de fluidisation Uf égale au double de la vitesse minimale de fluidisation mesurée pour cette taille de particule ($U_{mf} = 5 \times 10^{-3}$ m), lors d'une expansion homogène du lit obtenue analytiquement par inversion de la loi de traînée à partir de l'équation de quantité de mouvement. La valeur calculée est maximale du fait des nombreuses collisions se produisant dans le calcul numérique qui tendent à réduire cette expansion. De ce fait, les lois de traînée habituelles (Wen et Yu, Ergun) ne peuvent prédire précisément la porosité du lit pour cette distribution poly-disperse de particules non-sphériques. Un diamètre de particule de 40 μm a donc été imposé pour tenir en compte de ces phénomènes (cf Figure 11).

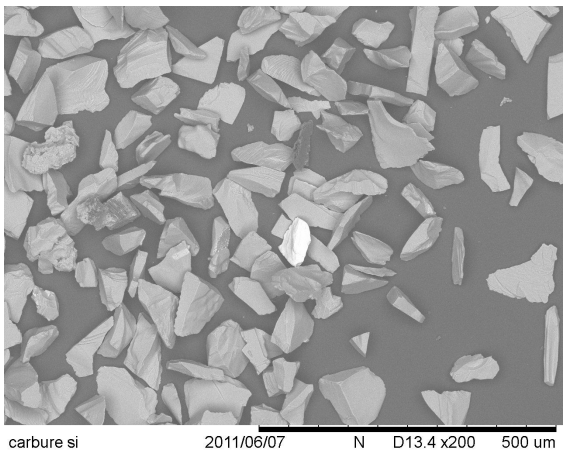

Figure 10: Photographie MEB des particules de SiC.

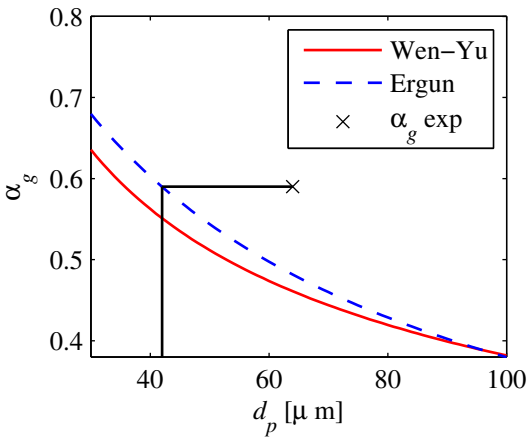

Figure 11: Porosité du lit en fonction de la taille de particule.

Les propriétés thermo-physiques des particules de SiC et de l'air sont fonctions de la température. Elles ont été codées sous formes d'équations fonctions de la température ou de l'enthalpie (les équations du code NEPTUNE_CFD fonctionnent avec l'enthalpie, il était donc nécessaire de calculer certaines propriétés avec l'enthalpie, avant que la température soit calculée). Les équations utilisées sont indiquées dans le Tableau 2.

La condition de chauffage imposée à la suspension dans le tube est une condition de densité de flux de chaleur. Cette condition a été choisie pour avoir la bonne valeur de flux de

Table 2: Propriétés des phases

Propriétés	**Valeurs/Équations**
	SiC particles
Diamètre	$d_p = 40\ \mu\text{m}$
Masse volumique	$\rho_p = 3210\ \text{kg/m}^3$
Capacité calorifique massique	$c_{p,p} = 8,564 \times 10^{-16} H_p^3 - 1,647 \times 10^{-9} H_p^2 + 1,39 \times 10^{-3} H_p + 717,5$ (1) in $\left[\text{J.kg}^{-1}\text{.K}^{-1}\right]$
Température	$T_p = 4,01 \times 10^{-16} H_p^3 - 7,35 \times 10^{-10} H_p^2 + 1,33 \times 10^{-3} H_p + 294,2$ (2) in [K]
	Air
Masse volumique	$\rho_g = \frac{P}{rT_g}$ (3) in $\left[\text{kg/m}^3\right]$
Capacité calorifique massique	$c_{p,g} = -1,346 \times 10^{-11} H_g^2 + 1,793 \times 10^{-4} H_g + 1003$ (4) in $\left[\text{J.kg}^{-1}\text{.K}^{-1}\right]$
Température	$T_g = -7,457 \times 10^{-11} H_g^2 + 9,931 \times 10^{-4} H_g + 293,3$ (5) in [K]
Viscosité dynamique	$\mu_g(T) = \mu_r \left(\frac{T_g}{T_r}\right)^m \frac{T_r+B}{T_g+B}$ (6) in [Pa.s] with $\mu_r = 1,716 \times 10^{-5}$ Pa.s, $T_r = 273,15$ K, $m = 1,54$, $B = 110,4$ K
Coefficient de diffusion laminaire	$LDC = -1,877 \times 10^{-17} H_g^2 + 5,878 \times 10^{-11} H_g + 2,631 \times 10^{-5}$ (7) in $\left[\text{kg.m}^{-1}\text{.s}^{-1}\right]$

chaleur. Dans le cas d'une condition de température, il aurait fallu ensuite imposer une condition d'échange de chaleur dans la couche limite permettant d'obtenir le flux mesuré. La densité de flux imposée est uniforme sur la circonférence du tube alors que dans la réalité, elle est plus importante à l'avant du tube, là où le soleil irradie directement le tube, que sur les côtés ou à l'arrière où le tube ne reçoit que du rayonnement réfléchi ou réémis par la cavité. Mais il était trop compliqué de mesurer la répartition du flux et c'est pourquoi cette approximation a été faite. Afin de reproduire au mieux les conditions expérimentales, des flux de chaleur négatifs ont été imposés après le passage dans la cavité. Ils correspondent aux pertes thermiques dans cette zone où le tube n'est pas isolé. Elles ont été estimées à l'aide de thermocouples placés dans le tube à l'extérieur de la cavité.

Trois cas expérimentaux ont été simulés : un cas débit de solide moyen-température moyenne initialement pris comme référence (Ref), un cas haut débit-température moyenne (HQ) et un cas bas débit-température haute (HT). Les conditions limites correspondant aux caractéristiques de chaque cas sont indiquées dans le Tableau 3. F_p est le débit de solide injecté, F_f le débit d'air de fluidisation, F_A le débit d'air d'aération, $T_{p,iDiFB}$ la température du lit fluidisé et $\varphi_{1/2/3}$ les densités de flux de chaleur imposées dans les différentes zones du tube.

Table 3: Conditions aux limites imposées

Case	F_p [kg/h]	F_f [kg/h]	F_A [kg/h]	$T_{p,iDiFB}$ [K]	φ_1 [kW/m^2]	φ_2 [kW/m^2]	φ_3 [kW/m^2]
Ref	59,8	0,483	$8,92 \times 10^{-2}$	575	128,9	120,9	20
HQ	147,4	0,483	$8,92 \times 10^{-2}$	601	189,7	172,6	25
HT	32,8	0,483	$1,78 \times 10^{-1}$	782	107,3	159,7	17

Les résultats montrent que les simulation surestiment le phénomère de recirculation, ce qui a pour effet d'augmenter la température dans la partie basse du tube. La Figure 12 montre les profils verticaux de température simulée au centre du tube et à 5 mm de la paroi et les mesures pour le cas HQ qui est le plus proche des valeurs expérimentales. Cela vient du fait que l'infuence de la recirculation diminue avec le débit. C'est une bonne nouvelle puisque l'application du procédé à grande échelle nécessitera de forts flux de solide pour maintenir une valeur raisonnable de température en sortie de tubes plus longs. Le modèle sera donc applicable dans ce cas.

Les profils radiaux à différentes hauteurs des simulations ont mis en évidence le forte influence de la température sur la vitesse de l'air par l'intermédiaire de sa masse volumique à été mise en évidence. La vitesse de l'air affecte ensuite l'ensemble des paramètres. Augmenter la vitesse de l'air elle diminue la fraction volumique de solide et augmente les variances de vitesses radiales et verticales des particules. La variance de la vitesse radiale des particules est largement supérieur à l'agitation particulaire sur tout le diamètre du tube cequi indique que le transfert de chaleur depuis la paroi du tube jusqu'au centre est dû au mouvement collectif des particules et non pas à l'agitation particulaire.

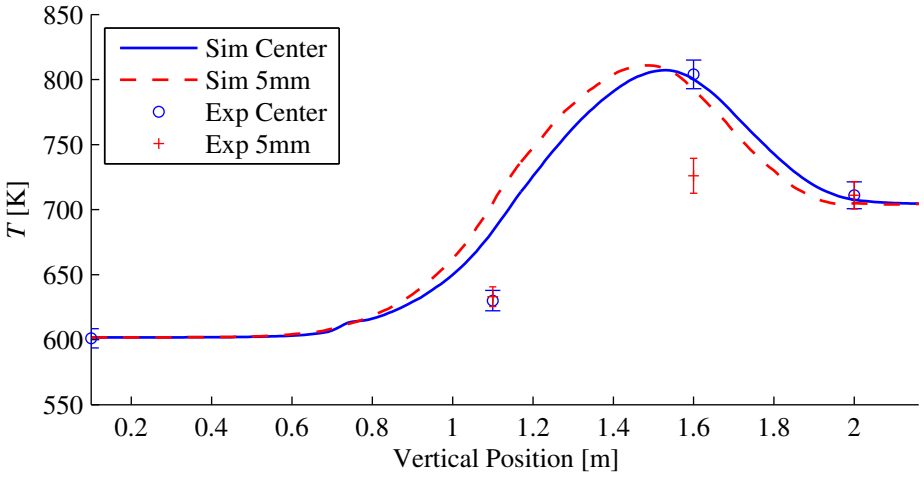

Figure 12: Profils verticaux de température au centre du tube et à 5 mm de la paroi pour le cas HQ.

Chapitre 4 : Étude d'un récepteur solaire pilote multitubulaire à suspension dense de particules de 150 $\mathrm{kW_{th}}$

Un récepteur solaire expérimental fonctionnant en boucle fermée à 16 tubes d'une puissance de 150 kWth a été testé au grand four solaire d'Odeillo afin de vérifier l'applicabilité du procédé de suspension dense de particules en écoulement ascendant à une échelle pilote en fonctionnant en boucle fermée. La Figure 13 donne le schéma du récepteur. L'ingénierie de détail et la construction de ce pilote ont été réalisées par l'entreprise COMESSA, partenaire du projet CSP2.

Le principe de fonctionnement de ce récepteur est le même que celui du récepteur mono-tubulaire. Les équipements supplémentaires permettent d'obtenir une circulation des particules en boucle fermée, ce qui n'avait pas été possible pour l'installation mono-tubulaire. Un lit fluidisé refroidisseur placé après le lit collecteur permet de refroidir le solide avant son retour dans la partie chauffante de la boucle.

En amont des tests sur le récepteur, des mesures de flux de flux solaire ont été effectuées pour caractériser la distribution du flux. Les héliostats ont été paramétrés afin d'avoir une densité de flux la plus uniforme possible en entrée de cavité. La Figure 14 montre les cartes de flux au niveau de l'entrée pour les 3 réglages utilisés (3 puissances). Des mesures de densité de flux au fond d'une cavité expérimentale "maquette" réalisées grâce à un fluxmètre inséré dans dans la paroi ont montré qu'en se plaçant hors du plan focal de la parabole la répartition du flux n'est plus uniforme, ce qui a engendré une non-uniformité des températures de tubes. Ceci a limité la température maximale moyenne de la suspension en sortie des tubes du fait du mélange entre le solide venant des tubes les plus chauds avec celui venant de tubes plus froids.

L'ensemble des gammes de paramètres opératoires explorées et des résultats obtenus sont présentées dans le Tableau 4. Les résultats indiqués sont des valeurs moyennées sur des périodes stables de 30 minutes au moins et allant jusqu'à plusieurs heures (le récepteur pilote a fonctionné plusieurs journée sans interruption du matin au soir). $\Phi_i n$ est la puissance solaire entrante, ΔT la différence de température entre le lit fluidisé nourrice et le le

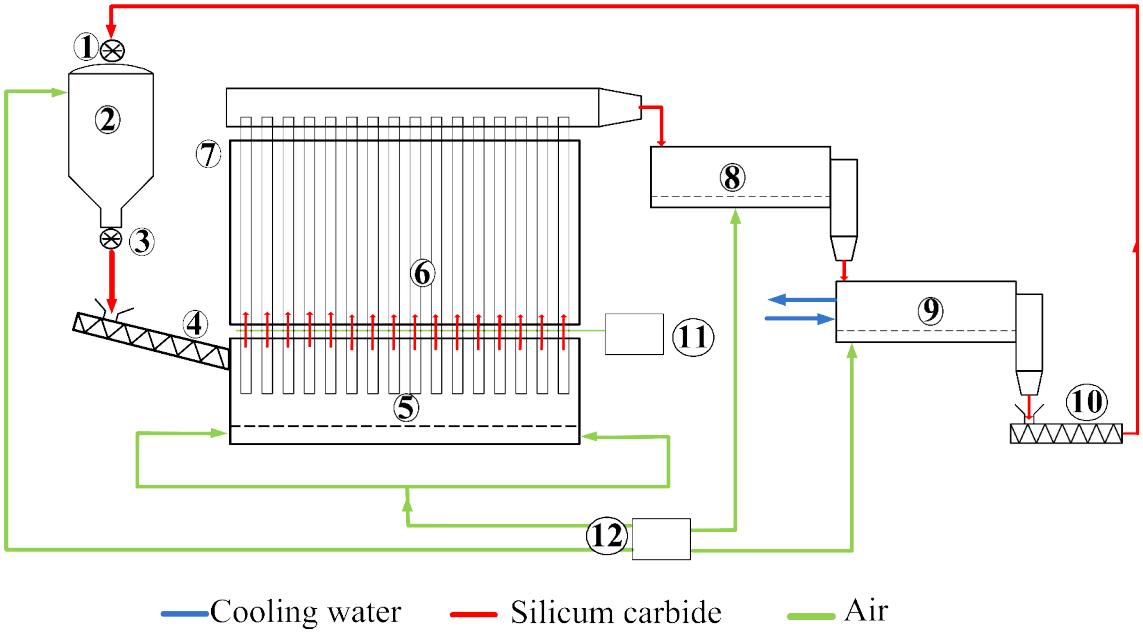

Figure 13: Schéma de fonctionnement de la boucle pilote à récepteur multitubulaire. 1) Vanne rotative 1, 2) Réservoir de stockage, 3) Vanne rotative 2, 4) Vis sans fin d'alimentation,5) Lit fluidisé nourrice, 6) Tubes irradiés, 7) Cavité réceptrice, 8) Lit fluidisé collecteur, 9) Lit fluidisé de refroidissement, 10) Vis sans fin de retour, 11) Aération, 12) Alimentation en air comprimé.

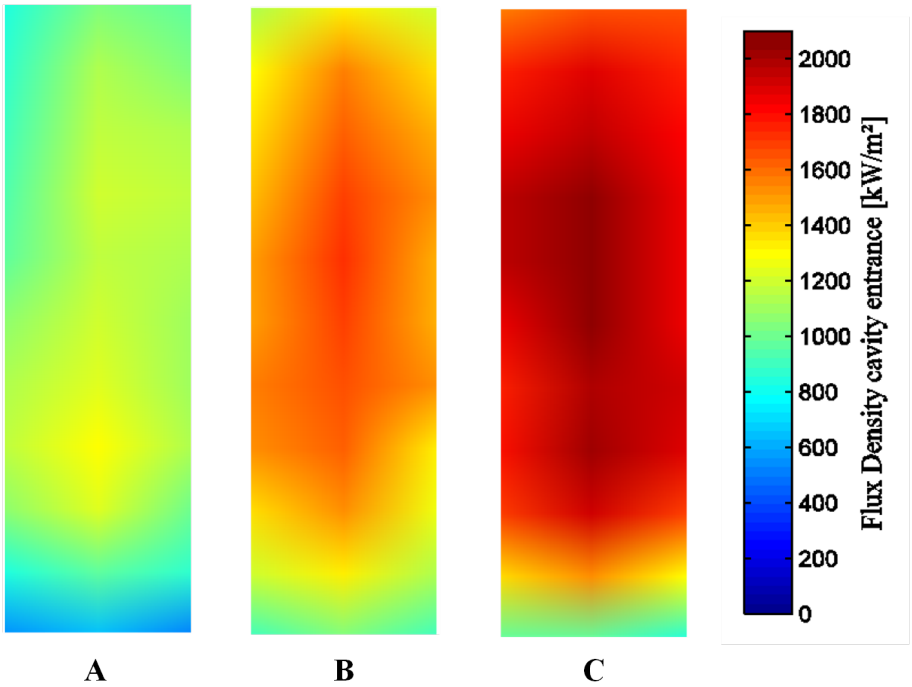

Figure 14: Densités de flux en entrée de cavité pour 3 différents réglages (Dimension de l'entrée de cavité : hauteur = 50 cm, largeur = 15cm).

lit fluidisé collecteur, $T_{w,tubes}$ la moyenne des températures de paroi des tubes, T_{ColFB} la température entre du lit fluidisé collecteur et $\Delta P/L$ la variation de linéaire pression avec la hauteur.

Table 4: Gammes des paramètres opératoires et des résultats obtenus.

Paramètres opératoires				**Résultats**					
$\Phi_i n$	F_p	G_p	T_{DiFB}	ΔT	$T_{w,tubes}$	$T_{p,i}$	$T_{p,o}$	T_{ColFB}	$\Delta P/L$
[kW]	[kg/h]	[kg/m^2.s]	[°C]	[°C]	[°C]	[°C]	[°C]	[°C]	[Pa/m]
63-142	662-1759	17-44	43-184	137-335	366-625	69-251	217-495	188-433	11340-11780

Le rendement thermique du récepteur a été calculé en divisant la puissance absorbée par la suspension, calculée par bilan d'enthalpie entre l'entrée et la sortie de la cavité, par la puissance solaire entrante, connue grâce aux précédentes mesures de flux et à la mesure en continue de l'irradiation normale directe. La Figure 15 montre l'évolution du rendement en fonction du flux de solide, pour les 3 configurations de flux solaire testées. Le choix de la température de sortie était incertain. En effet, la répartition non-uniforme du flux solaire sur les différents tubes a entraîné une distribution inégale, et non-mesurée, du flux de solide entre les tubes. Ainsi la puissance calculée en utilisant la température moyenne de sortie des tubes surestimait probablement le débit (les tubes avec plus de débit sont moins chauds en sortie) tandis que la puissance calculée en utilisant la température du collecteur sous-estimait le débit (pertes thermiques avant et dans le collecteur). Les rendements affichés sur la Figure 15 ont été calculés avec la température du collecteur et sont donc une estimation basse. Malgré cela, on voit que la cavité réceptrice a été bien conçue et que le procédé fonctionne de manière très satisfaisante puisque des rendements allant jusqu'à 90 % ont été atteints. Les tests sur ce récepteur pilote ont donc prouvé que le procédé de récepteur à suspension dense de particules était applicable en boucle ferméeà grande échelle.

Chapitre 5 : Modélisation de la cavité d'un récepteur solaire multitubulaire

Pour compléter l'analyse des résultats du pilote de récepteur multitubulaire, un modèle de ce récepteur a été réalisé. Il combine la méthode de Monte-Carlo de lancer de rayon, pour modéliser le flux solaire, et la méthode des radiosités, pour la détermination des échanges radiatifs à l'intérieur de la cavité. Le four solaire d'Odeillo, où les essais ont été effectués, a été modélisé avec le logiciel Solfast-4D. Ce logiciel a fourni les cartes de densité de flux solaire sur les parois de la cavité qui ont été utilisées comme conditions pour le modèle de cavité réceptrice réalisé avec ANSYS Fluent.

Lors de la modélisation du concentrateur solaire, les propriétés optiques ont été optimisées séparément pour chaque héliostat à partir de mesures du flux solaire effectuées dans le plan focal de la parabole. La Figure 16 donne un exemple des cartes de flux obtenues

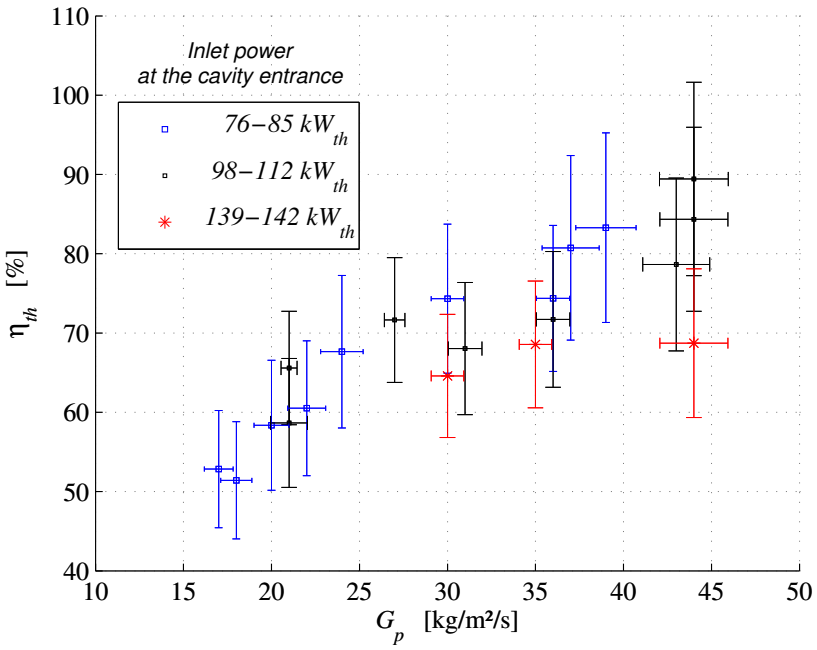

Figure 15: Rendement thermique du collecteur en fonction du flux de solide.

grâce à ces mesures et la Figure 17 illustre la correspondance entre la mesure et le modèle. Dans un second temps, les configurations de tir des héliostats ont été reproduites pour simuler le flux combiné de l'ensemble des héliostats utilisés pour les essais expérimentaux du récepteur multitubulaire. Le modèle a été capable de reproduire précisément le flux solaire comme le montre le profil de densité de flux en entrée de cavité de la Figure 18.

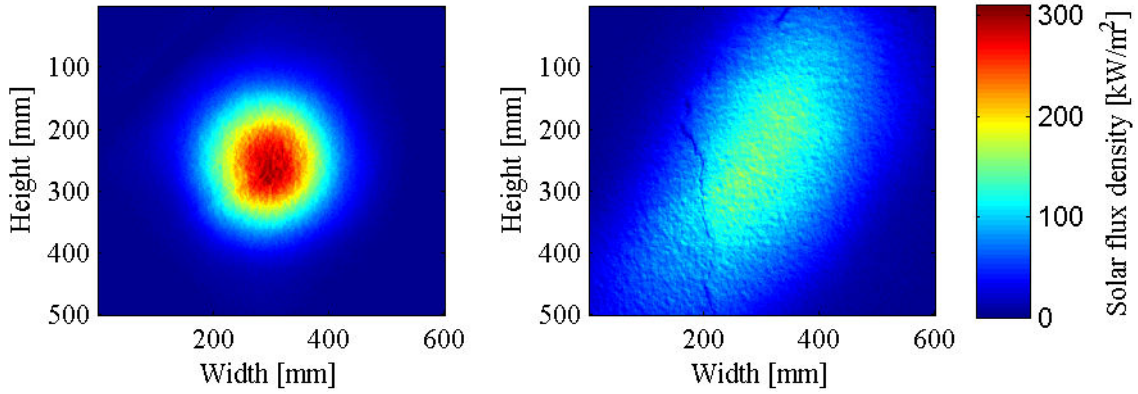

(a) H34. (b) H67.

Figure 16: Cartes de densité de flux en entrée de cavité pour les héliostats H34 et H67.

Après avoir modélisé le concentrateur solaire, nous avons modélisé la cavité réceptrice à l'aide du logiciel ANSYS Fluent. La hauteur de la cavité est 1 m, l'ouverture fait 15 cm de large et 50 cm de haut. 16 tubes verticaux organisés en 2 faisceaux de 8 tubes placés au fond de la cavité la traversent.

Pour la modélisation d'une géométrie complexe telle que celle-ci, le modèle des radiosités (Surface-to-Surface dans Fluent) a été utilisé puisqu'il permet de calculer précisément les

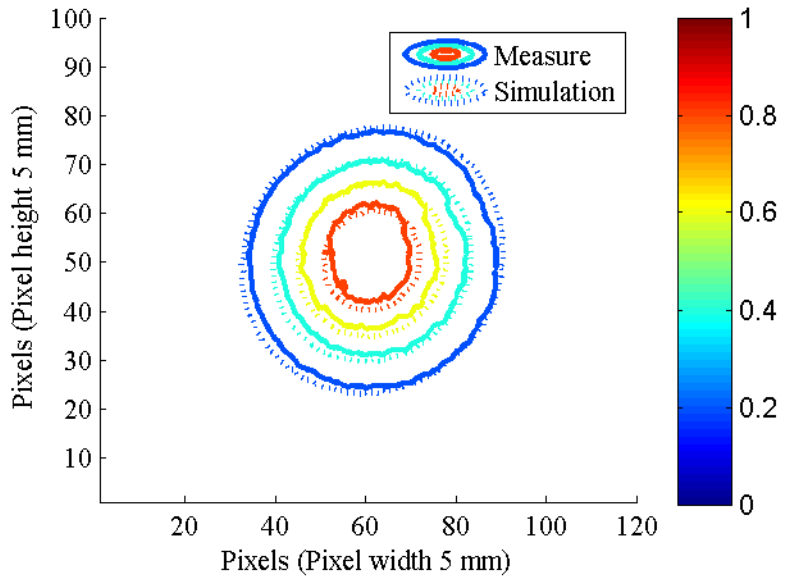

Figure 17: Contours de densités de flux normalisées pour l'héliostat H34 (erreur optique = 1,315 mrad).

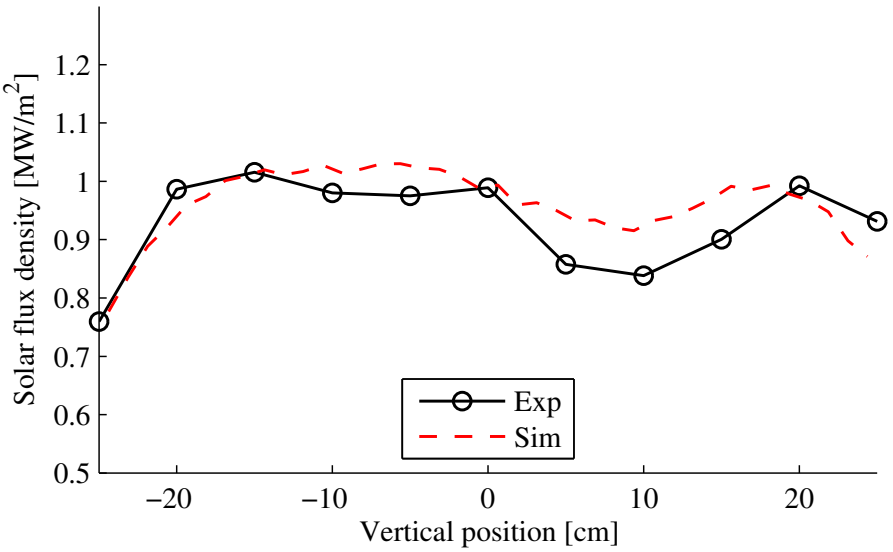

Figure 18: Profils verticaux de densité au milieu de l'ouverture de la cavité.

échanges entre surfaces rayonnantes grâce aux calculs de facteurs de formes. Ce modèle considère que toutes les surfaces sont des corps gris diffus. Les tubes dans la cavité ont été peints avec de la peinture Pyromark 2500 (peinture silicone haute température de Tempil) dont émissivité dans l'infrarouge vaut 0,88. L'isolant était composé de silice et de carbonate de calcium et son émissivité était 0,2. L'ouverture de la cavité est libre pour l'air, à pression atmosphérique. Un coefficient de convection appliqué aux parois d'isolant a permis de représenter les pertes par conduction. Un profil de température et un coefficient de convection à l'intérieur des tubes ont permis de représenter l'échange de chaleur avec la suspension en circulation, qui n'était pas simulée dans ce modèle.

Le coefficient de convection appliqué aux parois d'isolant a été adapté afin de reproduire la valeur de densité de flux de conduction à travers le matériau estimée grâce à des thermocouples insérés dans la paroi. Pour les tubes, du fait de la non-uniformité du flux solaire et du débit de solide inégalement réparti, il a fallu appliquer des profils de température et des coefficients de convection propres à chaque tube pour obtenir des températures de paroi correspondant à celles mesurées.

Le modèle a été appliqué à un cas expérimental et validé en comparant les températures à l'arrière des tubes où sont placés les capteurs. Les Figures 19, 20 et 21 montrent ces températures à mi-hauteur, en bas et en haut de la cavité respectivement. L'accord n'est pas parfait (il faudrait pour cela optimiser encore les valeurs de coefficient de convection et les profils de température) mais il est suffisant pour pouvoir tirer des conclusions concernant la répartition du flux entrant entre pertes par convection et rayonnement à travers l'ouverture, pertes par conduction à travers l'isolant et chaleur transmise aux particules.

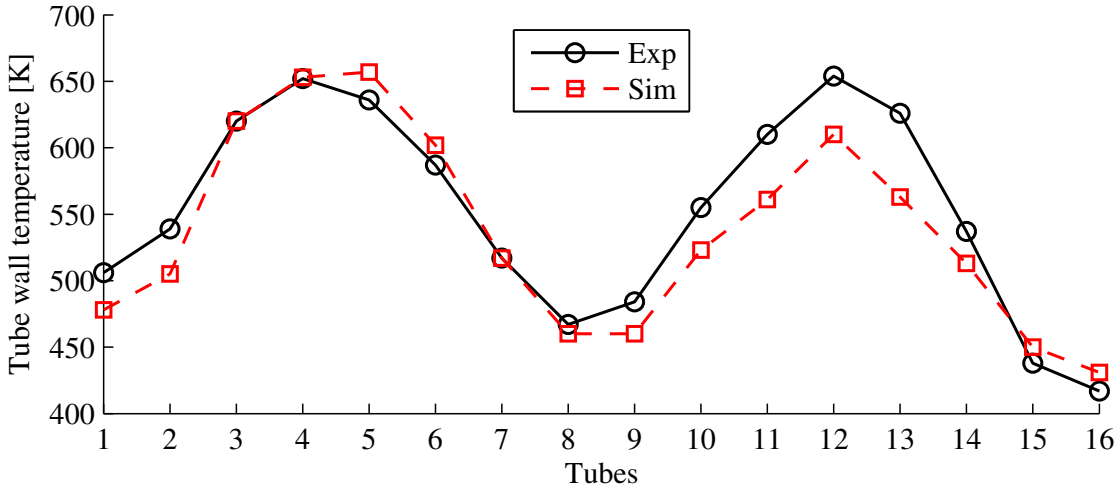

Figure 19: Températures à l'arrière des tubes à mi-hauteur dans la cavité.

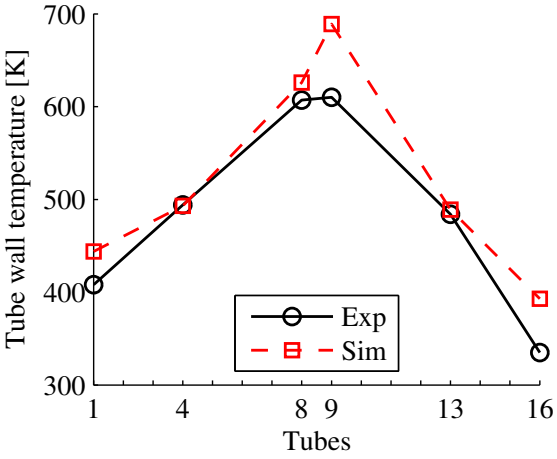

Figure 20: Températures à l'arrière des tubes, en bas de la cavité.

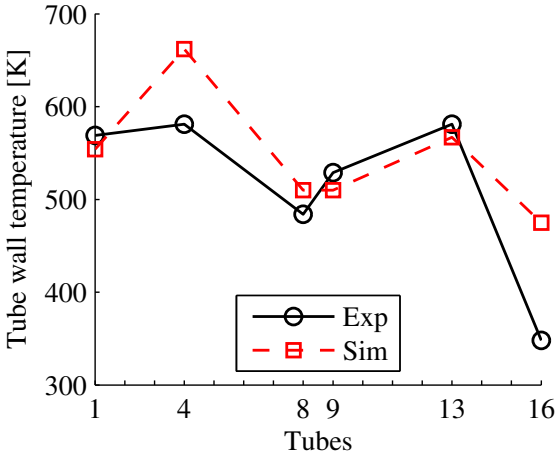

Figure 21: Températures à l'arrière des tubes en haut de la cavité.

Les résultats ont montré que la cavité a été bien conçue puisque seulement 1,3 kW sur les 84 kW de flux solaire en entrée sont réfléchis sans être absorbés. De plus le flux rayonné à travers l'ouverture n'est que de 2,9 kW. Les pertes à travers l'isolant sont elles aussi faibles et ne valent que 2,3 kW. La principale perte de chaleur est due à la convection avec l'air entrant dans la cavité du fait du courant créé par son échauffement et sa dilatation au contact des parois chauffées. Cette perte par convection est de 10,9 kW. Les 66,6 kW restants sont transmis à la suspension à travers la paroi des tubes.

Ainsi, on a pu confirmer que l'estimation de la chaleur transmise est bien sous-estimée par le bilan d'enthalpie utilisant la température du collecteur comme température de sortie (56,7 kW prévus). L'estimation avec la température moyenne de la suspension dans les tubes surestime cette valeur (72,7 kW prévus) mais elle est dans le cas étudié plus proche que l'autre estimation. Pour la suite de ce travail, il faudra affiner encore les coefficients de convection et les profils de températures appliqués aux tubes dans le cas déjà étudié. Par ailleurs, le modèle sera appliqué à d'autre cas expérimentaux ce qui permettra pour ceux-là aussi de déterminer précisément le flux de chaleur transféré à la suspension dense de particules. Si possible, une relation entre la valeur réelle du flux absorbé par les particules et les estimations par bilan d'enthalpie sera établie qui permettra de connaître le flux réel sans modéliser chaque cas.

Conclusion et perspectives

Les études menées au cours de cette thèse et dans le cadre du projet CSP2 ont permis de prouver que le procédé de récepteur solaire tubulaire à suspension dense de particules en écoulement ascendant fonctionnait en conditions réelles d'exposition au flux solaire concentré. Des températures de particules en sortie de cavité allant jusqu'à 750 °C ont été obtenues avec un récepteur expérimental mono-tubulaire, ce qui ouvre la possibilité d'utiliser ce type de récepteur avec des cycles de conversion à haut rendement comme les cycles de Brayton ou les cycles combinés.

L'analyse des simulations numériques 3D de l'écoulement dans un tube sous chauffage uniforme pour différentes valeur de flux de solide et à différentes températures a permis

de mieux comprendre le comportement de l'écoulement et les mécanismes de transfert de chaleur depuis la paroi jusqu'au centre des tubes. La forte influence de la température a notamment été mise en évidence.

Les expérimentations sur un récepteur multitubulaire d'une puissance de 150 kWth et de la boucle solide associée ont montré l'applicabilité du procédé à une échelle pilote en condition représentative d'un système solaire en boucle fermé.

La modélisation de ce récepteur par combinaison de la méthode du lancer de rayon de Monte-Carlo et de la méthode des radiosités a été validée. Elle permet de déterminer précisément la répartition du flux solaire entrant dans la cavité entre les pertes par convection et rayonnement et la chaleur effectivement transmise à la suspension dense de particules. Ce modèle sera appliqué à l'ensemble des résultats du pilote multitubulaire pour affiner leur analyse.

Il sera intéressant de continuer l'analyse du procédé afin de mieux comprendre l'écoulement et d'observer l'effet de la température et de la hauteur du tube sur le transfert. Ce projet a ouvert des perspectives pour d'autres projets à venir. En janvier 2016 débutera le projet SOLPART qui s'intéressera à la possibilité d'utiliser ce procédé pour traiter des minerais, et en particulier pour produire de la chaux par calcination.

D'autre part, un projet de récepteur de 4 MWth à installer à la centrale solaire Thémis, avec production hybride (solaire + carburant fossile) d'électricité grâce à une turbine à gaz, sera prochainement déposé.

Bibliography

[1] FP7 EC project CSP2. http://www.csp2-project.eu.

[2] M.T. Dunham and B.D. Iverson. High-efficiency thermodynamic power cycles for concentrated solar power systems. *Renewable and Sustainable Energy Reviews*, 30:758–770, 2014.

[3] N. Woudstra, T. Woudstra, A. Pirone, and T. van der Stelt. Thermodynamic evaluation of combined cycle plants. *Energy Conversion and Management*, 51(5):1099–1110, 2010.

[4] V. Gnielinski. On heat transfer in tubes. *International Journal of Heat and Mass Transfer*, 63:134–140, 2013.

[5] Y.-T. Wu, C. Chen, B. Liu, and C.-F. Ma. Investigation on forced convective heat transfer of molten salts in circular tubes. *International Communications in Heat and Mass Transfer*, 39:1550–1555, 2012.

[6] X. Cheng and N. Tak. Investigation on turbulent heat transfer to lead-bismuth eutectic flows in circular tubes for nuclear applications. *Nuclear Engineering and Design*, 236(4):385–393, 2006.

[7] G. Turzo. *Transport par fluidisation en phase hyperdense : amélioration technologique and modélisation et dimensionnement (in French) (Hyperdense phase transport by fluidization: technological improvement and modeling and design).* PhD thesis, Institut National Polytechnique de Toulouse (INP Toulouse), 2013.

General Introduction

Overview and Outlook of Concentrating Solar Power Technologies

Solar power is one of the renewable and clean energy sources that will be part of solving the current energy and environmental crisis. Concentrating Solar Power (CSP) systems may efficiently produce high temperature heat and electricity. Thanks to heat storage, this production can be continuous, or used when needed to complement other renewable energy technologies whose electricity generation is variable. Hybrid plants combining fossil fuel and solar energy are another option for stable electricity production with low CO_2 emission when combined with large heat storage [1]. CSP plants can therefore be easily integrated to the power grid. This technology, even if it is still improving, is mature, with power plants that have been in operation for consequent time periods and recent projects of several hundreds of MW_e. The plant design is well defined [2]. Moreover, CSP can also be used to produce solar fuels [3]. The CSP local and global potential is currently being studied [4–9]. According to the scenario established by the International Energy Agency (IEA) in 2014 [10], technologies will gradually mature and investment costs gradually fall until 2020. Global capacities will jump to 260 GW_e by 2030 (at the end of 2013, the total capacity was 3.6 GW_e with an annual installed capacity of 882 MW_e). By 2050 they reach 980 GW_e. This represents capacity increases of 27 GW_e per year on average, with a five-year peak of 40 GW_e per year from 2040 to 2045. Thermal storage is a key feature of CSP plants all along, and capacity factors grow regularly with increased solar field sizes and storage capacities, reaching on average 45 % (10.8 hours) in 2030. This allows the amount of solar thermal electricity to reach about 1 000 TWh by 2030, and 4 380 TWh by 2050, thus providing 11 % of the global electricity mix.

In CSP plants, reflectors concentrate the solar radiation onto a receiver. The receivers can differ in shape, size or composition, but their common purpose is to absorb the concentrated solar radiation and transmit it to a Heat Transfer Fluid (HTF). The HTF transports the heat to the energy conversion sub-system that includes heat storage, heat exchangers, an optional burner for fuel back-up, and a power block. Various thermodynamic cycles are available, each with its own range of working temperature. They are mainly Rankine cycles [11] (with saturated or super-heated steam) for large power plants, Brayton [12] and Stirling [13] cycles for medium and small-scale facilities. The type of thermodynamic cycle puts a constraint on the type of HTF to use. At the same time, the HTF's working conditions limits result in constraints on the solar receiver.

Each concentrating solar technology has its own reflector configuration to concentrate the sunrays onto a line or a central point, where the receiver is located. This leads to the distinction between linear systems (parabolic trough [14–17], linear Fresnel [17, 18] and point focusing systems (parabolic dish [19], central tower [20, 21]). The solar concentration ratio of linear systems is limited (< 100), while it is much higher for point focusing systems (in the range 300-1500). As a consequence, for identical solar power received, linear systems have a larger receiver surface than point focusing systems. In addition, the larger the receiver surface, the more important the heat losses. Therefore, linear systems have a lower thermal efficiency than point focusing systems, and their HTF temperature is limited (maximum 400 °C for parabolic trough), which compensates for the large heat exchange surface. According to Carnot's theorem, the hotter the HTF gets out of the receiver, the higher the efficiency of the energy conversion cycle will be [2, 22]. Hence, point

focusing systems have the potential to reach much higher solar-to-electricity conversion efficiency than linear systems. However, due to the receiver's heat losses that increase with temperature, an optimum temperature appears that depends on both the receiver design (configuration and materials) and the type of energy conversion cycle [23]. The parabolic dish strong point is to combine all the systems' components in a compact unit, which is perfect for a small delocalized electricity production (generally a few kW_e per unit, maximum 20). But its cost relative to the electrical power output is very high, which makes it unadapted to grid-scale electricity production. Finally, the best option for efficient and large scale electricity production is the solar tower, also called central receiver system. This technology cost is still high compared to linear systems, but current research focused on improved efficiency, as well as the increasing number of power plants installed, will lead to significant Levelized Electricity Cost (LEC) reductions. The current goal set by the American Department of Energy is reaching 0.06 $/kWh$_e$, or below, by 2020 [24].

Central Receiver Systems

In solar towers, sun-tracking heliostats reflect solar radiation to the top of a tower where the receiver, or solar absorber, is located. Various types of central solar receivers exist and have been assessed [20, 21]. There are two keys for these receivers to lead to highly efficient systems. The first, as mentioned, is to produce high temperature heat ($>$ 700 °C) that allows using high efficiency conversion cycles such as Brayton or combined cycles [23]. The second is to work at high concentration ratio, which reduces the receiver surface and, as a consequence, its heat losses [21]. Both conditions put constraints on the HTF that must be able to sustain high temperature and must have a high capacity for absorbing heat from a solid wall to prevent the receiver from overheating under high solar flux conditions.

Tubular receivers were designed for either liquid or gas HTFs. Tubular liquid receivers [25, 26] generally consist in an array of thin-walled tubes that are arranged to shuttle the working fluid in multiple passes through incident concentrated sunlight. The tube size and wall thickness are selected to maximize heat transfer while minimizing pumping losses, thus resulting in an optimum diameter. Current industrial power plants use this type of receiver with water/steam or nitrate salts as HTF. These existing HTF have drawbacks, in particular a limited working temperature domain for molten salts (typically 240-565 °C for binary sodium-potassium nitrate salt) and very high pressure for steam. Other prospective options, such as liquid metals, permit high flux limit on the receiver and extend operation to temperatures higher than 565 °C, as described by Pacio [27]. But this kind of HTF is highly corrosive and hazardous which explains why there is currently no industrial application. For tubular gas receivers, the main challenge is to overcome the limited convective heat transfer between the tube wall and the gas. Various prototypes have been developed [28–31]. The possible candidates are air, CO_2, helium and hydrogen. Presently, the possibility of using high efficiency supercritical CO_2 (s-CO_2) Brayton cycles with CSP leads to a particular interest in receivers using s-CO_2 as HTF [32].

Volumetric receivers [33] were conceived to let the concentrated solar radiation enter the absorber, which is a porous medium made of metallic wires or ceramic foam in this case. This way, the whole solid volume gets heated up and the external temperature is lower than it is for surface absorbers, which reduces the infrared radiation heat losses. The porous

structure acts as a convective heat exchanger where the HTF, mainly air, receives heat from the solid absorber. The big challenges of this kind of receiver are the unstable flow and heterogeneous heating caused by changes of the temperature-dependent working fluid properties, in particular viscosity and density, which may lead to overheating and local failures in the receiver material. Lastly, particle receivers work following various concepts. They are detailed in the next section.

Currently, even if the direct saturated steam generation technology is the most mature central receiver technology (PS10 started operation in 2007), the most efficient and complete (including storage) solar tower power technology is based on molten salt. In this design the nitrate salt is used as both HTF and energy storage medium. After the first commercial plant in operation in 2011 (Gemasolar, 20 MW, 15h storage), the biggest plant using this technology, Crescent Dunes (Nevada, USA), will start operation in 2015 with a production of 110 MW_e and 10 hours of thermal storage (500 GWh/year) [34]. Other projects are currently developed in Morocco, South Africa, Chile, China. Commercially used salt is the "solar salt" that is a binary compound of KNO3 and NaNO3, because of its good heat transfer properties. But the worldwide production of this component is limited, which is why alternative HTFs made from inexpensive and earth abundant materials are being intensively investigated [35]. More generally, molten salts are highly corrosive and require expensive alloys to be used as containment material. They are liquid in a limited temperature range before their decomposition (221-600 °C for solar salt). Therefore a heat tracing of the pipes and storage tanks is required that leads to parasitic energy consumption. Moreover, the upper temperature bound limits the energy conversion efficiency to a maximum of 42 % achieved with subcritical steam Rankine cycles [23].

Particle Receivers

General Principle

A general diagram of the complete setup using a solid particle receiver is given in Figure 22. The loop is composed of a solar receiver that delivers the particles to a hot storage tank , which feeds a fluid bed heat exchanger, where the particles transmit their energy to submerged tubes inside whose a working fluid (for example steam) is generated, the latter is then expanded in a turbine. Fluid bed heat exchanger is a classical device in the electrical power industry (mostly implemented for coal combustion in fluidized bed). The cooled particles exit the exchanger (continuous circulation) and are sent towards the cold storage tank; this can be done by either mechanical or pneumatic conveying or by gravity depending on the available space and on the facility geometry (tower configuration is particularly favorable to gravity for instance). Finally, connecting the cold bin to the solar receiver inlet by a conveying system raising the particles completes the loop. Consequently, solid particles are used as both the HTF and the heat storage medium. Actually, it should be noted that the proposed solar power plant is combined with a vapor cycle and steam turbine, but the system is very similar in the case of a gas turbine or a combined cycle, the main difference being the heat exchanger, which is adapted to the chosen type of turbine. In this concept, the particle solar receiver is the key component. The next paragraphs summarize the state-of-the-art in the field of solar receivers using particles as HTF.

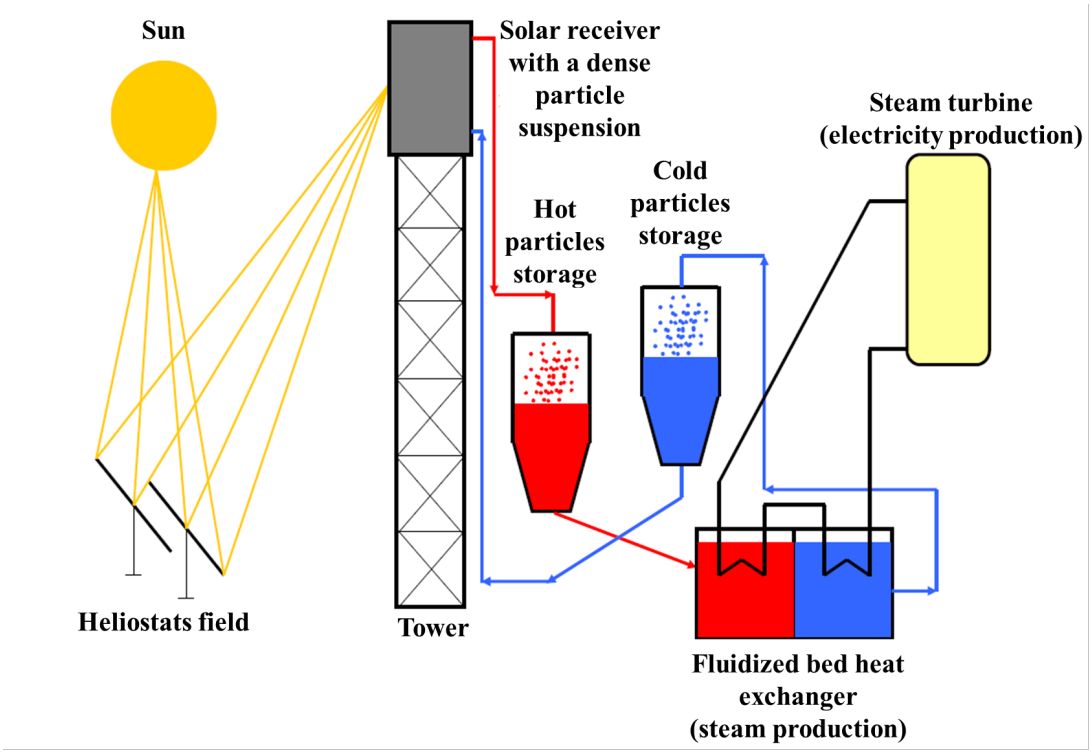

Figure 22: Schematic view of a thermal CSP plant with a receiver using particles as HTF.

State-of-the-Art of Particle Receivers

Solid particles may be used as a HTF in solar thermal concentrating systems in direct heating and indirect heating receivers. In the former case solid particles absorb directly the concentrated solar radiation, and in the latter case a heat transfer wall is used: the wall absorbs solar radiation and transfers the heat to a flowing heat transfer medium. In particular, tubular absorbers are mainly used in current solar thermal power plants. Solid particle solar receivers associated with solar tower concentrating systems offer very interesting options for high temperature and high efficiency power cycles, thermal storage integration (using the same particles as HTF and storage medium) and chemical applications of concentrated solar energy (thermo-chemical water splitting process to produce hydrogen, cement and ore processing, for example).

The first studies on direct absorption solar receivers started in the early 1980s with three concepts, the fluidized bed receiver [36], the falling particle curtain [37] and the rotary kiln receiver [38]. In the first concept, the solid particles are fluidized in a transparent tube but do not flow outside, there is no solid circulation. Consequently the system was used to heat air and to process reactive particles in batch operation, as indicated by Flamant et al. [39]. In the free falling particle curtain, particle selection and radiative heat transfer modeling have been proposed by Falcone et al. [40] and Evans et al. [41]. The French National Center for Scientific Research (in French: Centre National de la Recherche Scientifique = CNRS) developed a "Sand heater loop" using sand particles as HTF [38]. It combined a solar rotary kiln that delivered hot sand to a heat storage / heat recovery sub-system consisting of a hot and a cold heat storage bins and a multistage fluidized heat exchanger. In the particle curtain concept, the divided solid is dropped directly into the

concentrated solar beam from the top of the receiver and heated during the time of its pass through the concentrated radiative receiver. After about twenty years without any new development, this concept was again considered and proposed as a promising option for a new generation of high temperature solar thermal concentrating plants. Improved models have been developed [42] and validated by on-sun experiments at pilot scale [43]. The receiver prototype was tested at the National Solar Thermal Test Facility (NSTTF) in Albuquerque NM, USA. The cavity receiver was 6.3 m in height by 1.85 m in width and 1.5 m in depth with a 3 m high and 1.5 m wide aperture. Selected particles were aluminosilicate containing 7 % of Fe_2O_3 (marketed as CARBO HSP 20/40) with 697 μm mean diameter. Batch runs were performed from 3 min to about 7 min (for a total particle inventory of about 1800 kg). Measured temperature increase (from ambient temperature) during experiments ranged from 100 °C to about 250 °C for a single pass and solar power in the range 1.58-2.5 MW_{th}. The receiver efficiency increased generally with the particle flow rate and varied from about 35 % to 52 %, thus in good agreement with simulated data. A review of the falling particle receiver studies was proposed by Tan and Chen [44] with emphasize on the effect of wind speed on the receiver performances. Particle aerodynamics in this type of receiver is affected by the wind and various parasitic air flows inside the cavity induced by the falling particles and by the convection due to temperature difference, as well as by air jet flow if an aerowindow is used [45]. These effects may be partially avoided by using Röger et al.'s face-down solid particle receiver concept [46] in which the particle curtain lines the inner wall of a cylinder closed at its top; the bottom part facing the concentrated solar beam. In this study, a circa 350 MW_{th} receiver placed at the top a 309 m high tower surrounded by an heliostat field was modeled. It was shown that solid recirculation improves drastically the receiver efficiency from 79 % to 90 % at full load and from 45 to 86 % at 50 % load. The design of the falling-particle cavity receiver prototype developed at Sandia Albuquerque was described by [47]. The discrete phase model was used to simulate the flow behavior and temperature increase of the particle curtain. The parametric study shows that the operating parameter window that allows reaching 90 % efficiency, 200 °C particle temperature increase and back wall temperature less than 1200 °C is very narrow. Operation strategies of such receivers have been CFD-simulated by [48], who demonstrated that efficiency in excess of 90 % can be reached for face-down design receiver.

The Small Particle Heat Exchanger Receiver (SPHER) concept was demonstrated at lab-scale by Frederickson et al. [49] with a solar simulator: the outlet of the mixed air-CO2 gas flow reached 800 °C. Performance evaluation of a 5 MWth SPHER demonstrator was presented by Fernandez and Miller [50]. Gas temperatures up to 1200 °C, with receiver thermal efficiency of 85 % seem attainable. Alonso and Romero [51] have reviewed experiments with directly irradiated particles solar reactors used to perform gas-solid thermochemical reactions. Moving particles in cavity receivers offer various options for solar receiver concepts. Tescari at al. [52] modeled a solar rotary kiln in order to perform Co_3O_4 reduction. It was shown that particle temperature in the range 900-1000 °C can be reached at the reactor exit. The same laboratory (German Aerospace Center - DLR, Germany) demonstrated a new concept based on particle centrifugation [53]. Particle outlet temperature up to 900 °C was measured using a high flux solar simulator. Finally, Xiao et al. [54] have developed a new concept, the spiral solar particle receiver, in which the solid particles move along a spiral path thanks to an electromagnet. Solid particle temperatures up to about 650 °C were measured using a solar simulator.

Concerning the comparison of a solid particle solar power plant with other more standard options, Giuliano et al.'s study [1] gives interesting conclusions for solar-hybrid operation. It is clearly shown that none of the analyzed solar-hybrid plants can meet low CO_2 emission and low LEC. For example, a particle-receiver tower with a combined cycle has the lowest solar LEC (about 10 c€/kWh) but high specific CO_2 emission (high fossil fuel consumption). Moreover, one of the main conclusions is that solar-hybrid plants with high storage capacities (large solar fields) have a high potential to reduce CO_2 emission. In solar power plants using solid particle receivers, the same particles may be used as both HTF and thermal storage medium (similarly to molten salt solar plants). Heat recovery from the hot storage is then possible using a fluidized bed heat exchanger as described by Warerkar et al. [55], or a particle-air heat exchanger as tested by Al-Ansary et al. [56] in which particles flow through. In this last study, storage bins are integrated at the top of the tower.

Direct absorption systems using particles are very attractive because they do not require a window and they accept very high solar flux density (of the order of 1 MW/m^2), but from the engineering point of view, particle flow stability is difficult to control and convection losses may be high. Indirect absorption solid particle receivers tolerate lower flux density (in the range 300-400 kW/m^2) but they offer a better control of the particle circulation within the receiver and a possible management of operating pressure and atmosphere composition. Various options are possible, for example, Badie et al. [57] studied an annular fluidized bed reactor for ore processing, Lédé et al. [58] considered a cyclone reactor for biomass conversion.

One of the main issues for high power solar concentrating system using particles as HTF is the particle mass flow rate that can actually circulate inside the solar receiver. In industry, the Circulating Fluidized Bed (CFB) technique is well-developed at large scale in oil refineries and in combustion plants. For example, in fluid catalytic cracking process in petroleum refineries, solid catalytic flow rate as high as 2000 t/h is typical in a single reactor. The reactor (riser) operates at high gas velocity (several m/s) and dilute solid-gas flows (solid fraction less than 5 %). Consequently, CFB requires high mechanical energy consumption for compression while the high velocity and low solid fraction lead to a poor wall-to-particles Heat Transfer Coefficient (HTC). Moreover, the particles' high velocities provoke tube erosion and solid particle attrition. Plug-flow pneumatic conveying overcomes these two latter inconveniences, since it allows transporting solid at lower velocities but higher average volume fraction, as shown by Watson et al. [59]. However, this regime is mainly characterized by the alternation between solid plugs with a voidage close to that of a fixed bed and voids with almost no solid, which is not an appropriate configuration for efficient heat transfer. Dense phase fluidized bed can be used in fluid catalytic cracking standpipes to provide an important and steady downward flow of solid as showed by Bodin et al. [60]. In this regime, the suspension is uniform, it has a low voidage that induces high wall-to-suspension HTC, and it circulates slowly (a few cm/s), thus limiting the energy consumption and permitting its use as HTF.

Dense Particle Suspension Receiver

A new concept was proposed lately. It uses a dense suspension of small solid particles and was patented by Flamant and Hemati in 2010 [61]. This innovation was then developed in

the frame of both a National project (CNRS Energy Program PARTISUN) and a European project (FP7 EC project CSP2 [62]). This receiver principle consists in creating the upward circulation of a Dense Particle Suspension (DPS) (solid fraction about 30 %), also called Upward Bubbling Fluidized Bed (UBFB) in vertical absorbing tubes submitted to concentrated solar radiation. The DPS acts as a HTF with a heat capacity similar to that of a liquid HTF but with no temperature limitation but the working temperature limit of the absorbing tubes. The results of two experimental campaigns conducted on a single-tube pilot receiver (about 10 kW_{th}) set at the CNRS 1 MW solar furnace at Odeillo were published [63, 64], proving the feasibility of the DPS receiver concept. The first values of the wall-to-suspension HTC in this configuration were determined and analyzed as a function of the system parameters. Suspension temperatures up to 750 °C were achieved for metallic tubes, thus opening new opportunities for high efficiency thermodynamic cycles such as supercritical steam and carbon dioxide on which worked Pitz-Paal et al. [5]. Other experiments conducted on a 150 kW_{th} 16-tube pilot plant have demonstrated that the concept is applicable at larger scale. Assessments of this technology have shown that the thermal efficiency can be higher than 80 % for a 10 MW_{th} receiver [65] and the parasitic power consumption was estimated at 3.1 % of nominal power output for a 50 MW_e power plant [22].

Thesis Presentation

This doctorate adressed the Dense Particle Suspension receiver.

The first objective was to test this process with an experimental setup in real conditions of concentrated solar irradiation. These experiments aimed to prove the feasability of the concept by heating the DPS circulating upward in a vertical tube exposed the solar flux.

A second objective was to reach DPS temperatures at the tube outlet above 700 °C, a temperature higher than those achievable with current solar heat transfer fluids and necessary to power high efficiency conversion cycles.

A third objective was to validate the concept at pilot-scale with the DPS being heated while circulating continuously in multiple tubes.

The last objective was to study and understand the behavior of the DPS upward flow in heated tubes and the tube wall-to-DPS heat transfer by analyzing the experimental results and conducting numerical simulations of the process.

This thesis is composed of five chapters, a general introduction and a conclusion.

As mentioned, a main interest of the studied new concept is its capacity to produce high temperature heat to power high efficiency thermodynamic cycles. Therefore, in Chapter 1, these cycles are examined. Since DPS is not the only HTF they could be used with, a review of current and future solar HTFs is done, with emphasis on their HTCs, which are a critical issue when it comes to a solar receiver design. This work resulted in the publication of a review article [66].

In Chapter 2, the core of the matter is assessed. The single-tube DPS receiver tested at the focus of the CNRS solar furnace in Odeillo is presented. The achieved temperature and

the observed specific solid circulation pattern are underlined. The experimental results are analyzed in order to determine the Upflow Bubbling Fluidized Bed (UBFB) wall-to-suspension HTC. The effects of various system parameters on the heat transfer are studied and a correlation on the Nusselt number of the DPS flow in a vertical tube is established. The results of the experiments and their analysis were published [63, 64] and a short communication on the established Nusselt correlation was submitted for publication [67].

In Chapter 3, three-dimensional numerical simulations of the DPS flow in tube under heating are described and discussed. They were carried out using an Eulerian two-fluid modeling approach for turbulent and poly-dispersed fluid-particle flows, which is developed and implemented by the Fluid Mechanics Institute (in French: Institut de Mécanique des Fluides de Toulouse = IMFT) in a specific version of the NEPTUNE_CFD software. The numerical and experimental results are compared and the particle mixing between the tube wall and center is studied.

Chapter 4 focuses on the 150 kW_{th} 16-tube pilot plant. The experimental setup and its operation and presented. The key points of its conception put forward by the on-sun tests are explained. The results are compared to those of the one-tube receiver in terms of thermal power extracted relative to the absorber tube surface. The receiver's thermal efficiency is determined under various operating conditions. The first part of the results was submitted for publication [68].

In Chapter 5, the study of the 16-tube pilot plant is completed by a numerical model of the radiation heat exchange inside the cavity. The solar concentrator (i.e. the CNRS 1 MW solar furnace), was modeled by using the Monte Carlo ray-tracing technique with the software Solfast-4D. The virtual reflectors' optical properties (reflectivity and optical error) were optimized to fit solar flux density measurements. The concentrator model's results, in the form of solar flux density maps, were used as boundary conditions for the receiver cavity modeled with ANSYS Fluent, using the surface-to-surface radiation model. The calculated temperatures obtained are compared to the measured ones to validate the model. The solar furnace model, among other concentrator models, was presented in a study to validate the Monte Carlo integral formulation used in Solfast-4D [69].

In the general conclusion, all the results obtained are summarized. The search for answers often raises even more questions. The new interrogations that were born from the subject study and conceivable ways to investigate those are looked at. Finally, the DPS solar receiver process perspectives are examined.

Nomenclature

Abreviations

CFB	Circulating Fluidized Bed
CSP	Concentrating Solar Power
CNRS	French National Center for Scientific Research (in French: Centre National de la Recherche Scientifique)
DPS	Dense Particle Suspension
HTC	Heat Transfer Coefficient
HTF	Heat Transfer Fluid
IEA	International Energy Agency
LEC	Levelized Electricity Cost
SPHER	Small Particle Heat Exchanger Receiver
UBFB	Upward Bubbling Fluidized Bed

Bibliography

[1] S. Giuliano, R. Buck, and S. Eguigen. Analysis of Solar-Thermal Power Plants With Thermal Energy Storage and Solar-Hybrid Operation Strategy. *ASME Journal of Solar Energy Engineering*, 133:031007, 2011.

[2] H.L. Zhang, J. Baeyens, J. Degrève, and G. Cáceres. Concentrated solar power plants: Review and design methodology. *Renewable and Sustainable Energy Reviews 2013*, 22:466–481, 2013.

[3] M. Romero and A. Steinfeld. Concentrating solar thermal power and thermochemical fuels. *Energy and Environmental Science*, 5(11):9234–9245, 2012.

[4] Y. Zhang, S.J. Smith, G.P. Kyle, and P.W. Stackhouse Jr. Modeling the potential for thermal concentrating solar power technologies. *Energy Policy*, 38:7884–7897, 2010.

[5] R. Pitz-Paal, A. Amin, M.O. Bettzuge, P. Eames, G. Flamant, F. Fabrizi, J. Holmes, A. Kribus, H. van der Laan, C. Lopez, F. Garcia Novo, P. Papagiannakopoulos, E. Pihl, P. Smith, and H.-J. Wagner. Concentrating Solar Power in Europe and the Middle East and North Africa: A Review of Development Issues and Potential to 2050. *ASME Journal of Solar Energy Engineering*, 134:024501, 2012.

[6] T.M. Pavlović, I.S. Radonjić, D.D. Milosavljević, and L.S. Pantić. A review of concentrating solar power plants in the world and their potential use in Serbia. *Renewable and Sustainable Energy Reviews*, 16:3891–3902, 2012.

[7] G. Cáceres, N. Anrique, A. Girard, J. Degrève, J. Baeyens, and H.L. Zhang. Performance of molten salt solar power towers in Chile. *Journal of Renewable and Sustainable Energy*, 5(5):053142, 2013.

[8] H.L. Zhang, J. Baeyens, and J. Degrève. The Potential of a Hybrid Power Plant for the Dubrovnik - Neretva County (Southern Croatia). *Journal of Sustainable Development of Energy, Water and Environmental Systems*, 3(2):174–182, 2015.

[9] Q. Hang, Z. Jun, Y. Xiao, and C. Junkui. Prospect of concentrating solar power in China - the sustainable future. *Renewable and Sustainable Energy Reviews*, 12(9):2505–2514, 2008.

[10] International Energy Agency. Technology Roadmap - Solar Thermal Electricity, 2014.

[11] Torresol Energy Gemasolar. http://www.torresolenergy.com/TORRESOL/gemasolar-plant/en.

[12] W.G. Le Roux, T. Bello-Ochende, and J.P. Meyer. Operating conditions of an open and direct solar thermal Brayton cycle with optimised cavity receiver and recuperator. *Energy*, 36(10):6027–6036, 2011.

[13] H.L. Zhang, T. Gowing, J. Degrève, T. Leadbeater, and J. Baeyens. The re-birth of the Stirling Engine in sustainable energy applications. *Proceedings of EMChIE 2015, Tarragona, Spain*, 2015.

[14] H. Price, R. Forristall, T. Wendelin, A. Lewandowski, T. Moss, and C. Gummo. Field survey of parabolic trough receiver thermal performances. *Proc. of ISEC2006, June 8-13, 2006, Denver, Colorado, USA*, 2006. (available at http://www.osti.gov/bridge).

[15] R. Vasquez Padilla, G. Demirkaya, D.Y. Goswami, E. Stefanakos, and M.M. Rahmane. Heat transfer analysis of parabolic trough solar receiver. *Applied Energy*, 88(12):5097–5110, 2011.

[16] A. Fernández-García, E. Zarza, L. Valenzuela, and M. Pérez. Parabolic-trough solar collectors and their applications. *Renewable and Sustainable Energy Reviews*, 14(7):1695–1721, 2010.

[17] G. Cau and D. Cocco. Comparison of medium-size concentrating solar power plants based on parabolic trough and linear Fresnel collectors. *Energy Procedia*, 45:101–110, 2014.

[18] R. Abbas, J. Muñoz, and J.M. Martínez-Val. Steady-state thermal analysis of an innovative receiver for linear Fresnel reflectors. *Applied Energy*, 92:503–515, 2012.

[19] T. Mancini, P. Heller, B. Butler, B. Osborn, W. Schiel, V. Goldberg, R. Buck, R. Diver, C. Andraka, and J. Moreno. Dish-Stirling Systems: An Overview of Development and Status. *AISME Journal of Solar Energy Engineering*, 125(2):135–151, 2003.

[20] O. Behar, A. Khellaf, and K. Mohammedia. A review of studies on central receiver solar thermal power plants. *Renewable and Sustainable Energy Reviews*, 23:12–39, 2013.

[21] C.K. Ho and B.D. Iverson. Review of high temperature central receiver designs for concentrating solar power. *Renewable and Sustainable Energy Reviews*, 26:835–846, 2014.

[22] J. Spelling, A. Gallo, M. Romero, and J. González-Aguilar. A High-Efficiency Solar Thermal Power Plant using a Dense Particle Suspension as the Heat Transfer Fluid. *Energy Procedia*, 69:1160–1170, 2015.

[23] M.T. Dunham and B.D. Iverson. High-efficiency thermodynamic power cycles for concentrated solar power systems. *Renewable and Sustainable Energy Reviews*, 30:758–770, 2014.

[24] Sunshot initiative. http://energy.gov/eere/sunshot/mission.

[25] J.E. Pacheco. Final test and evaluation results from the solar two project. Technical Report SAND2002-0120, Sandia National Laboratories, Albuquerque, New Mexico, 2002.

[26] Z. Yao, Z. Wang, Z. Lub, and X. Wei. Modeling and simulation of the pioneer 1 MW solar thermal central receiver system in China. *Renewable Energy*, 34(11):2437–2446, 2009.

[27] J. Pacio and Th. Wetzel. Assessment of liquid metal technology status and research paths for their use as efficient heat transfer fluids in solar central receiver systems. *Solar Energy*, 93:11–22, 2013.

[28] L. Amsbeck, R. Buck, P. Heller, J. Jedamski, and R. Uhlig. Development of a tube receiver for a solar-hybrid microturbine system. *Proceedings of the 2008 SolarPACES Conference, Las Vegas, NV*, 2008.

[29] G. Delussu. A qualitative thermo-fluid-dynamic analysis of a CO_2 solar pipe receiver. *Solar Energy*, 86:926–934, 2012.

[30] K. Qiu, L. Yan, M. Ni, C. Wang, G. Xiao, Z. Luo, and K. Cen. Simulation and experimental study of an air tube-cavity solar receiver. *Energy Conversion and Management*, 103:847–858, 2015.

[31] M. Lubkoll, T.W. von Backström, T.M. Harms, and D.G. Kröger. Initial Analysis on the Novel Spiky Central Receiver Air Pre-heater (SCRAP) Pressurized Air Receiver. *Energy Procedia*, 69:461–470, 2015.

[32] C.S. Turchi, Z. Ma, T.W. Neises, and M.J. Wagner. Thermodynamic study of advanced supercritical carbon dioxide cycles for concentrated solar power. *ASME Journal of Solar Energy Engineering*, 35(4), 2013.

[33] A.L. Ávila-Marín. Volumetric receivers in Solar Thermal Power Plants with Central Receiver System technology: A review. *Solar Energy*, 85(5):891–910, 2011.

[34] SolarReserve. Crescent Dunes. http://www.solarreserve.com/en/global-projects/csp/crescent-dunes.

[35] K. Vignarooban, X. Xu, A. Arvay, K. Hsu, and A.M. Kannan. Heat transfer fluids for concentrating solar power systems - A review. *Applied Energy*, 146:383–396, 2015.

[36] G. Flamant. Theoretical and experimental study of radiant heat transfer in a solar fluidized-bed receiver. *AIChE Journal*, 28:529–535, 1982.

[37] J. Martin and J. Vitko. ASCUAS: a solar central receiver utilizing a solid thermal carrier. *Sandia National Laboratories*, Report SAND82-8203, 1982.

[38] D. Bataille, C. Laguerie, C. Royere, and D. Gauthier. Gas-solid heat exchangers with multistage fluidized beds in the range of average and high temperature (in french). *Entropie*, 25:113–126, 1989.

[39] G. Flamant, D. Hernandez, C. Bonet, and J.-P. Traverse. Experimental aspects of the thermochemical conversion of solar energy: Decarbonation of $CaCO_3$. *Solar Energy*, 24:385–395, 1980.

[40] P.K. Falcone, J.E. Noring, and J.M. Hruby. Assessment of a solid particle receiver for a high temperature solar central receiver system. *Sandia National Laboratories*, Report SAND85-8208, 1985.

[41] G. Evans, W. Houf, R. Grief, and C. Crowe. Gas-Particle Flow Within a High Temperature Solar Cavity Receiver Including Radiation Heat Transfer. *ASME Journal of Solar Energy Engineering*, 109:134–142, 1987.

[42] H. Chen, Y. Chen, H.T.Hsieh, and N. Siegel. CFD Modeling of Gas Particle Flow within a Solid Particle Solar Receiver. *ASME Journal of Solar Energy Engineering*, 129:160–170, 2007.

[43] N.P. Siegel, C.K. Ho, S.S. Khalsa, and G.J. Kolb. Development and Evaluation of a Prototype Solid Particle Receiver: On-Sun Testing and Model Validation. *ASME Journal of Solar Energy Engineering*, 132(2):021008, 2010.

[44] T. Tan and Y. Chen. Review of study on solid particle solar receivers. *Renewable and Sustainable Energy Reviews*, 14:265–276, 2010.

[45] T. Tan, Y.T. Chen, and Z. Chen. Performance of Solid Particle Receivers with or without the Protection of an Aerowindow. *ASME 2nd International Conference on Energy Sustainability, Aug 10-14, 2008, Jacksonville, Florida, USA*, ES 2008-54129, 2008.

[46] M. Röger, L. Amsberg, B. Gobereit, and R. Buck. Face-Down Solid Particle Receiver Using Recirculation. *ASME Journal of Solar Energy Engineering*, 133:031009, 2011.

[47] J. Christian, C.K. Ho, W. Kolb, J. Kelton, and D. Ray. Design and evaluation of an on-sun prototype falling-particle cavity receiver. *Proceedings of ASME 8th Int. Conf. on Energy Sustainability & 12th Fuel cell Science, Engineering and Technology Conference. June 30-July 2, Boston, MA, USA*, ES2014-6446, 2014.

[48] B. Gobereit, L. Amsbeck, and R. Buck. Operation strategies for falling particle receivers. *Proceedings of the 7th International Conference on Energy Sustainability, July 14-19, 2013, Minneapolis, USA*, ES-FuelCell2013-18354, 2013.

[49] L. Frederickson, M. Dordevich, and F. Miller. Lab-scale experimentation and CFD modelling of a small particle heat exchanger receiver. *Energy Procedia*, 49:363–372, 2014.

[50] P. Fernandez and F. Miller. Performance analysis and preliminary design optimization of a Small Particle Heat Exchanger Receiver for solar tower power plants. *Solar Energy*, 112:458–468, 2015.

[51] E. Alonso and M. Romero. Review of experimental investigation on directly irradiated particles solar reactors. *Renewable and Sustainable Energy Reviews*, 41:53–67, 2015.

[52] S. Tescari, C. Agrafiotis, S. Breuer, L. de Oliveira, M. Neises von Puttkamer, M. Roeb, and C. Sattler. Thermochemical Solar Energy Storage Via Redox Oxides: Materials and Reactor/Heat Exchanger Concepts. *Energy Procedia*, 49:1034–1043, 2014.

[53] W. Wu, L. Amsbeck, R. Buck, R. Uhlig, and R. Pitz-Paal. Proof of concept test of a centrifugal particle receiver. *Energy Procedia*, 49:560–568, 2014.

[54] G. Xiao, K. Guo, M. Ni, Z. Luo, and K. Cen. Optical and thermal performance of a high-temperature spiral solar particle receiver. *Solar Energy*, 109:200–213, 2014.

[55] S. Warerkar, S. Schmitz, J. Goettsche, B. Hoffschmidt, M. Reißel, and R. Tamme. Air-Sand Heat Exchanger for High-Temperature Storage. *ASME Journal of Solar Energy Engineering*, 133:021010, 2011.

[56] H. Al-Ansary, A. El-Leathy, Z. Al-Suhaibani, S. Jetre, D. Sadowski, A. Alrished, and M. Golob. Experimental Study of a Sand-Air Heat Exchanger for Use With a High-Temperature Solar Gas Turbine System. *ASME Journal of Solar Energy Engineering*, 134:041017, 2012.

[57] J.-M. Badie, C. Bonet, M. Faure, G. Flamant, R. Foro, and D. Hernandez. Decarbonation of calcite and phosphate rock in solar chemical reactors. *Chemical Engineering Science*, 35:413–420, 1980.

[58] J. Lédé, F. Verzaro, B. Antoine, and J. Villermaux. Flash pyrolysis of wood in a cyclone reactor. *Chemical Engineering and Processing: Process Intensification*, 20(6):309–317, 1986.

[59] R.J. Watson, R.B. Thorpe, and J.F. Davidson. Vertical plug-flow pneumatic conveying from a fluidised bed. *Powder Technology*, 224:155–161, 2012.

[60] S. Bodin, C. Briens, M.A. Bergougnou, and T. Patureaux. Standpipe flow modeling and experimental validation and design recommendations. *Powder Technology*, 124:8–17, 2002.

[61] G. Flamant and H. Hemati. Dispositif collecteur d'énergie solaire (Device for collecting solar energy). French patent FR 1058565, October 20, 2010. PCT extension WO2012052661, April 26, 2012.

[62] FP7 EC project CSP2. http://www.csp2-project.eu.

[63] G. Flamant, D. Gauthier, H. Benoit, J.-L. Sans, R. Garcia, B. Boissière B., R. Ansart, and M. Hemati. Dense suspension of solid particles as a new heat transfer fluid for concentrated solar thermal applications: On-sun proof of concept. *Chemical Engineering Science*, 102:567–576, 2013.

[64] H. Benoit, I. Pérez López, D. Gauthier, J.-L. Sans, and G. Flamant. On-sun demonstration of a 750 °C heat transfer fluid for concentrating solar systems: Dense particle suspension in tube. *Solar Energy*, 118:622–633, 2015.

[65] A. Gallo, J. Spelling, M. Romero, and J. González-Aguilar. Preliminary Design and Performance Analysis of a Multi-Megawatt Scale Dense Particle Suspension Receiver. *Energy Procedia*, 69:388–397, 2015.

[66] H. Benoit, L. Spreafico, D. Gauthier, and G. Flamant. Review of heat transfer fluids in tube-receivers used in concentrating solar thermal systems: Properties and heat transfer coefficients. *Renewable and Sustainable Energy Reviews*, 2015.

[67] H. Benoit, I. Pérez López, D. Gauthier, and G. Flamant. Nusselt correlation for upward bubbling fluidized bed circulating in tube exposed to highly concentrated solar flux. *Chemical Engineering Science*, (Submitted).

[68] *Nature Materials*, (Submitted).

[69] C. Caliot, H. Benoit, E. Guillot, J.L. Sans, A. Ferriere, G. Flamant, C. Coustet, and B. Piaud. Validation of a Monte Carlo Integral Formulation Applied to Solar Facility Simulations and Use of Sensitivities. *ASME Journal of Solar Energy Engineering*, 137(2):021019, 2015.

Chapter 1

Review of Heat Transfer Fluids in Tube-Receivers Used in Concentrating Solar Thermal Systems: Properties and Heat Transfer Coefficients

1.1 Introduction

1.1.1 Energy conversion cycles and heat transfer fluids for central receivers

Central receivers offer numerous options for producing heat at temperatures higher than 500 °C, temperatures that are needed to power efficient Rankine thermodynamic cycles. Recent research intends to develop Heat Transfer Fluids (HTFs) able to sustain temperatures higher than 700 °C, allowing the use of more efficient energy conversion cycles such as Brayton [1] and combined cycles [2].

Dunham and Iverson recently published an extensive review on high efficiency power cycles and their application to Concentrated Solar Power (CSP) systems [3]. At present, Rankine cycles applied to central tower systems have typically thermal-mechanical efficiencies in the range 37-42 % [4, 5] with turbine inlet temperatures limited below 600 °C due to the temperature limitations of current HTFs. Supercritical steam (s-H_2O) Rankine cycles [6–8] have the potential to reach efficiencies higher than 45 % but they face the problem of s-H_2O becoming highly corrosive above 627 °C, therefore requiring the use of high-nickel alloys [8]. Efficiencies of the order of 50 % are predicted for Helium Brayton cycles operated with a turbine inlet temperature from 750 to 850 °C [7]. Supercritical Brayton cycles have also been shown to have potentially high efficiencies, especially using supercritical carbon dioxide (s-CO_2) as the working fluid [9]. The interest of using supercritical fluids is that they have good heat transfer properties and are easily compressible, just as liquids. It makes their heating (before the turbine) and cooling (for heat regeneration) more efficient and reduces the compressor work. Efficiencies of 46 % for a s-CO_2 Brayton cycle with turbine inlet temperature of 550 °C , and 49.25 % for a helium Brayton cycle with turbine inlet temperature of 880 °C, have be achieved [10]. The fact that s-CO_2 thermophysical properties rapidly change in the vicinity of the critical point might limit its use to CSP plants with thermal storage to compensate for the variable heat source that is the solar flux. Combined Cycles are composed of a primary high temperature cycle (topping cycle) and at least one lower temperature cycle (bottoming cycle) that is powered by the heat rejected from the first cycle. Such cycles have been studied for more than 20 years since it is believed that they could allow reaching about 50 % efficiency [2, 11]. The bottoming cycles generally considered are Organic Rankine Cycles (ORC) [12, 13] whose efficiencies are in the range 10-20 %. The combination of a Brayton topping cycle with an ORC bottoming cycle is commonly considered. An air-toluene cycle [14] and a CO_2-isopentane cycle [15] showed efficiencies of 53 % and 47.5 % with turbine inlet temperature above 1027 °C and of 827 °C, respectively. Combined cycles working with a heat recovery steam generator can reach 60 % efficiency when the gas turbine inlet temperature is 1300 °C [16].

As mentioned before, high efficiency cycles imply high temperatures. This puts a first constraint on the HTF. Another one comes from the solar receiver. Indeed, Ho and Iverson [17] showed that, in order to have high solar-thermal efficiency, the receiver heat losses need to be reduced by diminishing the receiver size and increasing the solar concentration ratio. The maximum irradiance that a receiver can stand depends on its conception, on the manufacturing materials and on how the solar energy is transferred to the HTF. For most receiver concepts, the absorption is indirect, meaning that the solar radiation is first absorbed by an opaque solid absorber before being transmitted to the HTF. As a consequence, a temperature limit is imposed by the solid absorber, while the heat extraction

is limited by the exchange with the HTF flowing in the receiver. Therefore the HTF's capacity to receive heat from a solid, which depends solely on its inherent properties, has a major impact on both the maximum concentration ratio to which the receiver's absorber can be exposed and the solar-thermal efficiency, as was already stressed in the 1980s [18, 19].

When looking for the best solar-mechanical efficiency, the improvement of the thermal-mechanical efficiency of the cycle is opposed to the improvement of the solar-thermal efficiency of the receiver. Indeed, according to Carnot's Theorem [20, 21], increasing the temperature improves the cycle efficiency while it increases the thermal losses and, therefore, reduces the receiver efficiency. As a consequence, an optimum temperature appears that depends on the concentration ratio, the receiver design (configuration and materials) and the type of energy conversion cycle [3].

1.1.2 Chapter outline

This chapter describes first how the advanced thermodynamic cycles work and the potential efficiencies they could achieve in the coming years.

Second, all the HTFs that are or will be used in CSP plants are reviewed. Becker [19] already did such a study in 1980 but new HTFs were developed later. This work was published in a review article [22].

Section 1.3 reminds the requirements for solar HTFs and lists their operating temperature ranges.

As mentioned, a critical characteristic of HTFs is their capacity to exchange heat with a wall. This can be materialized by the heat transfer coefficient h. In Section 1.4, the importance of the heat transfer coefficient h is discussed. The only way to determine h in a theoretical study is by using a Nusselt number correlation. Many of these correlations are available in the literature and it can be difficult to choose which one to use in a specific case because it depends of the kind of fluid and the flow conditions. In order to make the choice of Nusselt correlation easier, this work regroups a selection of well-known correlations developed in the past century, as well as some new correlations established more recently.

Section 1.5 presents a compilation of equations allowing the calculation of the density, specific heat capacity, thermal conductivity and dynamic viscosity of the following fluids: Therminol® VP-1, solar salt, Hitec®, Hitec® XL, sodium, lead-bismuth eutectic, pressurized air, carbon dioxide, helium and hydrogen.

A practical application follows in Section 1.6 where the heat transfer coefficients of various fluids are calculated thanks to the properties equations and Nusselt correlations presented earlier. This includes a calculation of the heat transfer coefficient for boiling water. Since

this chapter focuses on the influence of the HTFs, a standard absorber configuration must be applied to all the fluids considered so that it does not impact the results. This standard configuration should be simple and as general as possible. According to the elements underlined in the Central Receiver System Section of the General Introduction, the tubular absorber was chosen. The main reproach that can be done to this choice of geometry is that it is more representative of a liquid absorber configuration than of a gas absorber. But it still allows comparing gases and liquids. Moreover, the absorber can be adapted by considering different velocities for liquids and gases to better correspond to actual flow conditions. Afterwards, the heat transfer coefficients obtained for the various fluids are compared.

Finally, in Section 1.7, the most recently developed solar HTFs are explored.

1.2 Advanced energy conversion cycles for solar towers

1.2.1 Regenerative Brayton cycle

Two types of Brayton cycles are presented here: the regenerative Brayton cycle and the recompression Brayton cycle. Figure 1.1 shows a component schematic of the regenerative Brayton cycle extracted from Dunham and Iverson's review [3]. The gas in its colder state (1) undergoes a first compression (C1). From state (2) to (3) heat exchanger (HEX) removes some of the gas heat to allow for a more efficient second compression (C2). The gas at his highest pressure (4) is pre-heated in the regenerator to reach state (5) in which it enters the heater. The heater can be either the solar receiver, or a heat exchanger where the solar HTF transfers its heat to the working fluid of the cycle. The high temperature high pressure gas (6) then enters the turbine where it is expanded to low pressure (7). Part of the remaining heat is used in the regenerator to pre-heat the cold side. Finally, the gas in state (8) is returned to the initial state by passing through a heat exchanger.

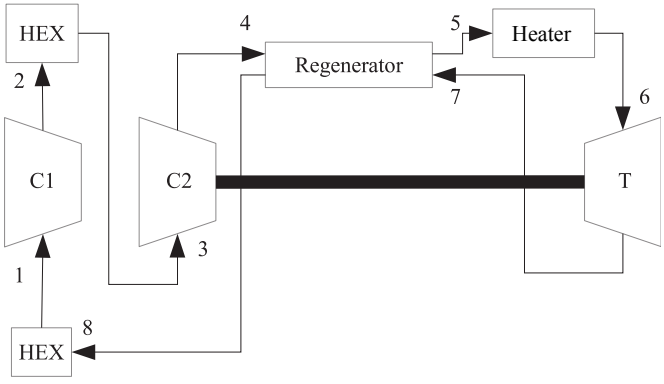

Figure 1.1: Component schematic of the regenerative Brayton cycle [3].

1.2.2 Recompression Brayton cycle

The recompression Brayton cycle was designed specifically for s-CO_2 to take advantage of its sharp changes in thermophysical properties near the critical point to minimize the

compression work [10]. It is more complex than the simple Brayton cycle. As can be seen in Figure 1.2 extracted from Dunham and Iverson's review [3], two compressors are used in parallel. A fraction of the fluid bypasses the cooler and passes through the additional compressor (C2), thus reducing the heat rejection from the cycle and increasing the efficiency [23]. This fraction then rejoins the main flow after the low temperature regenerator. The regeneration is split between two heat exchangers. As a consequence, both of them are designed for a lower heat duty and lower temperature drop than in the simple cycle. The cooler is also smaller because the flow passing through is reduced thanks to the splitting [24].

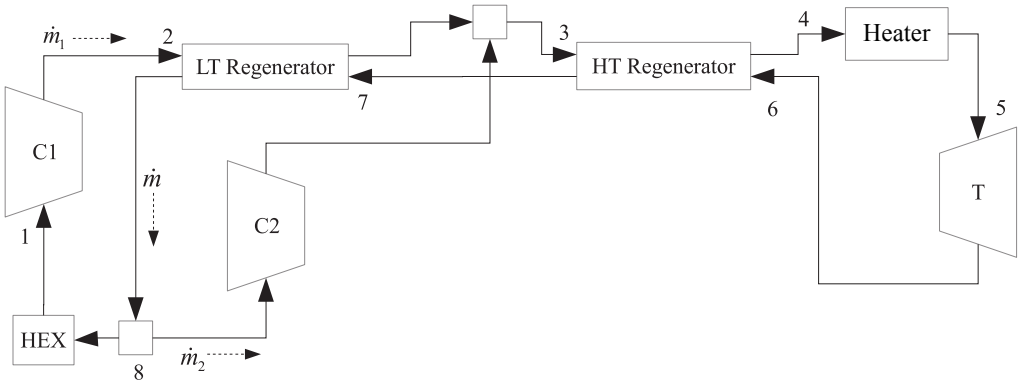

Figure 1.2: Component schematic of the recompression Brayton cycle [3].

1.2.3 Combined cycle

Figure 1.3 (source: [3]) shows an example of combined cycle with a regenerative Brayton topping cycle and an ORC bottoming cycle. The principle is to use the remaining heat at the outlet of the topping cycle turbine to power the bottoming cycle. There is no cooler before the compressor in the topping cycle because it would reduce the heat available for the bottoming cycle.

1.2.4 Potential efficiencies

A thermodynamic analysis of the presented cycles was made in order to determine their potential thermal-mechanical efficiencies for both dry and wet cooling [3]. The temperatures and pressure indicated correspond to the turbine inlet conditions (turbine of the topping cycle in the combined cycle case). The regenerative Brayton cycle is more efficient with Helium than with CO_2. At 30 MPa and 1100 °C, it reaches 55.7 % and 53.4 % for wet and dry cooling, respectively. Under the same pressure and temperature conditions, the s-CO_2 recompression Brayton cycle leads to efficiencies of 62.1 % and 57.7 % for wet and dry cooling, respectively. It reaches 50 % efficiency below 700 °C for wet cooling, and under 800 °C for dry cooling. The combined cycle was analyzed with CO_2 at 20 Mpa in the topping cycle. The efficiencies for R245fa and Isopentane is good for temperatures higher than 700 °C but they do not reach 50 % before 1100 °C and 1000 °C, respectively, with wet cooling. Dry cooling does not allow reaching 50 % efficiency for temperatures below 1100 °C. Finally, an analysis combining receiver and thermodynamic cycle efficiencies shows that the s-CO_2 recompression Brayton cycle at 30 MPa could reach solar-mechanical efficiencies of 42.9 % at 746 °C with wet cooling and 39.1 % at 766 °C with dry cooling.

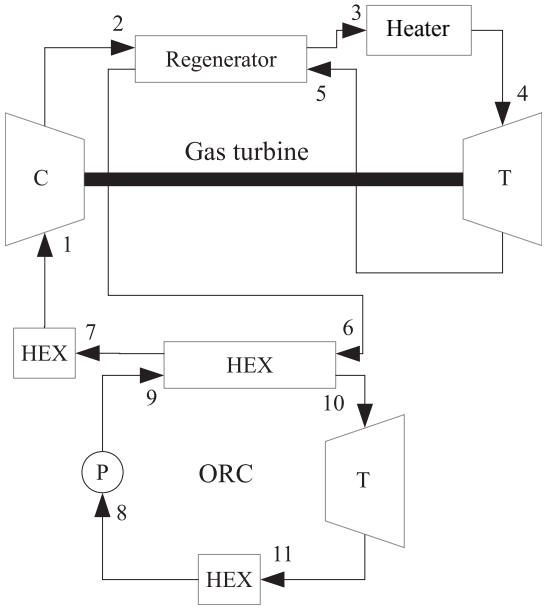

Figure 1.3: Component schematic of the regenerative Brayton-ORC cycle [3].

1.3 Importance of heat transfer fluids in concentrating solar technologies

1.3.1 Requirements

In general, HTFs must be compatible with the containment materials and storage media [25], be able to operate in the required temperature range, easily receive and transfer heat, and circulate well in a confined space. Consequently, to guarantee a good efficiency and to insure the previous characteristics, the main requirements for solar HTFs have been identified [17, 18] and they can be summarized as follows:

- Extended working temperature range and high thermal stability. This means a low melting point in order to reduce heat tracing requirements (heat tracing is used to avoid HTF solidification in pipes), and a high upper temperature limit that allows using efficient thermodynamic cycles.
- Good heat transfer properties play a key role since the temperature difference between the receiving surface and the HTF will be moderate, allowing the fluid to reach high temperatures without imposing too high a thermal stress on the surface. Therefore a high thermal conductivity λ of the HTF is desired to enhance the heat transfer coefficient. A low viscosity μ is beneficial to reduce the pressure drop and pumping power. A large specific heat capacity c_p allows direct thermal storage, although indirect solutions with a secondary medium are also possible.
- A low working pressure allows using thin tube walls. This reduces the wall temperature gradient and therefore the temperature-induced mechanical stress.
- Operational aspects such as safety and corrosion behavior play a major role. Therefore, low hazard properties and good material compatibility are strongly recommended, and even economical product and low maintenance cost have key roles.

To summarize, HTFs must be carefully designed to have high specific heat capacity, high thermal stability, high thermal conductivity and a broad operating temperature range.

1.3.2 Temperature limit of existing heat transfer fluids

The mean annual efficiency of CSP plants is currently about 16 % and it is mainly limited by the working fluid temperature. This is why selecting an appropriate HTF is important since it will minimize the cost of the solar receiver, thermal storage and heat exchangers, while allowing to achieve higher receiver and heat conversion cycle efficiencies. Up to now, organic oil, air at atmospheric pressure, water and molten salts have been used as working fluids for transferring heat in CSP plants. But research activities are currently being carried out to find more efficient fluids. Some current fluids and others under development are listed below. The water/steam couple which undergoes a phase change is kept apart.

- Liquid heat transfer fluids:
  - Thermal oil: Therminol® VP-1, Dowtherm®, etc.
  - Molten salts: Solar salt (60 %wt $NaNO_3$, 40 %wt KNO_3), Hitec® (7 %wt $NaNO_3$, 40 %wt $NaNO_2$, 53 %wt KNO_3), Hitec® XL (7 %wt $NaNO_3$, 45 %wt KNO_3, 48 %wt $Ca(NO_3)_2$), etc.
  - Liquid metals: Liquid sodium (Na), Lead-Bismuth Eutectic, LBE (44.5 %wt Pb, 55.5 %wt Bi), etc.
- Gas heat transfer fluid:
  - Pressurized gases: Air, CO_2, He, H_2
  - Supercritical fluids: s-CO_2, s-H_2O
- Water/Steam
- Particle suspensions used as heat transfer media.

The distinction between liquid, gas and two-phase fluids is necessary because the liquid HTFs' decomposition temperature is much lower (apart from liquid metals) than it is for pressurized gases and steam. Indeed, organic oils currently tend to break down at temperatures around 400 °C, inorganic nitrate salts decompose when the temperature exceeds 530 to 600 °C, and solidify between 130 and 220 °C, depending on their composition [26]. Therefore plants operating at high temperature must involve gases, steam, liquid metals or particles as heat transfer medium. Another noteworthy element is that, for water and carbon dioxide, critical state is reached at working conditions that are easily obtained with solar concentrating systems. This will be discussed in Section 1.7. A general view of several existing HTFs' temperature limits is summarized in Table 1.1 and illustrated in Figure 1.4. The suspension of silicon carbide (SiC) particles is also included since it behaves like a liquid [27–29].

Table 1.1: Operating temperature ranges of liquid HTFs and SiC particles

Heat Transfer Fluid	Temperature range [°C]
Thermal oil	
• Therminol® VP-1	12-400
Molten salts	
• Solar salt	260-600
• Hitec®	140-530
• Hitec® XL	130-550
Liquid metals	
• Na	98-883
• LBE	125-1670
Particle suspension	
• SiC	No lower limit-1620

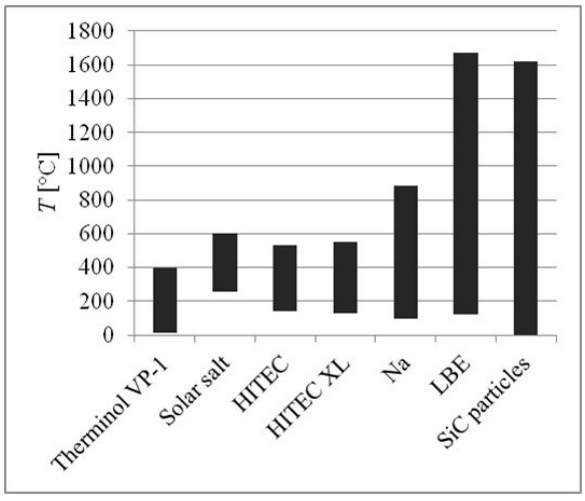

Figure 1.4: Operating temperature ranges for liquid heat transfer fluids.

1.4 Wall-to-fluid convection heat transfer coefficient

1.4.1 Heat transfer coefficient and heat transfer fluid

The wall-to-fluid convection heat transfer coefficient h is defined as the ratio of the heat flux density φ,also called heat flux, over the difference between the fluid bulk temperature T_b and the solid wall temperature T_w. The same heat flux is also equal to the heat flux by conduction between the solid wall and the fluid layer in contact with the wall. Therefore, h can be expressed as:

$$h = -\lambda_f \frac{dT_f/dy|_w}{T_w - T_b} \tag{1.1}$$

with λ_f the fluid thermal conductivity and $dT_f/dy|_w$ the fluid temperature gradient at the wall along the direction normal to the wall.

As explained in [17], increasing the concentration ratio of the incident solar flux has a beneficial effect on the receiver efficiency. But the solar receiver must evacuate heat efficiently to stand a high solar flux, which means that the heat flux exchanged with the HTF must be high. The heat flux can be increased in two ways: by increasing the temperature difference between the wall and the fluid or by increasing the heat transfer coefficient. The material from which the wall is made of imposes a limit to the temperature that it can stand. Moreover, the HTF in contact with the wall has the same temperature locally. For some HTFs like molten salts and thermal oil which disintegrate at high temperature, this imposes an even lower temperature limit to the wall. For these two reasons, the temperature difference between the wall and the fluid is limited. As a consequence, the heat transfer coefficient h must be increased to further increase the heat flux density φ. Eq (1.1) shows that, for a constant temperature difference $T_w - T_b$, h can be increased by increasing the fluid conductivity λ_f or the temperature gradient $dT_f/dy|_w$. The conductivity λ_f is directly dependent on the HTF used. The temperature gradient $dT_f/dy|_w$, for a given HTF, can only be increased by increasing the fluid velocity along the wall. This will also increase the friction between the wall and the HTF, resulting in a pumping power loss.

Previous remarks underline how important the choice of the HTF is for the solar receiver efficiency. If the HTF is bad at exchanging heat with a wall, it will limit the concentration ratio, hence the thermal efficiency, unless the HTF circulates at high velocity, which will result in pumping losses, thus lowering the whole system's efficiency. A compromise must be found between these two effects to reach an optimum for a given HTF in a given solar receiver configuration.

1.4.2 Nusselt number correlations

In practice, the wall-to-fluid convection heat transfer coefficient h is calculated from the Nusselt number Nu:

$$Nu = \frac{hd}{\lambda_f} \tag{1.2}$$

with d the characteristic length, which is the diameter D in the case of a tube, and λ_f the fluid thermal conductivity.

Many empirical correlations have been developed to estimate the Nusselt number of flows in pipes since 1930 and Dittus and Boelter's heat exchanger study [30]. Most of the time, it is expressed as a function of their Reynolds number (Re) and Prandtl number (Pr):

$$Pr = \frac{c_p \mu}{\lambda} \tag{1.3}$$

with c_p the specific heat capacity, μ the dynamic viscosity and λ the thermal conductivity.

Selected Nusselt correlations were tested in this study: Dittus-Boelter equation modified by McAdams [31], Sieder-Tate correlation [32], Hausen correlation [33] and Petukhov formula [34]. They were assessed by Gnielinski [35, 36] who determined a new equation that is more precise than most of the previous ones and has a wider validity range that includes laminar and transition regimes. For simplification, only the equation for fully developed turbulent flow is shown here because, as we will see, for this study's chosen conditions, only Hitec® XL at low temperature has a Reynolds number inferior to 4000. The usual Nusselt correlations can be applied to water, thermal oil and pressurized gases. It was recently verified that they also work for molten salts, and their coefficients were adapted to match some new experimental data [37, 38]. The new correlations have only been validated for narrow ranges of Re and Pr but it is supposed that they could work well in wider ranges, comparable to the usual correlations. However, liquid metals do not fall in the validity domain of the other equations because of their very small Pr which originates from their very high conductivity and rather low specific heat capacity. In this particular case, the dominant parameter is the Peclet number Pe. It is defined as the ratio of heat advection rate over heat diffusion rate, which leads to the formula being the product of Re and Pr ($Pe = RePr$). Martinelli [39] was the first to propose a heat transfer theory specific to liquid metals, from which Lyon [40] derived a semi-empirical equation for calculating the heat transfer in liquid metals for the case of constant heat flux, which is now known as the Lyon-Martinelli equation. Equations based on measurements made on liquid sodium were proposed by Sleicher and Rouse [41]. In the case of fully developed turbulent flow, Cheng and Tak [42] observed that the Lyon-Martinelli correlation gives good results for liquid sodium, but overestimates Nu for other liquid metals. This is why they developed new correlations specific to the lead-bismuth eutectic [42]. All Nusselt correlations are shown in Table 1.2 for the case of fluid heating with constant heat flux. Note that some coefficients will change for the case of cooling or for constant wall temperature. The original Dittus-Boelter equation was replaced by the one introduced by McAdams [31] a few years later. A clear difference can be seen between the correlations for usual fluids and those for liquid metals that are valid for $Pr < 0.1$ and have a constant value added to the product of Re and Pr.

The Nusselt correlations were initially established for the reference case of fully developped flow and constant fluid temperature over the tube section. But it can be necessary to estimate Nu in cases when the flow is not fully developped or when a high heat flux density at the wall creates a difference between the fluid temperature near the wall and that at the

tube center. For these cases, correction factors were defined. They correspond to the ratio Nu/Nu_0,with Nu_0 the Nusselt number of the reference case and Nu the actual Nusselt number.

In his work, Hausen [33] introduced a correction factor to take into account the dependence of the heat transfer coefficient on the tube length, which is important in relatively short tubes, when the ratio tube length L over tube diameter D is low:

$$Nu/Nu_0 = 1 + (D/L)^{2/3} \tag{1.4}$$

The value at which the flow is generally considered to be fully developed is $L/D > 60$. In this study, only fully developed flow is considered and the factor is taken equal to 1.

Other correction factors are used to take into account the variability of the fluid properties when there is an important difference between the fluid bulk temperature and the wall temperature. This occurs when the heat flux is high, as in CSP applications. The property-based correction factors are called K. The first one was expressed by Sieder and Tate [32] and takes the form:

$$K = Nu/Nu_0 = (\mu_b/\mu_w)^{0.14} \tag{1.5}$$

Petukhov [34] uses two different property-based corrections factors for liquids and gases. In the case of liquid heating, he takes a Sieder-Tate type correction factor (Eq (1.5)) but indicates that an exponent value of 0.11 fits experimental data better than 0.14. For gas heating, he recommends a property-based correction factor of the form:

$$K = Nu/Nu_0 = (T_w/T_b)^n \tag{1.6}$$

with

$$n = -0.3 \log_{10}(T_w/T_b) - 0.36 \tag{1.7}$$

Sleicher and Rouse [41] found that their data was better correlated by applying to Eq (1.6) the exponent:

$$n = -\left(\log_{10}(T_w/T_b)\right)^{1/4} + 0.3 \tag{1.8}$$

Another property correction factor was defined by Burck and Riebold [43] as:

$$K = Nu/Nu_0 = (Pr_b/Pr_w)^{0.11} \tag{1.9}$$

For most fluids, Eq (1.9) gives results close to Eq (1.5) (with exponent 0.11) because the ratio specific heat over thermal conductivity is a limited function of temperature, as shown in [41].

Table 1.2: Nusselt number correlations

Author	Correlation		Validity range
	Usual correlations		
Dittus-Boelter [31]	$Nu = 0.023 Re^{0.8} Pr^{0.4}$	(1.10)	$0.7 \leqslant Pr \leqslant 120$ $10^4 \leqslant Re \leqslant 1.2 \times 10^5$ $L/D > 60$
Sieder-Tate [32]	$Nu = 0.027 Re^{0.8} Pr^{1/3} \left(\frac{\mu_b}{\mu_w}\right)^{0.14}$	(1.11)	$0.7 \leqslant Pr \leqslant 120$ $Re \geqslant 10^4$ $L/D > 60$
Hausen [33]	$Nu = 0.037 \left(Re^{0.75} - 180\right) Pr^{0.42}$ $\left[1 + \left(\frac{D}{L}\right)^{2/3}\right] \left(\frac{\mu_b}{\mu_w}\right)^{0.14}$	(1.12)	$0.5 \leqslant Pr \leqslant 1000$ $2300 \leqslant Re \leqslant 1.2 \times 10^6$
Petukhov [34]	$Nu = \frac{Re_b Pr_b (\xi/2)}{1.07 + 12.7\left(Pr_b^{2/3} - 1\right)\sqrt{\xi/2}} K$ with the friction factor $\xi = \left[1.82 \log_{10}(Re_b) - 1.64\right]^{-2}$ (1.15) Correction for liquids: $K = \left(\frac{\mu_b}{\mu_w}\right)^{0.11}$ Correction for gases: $K = \left(\frac{T_b}{T_w}\right)^n$ with $n = -\left(\log_{10}(T_w/T_b)\right)^{1/4} + 0.3$	(1.13) (1.14) (1.16) (1.6) (1.8)	$0.5 \leqslant Pr \leqslant 2000$ $10^4 \leqslant Re \leqslant 5 \times 10^6$
Gnielinski [36]	$Nu = \frac{(\xi/8)(Re_b - 1000) Pr_b}{1 + 12.7\sqrt{\xi/8}\left(Pr_b^{2/3} - 1\right)} K$ with the friction factor $\xi = \left[1.84 \log_{10}(Re_b) - 1.64\right]^{-2}$ Correction for liquids: $K = \left(\frac{\mathrm{Pr}_b}{\mathrm{Pr}_w}\right)^{0.11}$ Correction for gases: $K = \left(\frac{T_b}{T_w}\right)^n$ with $n = -\left(\log_{10}(T_w/T_b)\right)^{1/4} + 0.3$	(1.17) (1.18) (1.9) (1.6) (1.8)	$0.5 \leqslant Pr \leqslant 2000$ $4 \times 10^3 \leqslant Re \leqslant 5 \times 10^6$
	Correlations specific to molten salts		
Liu et al [37]	$Nu = 0.0242 Re^{0.81} Pr^{\frac{1}{3}} \left(\frac{\mu_b}{\mu_w}\right)^{0.14}$	(1.19)	$12.7 \leqslant Pr \leqslant 14.7$ $17000 \leqslant Re \leqslant 45000$
Wu et al [38]	Transition flow: $Nu = 0.0154 Re^{1.1} Pr^{1/3}$ Turbulent flow: $Nu = 0.02948 Re^{0.787} Pr^{1/3}$	(1.20) (1.21)	$1.6 \leqslant Pr \leqslant 23.9$ $2300 \leqslant Re \leqslant 10^4$ $1.6 \leqslant Pr \leqslant 23.9$ $10^4 \leqslant Re \leqslant 4.6 \times 10^4$
	Correlations specific to liquid metals		

Table 1.2: Nusselt number correlations

Author	Correlation	Validity range
Lyon-Martinelli [40]	$Nu = 7 + 0.025\left(\frac{Pe}{Pr_t}\right)^{0.0.8}$ (1.22) with Pr_t the turbulent Prandtl number	
Sleicher-Rouse [41]	$Nu = 6.3 + 0.0167 Re_{film}^{0.85} Pr_w^{0.93}$ (1.23)	$Pr \leqslant 0.1$ $10^4 \leqslant Re \leqslant 10^6$
Cheng and Tak [42]	$Nu = Nu_{Pe=0} + 0.018 Pe^{0.8}$ (1.24) with $Nu_{Pe=0} = \begin{cases} 4.5 \\ 5.4 - 9 \times 10^{-4} Pe \\ 3.6 \end{cases}$	$Pe \leqslant 1000$ $1000 \leqslant Pe \leqslant 2000$ $Pe \geqslant 2000$

1.5 Thermophysical properties of the heat transfer fluids

As introduced before, the HTFs' thermophysical properties strongly influence the whole system performance. It is necessary to accurately know the following properties for a good evaluation of the heat transfer coefficient: density ρ, specific heat capacity c_p, thermal conductivity λ and dynamic viscosity μ. In this study, they were estimated with correlations specific to each HTF found in the literature or established from data tables.

1.5.1 Thermal Oil

CSP plants initially started implementing synthetic oil, most widely known under its brand names Therminol® VP-1 or Dowtherm® A, in order to avoid the high pressure requirement and phase transition when using water. This synthetic organic fluid can operate at temperature as high as 400°C to collect and transport heat in CSP applications. When it is heated above 400°C, the hydrocarbons break down quickly, thus producing hydrogen. Degradation can increase makeup fluid requirements, reduce overall fluid lifetime, and cause build-up of sludge or other byproducts that reduce the system heat transfer efficiency and increase maintenance costs. The commercial oil Therminol® VP-1 was chosen for this study. It is an eutectic mixture of diphenyl oxide and biphenyl. It is thermally stable in the temperature range 12-400 °C. Its thermal properties may be found in Solutia's technical bulletin [44]. Correlations were established from the data tables and are indicated in Table 1.3. They are valid in the whole stability range and their errors do not exceed 3%.

1.5.2 Molten salts

Solar molten salts are salt mixtures, mainly nitrates, which can be used for thermal storage applications as well as heat transfer fluids thanks to their chemical characteristics. Molten salts exhibit many desirable heat transfer qualities at high temperature: high density,

high specific heat capacity, high thermal stability and very low vapor pressure. Moreover, molten salts are cheaper and have less environmental impact than synthetic oil: they are non-polluting, nonflammable, more abundant and permit cost savings because of reduced thermal tanks and piping. The major challenge of molten salts is their high freezing point which leads to operations and maintenance costs for freeze protection. The currently used synthetic oil freezes at about 15 °C, whereas ternary and binary molten salts freeze in the temperature range 120-220 °C [45]. The heat transfer characteristics depend on the molten salt composition. Three of them are analyzed hereafter: solar salt, Hitec® and Hitec® XL.

1.5.2.1 Solar salt

Sodium nitrate-potassium nitrate, also known as solar salt, is the basic solar salt used in CSP technology. The solar salt composition, expressed in mass fractions, is 60 %wt $NaNO_3$ + 40 %wt KNO_3. Its properties can be calculated using the correlations listed in Table 1.3. They can be used in the entire operating temperature range which goes from 260 °C to 600 °C [46].

1.5.2.2 Hitec®

Hitec® is a ternary molten salt whose composition, expressed in mass fractions, is 53 %wt KNO_3 + 40 %wt $NaNO_2$ + 7 %wt $NaNO_3$. It is liquid and stable in the range 142-535 °C. Its properties can be calculated using the correlations expressed in [47], based on measurements presented in [48]. The correlations are listed in Table 1.3.

1.5.2.3 Hitec® XL

Hitec® XL is also a ternary molten salt, more recent than Hitec®, whose composition, expressed in mass fractions, is 43 %wt KNO_3 + 42 %wt $Ca(NO_3)_2$ + 15%wt $NaNO_3$. It is liquid and stable in the range 130-550 °C. Its properties can be calculated with the correlations from [47]. The equation for specific heat was established to match the curve from the same reference. The correlations are listed in Table 1.3.

1.5.3 Liquid metals

Liquid metals are efficient heat transfer fluids that could substantially lead to the further development of concentrated solar thermal systems. The main advantages are their operating temperatures and heat transfer coefficients higher than those of other liquid HTFs. Both aspects are interesting for improving the system efficiency and therefore reducing costs. The use of liquid metals is limited by their low specific heat capacity, which discourages their use as a storage medium, and by strong corrosion properties for current metals. At this point, two main candidates have been studied: sodium (Na) and lead-bismuth eutectic (PbBi or LBE).

1.5.3.1 Liquid sodium Na

At atmospheric pressure, sodium is liquid in the temperature range 98-882 °C. Its properties may be calculated with the correlations from [49, 50], which are listed in Table 1.3.

1.5.3.2 Lead-Bismuth Eutectic LBE

The Lead-Bismuth eutectic thermal properties have been extensively studied by Sobolev [51] who established correlations to calculate them. This alloy is liquid in the range 397-1943 K, but the formulas do not cover this entire range. Those for specific heat and viscosity are valid for temperatures ranging between 400 and 1500 K. The thermal conductivity equation is valid in the range 400-1100 K, and the one for density in the range 400-1300 K. Sobolev's equations [51] are listed in Table 1.3.

1.5.4 Pressurized Air

The main advantages of air are the wide range of operating temperature, and its low cost. Moreover, it is abundant, free, environmentally benign and easy to handle. But on the other hand, it presents significant drawbacks, such as limited heat transfer properties and large pumping power requirements due to the high pressure needed. Currently studied pressurized-air receivers are designed for heating compressed air to the entrance conditions of a gas turbine. The thermal properties were defined with the help of the data tables given in Perry's Chemical Engineers' Handbook [52] which were generated from the NIST REFPROP software [53] (primary source [54, 55]). The density was calculated by applying the ideal gas law which gives a maximum error of 1.8 % for the ranges of pressure 1-50 bar and temperature 500-1500 K. For specific heat and thermal conductivity, polynomial equations were fitted to the reference data. The dynamic viscosity was calculated with Sutherland's formula, with a modification of the exponent that was changed from 1.5 to 1.54 that fits better the reference data. All equations are valid in the range 500-1500 K with a maximum error of 1.1 %. They are listed in Table 1.3.

1.5.5 Pressurized Carbon Dioxide CO_2

Recently, carbon dioxide has been considered as a possible working fluid, mainly due to its unique combination of ecological and personal safety. A review of thermodynamic cycles and working fluids was published in [12] but for low-grade heat. Carbon dioxide appears to be a good candidate because it is a non flammable and non toxic fluid; it is widely available, in sufficient quantities and at a very reasonable cost. The thermal properties were defined with the help of the NIST database [56] (primary source [57–60]). The density was calculated by applying the ideal gas law which gives a maximum error of 1.1 % for the ranges of pressure 10-50 bar and temperature 650-1100 K. For specific heat, thermal conductivity and viscosity, polynomial equations were fitted to the reference data. All equations are valid in the range 650-1100 K with a maximum error of 2.3 %. They are given in Table 1.3.

1.5.6 Helium He

The first practical use of helium as a working fluid was developed for cryogenic processes in gas turbines, and the first two small fossil-fired helium gas turbines were operated in the US for air liquefaction and nitrogen production facilities. A larger helium gas turbine plant and helium test facilities were built and operated in Germany in the 1970's to establish technological bases for a future high efficiency large nuclear gas turbine power plant

concept based on closed power cycles [61, 62]. Then helium was considered as a possible working fluid in CSP technologies. The main advantages of helium for large power plants are that it is chemically inert and its specific heat is fivefold that of air.

Helium thermal properties were defined with the help of the NIST database [56] (primary source [63–65]). The density was calculated by applying the ideal gas law which gives a maximum error of 1.9 % for a pressure of 75 bar and temperatures in the range 500-1500 K. For specific heat, thermal conductivity and viscosity, polynomial equations were fitted to the reference data. All equations are valid in the range 500-1500 K with a maximum error of 0.5 %. They are shown in Table 1.3.

1.5.7 Hydrogen H_2

Hydrogen is the most abundant element in the universe and it is the lightest gas on Earth. H_2 is a promising energy carrier, especially in relation to the possible development of renewable energy sources, and may be the best answer for storage. The main problem about this gas is that it is not present in nature and should be obtained from other elements. This implies a significant drain of energy, and therefore a cost increase. Hydrogen has been used as HTF in solar dish-Stirling systems [66].

Hydrogen thermal properties were defined with the help of the National Institute of Standards and Technology (NIST) database [56] (primary source [67–69]. The density was calculated by applying the ideal gas law which gives a maximum error of 2.1 % for a pressure of 75 bar and temperatures in the range 500-1000 K. For specific heat, thermal conductivity and viscosity, polynomial equations were fitted to the reference data. All the equations are valid in the range 500-1000 K with a maximum error of 0.2 %. They are shown in Table 1.3.

1.5.8 HTFs properties

The equations to calculate the HTFs' properties necessary for determining the heat transfer coefficient are compiled in Table 1.3. These properties are: the density ρ in [kg.m^{-3}], the specific heat capacity c_p in [J.kg^{-1}.K^{-1}], the thermal conductivity λ in [W.m^{-1}.K^{-1}], and the dynamic viscosity μ in [Pa.s]. The equations were established for temperatures in kelvins. Their validity ranges are indicated. R is the universal gas constant in [J.mol^{-1}.K^{-1}], r the specific gas constant in [J.kg^{-1}.K^{-1}] and P the pressure in [Pa].

Table 1.3: Heat transfer fluids thermophysical properties

Property equation	Validity range [K]
LIQUIDS	
Therminol VP-1 (after [44])	

Table 1.3: Heat transfer fluids thermophysical properties

Property equation		Validity range [K]
$c_p = 2.82T + 716$	(1.25)	$285 \leqslant T \leqslant 673$
$\lambda = 1.73 \times 10^{-7}T^2 + 7.62 \times 10^{-6}T + 0.14$	(1.26)	
$\rho = -7.61 \times 10^{-4}T^2 - 2.24 \times 10^{-1}T + 1191$	(1.27)	
$\mu = \left(-2.3 \times 10^{-5}T^3 + 5.61 \times 10^{-3}T^2 - 19.89T + 1822\right)^{-1}$	(1.28)	
Molten salts		
Solar salt (after [46])		
$c_p = 0.172\,(T - 273.15) + 1443$	(1.29)	$533 \leqslant T \leqslant 873$
$\lambda = 1.9 \times 10^{-4}\,(T - 273.15) + 0.443$	(1.30)	
$\rho = -0.636\,(T - 273.15) + 2090$	(1.31)	
$\mu = -1.474 \times 10^{-10}\,(T - 273.15)^3 + 2.281 \times 10^{-7}\,(T - 273.15)^2 - 1.2 \times 10^{-4}\,(T - 273.15) + 2.2714 \times 10^{-2}$	(1.32)	
Hitec (after [47])		
$c_p = 1560$	(1.33)	$415 \leqslant T \leqslant 808$
$\lambda = -1.54 \times 10^{-6}\,(T - 273.15)^2 + 4.36 \times 10^{-4}\,(T - 273.15) + 0.411$	(1.34)	
(The "-" sign before 1.54 is not a mistake but a correction of a misprint in the reference)		
$\rho = -0.74\,(T - 273.15) + 2084$	(1.35)	
$\mu = 10^{2.7374}\,(T - 273.15)^{-2.104}$	(1.36)	
Hitec XL (after [47])		
$c_p = -0.33T + 1634$	(1.37)	$403 \leqslant T \leqslant 823$
$\lambda = 0.519$	(1.38)	
(reported as a constant value)		
$\rho = -0.827\,(T - 273.15) + 2240$	(1.39)	
$\mu = 10^{6.1374}\,(T - 273.15)^{-3.36406}$	(1.40)	
Liquid metals		
Sodium (after [49, 50])		
$c_p = 4.4541 \times 10^{-4}T^2 - 0.8479T + 1658.2 - 2.9926 \times 10^{6}T^{-2}$	(1.41)	$371 \leqslant T \leqslant 1255$
$\lambda = -1.1842 \times 10^{-8}T^3 + 5.5226 \times 10^{-5}T^2 - 0.11381T + 124.67$	(1.42)	
$\rho = 275.32\,(1 - {}^{T}/_{2503.7}) + 511.58\,(1 - {}^{T}/_{2503.7})^{0.5} + 219$	(1.43)	
$\mu = \exp\left(-6.4406 - 0.3958 \ln T + 556.835/T\right)$	(1.44)	
Lead-bismuth eutectic (after [51])		
$c_p = 7.12 \times 10^{-6}T^2 - 2.72 \times 10^{-2}T + 159$	(1.45)	$400 \leqslant T \leqslant 1500$
$\lambda = -1.741 \times 10^{-6}T^2 + 1.517 \times 10^{-2}T + 3.61$	(1.46)	
$\rho = -1.3236T + 11096$	(1.47)	
$\mu = 4.94 \times 10{-}4 \exp\left({}^{6270}/_{RT}\right)$	(1.48)	
GASES		

Table 1.3: Heat transfer fluids thermophysical properties

Property equation		Validity range [K]
Air (after [52])		
$c_p = 0.1805T + 950.1$	(1.49)	$500 \leqslant T \leqslant 1500$
$\lambda = -9.72 \times 10^{-9}T^2 + 7.14 \times 10^{-5}T + 6.22 \times 10^{-3}$	(1.50)	
$\rho = {}^{P}/_{r_{air}T}$	(1.51)	
$\mu = \mu_r \left(\frac{T}{T_r}\right)^{1.54} \frac{T_r+B}{T+B}$	(1.52)	
with $T_r = 273.15$ K the reference temperature, $\mu_r = 1.716$ Pa.s the reference viscosity and $B = 110.4$ K Sutherland's constant for air.		
Carbon dioxide (after [56])		
$c_p = -3.32 \times 10^{-4}T^2 + 0.918T + 651$	(1.53)	$650 \leqslant T \leqslant 1100$
$\lambda = -1.57 \times 10^{-8}T^2 + 9.74 \times 10^{-5}T - 1.1 \times 10^{-2}$	(1.54)	
$\rho = {}^{P}/_{r_{CO_2}T}$	(1.55)	
$\mu = -1.23 \times 10^{-11}T^2 + 5.3 \times 10^{-8}T + 5.94 \times 10^{-7}$	(1.56)	
Helium (after [56])		
$c_p = -2.58 \times 10^{-6}T^2 + 8.97 \times 10^{-3}T + 5183$	(1.57)	$500 \leqslant T \leqslant 1500$
$\lambda = -3.91 \times 10^{-8}T^2 + 3.33 \times 10^{-4}T + 7.08 \times 10^{-2}$	(1.58)	
$\rho = {}^{P}/_{r_{He}T}$	(1.59)	
$\mu = -4.7 \times 10^{-12}T^2 + 4.23 \times 10^{-8}T + 8.64 \times 10^{-6}$	(1.60)	
Hydrogen (after [56])		
$c_p = 1.72 \times 10^{-3}T^2 - 1.72T + 14994$	(1.61)	$500 \leqslant T \leqslant 1000$
$\lambda = 3.6 \times 10^{-8}T^2 + 4.32 \times 10^{-4}T + 5.94 \times 10^{-2}$	(1.62)	
$\rho = {}^{P}/_{r_{H_2}T}$	(1.63)	
$\mu = -3.08 \times 10^{-12}T^2 + 1.97 \times 10^{-8}T + 3.69 \times 10^{-6}$	(1.64)	

1.6 Heat transfer coefficients for HTFs used in CST

1.6.1 Conditions of the study

As explained earlier, this work aims to compare the solar HTFs on the basis of their heat transfer coefficients. This requires choosing standard conditions and applying it to all fluids. The adopted configuration is the tubular receiver because, as explained in the introduction, it is the most widely spread. The selected tube internal diameter is 0.025 m, which corresponds to a usual tube size. The actual flow conditions of each fluid combined with their distinct properties can lead to very different values of Reynolds number. Therefore it was decided not to compare the HTFs at the same Re, but at the same fluid velocity. The fluid velocities were chosen to correspond to the order of magnitude of the usual velocities found in CSP receivers [42, 70, 71]. The selected fluid velocity is 2 m/s for liquids and 15 m/s for gases. The resulting Reynolds numbers are plotted in Figures 1.5 and 1.6 as a function of the temperature for the liquids and gases, respectively. It can

be seen that, in the chosen conditions, all but Hitec® and Hitec® XL are always above $Re = 10^4$. Figure 1.6 shows that, for the chosen conditions, CO_2 has a Reynolds number one order of magnitude higher than those of the other gases which is due to its higher density.

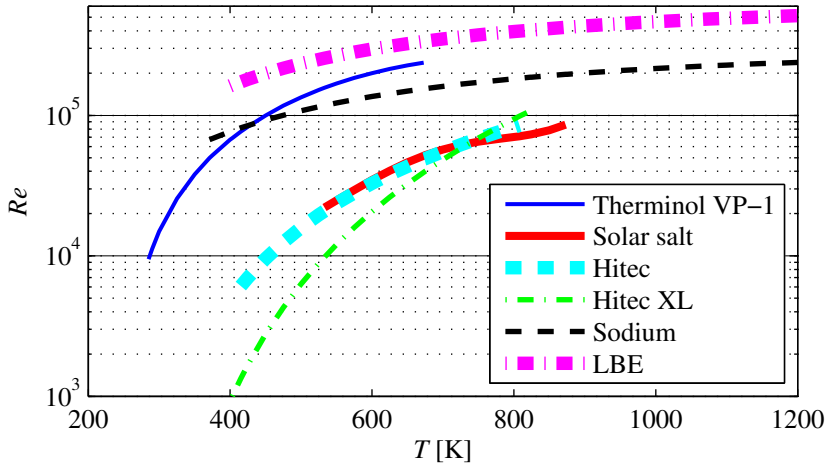

Figure 1.5: Reynolds numbers of liquid HTFs as a function of temperature for a 0.025 m tube diameter and a 2 m/s velocity.

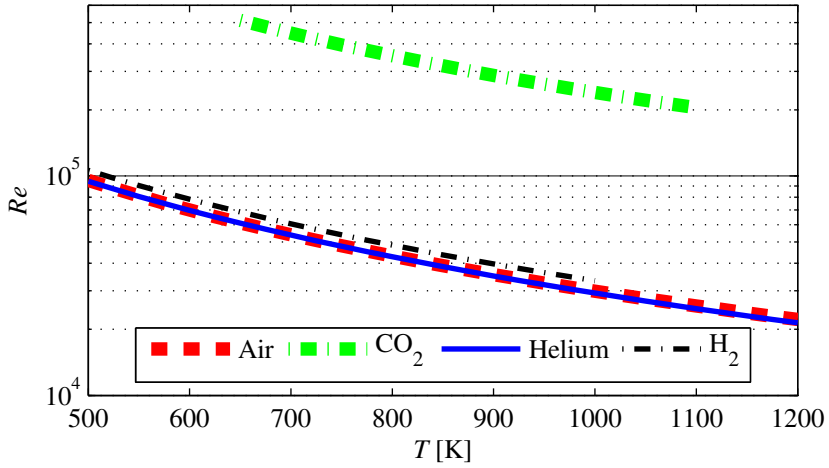

Figure 1.6: Reynolds numbers of gaseous HTFs as a function of temperature for a 0.025 m tube diameter and a 15 m/s velocity.

The appropriate correlation for each fluid was selected with the following method. When a study was done for a specific HTF, the correlation from this study was selected. This is the case for molten salts with the Liu et al. [37] (Eq (1.19)) and Wu et al. [38] (Eqs (1.20) and (1.21)) correlations. The more recent correlation of Wu et al. was preferred among these because it is an update by the same authors. For liquid metals, the appropriate correlations are: Lyon-Martinelli [40] (Eq (1.22)), Sleicher-Rouse [41] (Eq (1.23)), Cheng and Tak [42] (Eq (1.24)). The difficulty in using Lyon-Martinelli correlation is due to the choice of the turbulent Prandtl number Pr_t value. Kirillov [72] found that taking Prt = 1 always overestimated test data. It was confirmed with our calculations that showed that Lyon-Martinelli's correlation with $Pr_t = 1$ gave values 50 % higher than the other two

correlations. For this reason, Lyon-Martinelli's correlation was discarded. The most recent correlation of Cheng and Tak is based on experimental data while the Sleicher-Rouse correlation was offered tentatively and not compared to experimental results. Therefore, Cheng and Tak's correlation (Eq (1.24)) was chosen. For all the other HTFs that do not have specific correlations, Gnielinski's correlation [36] (Eq (1.17)) was applied.

Since the heat flux impacts the wall temperature, it also impacts the value of the heat transfer coefficient, which is acounted for by the use of the property-based correction factors. This is why a heat flux was chosen to compare the heat transfer fluids. Two different heat fluxes were applied: a low heat flux of 50 kW/m^2, corresponding to the case of a linear receiver and a high heat flux of 500 kW/m^2, corresponding to a central receiver system. For liquids, the heat transfer coefficients calculated were 3-19 % higher at the high heat flux. Air at 10 bar was not able to stand the high heat flux in the chosen conditions. For the other gases, the heat transfer coefficients obtained were 3-7 % lower for the high heat flux. Only the results for the 50 kW/m^2 heat flux are presented.

The upper temperature bound of the calculations corresponds to the fluid bulk temperature at which the wall temperature reaches the maximum temperature that the HTF can stand, or in some cases, the maximum temperature at which the fluid properties can be determined. Going over this temperature would mean breaking down the fluid, or in the second case it would have no meaning since the fluid properties would be inaccurate. The lower temperature bound was determined by the HTFs minimum temperatures or by the validity range of the properties equations from Table 1.3.

At high temperature, the radiation contribution to the heat exchange must be taken into account. But in the case of the fluids studied here, it has no impact. Indeed, for liquid metals, the temperature difference between the wall and the fluid is very small, which leads to a negligible radiative heat transfer. The molten salts IR absorption is low; moreover the correlations were established accounting for all the heat transferred to the fluid so they would take radiation into account. Air, He, H_2 are transparent to radiation. CO_2 is an absorbing gas but it becomes optically thick at high pressure ($>$ 50 bar) which leads to a very low influence of radiation on the heat transfer [73].

The results are presented in the form of graphs where the heat transfer coefficient is plotted as a function of the fluid temperature. In the graphs, the Nusselt numbers subscripts refer to the correlations' numbers given in Table 2. The liquid and gaseous HTFs are considered separately because they are used under different operating conditions that strongly influence the heat transfer performance in the solar receiver tubes.

1.6.2 Liquid heat transfer fluids

This section presents the heat transfer coefficients obtained for the selected liquid HTFs, apart from water that is studied in Subsection 1.6.4. The calculations were done for a 0.025 m tube diameter and a 2 m/s fluid velocity. The figures presented in this section correspond to the case of the 50 kW/m^2 heat flux.

1.6.2.1 Oil: Therminol® VP-1 (Diphenyl-Biphenyl Oxide)

The heat transfer coefficient h was calculated with Gnielinski's correlation (Eq (1.17)). Figure 1.7 plots the heat transfer coefficient of Therminol® VP-1 versus the fluid bulk temperature. The heat transfer coefficient h ranges between 1000 and 3500 W/m^2.K. It increases with T_b up to a maximum, just below 600 K, then decreases. This fall is due to the thermal conductivity which decreases with the temperature.

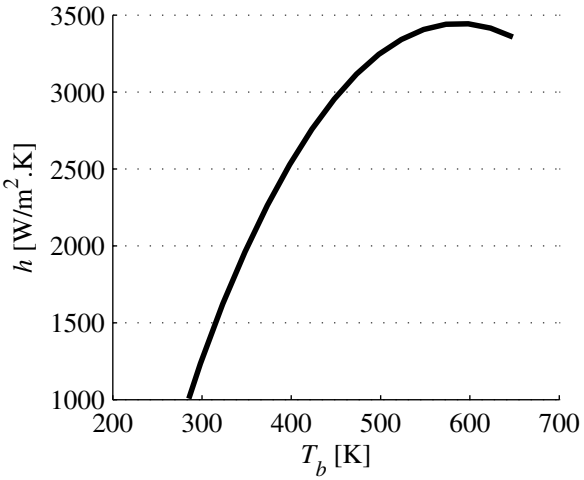

Figure 1.7: Therminol® VP-1 heat transfer coefficient versus temperature at 2 m/s; Gnielinski's correlation Eq (1.17).

1.6.2.2 Molten salts

The correlation applied to molten salts is Wu et al.'s correlation (Eqs (1.20) and (1.21)). Figure 1.8 plots the heat transfer coefficient of molten salts versus the fluid bulk temperature. For solar salt, h ranges between 3600 and 6700 W/m^2.K. It increases with the temperature with an inflection at 700 K. This is due to the dynamic viscosity fall with temperature that gets slower. For Hitec®, h ranges between 1500 and 4000 W/m^2.K. The same evolution as that of Therminol® VP-1 is observed with the heat transfer coefficient increasing up to 700K and then decreasing. Once again, this is because the thermal conductivity decreases with temperature. For Hitec® XL, h ranges between 400 and 6800 W/m^2.K. The low h at low temperature is due to the viscosity being high which leads to a low Re. Since the thermal conductivity considered is constant, the heat transfer coefficient keeps increasing with temperature.

For the three molten salts, the heat transfer coefficient values are close to each other, with solar salt a little better at low temperature and Hitec® XL at high temperature. Finally, the decisive factors to choose between these fluids will be the temperature range and the price. Hitec® and Hitec® XL will therefore be preferred because they solidify at lower temperature than solar salt and are less expensive. The only inconvenient is that their maximum temperature limit is slightly lower than that of solar salt.

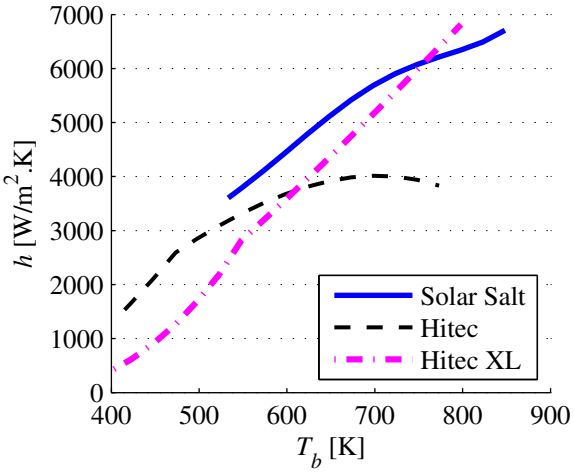

Figure 1.8: Heat transfer coefficients of molten salts versus temperature at 2 m/s; Wu et al.'s correlation Eqs (1.20) and (1.21).

1.6.2.3 Liquid metals

Cheng and Tak's correlation (Eq (1.24)) is applied to liquid metals. Figure 1.9 plots the heat transfer coefficient of liquid metals versus the fluid bulk temperature. For sodium, h ranges between 28500 and 18000 W/m^2.K. The decreasing thermal conductivity with temperature explains why the heat transfer coefficient decreases. For LBE, h ranges between 10600 and 11900 W/m^2.K. The thermal conductivity increases with temperature, inducing a heat transfer coefficient increase in spite of the decreasing Peclet number.

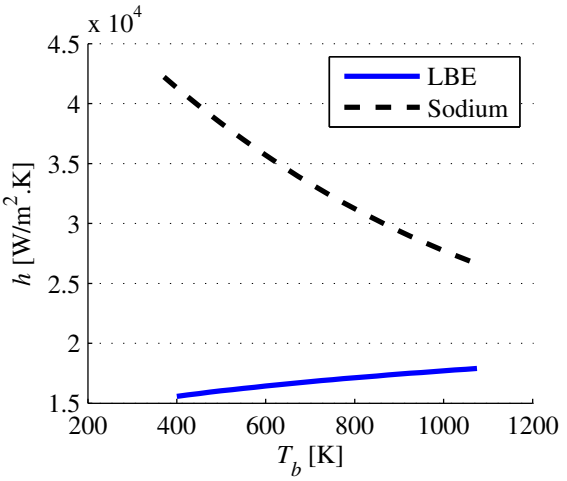

Figure 1.9: Liquid metals heat transfer coefficients versus temperature at 2 m/s; Cheng and Tak's correlation Eq (1.24).

1.6.3 Gaseous heat transfer fluids

This section presents the heat transfer coefficients of all gases, apart from steam that is studied in Subsection 1.6.4. The calculations were done for a 0.025 m tube diameter and

a 15 m/s fluid velocity. Gnielinski's correlation (Eq (1.17)) was applied. Figure 1.10 plots the heat transfer coefficient of all considered gases as a function of the fluid bulk temperature for a 50 kW/m^2 heat flux. For all gases, the sharp density decrease with temperature is responsible for the heat transfer coefficient fall.

Air was considered at a pressure of 10 bar and h ranges between 245 and 168 W/m^2.K. It is one or two orders of magnitude lower than liquid heat transfer coefficient. In a solar receiver, air will actually never circulate in a tube with 0.025 m internal diameter. To increase the heat transfer coefficient, various configurations have been developed such as micro-channels [74, 75] and surface structuring [76]. Air is also used in volumetric receivers made of ceramic foam [77, 78].

CO_2 was considered at a pressure of 50 bar and h ranges between 1200 and 1000 W/m^2.K.As for air, carbon dioxide will preferably circulate in configurations increasing the heat transfer coefficient, using fins for example.

Helium and hydrogen were considered at a pressure of 75 bar. h ranges between 1460 and 770 W/m^2.K for Helium, and 2000 and 1440 W/m^2.K for H_2, which is higher thanks to its very high specific heat capacity. This is almost as high as the heat transfer coefficient of Therminol® VP-1. Recent measurements in the hot-side heat exchanger of a Stirling engine [79, 80] under similar pressure and flow conditions, found a heat transfer coefficient of 1200 to 1500 W/m^2.K at T_b of 750 K, very close to Gnielinski's correlation predictions.

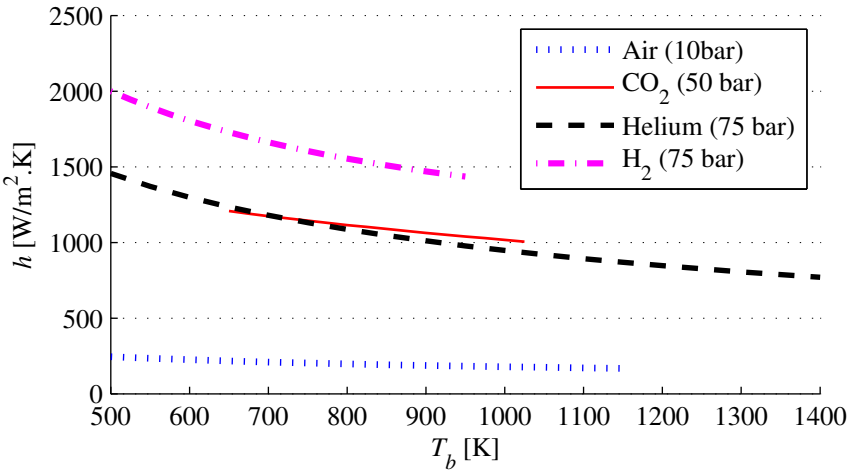

Figure 1.10: Gases heat transfer coefficients versus temperature at 15 m/s; Gnielinki's correlation Eq (1.17).

1.6.4 Water/Steam

Water has good physical properties to be used as a heat transfer fluid. It is well-known and cheap. The main problem to use it as a working fluid is that it may be unstable and difficult to manage at high temperature/high pressure. Water is chemically stable up to very high temperature, but it undergoes a phase transition from liquid to vapor. The

higher the pressure, the higher the saturation temperature at which evaporation occurs. It is more interesting to heat liquid water than steam because of its higher density, specific heat capacity and thermal conductivity. The first resulting constraint is to find a compromise between the required high pressure to operate at high temperature and the induced technological difficulties, such as the necessarily thick tube walls, which is an obstacle to heat transfer. In most water/steam receivers, the liquid water heating and evaporation (steam production) part is separated from the steam superheating part, because they have very different characteristics in terms of heat transfer. In the steam production part of the process, another challenge is to control the boiling for avoiding energy losses due to the water recirculation. But this control must be achieved without reaching the point of complete dryness where the sudden heat transfer coefficient drop would provoke a violent tube temperature increase and therefore threaten the piping integrity. Finally, the upper limit at which water can be used as a heat transfer fluid in the saturated state for thermodynamic cycles is 374°C and 221 bar, when it becomes supercritical. Steam superheating at pressure lower than the supercritical pressure allows increasing the working temperature. For example, molten salt central receiver solar power plants use typically 550 °C/126 bar superheated steam.

Water and steam properties were calculated using the industrial standard IAPWS-IF97 [81]. Two cases were considered: a high pressure (150 bar) high flux density (500 kW/m^2) case, corresponding to a central receiver, and a medium pressure (80 bar) medium flux density (50 kW/m^2), corresponding to a linear receiver. In each case, the mass flux was calculated for a 2 m/s liquid velocity at saturation temperature and a 0.025 m tube internal diameter.

The water boiling flow can be separated into three zones where various types of heat transfer take place. Figure 1.11, extracted from Kandlikar's work [82] gives a detailed schematic representation of the boiling flow. It is decomposed into six regions. In the first region, the liquid water is heated and approaches the saturation temperature. At point B, the saturation temperature is reached first near the wall since the liquid temperature is not uniform. Point C is the beginning of the subcooled boiling where gas bubbles may begin to form depending on the wall properties, heat flux and flow conditions. It comprises the partial boiling, the fully developed boiling, and the significant void flow regions. Then, when the bulk temperature surpasses the saturation temperature, at point H, the saturated boiling region is reached. Finally, when all the water is evaporated, the state of superheated steam is reached.
The method used to calculate the heat transfer coefficient during water/steam evaporation is described in [82].

Liquid water region: The heat transfer coefficient h_l in the liquid water region is calculated using Petukhov's correlation [34] already presented in Table 1.2 (Eq (1.13)) and the property correction factor for liquids (Eq (1.16). An iterative scheme is needed to calculate h and T_w at given values of T_b and φ.

Onset of Nucleate Boiling (ONB): The subcooled boiling region begins at the onset of nucleate boiling ONB (point C on Figure 1.11). The wall superheat ΔT_{sat} is the difference between the wall temperature and the liquid saturation temperature. The liquid

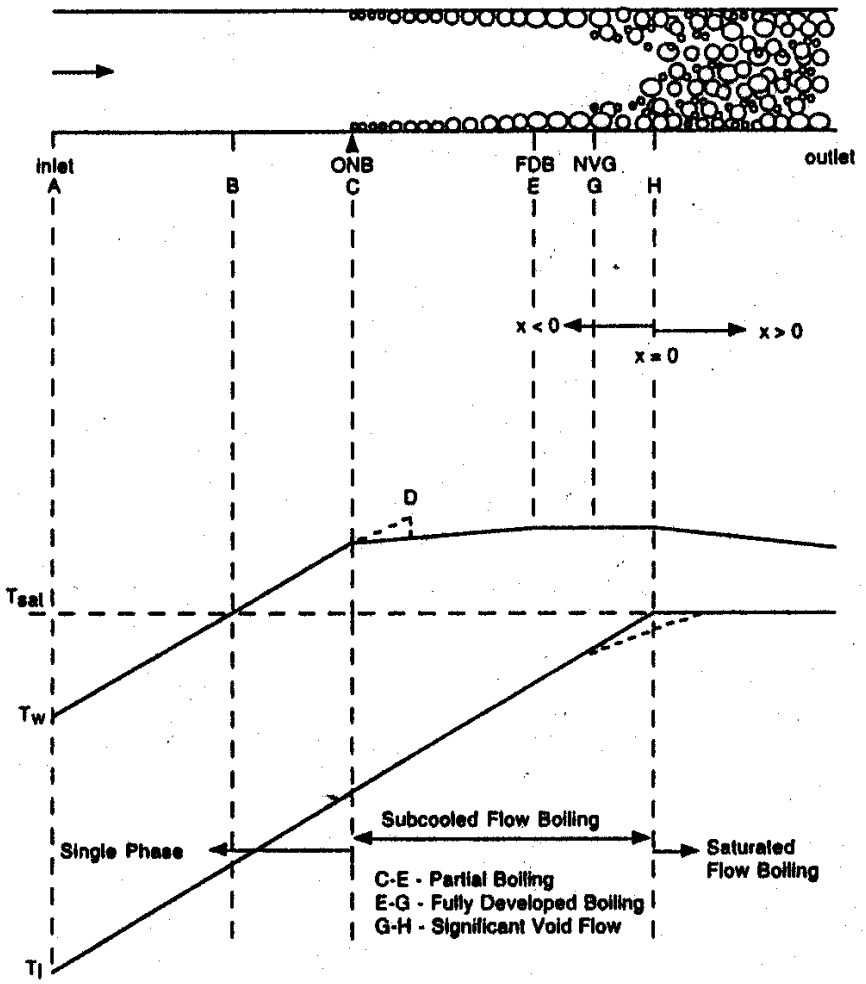

Figure 1.11: Schematic representation of the boiling flow, after [82].

subcooling ΔT_{sub} is the difference between the liquid saturation temperature and the liquid bulk temperature. Both ΔT_{sat} and ΔT_{sub} are positive in the subcooled region. The wall superheat at ONB, $\Delta T_{sat,ONB}$ is determined from the equation proposed in [83]:

$$\varphi_{ONB} = \frac{\lambda_l H_{lg}}{8\gamma\nu_{lg}T_{sat}} \left(\Delta T_{sat,ONB}\right)^2 \tag{1.65}$$

where H_{lg} is the specific enthalpy of vaporization, γ the surface tension, ν_{lg} the specific volume difference between water and steam at the saturation temperature.

Once $\Delta T_{sat,ONB}$ is known, the liquid subcooling $\Delta T_{sub,ONB}$ is determined by applying the following equation presented in [84]:

$$\Delta T_{sat,ONB} = \frac{4\gamma T_{sat}\nu_{lg}h_{lo}}{\lambda_l H_{lg}} \left(1 + \sqrt{\frac{\lambda_l H_{lg}\Delta T_{sub,ONB}}{2\gamma T_{sat}\nu_{lg}h_{lo}}}\right) \tag{1.66}$$

with h_{lo} the heat transfer coefficient for liquid only, calculated with Eqs (1.13) and (1.16). An iterative scheme is needed to solve (1.66) for $\Delta T_{sub,ONB}$ at given value of $\Delta T_{sat,ONB}$. The properties in Eqs (1.65)and (1.66) are evaluated at the saturation temperature T_{sat}, except for h_{lo} that is determined at T_b.

Fully Developed Boiling (FDB) region: After ONB, two heat transfer modes are combined: the single-phase convective mode, and the nucleate boiling mode. FDB begins when the heat transfer is essentially due to the nucleate boiling mode. The model defined in [85] is applied considering that, in the FDB region, the two-phase convective contribution is insignificant. Therefore, the nucleate boiling contribution is expected to be responsible for the whole heat transfer. Thus, the equation to calculate the heat transfer coefficient in the nucleate boiling dominant region is given by:

$$h_{TP} = 1058 Bo^{0.7} h_{lo} \tag{1.67}$$

with h_{TP} the two-phase heat transfer coefficient and Bo the boiling number:

$$Bo = \frac{\varphi}{G H_{lg}} \tag{1.68}$$

with G the mass flux.

The heat transfer in the FDB region of the subcooled flow is expressed as a function of the temperature difference between the water and the wall:

$$\varphi = h_{TP}\Delta T_{sat} = h_{FDB}\left(\Delta T_{sat} + \Delta T_{sub}\right) \tag{1.69}$$

By combining Eqs (1.67)-(1.69), the expression for φ in the FDB region is obtained as:

$$\varphi = \left[1058\,(GH_{lg})^{-0.7}\,h_{lo}\Delta T_{sat}\right]^{1/0.3} \tag{1.70}$$

To locate the point where FDB begins, noted E in Figure 1.11, the model defined in [86] is used. The intersection of the liquid phase and FDB heat transfer coefficients for a constant subcooling, noted F in Figure 1.11, must be identified by solving the set of heat flux equations: $q = h_{lo}\,(\Delta T_{sat} + \Delta T_{sub})$ for the liquid phase and Eq (1.70) for FDB. Combioning the two equations gives:

$$1058\,(GH_{lg})^{-0.7}\,\varphi_F - \varphi_F^{0.3} - 1058 h_{lo}\,(GH_{lg})^{-0.7}\,\Delta T_{sub,F} = 0 \tag{1.71}$$

The model indicates that the heat flux at point F is:

$$\varphi_F = \varphi_E/1.4 \tag{1.72}$$

An iterative scheme is needed to solve Eq (1.71) for ΔT_{sub} at given φ_F and G. Then $\Delta T_{sat,FDB}$ is determined using Eq (1.70) and finally h_{FDB} is obtained from Eq (1.67).

Partial boiling region: The partial boiling region is identified as the region between ONB and the beginning of FDB, respectively corresponding to points C and E on Figure 1.11. A method was developed to assure a smooth transition from the single-phase region to the partial boiling region, and then to the FDB region [87, 88]. To be applicable, it requires a heat flux difference between ONB and E. In the present study, the heat flux is uniform but a near zero difference can be supposed between ONB and E: $\varphi_E - \varphi_{ONB} = 10^{-5}$ W/m^2. The heat transfer is obtained by the following equation:

$$\varphi = a + b\,(T_w - T_{sat}) \tag{1.73}$$

The equations to determine the coefficients b, a, m, p and c are as follows:

$$b = \frac{\varphi_E - \varphi_{ONB}}{\Delta T_{sat,E}^m - \Delta T_{sat,ONB}^m} \tag{1.74}$$

$$a = \varphi_{ONB} - b\Delta T_{sat,ONB}^m \tag{1.75}$$

$$m = c + pq \tag{1.76}$$

$$p = \frac{1/0.3 - 1}{\varphi_E - \varphi_{ONB}} \tag{1.77}$$

$$c = 1 - p\varphi_{ONB} \tag{1.78}$$

By discretizing the partial boiling region and interpolating linearly the heat flux between ONB and E, the wall temperature T_w may be determined from Eq (1.73) for each point of the discretization:

$$\varphi_i = \varphi_{ONB} + (\varphi_E - \varphi_{ONB}) \frac{i}{N} \tag{1.79}$$

with N the number of intervals taken for the discretization and $i \in [|0; N|]$ the iteration number corresponding to the discretized point considered.

$$T_{w,i+1} = T_{sat} + \frac{\varphi_i - a_i}{b_i} \tag{1.80}$$

Note that φ_i, m_i, b_i and a_i must be calculated at each iteration.

Then, by approximating the specific heat capacity between points (i) and $(i+1)$ as $c_p\,(T_{b,i})$, the bulk liquid temperature can be calculated with the formula:

$$T_{b,i+1} = T_{b,i} + \frac{T_E - T_{ONB}}{N} \frac{c_p T_{b,i}}{\bar{c_p}_{partial\ boiling}} \tag{1.81}$$

with $\bar{c_p}_{partial\ boiling}$ the mean specific heat capacity between T_{ONB} and T_E. Note that $T_{b,0} = T_{b,ONB}$ and $T_{b,N} = T_{b,E}$.

In this study, the partial boiling region was discretized in $N = 40$ intervals, which proved to be enough to obtain the right value of $T_{b,E}$, when starting from $T_{b,ONB}$. Finally, the last step is to calculate the heat transfer coefficient using the deduced temperatures.

Significant void flow region: The point of Net Vapor Generation (NVG) identifies the location in the subcooled flow where the net void fraction begins to be significant. The thermodynamic quality relative to the saturation state is defined as:

$$x = \frac{l_l - l_{sat}}{H_{lg}} = \frac{c_{p,l} \Delta T_{sub}}{H_{lg}} \tag{1.82}$$

The resulting quality is negative in the subcooled region. The correlation established by Saha and Zuber [89] for the case $Re_l Pr_l > 70000$, is applied to determine the thermodynamic quality at the point of NVG:

$$x_{NVG} = -154 Bo \tag{1.83}$$

It is postulated in [82] that the saturated boiling correlations are applicable in this region. The dryness fraction, which is normally used in the correlations, is replaced in the subcooled region by an apparent thermodynamic quality called x_a, accounting for the non-equilibrium

effects. Although the thermodynamic quality x is negative in this region, x_a, which is based on the void fraction, is positive. It is defined as follows:

$$x_a = \frac{x - x_{NVG} \exp\left(x/x_{NVG} - 1\right)}{1 - x_{NVG} \exp\left(x/x_{NVG} - 1\right)} \tag{1.84}$$

Once the apparent quality x_a has been defined, the saturated boiling correlations in [85] are applied. In these correlations, the ratio of the two-phase heat transfer coefficient over the liquid heat transfer coefficient, for water flowing in horizontal or vertical tubes with a liquid Froude number higher than 0.04, is expressed as follows:

$$\frac{h_{TP}}{h_{lo}} = C_1 Co^{C_2} + C_3 Bo^{C_4} \tag{1.85}$$

where Co is the convection number defined as:

$$Co = \left(\frac{1 - x_a}{x_a}\right)^{0.8} \left(\frac{\rho_g}{rho_l}\right)^{0.5} \tag{1.86}$$

Note that, in this case, x_a is used instead of the dryness factor.

The values of the parameters C_1-C_4 depend on the convection number Co. They are presented in Table 1.4. The two sets of values correspond to the convective boiling and nucleate boiling regions, respectively. The heat transfer coefficient at any given condition is evaluated using the sets of constants for the two regions, and the highest of the two values represents the predicted heat transfer coefficient from the proposed correlation.

Table 1.4: Values of parameters C_1-C_4 used in Eq (1.85)

Constants	Convective boiling region	Nucleate boiling region
C_1	1.1360	0.6683
C_2	-0.9	-0.2
C_3	667.2	1058
C_4	0.7	0.7

Saturated boiling region: For the saturated boiling region, the same correlations as in the significant void flow region are applied, with the dryness factor instead of the thermodynamic quality. A recirculation ratio of 25 % for the water heating and evaporation part is recommended in [90] for steam generation in parabolic trough receivers. The recirculation ratio is lower in the case of central receivers, which means that less water is vaporized. This is done for safety reasons because the heat transfer falls drastically when complete dryness is achieved. The two-phase heat transfer coefficient h_{TP} was calculated until the point where half the water was evaporated for both studied cases. Figure 1.12 shows the

heat transfer coefficient h evolution, from the liquid region to the saturated boiling region, with a constant mass flux of 1444 kg/m^2.s, as a function of the apparent thermodynamic quality xa. The mass flux of 1444 kg/m^2.s corresponds to a velocity of 2 m/s for water at 80 bar and the saturation temperature. x_a is calculated from Eq (1.84), in which x is either the thermodynamic quality defined by Eq (1.82) when the bulk temperature is below the saturation temperature, or the dryness factor when the saturation temperature is reached. In the liquid region, there is almost no difference between the two cases with huge values of the heat transfer coefficient around 11000 W/m^2.K .It can be seen that because of the higher heat flux received, and therefore the higher boiling number, the subcooled boiling starts earlier for the high pressure (150 bar) high flux (500 kW/m^2) case. The heat transfer quickly rises to a value of 80 000 W/m^2.K. On the other hand, the low heat flux (50 kW/m^2) received by the fluid in the other case prevents the flow from reaching the point of fully developed boiling before the saturation temperature (Eq (1.70) does not have a solution). Practically speaking, the bubbles that form on the wall surface do not detach, which is a hindrance to the single-phase convective heat transfer and leads to a heat transfer coefficient drop just before reaching the saturation temperature (just before $x_a = 0$). Then in the saturated boiling region, the heat transfer progressively increases to reach very high values, over 50000 W/m^2.K in our case.

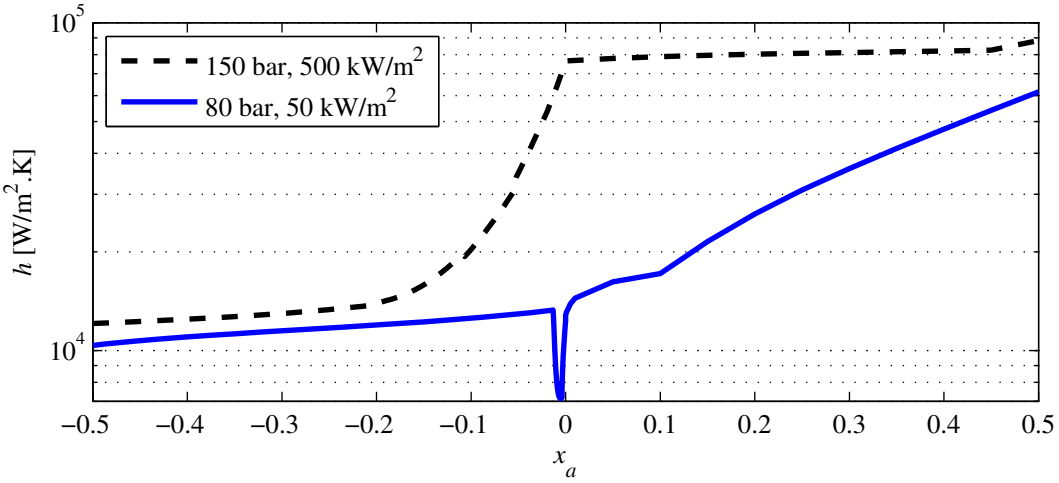

Figure 1.12: Water heat transfer coefficient from the liquid region to the saturated boiling region as a function of the apparent thermodynamic quality with a constant mass flux of 1444 kg.m^{-2}.s^{-1}.

Superheated steam region: The great difference of heat transfer characteristics between the liquid state and the vapor state is a strong incentive to separate the two flows in a heat exchanger, and solar receivers are no exception. Therefore the steam heat transfer calculations done in this study are separated from those for the liquid water heat transfer. The heat transfer coefficient h_g in the steam region is calculated using Petukhov's correlation [34] already presented in Table 1.2, Eq (1.13), and the property correction factor for gases, Eq (1.6). Figure 1.13 shows the heat transfer coefficient of superheated steam as a function of temperature, for a constant velocity of 15 m/s, for both studied cases. It can be seen that the pressure has a beneficial effect on the heat transfer coefficient. Indeed, it has a direct effect on the steam density. But as temperature increases, the decrease in specific heat and density makes the heat transfer fall, and the difference between the

two cases gets lower at high temperature. For the 150 bar case, the highest value of heat transfer coefficient is almost 17000 W/m^2.K at 615 K and it falls to 2350 W/m^2.K at 850 K. For the 80 bar case, the heat transfer coefficient decreases from 4370 W/m^2.K to 1350 W/m^2.K when the temperature increases from 570 to 850 K.

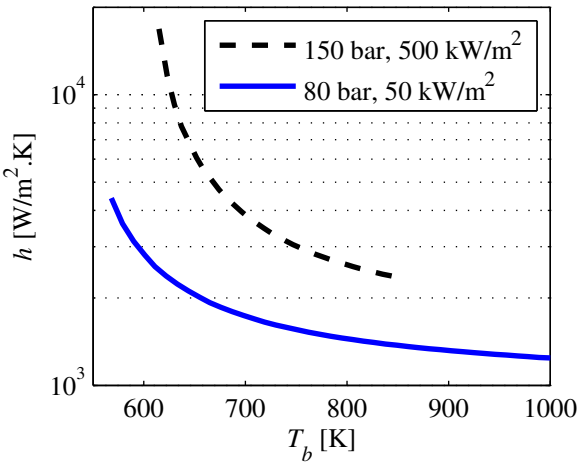

Figure 1.13: Steam heat transfer coefficient as a function of the temperature for a constant velocity of 15 m/s; Petukhov's correlation Eq (1.13).

1.6.5 Comparison

In the case of liquid HTFs, liquid metals, and especially sodium, have the highest heat transfer coefficients, especially due to their high thermal conductivity. Water also has a high heat transfer coefficient but it starts boiling at low temperature in comparison to the other liquid HTFs. In comparison to molten salts, Na and LBE present a lower specific heat capacity. Therefore liquid metals are not economically competitive for being used as storage medium because the unit cost is higher, due to lower storage density. Nevertheless, they are very promising for new generation CSP plants working at higher temperature and higher solar concentration ratio.

In the case of gases, 80 bar steam has the highest heat transfer coefficient at low temperature but it falls quickly when temperature increases. The lack of data for water above 1073 K does not allow calculations at higher temperature. Apart from steam, Hydrogen is the best gaseous HTF with a heat transfer coefficient comprised between 2000 and 1440 W/m^2.K. Air has the lowest heat transfer coefficient, this is why special configurations are developed to enhance its heat transfer coefficient.

1.7 Innovative heat transfer media

This section deals with the recent developments on HTFs. Molten salts, liquid metals, supercritical fluids and particle flows are concerned.

1.7.1 Liquid heat transfer fluids

1.7.1.1 Nitrate molten salt with low melting point and high thermal stability

A new advanced molten salt HTF has been studied and developed [91] for solving the molten salts main limitation, i.e. their high melting point, and warranting a high thermal stability. Such a novel material would enable higher temperature operation and increased efficiency in converting solar energy to electricity. This is why it could be perfect for use in concentrating solar power applications or other high temperature processes. This advanced HTF embodies a novel composition of materials, and consists in a mixture of nitrate salts of lithium, sodium, potassium, cesium and calcium (8 %wt $LiNO_3$, 6 %wt $NaNO_3$, 23 %wt KNO_3, 44 %wt $CsNO_3$, 19 %wt $Ca(NO_3)_2$-$4H_2O$).

This unique mixture exploits eutectic behavior resulting in a low melting point of 65 °C and thermal stability up to over 500 °C. This is due especially to cesium addition, which enables a melting point reduction of 25 °C relative to the quaternary eutectic. The identified eutectic is likely the mixture of these components with the lowest possible melting point.

Cost is an important consideration for a commercially viable heat transfer fluid. The cost of raw materials for this advanced HTF is considerably higher than that of the simpler binary solar salt. Fortunately, this cost may be reduced by optimizing the mixture to limit the cesium nitrate and lithium nitrate amounts while maintaining acceptable physical properties.

Another quaternary nitrate salt mixture was identified in [92], with composition 17.5 %wt $LiNO_3$, 14.2 %wt $NaNO_3$, 50.5 %wt KNO_3 and 17.8 %wt $NaNO_2$, with a melting point of 99 °C and thermal stability up to 500 °C.

1.7.1.2 Other options for molten salts

Halide-based molten salt was examined in [93] with working temperature up to 800 °C as objective. Single and eutectic salts based on five key species of halide salts - $AlCl_3$, $ZnCl_2$, $FeCl_3$, NaCl, and KCl - were reviewed. Research is still under development, in particular dealing with thermophysical properties and corrosion [94]. If some Nickel based alloys can have a good resistance with corrosion rates of 10 μ_m/year, they are nearly four times more expensive than iron-based steels.

1.7.1.3 Liquid metals

Apart from sodium and lead-bismuth eutectic, liquid tin is also a potential candidate [38]. But operation at temperature higher than 500 °C results in strong compatibility issues. Na-K eutectic (22.2 %wt Na, 77.8 %wt K) that melts at -12.6 °C and boils at 785 °C may also be used [95]. Recently, a review of current researches on liquid metals as HTF for solar power plants in Germany was published [96].

1.7.2 Supercritical fluids

1.7.2.1 Supercritical water s-H_2O

Supercritical water (s-H_2O, 374 °C and 221 bar) has been used as the working fluid in conventional power plants for decades. The steam parameters of the corresponding ultra-super critical steam are 620 °C / 310 bar [97]. These plants reach a net efficiency of about 45 % (power in the range 200-1000 MW). A study of the benefits and encountered problems during the operation of a 600 MW power plant was published [98]. The target for future generation is efficiency higher than 50 % with a turbine working at inlet temperature ranging between 700 °C and 760 °C [99]. There is currently no solar thermal power plant operating with s-H_2O as HTF due to technical issues (high pressure and high temperature) and power range of existing turbines. A feasibility study was published [100], and the steam turbines will need to be scaled-down for solar power tower plants [29].

1.7.2.2 Supercritical CO_2 s-CO_2

The CO_2 supercritical state (s-CO_2) is observed at 73.8 bar and 304.5 K, and favorable heat transfer and viscous supercritical properties permit to design innovative conversion systems. One challenge of using CO_2 as the receiver heat transfer fluid is its integration with storage. Indeed, thermal storage of supercritical fluids was shown not to be viable, thus requiring intermediate heat exchange with a separate storage medium. Possible configurations are described in [101]. In addition, s-CO_2 requires high pressure, thus imposing thicker pipes and new welds and ball joints. Therefore, it seems to be more suitable for central tower systems than for trough CSP systems [1, 71]. s-CO_2 cycles show higher efficiencies than state-of-the-art steam or air cycles. The great potential of advanced s-CO_2 power cycles for concentrated solar energy conversion was demonstrated [1] with configurations such as recompression cycles, combined with intercooling and/or turbine reheat able to achieve efficiencies higher than 50 % for turbine inlet temperatures higher than 700 °C. CO_2 recompression Brayton cycles were shown to have thermal efficiency potentially exceeding 60 % at 30 MPa maximum pressure and above 1000 °C maximum temperature with wet cooling [3]. A review of s-CO_2 applications in nuclear power plants was published [102]. s-CO_2 cycles have never been applied to solar thermal power plant because several critical components are not available [103]. The US-DOE SunShot initiative finances the development of a 10 MW s-CO_2 turbine for application in solar thermal power plants at Sandia National Laboratories [104, 105] to contribute to the development of these key components.

1.7.3 Particle suspensions

Particle receivers work following various particle circulation concepts: moving bed, falling film, bubbling fluidized bed, spouted bed, upflow bed [27, 28], circulating fluidized bed [106]. They were recently reviewed by Zhang et al. [29]. Some examples were selected, corresponding to either direct or indirect particle irradiation. Direct absorption systems using particles are very attractive because no window is necessary and they accept very high solar flux density (of the order of 1 MW/m^2), but the main drawback is that particle flow stability is difficult to control and convection losses may be high. Indirect absorption

solid particle receivers accept lower flux density only (in the range 300-400 kW/m^2) but they offer a better control of particle circulation within the receiver, and a possible management of operating pressure and atmosphere composition. Researches in both fields are commented hereafter.

1.7.3.1 Direct absorption particle suspension flow

The free falling particle curtain concept was developed in the 80's. The solid is heated directly by the concentrated solar beam. Particles drop from the top of the receiver and are heated during the residence time of their pass through the concentrated radiation. Particle selection and radiative heat transfer modeling have been proposed in [107, 108]. This concept was then developed at pilot scale, because it seemed to be a promising option for a new generation of high temperature solar thermal concentrating plants. Improved models were developed [109] and validated by on-sun experiments at pilot scale [110]. The receiver prototype was tested at the National Solar Thermal Test Facility (NSTTF) in Albuquerque (NM, USA) with solar power in the range 1.58-2.5 MW_{th}. Aluminosilicate particles containing 7 % Fe_2O_3 (CARBO HSP 20/40) with 697 μ_m mean diameter were used. Another option was proposed in [111]. In this face-down solid particle receiver concept, the particle curtain lines the inner wall of a cylinder closed at its upper part; the bottom part facing the concentrated solar beam. Finally, the solid particle solar power plant was compared with more standard options [112], which showed that a particle-receiver tower with a combined cycle has the lowest solar leveled electricity cost (about 10 c€/kWh). Moreover, storage may be achieved using the same particles as the HTF in particle receiver solar power plants similarly to molten salt solar plants.

1.7.3.2 Indirect absorption particle suspension flow

The concept of circulating dense particle suspension as a HTF was proposed [113] and developed very recently [27, 28]. It consists in creating an upward flow of solid particles inside tubes that constitute the solar receiver. The apparent suspension density is about 1000 kg/m^3, that-is-to-say approximately 1000 times higher than that of air at atmospheric pressure. Therefore, the solid carries almost all the energy, whereas the medium has almost the properties of a liquid. Particle temperature of about 750 °C was reached with metallic tubes and temperature over 1000 °C should be reached with ceramic tube. In the conditions of the study, experimental wall-to-suspension heat transfer coefficient varied in the range 400-1100 W/m^2.K as a function of solid flux, temperature and suspension density.

1.8 Conclusion

Thermodynamic cycle efficiency in the range 35-42 % may be achieved with current liquid and two-phase heat transfer fluids used in solar thermal power plants: thermal oil, molten salt and water-steam. Cycle efficiency of 50 % and more are attainable with new HTFs that are stable at 700 °C and above. New molten salts, liquid metals, supercritical water and carbon dioxide, pressurized gases and particles are possible HTFs candidates for reaching this aim. Researches on thermophysical properties, chemical stability, heat transfer performances and material compatibility are strongly necessary to achieve this

technological goal. Moreover, the coupling between heat transfer fluid characteristics and storage performances is of prime importance for plant design and cost. Obviously, the best solution consists in using the same fluid for HTF and storage medium.

1.9 Nomenclature

Abreviations

CSP	Concentrating Solar Power	NVG	Net Vapor Generation
FDB	Fully Developed Boiling	ONB	Onset of nucleate boiling
HTC	Heat Transfer Coefficient	ORC	Organic Rankine Cycles
HTF	Heat Transfer Fluid	s-CO_2	Supercritical carbon dioxide
LBE	Lead-Bismuth Eutectic	s-H_2O	Supercritical steam
NIST	National Institute of Standards and Technology		

Latin symbols

a,b,c,m,p	Coefficients in Eqs (1.73)-(1.78)	H	Specific enthalpy [J/kg]
Bo	Boiling number	N	Number of intervals for discretization in Eq (1.79)
Co	Convection number	n	Exponent for the gas property correction factor
C_{1-4}	Coefficients in Eq (1.85)	Nu	Nusselt number
c_p	Specific heat capacity at constant pressure [J/kg/K]	Pe	Peclet number
D	Tube diameter [m]	Pr	Prandtl number
d	Characteristic dimension [m]	r	Specific gas constant [$J.kg^{-1}.K^{-1}$]
G	Mass flux [$kg.m^{-2}.s^{-1}$]	T	Temperature [K]
h	Convective heat transfer coefficient [$W.m^{-2}.K^{-1}$]	v	Specific volume [m^3/kg]
i	Iteration number for discretization in Eq (1.79)	x	Thermodynamic quality
K	Property based correction factor	x_a	Apparent thermodynamic quality
L	Tube length [m]	y	Coordinate along the direction radial to the wall [m]

Greek symbols

ΔT_{sat}	Wall superheat [K]	μ	Dynamic viscosity [Pa.s]
ΔT_{sub}	Fluid subcooling [K]	ξ	Friction factor
γ	Surface tension [N/m]	ρ	Density [kg/m^3]
λ	Thermal conductivity [$[W.m^{-1}.K^{-1}$]	φ	Heat flux density [W/m^2]

Subscripts, Superscripts

b	Refers to the fluid bulk temperature	lo	Liquid Only (opposed to two-phase)
f	Fluid	sat	Saturation
$film$	Refers to the fluid film temperature	sub	Subcooling
g	Gas	t	Turbulent
l	Liquid	TP	Two-phase
lg	Vaporization	w	Wall

Bibliography

[1] C.S. Turchi, Z. Ma, T.W. Neises, and M.J. Wagner. Thermodynamic study of advanced supercritical carbon dioxide cycles for concentrated solar power. *ASME Journal of Solar Energy Engineering*, 35(4), 2013.

[2] O. Bolland. A comparative evaluation of advanced combined cycle alternatives. *ASME Journal of Engineering for Gas Turbines and Power*, 113(2):190–197, 1991.

[3] M.T. Dunham and B.D. Iverson. High-efficiency thermodynamic power cycles for concentrated solar power systems. *Renewable and Sustainable Energy Reviews*, 30:758–770, 2014.

[4] G.J. Kolb, C.K. Ho, T.R. Mancini, and J.A. Gary. Power tower technology roadmap and cost reduction plan. Technical Report SAND2011-2419, Sandia National Laboratories, Albuquerque, NM, 2011.

[5] G. Barigozzi, G. Bonetti, G. Franchini, A. Perdichizzi, and S. Ravelli. Thermal performance prediction of a solar hybrid gas turbine. *Solar Energy*, 86(7):2116–2127, 2012.

[6] G. Tsiklauri, R. Talbert, B. Schmitt, G. Filippov, R. Bogoyavlensky, and E. Grishanin. Supercritical steam cycle for nuclear power plant. *Nuclear Engineering and Design*, 235(15):1651–1664, 2005.

[7] C.W. Forsberg, P.F. Peterson, and H. Zhao. High-Temperature Liquid-Fluoride-Salt Closed-Brayton-Cycle Solar Power Towers. *ASME Journal of Solar Energy Engineering*, 129(2):141–146, 2006.

[8] J.M. Wheeldon. Engineering and Economic Evaluation of 1300F Series Ultra-Supercritical Pulverized Coal Power Plants: Phase 1. Technical Report 1015699, Electric Power Research Institute, Palo Alto, CA, 2008.

[9] B.D. Iverson, T.M. Conboy, J.J. Pasch, and A.M. Kruizenga. Supercritical CO_2 Brayton cycles for solar-thermal energy. *Applied Energy*, 111:957–970, 2013.

[10] V. Dostal, P. Hejzlar, and M.J. Driscoll. The supercritical carbon dioxide power cycle: Comparison to other advanced power cycles. *Nuclear Technology*, 154(3):283–301, 2006.

[11] A. Kribus, P. Doron, R. Rubin, J. Karni, R. Reuven, S. Duchan, and E. Taragan. A Multistage Solar Receiver: The Route To High Temperature. *Solar Energy*, 67(1-3), 1999.

[12] H. Chen, D.Y. Goswami, and E.K. Stefanakos. A review of thermodynamic cycles and working fluids for the conversion of low-grade heat. *Renewable and Sustainable Energy Reviews*, 14(9):3059–3067, 2010.

[13] F.J. Fernández, M.M. Prieto, and I. Suárez. Thermodynamic analysis of high-temperature regenerative organic Rankine cycles using siloxanes as working fluids. *Energy*, 36(8):5239–5249, 2011.

[14] R. Chacartegui, D. Sánchez, J.M. Muñoz, and T. Sánchez. Alternative ORC bottoming cycles for combined cycle power plants. *Applied Energy*, 86(10):2162–2170, 2009.

[15] R. Chacartegui, J.M. Muñoz de Escalona, D. Sánchez, B. Monje, and T. Sánchez. Alternative cycles based on carbon dioxide for central receiver solar power plants. *Applied Thermal Engineering*, 31(5):872–879, 2011.

[16] N. Woudstra, T. Woudstra, A. Pirone, and T. van der Stelt. Thermodynamic evaluation of combined cycle plants. *Energy Conversion and Management*, 51(5):1099–1110, 2010.

[17] C.K. Ho and B.D. Iverson. Review of high temperature central receiver designs for concentrating solar power. *Renewable and Sustainable Energy Reviews*, 26:835–846, 2014.

[18] M.J. Bignon. The Influence of the Heat Transfer Fluid on the Receiver Design. *Electric Power Systems Research*, 3:99–109, 1980.

[19] M. Becker. Comparison of heat transfer fluids for use in solar thermal power stations. *Electric Power Systems Research*, 3:139–150, 1980.

[20] H.L. Zhang, J. Baeyens, J. Degrève, and G. Cáceres. Concentrated solar power plants: Review and design methodology. *Renewable and Sustainable Energy Reviews 2013*, 22:466–481, 2013.

[21] J. Spelling, A. Gallo, M. Romero, and J. González-Aguilar. A High-Efficiency Solar Thermal Power Plant using a Dense Particle Suspension as the Heat Transfer Fluid. *Energy Procedia*, 69:1160–1170, 2015.

[22] H. Benoit, L. Spreafico, D. Gauthier, and G. Flamant. Review of heat transfer fluids in tube-receivers used in concentrating solar thermal systems: Properties and heat transfer coefficients. *Renewable and Sustainable Energy Reviews*, 2015.

[23] J. Sarkar. Second law analysis of supercritical CO_2 recompression Brayton cycle. *Energy*, 34:1172–1178, 2009.

[24] M.J. Hexemer. Supercritical CO_2 Brayton recompression cycle design and control features to support startup and operation. *4^{th} International Symposium on Supercritical CO_2 Power Cycles Technologies for Transformational Energy Conversion, September 9-10, 2014, Pittsburgh, Pennsylvania*, 2014.

[25] S. Kuravi, J. Trahan, D.Y. Goswami, M.M. Rahman, and E.K. Stefanakos. Thermal energy storage technologies and systems for concentrating solar power plants. *Progress in Energy and Combustion Science*, 39(4):285–319, 2013.

[26] K. Vignarooban, X. Xu, A. Arvay, K. Hsu, and A.M. Kannan. Heat transfer fluids for concentrating solar power systems - A review. *Applied Energy*, 146:383–396, 2015.

[27] G. Flamant, D. Gauthier, H. Benoit, J.-L. Sans, R. Garcia, B. Boissière B., R. Ansart, and M. Hemati. Dense suspension of solid particles as a new heat transfer fluid for concentrated solar thermal applications: On-sun proof of concept. *Chemical Engineering Science*, 102:567–576, 2013.

[28] H. Benoit, I. Pérez López, D. Gauthier, J.-L. Sans, and G. Flamant. On-sun demonstration of a 750 °C heat transfer fluid for concentrating solar systems: Dense particle suspension in tube. *Solar Energy*, 118:622–633, 2015.

[29] H.L. Zhang, H. Benoit, D. Gauthier, J. Degrève, J. Baeyens, I. Pérez López, M. Hemati, and G. Flamant. Particle circulation loops in solar energy capture and storage: gas-solid flow and heat transfer considerations. *Applied Energy*, 2015.

[30] F.W. Dittus and L.M.K Boelter. Heat transfer in automobile radiators of the tubular type. *University of California Publications in Engineering*, 2:443–461, 1930.

[31] W.H. McAdams. *Heat Transmission*. McGraw-Hill, 2^{nd} edition, 1942.

[32] E.N. Sieder and G.E. Tate. Heat transfer and pressure drop of liquids in tubes. *Industrial and Engineering Chemistry*, 28(12):1429–1435, 1936.

[33] H. Hausen. Neue Gleichungen für die wärmeübertragung bei freier oder erzwungener Stromüng (New equations for heat transfer in free or forced flow). *Allg Wärmetechn*, 4(5):75–79, 1959.

[34] B.S. Petukhov. Heat transfer and friction in turbulent pipe flow with variable physical properties. *Advances In Heat Transfer*, 6:503–564, 1970.

[35] V. Gnielinski. New equations for heat and mass transfer in turbulent pipe and channel flow. *International Journal of Chemical Engineering*, 16(2):359–368, 1976.

[36] V. Gnielinski. On heat transfer in tubes. *International Journal of Heat and Mass Transfer*, 63:134–140, 2013.

[37] B. Liu, Y.-T. Wu, C.-F. Ma, M. Ye, and H. Guo. Turbulent convective heat transfer with molten salt in a circular pipe. *International Communications in Heat and Mass Transfer*, 36:912–916, 2009.

[38] Y.-T. Wu, C. Chen, B. Liu, and C.-F. Ma. Investigation on forced convective heat transfer of molten salts in circular tubes. *International Communications in Heat and Mass Transfer*, 39:1550–1555, 2012.

[39] R.C. Martinelli. Heat transfer to molten metals. *Transaction of ASME*, 69:47–59, 1947.

[40] R.N. Lyon. Liquid metal heat transfer coefficients. *Chemical Engineering Progress*, 47:75–79, 1951.

[41] C.A. Sleicher and M.W. Rouse. A convenient correlation for heat transfer to constant and variable property fluids in turbulent pipe flow. *International Journal of Heat and Mass Transfer*, 18(5):677–683, 1975.

[42] X. Cheng and N. Tak. Investigation on turbulent heat transfer to lead-bismuth eutectic flows in circular tubes for nuclear applications. *Nuclear Engineering and Design*, 236(4):385–393, 2006.

[43] W. Hufschmidt, E. Burck, and W. Riebold. Die Bestimmung Örtlicher und Mittlerer Wämeubergangzahlen in Rohrer bei Hohen Wärmestromdichten (in German) (Determination of local and mean heat transfer coefficients in pipes at high heat flux densities). *International Journal of Heat and Mass Transfer*, 9:539–565, 1966.

[44] Therminol VP-1, Heat Transfer Fluids by Solutia. Technical bulletin 7239115C (Supersedes 7239115B), Solutia. (available at http://www.sintelub.com/files/therminol_vp1.pdf).

[45] K. Coscia, S. Nelle, T. Elliott, S. Mohapatra, A. Oztekin, and S. Neti. Thermophysical properties of $LiNO_3$-$NaNO_3$-NO_3 mixtures for use in concentrated solar power. *ASME Journal of Solar Energy Engineering*, 35(3):034506, 2013.

[46] A.B. Zavoico. Solar power two. design basis document. Technical Report SAND2001-2100, Sandia National Laboratories, 2001.

[47] N.P. Siegel, R.W. Bradshaw, J.B. Cordaro, and A.M. Kruizenga. Thermophysical property measurement of nitrate salt heat transfer fluids. *Proceedings of the ASME 5^{th} International Conference on Energy Sustainability ES2011, August 7-10, 2011, Washington, DC, USA*, 2011.

[48] HITEC® Heat Transfer Salt. Technical bulletin, Coastal Chemical Co., L.L.C. (available at http://stoppingclimatechange.com/MSR%20-%20HITEC%20Heat%20Transfer%20Salt.pdf).

[49] J.K. Fink and L. Leibowitz. Thermodynamic and Transport Properties of Sodium Liquid and Vapour. Technical report, Reactor Engineering Division, Argonne National Laboratory, 1995.

[50] J.D. Cox, D.D. Wagman, and V.A. Medvedev. *CODATA Key Values for Thermodynamics*. New York: Hemisphere Publishing Corp, 1989.

[51] V. Sobolev. Thermophysical properties of lead and lead-bismuth eutectic. *Journal of Nuclear Materials*, 362(2-3):235–247, 2007.

[52] D.W. Green and R.H. Perry. *Perry's Chemical Engineers' Handbook*. McGraw-Hill Professional, 8^{th} edition, 2008. (Section 2, Thermodynamic Properties).

[53] E.W. Lemmon, M.O. McLinden, and M.L. Huber. *NIST Standard Reference Database 23: Reference Fluid Thermodynamic and Transport Properties*. REFPROP, National Institute of Standards and Technology, Standard Reference Data Program, Gaithersburg Md, Version 7.1, 2002.

[54] E.W. Lemmon, R.T. Jacobsen, S.G. Penoncello, and D.G. Friend. Thermodynamic Properties of Air and Mixtures of Nitrogen, Argon, and Oxygen from 60 to 2000 K at Pressures to 2000 MPa. *Journal of Physical and Chemical Reference Data*, 29(3):331–385, 2000.

[55] E.W. Lemmon and R.T. Jacobsen RT. . Int J Thermophys. Viscosity and Thermal Conductivity Equations for Nitrogen, Oxygen, Argon, and Air. *International Journal of Thermophysics*, 25:21–69, 2004.

[56] *NIST Standard Reference Database 69: NIST Chemistry WebBook.*

[57] J.F. Ely, J.W. Magee, and W.M. Haynes. Thermophysical properties for special high CO_2 content mixtures. Research Report RR-110, Gas Processors Association, Tulsa, OK, 1987.

[58] V. Vesovic, W.A. Wakeham, G.A. Olchowy, J.V. Sengers, J.T.R. Watson, and J. Millat. The transport properties of carbon dioxide. *Journal of Physical and Chemical Reference Data*, 19:763–808, 1990.

[59] R. Span and W. Wagner. A New Equation of State for Carbon Dioxide Covering the Fluid Region from the Triple-Point Temperature to 1100 K at Pressures up to 800 MPa. *Journal of Physical and Chemical Reference Data*, 25(6):1509–1596, 1996.

[60] A. Fenghour, W.A. Wakeham, and V. Vesovic. The Viscosity of Carbon Dioxide. *Journal of Physical and Chemical Reference Data*, 27:31–44, 1998.

[61] C.M. Invernizzi. *Closed power cycles: fundamentals and applications*. Springer-Verlag London, 2013.

[62] C.F. McDonald. Helium turbomachinery operating experience from gas turbine power plants and test facilities. *Applied Thermal Engineering*, 44:108–142, 2012.

[63] B.A. Hands and V.D. Arp. A Correlation of Thermal Conductivity Data for Helium. *Cryogenics*, 21(12):697–703, 1981.

[64] R.D. McCarty and V.D. Arp. A New Wide Range Equation of State for Helium. *Advanced Cryogenic Engineering*, 35:1465–1475, 1990.

[65] V.D. Arp, R.D. McCarty, and D.G. Friend. Thermophysical Properties of Helium-4 from 0.8 to 1500 K with Pressures to 2000 MPa. Technical Note 1334, National Institute of Standards and Technology, Boulder, CO, 1998.

[66] F. Nepveu, A. Ferriere, and F. Bataille. Thermal model of a dish/Stirling system. *Solar Energy*, 83(1):81–89, 2009.

[67] R.D. McCarty, J. Hord, and H.M. Roder. Selected Properties of Hydrogen (Engineering Design Data). NBS Monograph 168, National Bureau of Standards, Boulder, CO, 1981.

[68] J.W. Leachman, R.T. Jacobsen, and E.W. Lemmon. Fundamental Equations of State for Parahydrogen, Normal Hydrogen, and Orthohydrogen. *Journal of Physical and Chemical Reference Data*, 38:721, 2009.

[69] O. Kunz, R. Klimeck, W. Wagner, and M. Jaeschke. The GERG-2004 Wide-Range Reference Equation of State for Natural Gases and Other Mixtures. *Journal of Physical and Chemical Reference Data*, 57(11):3032–3091, 2012.

[70] W.J.C Schiel and M.A. Geyer. Testing an External Sodium Receiver up to Heat Fluxes of 2.5 MW/m^2: Results and Conclusions from the IEA-SSPS High Flux Experiment Conducted at the Central Receiver System of the Plataforma Solar de Almeria (Spain). *Solar Energy*, 41(3):255–265, 1988.

[71] G. Delussu. A qualitative thermo-fluid-dynamic analysis of a CO_2 solar pipe receiver. *Solar Energy*, 86:926–934, 2012.

[72] P.L. Kirillov. Generalization of experimental data on heat transfer in molten metals. *Atomic Energy*, 13(1):1103–1106, 1963.

[73] C. Caliot and G. Flamant. Pressurized Carbon Dioxide as Heat Transfer Fluid: Influence of Radiation on Turbulent Flow Characteristics in Pipe. *AIMS Energy*, 2(2):172–182, 2014.

[74] Q. Li, G. Flamant, X. Yuan, P. Neveu, and L. Luo. Compact heat exchangers: A review and future applications for a new generation of high temperature solar receivers. *Renewable and Sustainable Energy Reviews*, 15(9):4855–4875, 2011.

[75] Q. Li, N. Guérin de Tourville, I. Yadroitsev, X. Yuan, and G. Flamant. Micro-channel pressurized-air solar receiver based on compact heat exchanger concept. *Solar Energy*, 91:186–195, 2013.

[76] X. Daguenet-Frick, A. Toutant, F. Bataille, and G. Olalde. Numerical investigation of a ceramic high-temperature pressurized-air solar receiver. *Solar Energy*, 90:164–178, 2013.

[77] F. Bai. One dimensional thermal analysis of silicon carbide ceramic foam used for solar air receiver. *International Journal of Thermal Sciences*, 49:2400–2404, 2010.

[78] Z. Wua, C. Caliot, G. Flamant, and Z. Wang. Coupled radiation and flow modeling in ceramic foam volumetric solar air receivers. *Solar Energy*, 85:2374–2385, 2011.

[79] I. Urieli and D.M. Berchowitz. *Stirling Cycle Engine Analysis*. Hilkger A Ltd, Bristol, 1984. Updated by Ohio University (2012): http://www.ohio.edu/mechanical/stirling/me422.htlm.

[80] H.L. Zhang, F. Pitié, J. Degrève, and T. Van Gerven. Metallic Foam in Heat Transfer Enhancement. *Proceedings of the Eurotherm Seminar N° 99: Advances in Thermal Energy Storage, Lleida, Spain; May 28-30, 2014*, 2014.

[81] W. Wagner and A. Pruss. The IAPWS Formulation 1995 for the Thermodynamic Properties of Ordinary Water Substance for General and Scientific Use. *Journal of Physical and Chemical Reference Data*, 31:387–535, 2002.

[82] S.G. Kandlikar. Further Developments in Subcooled Flow Boiling Heat Transfer. *Proceedings of the Engineering Foundation conference on Convective and Pool Boiling, Irsee, Germany, May 1997*, pages 18–25, 1997.

[83] T. Sato and H. Matsumura. On the Conditions of Incipient Subcooled Boiling With Forced Convection. *Bulletin of JSME*, 7(26):392–398, 1964.

[84] Y.Y. Hsu. On the size range of active nucleation cavities on a heating surface. *ASME Journal of Heat Transfer*, 84, 1962.

[85] S.G. Kandlikar. A General Correlation for Saturated Two-Phase Flow Boiling Heat Transfer Inside Horizontal and Vertical Tubes. *ASME Journal of Heat Transfer*, 112:219–228, 1990.

[86] W.R. Bowring. Physical model of bubble detachment and void volume in subcooled boiling. Halden Reactor Project Report HPR-10, Organisation for Economic Cooperation and Development (OECD), 1962.

[87] S.G. Kandlikar. Development of a Flow Boiling Map for Subcooled and Saturated Flow Boiling of Different Fluids in Circular Tubes. *ASME Journal of Heat Transfer*, 113:190–200, 1991.

[88] S.G. Kandlikar. Heat Transfer Characteristics in Partial Boiling, Fully Developed Boiling, and Significant Void Flow Regions of Subcooled Boiling. *ASME Journal of Heat Transfer*, 120:395–401, 1998.

[89] P. Saha and N. Zuber. Point of net vapor generation and vapor void fraction in subcooled boiling. *Proceedings of the 5th International Heat Transfer Conference; Tokyo, Japan; 3 Sep 1974*, pages 175–179, 1974.

[90] M. Eck, E. Zarza, M. Eickhoff, J. Rheinländer, and L. Valenzuela. Applied research concerning the direct steam generation in parabolic troughs. *Solar Energy*, 74:341–351, 2003.

[91] J.W. Raade and D. Padowitz. Development of molten salt heat transfer fluid with low melting point and high thermal stability. *ASME Journal of Solar Energy Engineering*, 133:031013, 2011.

[92] T. Wang, D. Mantha, and R.G. Reddy. Novel low melting point quaternary eutectic system for solar thermal energy storage. *Applied Energy*, 102:1422–1429, 2013.

[93] C.J. Li, P. Li, K. Wang, and E.E. Molina. Survey of properties of key single and mixture halide salts for potential application as high temperature heat transfer fluid for concentrated solar power systems. *AIMS Energy*, 2(2):133–157, 2014.

[94] K. Vignarooban, P. Pugazhendhi, and C. Tucker. Corrosion resistance of Hastelloys in molten metal-chloride heat-transfer fluids for concentrating solar power applications. *Solar Energy*, 103:62–69, 2014.

[95] O.J. Foust. *Sodium-NaK Engineering Handbook*. Gordon and Breach, Science Publishers, Inc, New York, 1972.

[96] T. Wetzel, J. Pacio, and L. Marocco. Liquid metal technology for concentrated solar power systems: Contribution by the German research program. *AIMS Energy*, 2(1):89–98, 2014.

[97] M. Boss, T. Gadoury, S. Feeny, and M. Montgomery. Recent advances in ultra super critical steam turbine technology. Technical report, General Electrics Energy, Steam Turbine Technology, 2007.

[98] P.S. Weitzel. Steam Generator for Advanced Ultra-Supercritical Power Plants 700 to 760 °C. *Proceedings of the ASME 2011 Power Conference*, pages 281–291, 2011.

[99] S. Hu, H. Gao, and X. Jia. Regulating Characteristics Analysis of Boiler Feed-water Pump when 600 MW Unit Sliding-pressure Operating. *Energy Procedia*, 17(B):1153–1160, 2012.

[100] C. Singer, R. Buck, R. Pitz-Paal, and H. Müller-Steinhagen. Assessment of solar power tower driven ultrasupercritical steam cycles applying tubular central receivers with varied heat transfer media. *ASME Journal of Solar Energy Engineering*, 132(4):041010, 2010.

[101] J. Liu, H. Chen, Y. Xu, L.Wang, and C. Tan. A solar energy storage and power generation system based on supercritical carbon dioxide. *Renewable Energy*, 64:43–51, 2014.

[102] V. Dostal. *A supercritical carbon dioxide cycle for next generation nuclear reactors*. PhD thesis, Department of Nuclear Engineering, MIT, 2004. (available at: http://dspace.mit.edu/handle/1721.1/17746).

[103] R.L. Fuller and W. Batton. Practical Considerations in Scaling Supercritical Carbon Dioxide Closed Brayton Cycle Power Systems. *Proceedings of Supercritical CO_2 Power Cycle Symposium 2009, Troy, NY*, 2009. (available at: http://www.sco2powercyclesymposium.org/resource_center/turbomachinery/

practical-considerations-in-scaling-supercritical-carbon-dioxide-closed-brayton-cycle-power-systems).

[104] http://energy.sandia.gov/wp/wp-content/gallery/uploads/ARPAE_Brayton_SAND20140672.pdf.

[105] http://energy.sandia.gov/wp/wp-content/gallery/uploads/Brayton-ARPA-E-SAND-2014-0672-P.pdf.

[106] H.L. Zhang, J. Baeyens, J. Degrève, A. Brems, and R. Dewil. The convection heat transfer coefficient in a Circulating Fluidized Bed (CFB). *Advanced Powder Technology*, 25:710–715, 2014.

[107] P.K. Falcone, J.E. Noring, and J.M. Hruby. Assessment of a solid particle receiver for a high temperature solar central receiver system. *Sandia National Laboratories*, Report SAND85-8208, 1985.

[108] G. Evans, W. Houf, R. Grief, and C. Crowe. Gas-Particle Flow Within a High Temperature Solar Cavity Receiver Including Radiation Heat Transfer. *ASME Journal of Solar Energy Engineering*, 109:134–142, 1987.

[109] H. Chen, Y. Chen, H.T.Hsieh, and N. Siegel. CFD Modeling of Gas Particle Flow within a Solid Particle Solar Receiver. *ASME Journal of Solar Energy Engineering*, 129:160–170, 2007.

[110] N.P. Siegel, C.K. Ho, S.S. Khalsa, and G.J. Kolb. Development and Evaluation of a Prototype Solid Particle Receiver: On-Sun Testing and Model Validation. *ASME Journal of Solar Energy Engineering*, 132(2):021008, 2010.

[111] M. Röger, L. Amsberg, B. Gobereit, and R. Buck. Face-Down Solid Particle Receiver Using Recirculation. *ASME Journal of Solar Energy Engineering*, 133:031009, 2011.

[112] S. Giuliano, R. Buck, and S. Eguigen. Analysis of Solar-Thermal Power Plants With Thermal Energy Storage and Solar-Hybrid Operation Strategy. *ASME Journal of Solar Energy Engineering*, 133:031007, 2011.

[113] G. Flamant and H. Hemati. Dispositif collecteur d'énergie solaire (Device for collecting solar energy). French patent FR 1058565, October 20, 2010. PCT extension WO2012052661, April 26, 2012.

Chapter 2

Experimental Study of Heat Transfer between an Upward Dense Particle Suspension and a Tube during On-Sun Heating

2.1 Introduction

This chapter presents the experimental results that were obtained during two on-sun campaigns with a single tube Dense Particle Suspension (DPS) receiver, also called Upward Bubbling Fluidized Bed (UBFB) receiver, at the focus of the CNRS solar facility in Odeillo. The first campaign was conducted in autumn 2013 at "low" temperature (particle outlet temperature less than 350 °C). It proved the feasibility of the DPS receiver concept and allowed determining the first values of wall-to-suspension Heat Transfer Coefficient (HTC) in this configuration. For the second campaign, conducted in spring 2014, the experimental setup was modified in order to preheat the solid particles and operate at high temperature in the absorber tube (up to more 700 °C). The temperature measurements indicated an intense solid recirculation near the absorber tube wall thus leading to a modified approach for heat transfer calculation. Data from both experimental campaigns were then processed with this new approach, showing a strong coherence of measurement data.

The the system principle is explained and the experimental setup and operating conditions are detailed hereafter. Then, the experimental test results of both campaigns dealing with the temperature distribution and increase during experiments are presented. Global wall-to-suspension Heat Transfer Coefficients (HTC) are derived and analyzed as a function of the system pertinent parameters. They ranged from 420 $W/m^2.K$ to 1100 $W/m^2.K$ for solid mass fluxes of 10 $kg.m^{-2}.s^{-1}$ and 45 $kg.m^{-2}.s^{-1}$ respectively. The positive effects on the heat transfer of the solid mass flux, particle volume fraction and temperature were observed. The experimental results were finally used to correlate the DPS flow Nusselt number with the particle flow properties. To conclude, a comparison with existing technologies is drawn and the potential future applications are discussed. These results were recently published [1, 2] and a short communication was submitted to describe how the Nusselt correlation was established [3].

2.2 Experimental setup and procedure

2.2.1 Description of the experimental receiver rig

This study was conducted on a small solar rig (about 10 kW_th) set at the focus of the CNRS 1 MW solar furnace at Odeillo. The rig involved a solar receiver with a single opaque tube containing the solid-gas dense suspension circulating upward. The general principle of this 1-tube solar setup operating in batch is illustrated in Figure 2.1.

The solar absorber is located inside a cylindrical cavity (diameter=0.15 m, height=0.5m) made of alkaline-earth silicate (Insulfrax®), and submitted to the concentrated solar radiation. The cavity is irradiated through a rectangular opening 0.3 m wide and 0.50 m high, set at the focus plane. As we get further away from the parabola, its width reduces until it is only 0.1 m, which determines the cylindrical cavity entrance. The aperture angle formed by the two vertical walls getting closer is 58 °. Figure 2.2 shows a horizontal cross sectional view of the receiver cavity.

The AISI 304L stainless steel complete laboratory facility involves 2 fluid beds that permit the system to be homogeneous and ensure the suspension upward flow in the irradiated

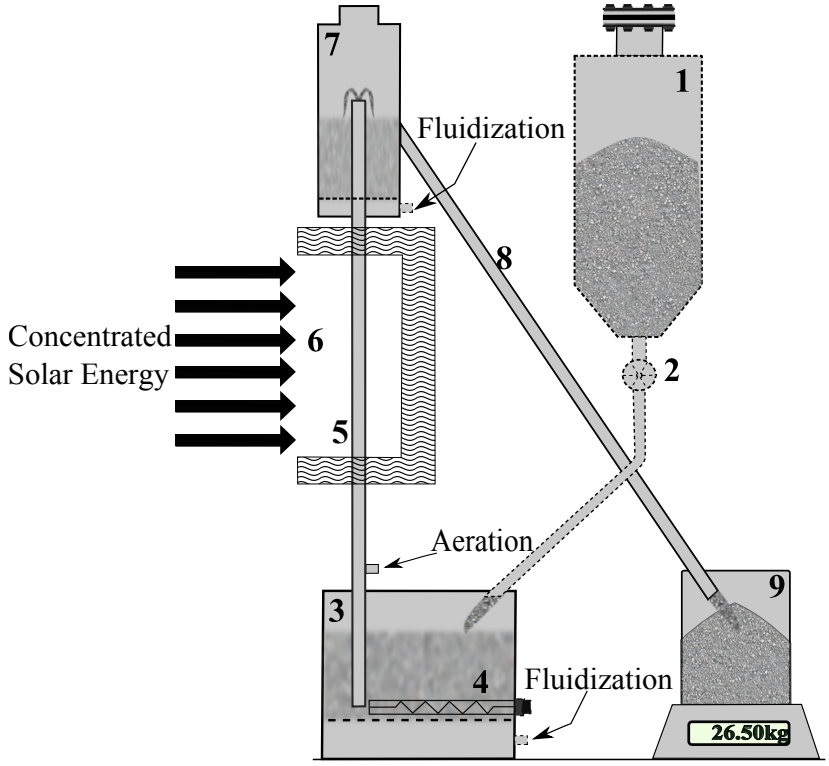

Figure 2.1: Schematic cross-sectional view of the lab-scale solar rig: 1. Solid storage tank, 2. Rotary valve feeder, 3. Dispenser fluidized bed (DiFB), 4. Electrical resistances, 5. Solar absorber metallic tube, 6. Solar receiver cavity, 7. Collector fluidized bed (ColFB), 8. Solid evacuation tube, 9. Weighing scale.

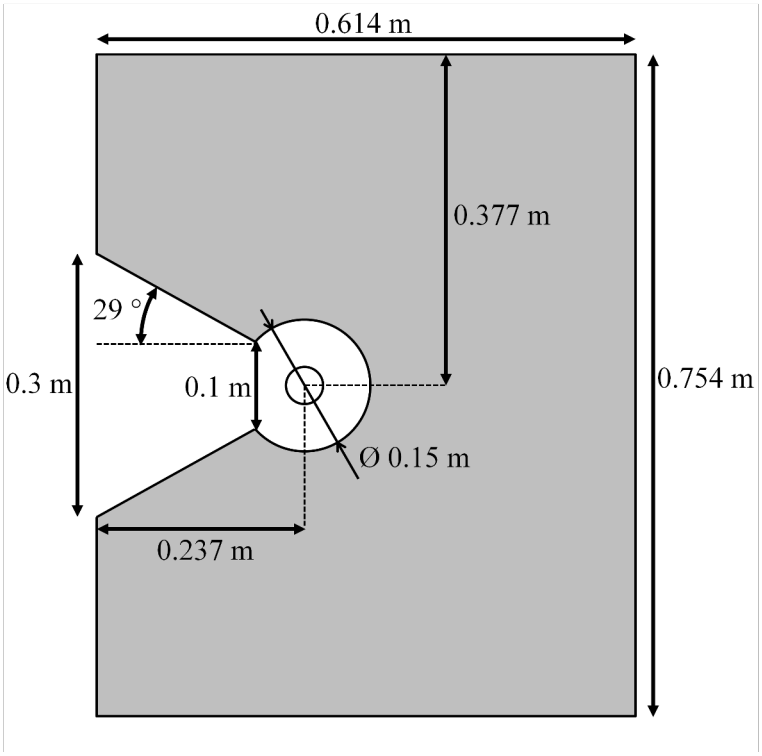

Figure 2.2: Horizontal cross sectional view of the receiver cavity.

tube. Each fluidized bed includes a fluidization distributor made of sintered stainless steel balls thus allowing both mechanical strength and good pressure drop whilst withstanding high temperature. Finally, a pressurized hopper works as a solid storage. The whole experimental setup is set behind a water-cooled aluminum shield that protects both personnel and equipment from the high solar flux when running solar experiments.

The DPS moves upward vertically in the tube constituting the solar absorber thanks to the pressure difference imposed between the Dispenser Fluidized Bed (DiFB) at the tube bottom and the Collector Fluidized Bed (ColFB) at the tube top. In the first campaign, the DiFB was cylindrical (inside diameter 0.136 m). It was modified for the second campaign to increase its volume so that it would contain 35 kg of particles, instead of only 15 kg initially, and could operate as a powder buffer, thus stabilizing the flow. The new DiFB has a square section of 0.40 m x 0.40 m and is 0.3 m high. It was also improved by adding three 1.5 kW electrical resistances (UTC type 3 ULTRAMAX Cartridges, by Rotfil) to uniformly heat the fluidized bed before the particles flow into the solar absorber. The ColFB is cylindrical with an inside diameter of 0.136 m. The absorber tube has an outside diameter of 0.0424 m, a wall thickness of 0.0032 m and is made of AISI 310S stainless steel. It is submitted to the concentrated solar radiation over a height of 0.50 m. The solar absorber tube is suspended on a horizontal metallic frame, thus allowing its thermal expansion through 2 end-fitted compensators. A side photograph of the pilot plant is shown in Figure 2.3. The sun protective shield and the insulated cavity can be seen on the left and the particle hopper on the right.

Figure 2.3: Side photograph of the experimental setup.

Figure 2.4 displays a photograph of the sun-heated absorber tube in the solar receiver, when cooling down. The tube bottom is colder (grey) than the top (red-hot) because of the cold particle feed. Particles get hotter while passing through the tube inside the irradiated cavity.

Figure 2.4: Front photograph of the sun-heated tube.

2.2.2 Powder Characteristics

The solid particles in the suspension are silicon carbide (SiC) particles, mainly because of the thermal properties (high sintering temperature, high heat capacity), availability and rather low cost of this material. The powder was selected after the first step of Boissière's study [4]. The chosen particles' mean diameter (Sauter mean diameter: $d_{32} = 63.9$ μm) permits a good fluidization quality with almost no bubbles, for very low air fluidization velocities ($U_{mf} = 5$ mm/s at 20 °C) since they belong to Group A of particles as defined by Geldart [5]. Table 2.1 lists the properties of the SiC powder. ρ is the density, c_p the specific heat capacity (therefore the product ρc_p is the volumetric heat capacity), $T_{sintering}$ the sintering temperature, ε the suspension voidage or void fraction and U the superficial velocity. The subscript p refers to the particles, mf to the minimum fluidization, mb to the minimum bubbling.

Table 2.1: Physical properties of SiC particles

ρ_p [kg/m^3]	$\rho_p c_{p,p}$ [kJ/m^3.K]	$T_{sintering}$ [K]	ε_{mf}	ε_{mb}	U_{mf} [10^{-3} m/s]	U_{mb} [10^{-3} m/s]	d_{32} [μm]
3210	3000	1620	0.59	0.57	5	8	63.9

2.2.3 Solid Flow Control

In solar experiments, the rig was operated semi-continuously. There were some differences between the two campaigns because of setup improvements after the first series of experiments. The DiFB was first preheated to the desired temperature by means of the electrical resistances (only for the second campaign). Then it was fed with particles issued from a 14 L hopper at ambient temperature. During the first campaign, the feeding rate was not controlled and all the powder that could pass from the hopper to the DiFB did, meaning

that all the solid flowing out of the DiFB was immediately replaced. During the second campaign, the addition of the rotary valve between the hopper and the DiFB allowed controlling the particle feeding rate. When the DiFB was heated, the bed temperature homogeneity was guaranteed by a good mixing, obtained by using a gas velocity 3 to 4 times the minimum fluidization velocity of 5 mm/s at ambient temperature [6]. The freeboard pressure of the DiFB $P_{freeDiFB}$ was regulated by a valve set on the fluidizing air outlet.

The pressure at the the tube inlet in the DiFB P_{iDiFB} is equal to the sum of the freeboard pressure and the hydrostatic pressure of the bed between the freeboard and the tube inlet ΔP_{bed}:

$$P_{iDiFB} = P_{freeDiFB} + \Delta P_{bed} \tag{2.1}$$

The flow driving pressure ΔP_{drive} is the difference between the pressure at the tube inlet and that at the tube outlet, the outlet being at atmospheric pressure P_{atm}.

$$\Delta P_{drive} = P_{iDiFB} - P_{atm} \tag{2.2}$$

ΔP_{drive} also corresponds to the pressure drop through the tube and is therefore equal to the sum of the hydrostatic pressure of the suspension and the pressure loss due to friction with the wall:

$$\Delta P_{drive} = (\alpha_p \rho_p + \varepsilon \rho_g)\, g\, (z_{tube} - z_{base}) + \Delta P_{friction} \tag{2.3}$$

with ρ_g the gas density (air in our case), ρ_p the particles density (SiC in our case), g the gravitational acceleration, z_{tube} the suspension height in the tube, z_{base} the height of the tube base, ε the suspension voidage, $\alpha_p = 1 - \varepsilon$ the particle volume fraction and $\Delta P_{friction}$ the friction pressure loss.

When there is no solid circulation, the system maintains the pressure equilibrium by changing z_{tube} when $P_{freeDiFB}$ changes. A continuous flow is established by setting the regulation valve so that ΔP_{drive} is slightly higher than the hydrostatic pressure obtained when the suspension level reaches the tube outlet. The difference between the two is then equal to the friction pressure loss of the suspension flow. The higher the difference, the higher the suspension flow.

It was necessary to inject a secondary gas flow into the tube, called aeration, at a short distance from its bottom (injector diameter 8.5 mm at 0.28 m from the tube bottom). It helps stabilizing the solid flow that would otherwise be possibly blocked by the suspension subsidence and it allows controlling the suspension voidage inside the tube. Finally, particles at the desired temperature flowed upward through the opaque absorber tube as a dense suspension. In the ColFB, particles flowed as a low velocity fountain as can be seen in Figure 2.5a, with particle jets when bubbles were passing (Figure 2.5b). Ultimately, the particles reached the collecting bin by overflow. This bin was set on an electronic weighing scale that displayed the mass on-line, thus permitting solid flow rate measurement. Depending on the

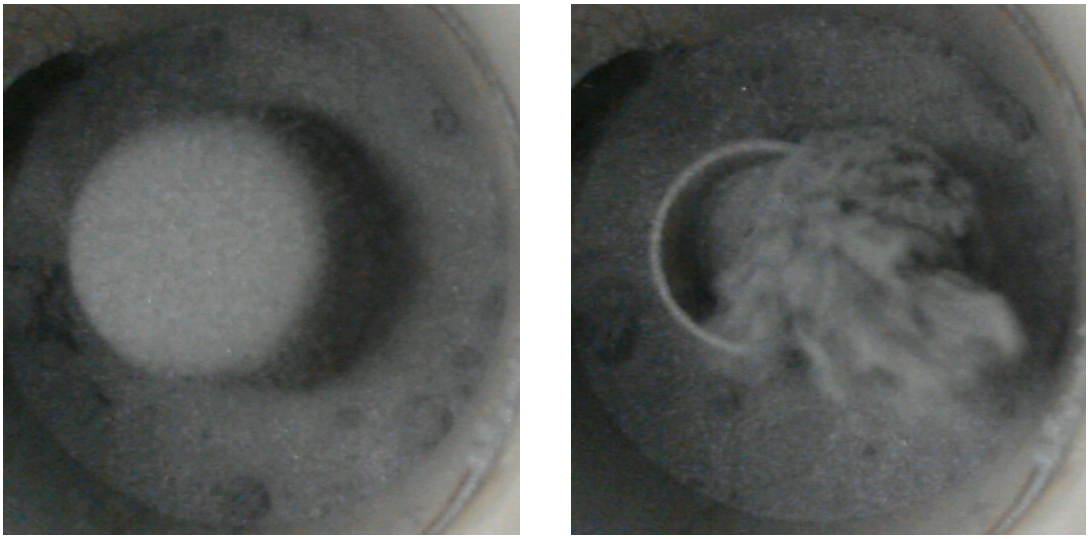

(a) Particle fountain. (b) Particle jet when a bubble passes.

Figure 2.5: Photograph of particles flowing out of the tube in the ColFB.

solid mass flow rate, semi-continuous stable time periods ranged between 6 and 30 minutes.

Thermodynamic mass flow-meters, with 1 % accuracy, measured the air flow rate entering each fluidized bed, and another measured the aeration. The solid mass flow rate inside the tube was controlled by the combination of the air pressure in the DiFB freeboard relative to the atmospheric pressure in the ColFB freeboard, the aeration flow rate and the particle flow rate between the hopper and the DiFB set by the rotary valve. A detailed analysis of the hydrodynamics of this type of gas-solid flow was published by Boissière et al. [6].

2.2.4 Operating parameters

The system operating parameters are: the solid mass flux (only set by the DiFB pressure for the first campaign and also by the rotary valve for the second campaign), the DiFB temperature (managed by the electrical resistances that pre-heated the suspension in the DiFB for the second campaign), the aeration, and the concentrated solar flux density (depending on the number of heliostats shooting and the opening width of the solar furnace doors). They are presented separately for each experimental campaign.

For the first campaign, the solid mass flux was varied from 9.5 to 21.7 $kg.m^{-2}.s^{-1}$. The suspension in the DiFB was close to ambient temperature since there was no pre-heating, but it increased for low solid mass fluxes due to particle recirculation as explained in Subsection 2.3.2. It ranged between 6 and 65 °C. The average particle outlet temperature ranged between 241 and 351 °C. Five aeration flux values were tested: 0.011, 0.022, 0.044, 0.065, 0.087 and 0.109 $Nm^3.m^{-2}.s^{-1}$ (corresponding flow rates: 40, 80, 160, 240, 320 and 400 Nm^3/h). The solar flux density distribution was measured before testing the receiver with a camera filming a water-cooled magnesia-coated probe, both at the receiver cavity entrance and at the absorbing tube position. The images were calibrated by measuring the flux at given positions (center of the cavity entrance, middle of the cavity height at the

tube position) with a fluxmeter. The homogeneity was better than 15 %. Four different irradiation conditions were tested. They differed not only by the solar flux density impinging on the tube but also by its repartition that was not perfectly uniform. Therefore, it cannot be concluded if the solar flux density impacts positively or negatively the heat transfer, because the variations might be due to some hot spots present in one configuration only. The four configurations correspond to solar flux density values of 143, 170, 221 and 242 kW/m^2 at the cavity entrance. Since the experiments were conducted with a Direct Normal Irradiation (DNI) varying in the range 912-1023 W/m^2 (with an average value of 1017 W/m^2), these values are normalized to a 1 kW/m^2 DNI[1]. The DNI being measured at all times, the exact solar flux density for any run is known. The ranges of operating parameters explored during the first experimental campaign are reminded in Table 2.2. Among the performed runs, 29 were satisfactory in terms of stability and stable period duration.

For the second campaign, the solid mass flux was varied from 10.2 to 45.1 kg.m^{-2}.s^{-1}. The DiFB temperature ranged between 229 and 503 °C. The average particle outlet temperature ranged between 446 and 723 °C. Two aeration flux values were tested: 0.021 and 0.042 Nm^3.m^{-2}.s^{-1} (corresponding flow rates: 77 and 155 Nm^3/h). Three different irradiation conditions were tested that correspond to normalized solar flux density values of 217, 272, 387 kW/m^2 at the cavity entrance. Experiments were conducted with a DNI varying in the range 696-1037 W/m^2 (with an average value of 908 W/m^2). The ranges of operating parameters explored during the second experimental campaign are reminded in Table 2.2. Among the performed runs, 26 were satisfactory in terms of stability and stable period duration.

It must be noted that the solid mass flux, which reached a maximum of 45.1 kg.m^{-2}.s^{-1} during these experiments, was limited not by the process itself, but by the experimental setup capability. Indeed, we were limited by the rotary valve maximum flow rate and by the solid storage capability that did not hold a sufficient solid quantity for long enough runs at higher mass fluxes. It was proven by Turzo [7] that the solid mass flux can be as high as 700 kg.m^{-2}.s^{-1} in a DPS process.

Table 2.2: Ranges of operating parameters

G_p [kg.m^{-2}.s^{-1}]	Aeration [Nm^3/m^2.s]	Solar flux density[2] [kW/m^2]	Average DiFB temperature [K]	Average outlet temperature [K]
1^{st} experimental campaign				
9.5-21.7	0.011-0.109	144-248	6.5-65	241-351
2^{nd} experimental campaign				
10.2-45.1	0.021-0.042	213-393	229-503	446-723

[1] The solar flux density measured for a given DNI is multiplied by 1 kW/m^2 and divided by the actual DNI value. Hence we obtain the value that would have been measured for a 1 kW/m^2 DNI.

[2] Actual values calculated from the normalized values and the actual DNI.

2.2.5 Pressure and temperature sensors

The facility is equipped with 6 pressure sensors and 4 differential pressure sensors, to continuously measure the fluidized bed pressure drops, the pressures before their distributors and in their disengaging heights, and the pressure drop of the DPS inside the absorber tube. As shown in Figure 2.6, sheathed K thermocouples measure the air and solid temperatures that are equal as demonstrated by Baeyens and Goossens [8]. Along the suspension path, the particle temperature is measured by thermocouples placed at the tube inlet in the DiFB, and at the inlet and outlet of the part of the absorber tube exposed to high flux, at the tube center and at 5 mm from the internal wall. In addition, several K thermocouples are directly welded onto the stainless steel absorber tube for wall temperature measurement: both Chromel® and Alumel® bare wires are welded on the tube and, therefore, the thermocouple hot point is the tube itself. Indeed, temperature can be obtained this way with an error below 1 % because direct welding significantly limits the thermal contact resistance. The thermocouple measuring the front wall temperature in the middle of the cavity was not installed for the first campaign and it was added for the second one.

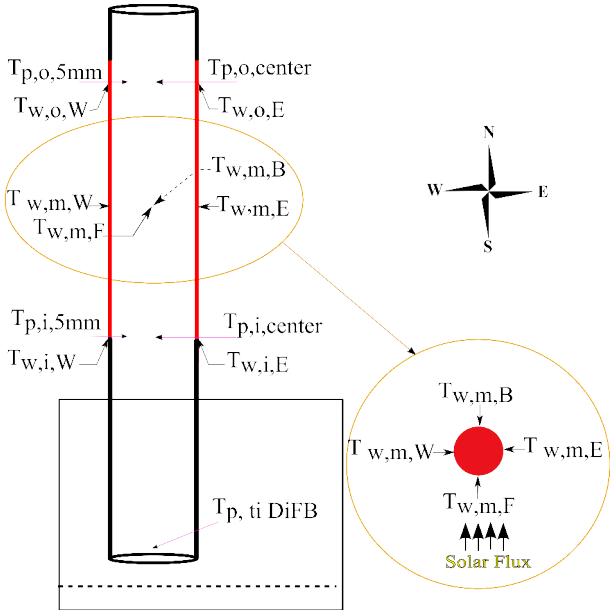

Figure 2.6: Schematic view of the thermocouples positions in the tube (in red the irradiated part of the tube). Subscripts F/B/W/E correspond to front/back/west/east, w/p to wall/particles, i/o/m to inlet/outlet/middle of the irradiated part, iDiFB to inlet of the tube in the dispenser fluidized bed and center/5 mm to the thermocouple position inside the tube, at the center and 5 mm from the wall.

2.2.6 Temperature measurement uncertainty

As mentioned before, all thermocouples are type K thermocouples. The uncertainty considered for these thermocouples corresponds to the class 2 tolerance of the EN 60 584 standard. This tolerance is defined as the highest value between 2.5 K and 0.0075 T (in °C). The maximum absolute uncertainty for wall temperatures, apart from the front wall temperature, is 6.2 K. Then the maximum relative uncertainty for wall temperatures is

0.6 %. Similarly, the maximum absolute uncertainty for DPS temperatures is 6.0 K, and the maximum relative uncertainty for them is 0.9 %. In most cases, the actual uncertainty is smaller than the tolerance. Therefore, the announced uncertainties are an upper limit.

Concerning the thermocouples welded on the tube wall, it is assumed that the very small contact resistance between the wires and the tube does not increase the uncertainty. The case of the thermocouple set on the front face of the tube in the middle of the cavity, which measures $T_{w,m,F}$, is an exception. Indeed, being directly exposed to the concentrated solar flux, it is hotter than the tube wall, the latter being cooled by the inside DPS flow. In this case, the measurement error was estimated by a simplified power balance on a thermocouple wire. The wire is approximated as a flat surface. It absorbs the concentrated solar flux as a grey body with an absorptivity/emissivity of 0.8, which is that of nickel, the main component of the wire alloys, slightly overestimated to account for a possible oxidation. The radiation received from the environment is neglected in respect to the concentrated solar flux. The wire emits infrared radiation from the same surface, at the temperature given by the thermocouple. Neglecting the convective exchange, the difference between the absorbed radiation and that emitted is transferred to the tube wall by conduction through the same area. This way, the power balance is respected. The thermal contact resistance value is about 0.7×10^{-4} m^2.K/W [9]. It corresponds to the lower limit for the case of two surfaces put in contact with a pressure exceeding 10^7 Pa, and is actually an overestimate of the actual thermal contact resistance, since contact by welding is better than contact by pressure. The temperature difference between the thermocouple wires and the tube wall, as well as the actual tube wall temperature at the front, can be calculated with:

$$\varphi_{wire-tube} = \varepsilon_{Nickel} \left(\varphi_{solar} - \sigma T_{wire,m,F}^4 \right) = \left(T_{wire,m,F} - T_{tube,m,F} \right) / R_{contact} \tag{2.4}$$

with $\varphi_{wire-tube}$ the flux density passing from the wire to the tube wall, ε_{Nickel} the wire emissivity equal to 0.8, φ_{solar} the concentrated solar flux density reaching the tube, σ Stefan-Boltzmann constant (5.67×10^{-8} W/m^2.K^4), $T_{wire/tube,m,F}$ the temperature of the wire/tube wall at the front of the tube in the middle of the cavity and $R_{contact}$ the thermal contact resistance.

The largest temperature difference between the thermocouple wires and the tube wall estimated with this method is 7.6 K. Thereafter, the value used for $T_{w,m,F}$ is $T_{wire,m,F}$ and the temperature difference calculated for each case is added to the uncertainty.

2.3 Particle suspension temperature

2.3.1 Highest temperature reached

Focusing on the parameters impact on the solid temperature, experiments showed that a combination of high aeration, high solar flux density and low solid mass flux leads to the highest outlet DPS temperature.

Figure 2.7 displays an example of measured $T_{p,o,center}$, the DPS temperature at the outlet of the irradiated part of the tube, in the center, and $T_{p,iDiFB}$, the DPS temperature at

the tube inlet in the DiFB, during 18 minutes of steady state experiment. Measures were taken every second. Because of this short acquisition frequency, the suspension agitation effect can be seen. It leads to significant temperature variations in the tube. The DPS average temperature increase between the DiFB and the cavity outlet was 197 °C. An average outlet DPS temperature of 731 °C was reached, with spikes up to 798 °C.

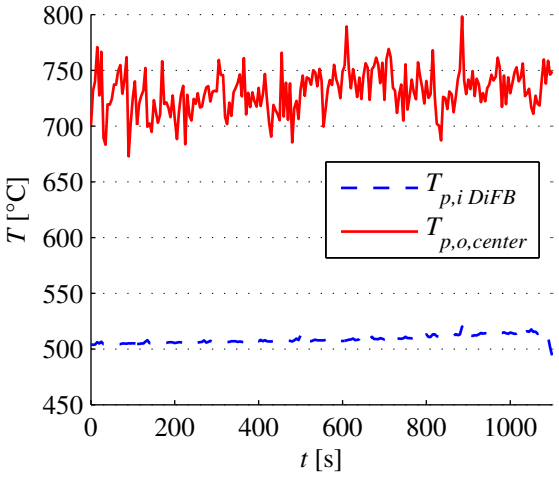

Figure 2.7: DPS temperature versus time, at the tube inlet in the DiFB ($T_{p,iDiFB}$) and at the outlet of the irradiated cavity, at the tube center ($T_{p,o,center}$) during steady state (average solid mass flux = 10.02 kg.m^{-2}.s^{-1}, aeration = 0.042 Nm^3.m^{-2}.s^{-1}, solar flux density at the cavity entrance = 346 kW/m^2).

2.3.2 Particle temperature distribution and recirculation

Figure 2.8 shows the wall and suspension temperature profiles inside the cavity, for the same case that is displayed in Figure 2.7. The values are averaged over a stable time period. The outside wall side temperature (average of east and west) is shown at the inlet, middle and outlet of the cavity. The suspension temperatures measured at 5 mm from the wall and in the tube center are shown at the inlet and outlet. The front wall temperature in the middle, which is the highest temperature measured, is also displayed. The shape of the wall temperature profile, with a steep increase in the lower part that and a stabilization in the upper part, led us to use the logarithmic-mean temperature difference in the HTC calculations (see Subsection 2.4.1.2).

Figures 2.9 and 2.10 display examples of the DPS temperature time variations at several specific and relevant positions at low and high temperatures, respectively. In order to plot clearer curves, the temperatures shown here are averaged over 15 s. The said positions are: the the tube inlet in the DiFB ($T_{p,iDiFB}$), and at the irradiated cavity inlet and outlet at both the tube center and 5 mm from the wall $T_{p,i,center}$, $T_{p,i,5mm}$, $T_{p,o,center}$ and $T_{p,o,5mm}$, respectively. At the cavity outlet, the DPS temperature is higher at the tube center than close to the wall. On the contrary, at the cavity inlet, the particle temperature 5 mm from the wall is higher than that at the tube center. As reported by Flamant et al. [1], this opposite behavior disappears when the solar irradiation is stopped. This is due to a recirculating particle flow: particles flow upward in the central zone of the tube and they flow downward close to the wall. This flow pattern, with rising bubbles inducing an upward flow in their wake and drift and downward flow near the wall was already shown

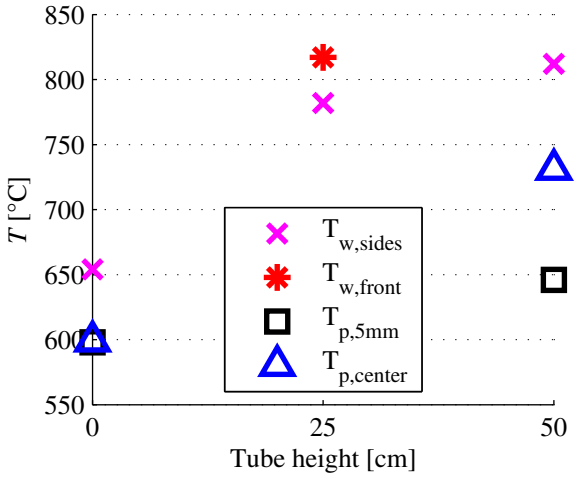

Figure 2.8: Wall and suspension temperature profiles inside the cavity (average solid mass flux = 10.02 kg.m^{-2}.s^{-1}, aeration = 0.042 Nm^3.m^{-2}.s^{-1}, solar flux density at the cavity entrance = 346 kW/m^2).

a long time ago in the bubbling fluidized bed case [10]. However, it is a new result in the case of DPS flow in tube. It was first noticed due to the temperature distribution in the tube, before being confirmed by measurements conducted by our CSP2 project partners with the Positron Emission Particle Tracking (PEPT) method (Garcia-Triñanes P. et al., 2015 [11]). On the one hand, at the cavity outlet, the particles flowing upward in the center have just been heated, whereas on the other hand, the particles flowing downward close to the wall have lost heat outside the insulated cavity, in the upper part of the tube. Oppositely, at the cavity inlet, the particles flowing downward close to the wall are coming out of the heated cavity and they are therefore at higher temperature than those flowing upward that come from an unheated zone. This flow pattern is schemed in Figure 2.11. Moreover, if all particles were flowing upward only, they would have the same temperature at the tube inlet in the DiFB and at the irradiated cavity inlet. On the contrary, particles are colder at the tube inlet in the DiFB than at the irradiated cavity inlet, because of the mixing of both upward cold flow and downward hot flow below the heated cavity. As shown in Figure 2.10, $T_{p,i,5mm}$ can be up to 108 °C higher than $T_{p,iDiFB}$, and $T_{p,i,center}$ can be up to 84 °C higher than $T_{p,iDiFB}$.

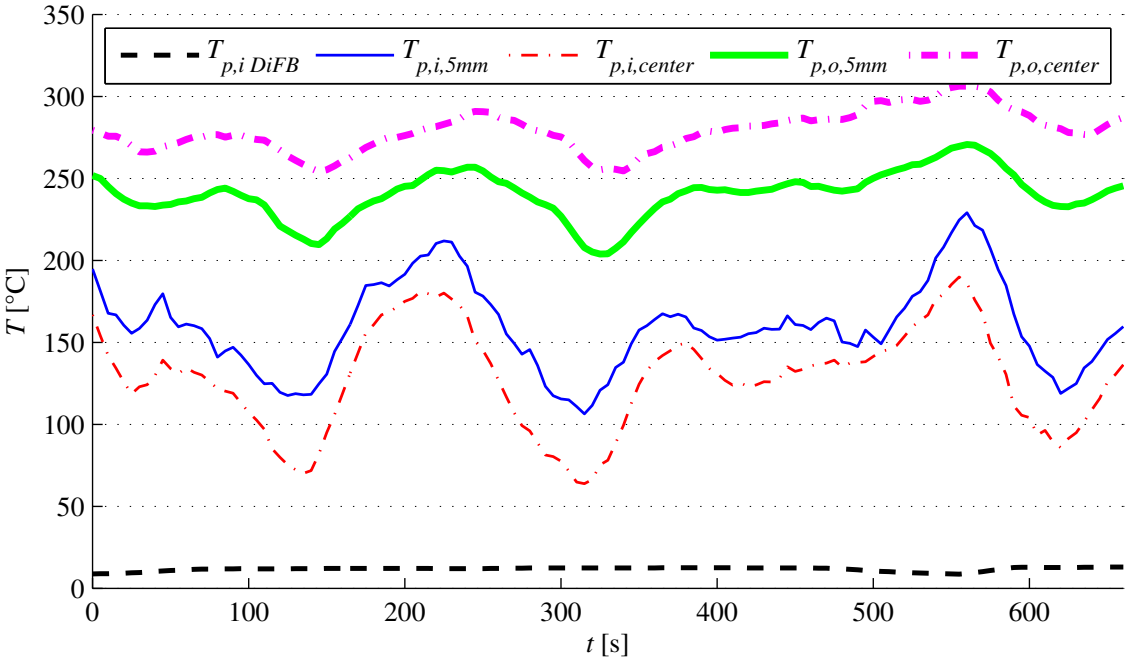

Figure 2.9: Solid temperature as a function of time (average solid mass flux = 13.00 $kg.m^{-2}.s^{-1}$, aeration = 0.042 $Nm^3.m^{-2}.s^{-1}$; solar flux density at the cavity entrance = 225 kW/m^2).

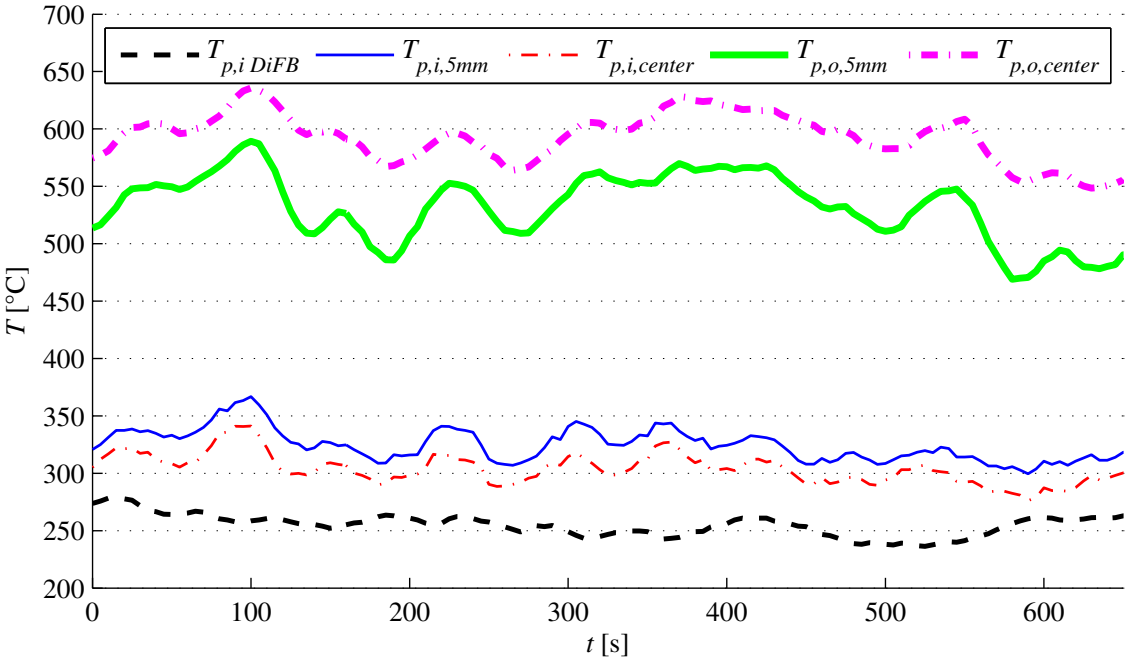

Figure 2.10: Solid temperature as a function of time (average solid mass flux = 17.00 $kg.m^{-2}.s^{-1}$, aeration = 0.042 $Nm^3.m^{-2}.s^{-1}$, solar flux density at the cavity entrance = 345 kW/m^2).

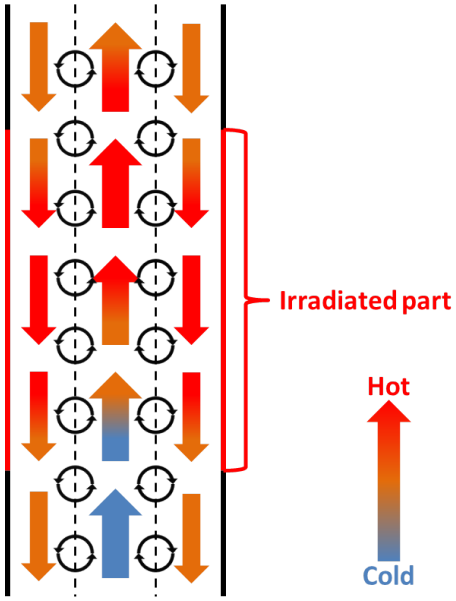

Figure 2.11: Schematic view of the particle reflux.

2.4 Wall-to-suspension heat transfer coefficient

2.4.1 Calculation method

2.4.1.1 Heat transfer coefficient calculation

In solar receivers, the efficiency of the heat transfer between the receiver walls and the Heat Transfer Fluid (HTF) is of primary importance, to remain undoubtedly under the degradation temperatures of the wall and HTF (see Chapter 1). Therefore, the HTF must be able to retrieve heat from the wall with the lowest temperature difference between them. The convective heat transfer coefficient h is a good way to represent the heat transfer efficiency. It is defined locally as:

$$h = \varphi_{w-HTF} / \left(T_w^{int} - T_b\right) \tag{2.5}$$

with φ_{w-HTF} the heat flux density between the wall and the HTF, T_w^{int} the internal wall temperature, and T_b the HTF bulk temperature.

Practically speaking, it is very difficult to measure the local HTC. In this study, measurements were done to calculate a global wall-to-suspension HTC, called h_{tube}, over the receiver tube height exposed to the concentrated solar radiation. The receiver tube is considered as a heat exchanger between the sun and the HTF, thus the logarithmic-mean temperature difference ΔT_{lm} may be used to represent an average temperature difference between the wall and the DPS, over the tube height and circumference. In this approach, h_{tube} is defined as:

$$h_{tube} = \Phi_{DPS} / \left(A \Delta T_{lm}\right) \tag{2.6}$$

with Φ_{DPS} the total heat received by the DPS and A the internal surface area of the irradiated part of the receiver tube.

2.4.1.2 Logarithmic-mean temperature difference calculation

The definition of the logarithmic-mean temperature difference ΔT_{lm} is:

$$\Delta T_{lm} = \frac{\left(T_{w,i}^{int} - T_{p,i}\right) - \left(T_{w,o}^{int} - T_{p,o}\right)}{\ln \frac{T_{w,i}^{int} - T_{p,i}}{T_{w,o}^{int} - T_{p,o}}} \tag{2.7}$$

with subscripts i/o corresponding to inlet/outlet of the irradiated part of the tube, subscripts w/p corresponding to tube wall and particles, and superscript int corresponding to the internal side of the tube wall.

The particle temperatures used in this calculation are the averages of the center and near wall temperatures.

For the wall temperature, a calculation method was developed that takes into account the temperature all around the tube. The external tube wall temperatures were measured with welded thermocouples. As shown in Figure 2.6, at the cavity inlet and outlet, the temperature was only measured on the east and west sides of the tube. Therefore, the corresponding temperatures at the tube front and back had to be extrapolated from those measured in the middle of the cavity. The impinging solar flux discrepancies create temperature differences between the east and west side of the tube, which can be as high as 70 K. The so-called "side temperature" in Eq (2.8) corresponds to the average of these two measures. The measurements showed that the front temperature was 80 to 140 K higher than the side temperature, depending on the experimental conditions. Indeed the tube front receives the concentrated solar irradiation perpendicularly while it is tangent on its sides. On the other hand, the difference between the tube backside temperature and the tube side temperature is less than 10 K, since it receives reflected and infrared radiation only. Figure 2.12 shows an example of temperature distribution around the tube in the middle of the cavity. The differences between front and side temperatures, and back and side temperatures, measured in the middle (Eq (2.9)), were then extrapolated to the cavity inlet and outlet to estimate the missing temperatures, and to allow the calculation of temperatures averaged over the tube circumference (Eq (2.10)). The wall internal temperature T_w^{int} was calculated from the wall external temperature T_w and the heat passing through the wall (Eq (2.11)). The heat flux density was considered to be uniform across the tube, since data of the distribution along the tube wall could not be measured. The equations for the various temperatures mentioned above are presented below:

$$T_{w,i/o/m,side} = \left(T_{w,i/o/m,W} + T_{w,i/o/m,E}\right)/2 \tag{2.8}$$

with the subscripts $i/o/m$ corresponding to inlet/outlet/middle of the irradiated part of the tube, W/E indicating the location west/east and side corresponding to the side temperature, which is the average of the east and west temperatures.

$$\Delta T_{w,F/B-side} = T_{w,m,F/B} - T_{w,m,side} \tag{2.9}$$

with the subscripts F/B corresponding to front/back.

$$\begin{aligned} T_{w,i/o} &= \frac{T_{w,i/o,E} + T_{w,i/o,W} + \left(T_{w,i/o,side} + \Delta T_{w,F-side}\right) + \left(T_{w,i/o,side} + \Delta T_{w,B-side}\right)}{4} \\ &= T_{w,i/o,side} + \frac{\Delta T_{w,F-side} + \Delta T_{w,B-side}}{4} \end{aligned} \tag{2.10}$$

$$T_{w,i/o}^{int} = T_{w,i/o} - \frac{\Phi_{DPS}}{2\Pi\lambda_{steel}L_{exposed}} \ln\frac{D_{ext}}{D_{int}} \tag{2.11}$$

with λ_{steel} the steel conductivity, Φ_{DPS} the heat passing through the wall (equal to the heat received by the DPS), and the geometric characteristics of the tube: $D_{int/ext}$ the internal/external diameter, $L_{exposed}$ the length exposed to solar radiation.

As mentioned before, the tube wall temperature on the front was only measured during the second experimental campaign. Therefore, a way to calculate a posteriori this temperature from other data was needed for the first campaign. A correlation was established to estimate the difference between the front and side temperatures as a function of $\Delta T_{lm,side}$, the logarithmic-mean temperature difference calculated with the tube side temperature only:

$$\Delta T_{lm,side} = \frac{\left(T^{int}_{w,i,side} - T_{p,i}\right) - \left(T^{int}_{w,o,side} - T_{p,o}\right)}{\ln \frac{T^{int}_{w,i,side} - T_{p,i}}{T^{int}_{w,o,side} - T_{p,o}}} \tag{2.12}$$

When exploiting the second campaign results, the temperature difference between the tube front and side could be predicted by the following equation with a maximum error of 9.1 % and an average error of 5.3 %:

$$\Delta T_{w,F-side} = 0.616 \Delta T_{lm,side} + 48.9 \tag{2.13}$$

Eq (2.13) was applied to the results of the first campaign and we were then able to calculate ΔT_{lm} including the front wall temperature. The additional relative error resulting from the use of this correlation is low because $\Delta T_{w,F_side}$ is divided by 4 in Eq (2.10) and, moreover, it is several times lower than $T_{w,i/o,side}$.

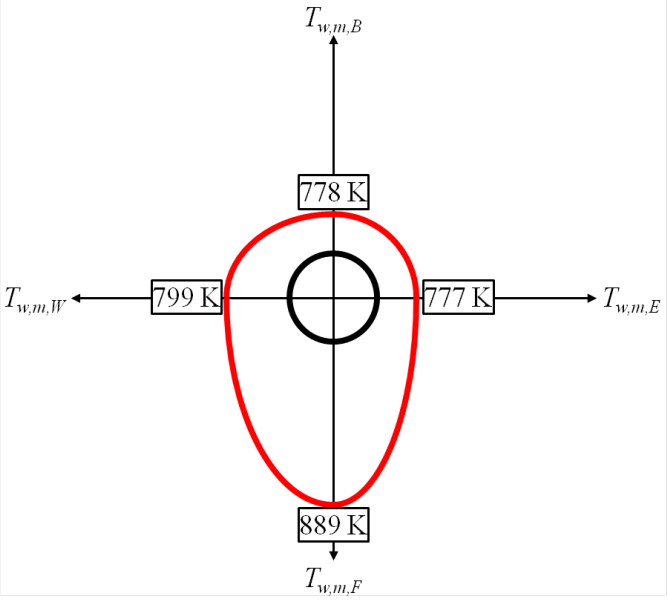

Figure 2.12: Temperature distribution around the tube in the middle of the cavity (average solid mass flux = 10.02 kg.m^{-2}.s^{-1}, aeration = 0.042 Nm^3.m^{-2}.s^{-1}, solar flux density at the cavity entrance = 346 kW/m^2).

2.4.1.3 Heat flux calculation

The power transmitted to the suspension is clearly a paramount point to calculate the HTC. The heat flux received by the particles is calculated by an enthalpy balance between

the inlet and outlet of the tube irradiated part. However, because of the particle reflux inside the tube (see Subsection 2.3.2), the temperatures to be used for the enthalpy balance cannot simply be the average temperatures at the inlet and outlet of the irradiated part. Indeed, there is enthalpy exiting the irradiated part at the bottom and entering at the top, transported by the solid close to the tube wall. Therefore, the right temperatures to be used in the balance must be carefully identified. As mentioned in Subsection 2.3.2, the temperatures measured at the cavity inlet correspond to particles that have already been heated, either because close to the wall they descend from the irradiated part of the tube, or because in the tube center the cold upward flux is mixed with the hot downward flux. Therefore, the particles' temperature before they receive any heat from the irradiated tube can only be measured below the cavity, far enough from its inlet. Specifically, $T_{p,iDiFB}$ was measured in the dispenser fluidized bed -DiFB-, at the tube inlet. Concerning the particle outlet temperature, it cannot be that measured close to the wall, because it concerns descending particles that have lost heat by exchange with the cold tube above the cavity. As a consequence, it seems reasonable to consider heated-up particles only, which are those flowing upward at the tube center, and therefore the particle temperature at the center $T_{p,o,center}$ is considered in the calculation. Even with this method, the heat received will still be slightly underestimated because the descending particles at the outlet mix with the upward flow in the irradiated part, thus rendering $T_{p,o,center}$ colder than it would have been without the heat loss after the cavity. But the lack of precise data on the heat loss and on the upward and downward solid mass fluxes makes the use of $T_{p,o,center}$ the best available option for the particle outlet temperature. The air heat capacity is neglected in front of that of the solid. The latter is calculated with a polynomial expression established from the values given by the National Institute of Standards and Technology (NIST) database (source: [12]):

$$c_{p,p}(T) = aT^3 + bT^2 + cT + d \tag{2.14}$$

with T in K and $a = 2.25 \times 10^{-7}$ J.kg^{-1}.K^{-4}, $b = -9.88 \times 10 - 4$ J.kg^{-1}.K^{-3}, $c = 1.62$ J.kg^{-1}.K^{-2}, $d = 320$ J.kg^{-1}.K^{-1}.

Finally, the formula used for calculating the heat received by the particle suspension Φ_{DPS} is:

$$\Phi_{DPS} = F_p c_{p,p} (T_{p,o,center} - T_{p,iDiFB}) \tag{2.15}$$

with F_p the particle mass flow rate, $c_{p,p}$ the particle specific heat capacity calculated at the average of the inlet and outlet temperatures, $T_{p,o,center}$ the particle temperature at the tube center at the cavity outlet, $T_{p,iDiFB}$ the particle temperature at the tube inlet inside the dispenser fluidized bed.

2.4.1.4 Time averages, standard deviations and confidence intervals

Combining both campaigns, almost eighty experimental runs were performed in total, of duration ranging between 15 and 40 minutes depending on the particle mass flow rate imposed at the bin outlet by the rotary valve. Several of them were excluded because

they were unstable due to meteorological conditions, bad settings, or in a few cases were unusable due to thermocouples breaking. All remaining 56 assays displayed a transitory regime (cavity heating up), then stable temperatures were reached, corresponding to the established regime, which is the interesting part for the HTC analysis. The results were averaged over the longest stable time periods possible, which ranged between 5.8 and 30 minutes. For each averaged data X, the resulting standard deviation σ_X was calculated.

Measures were taken every 5 seconds. Hence, the number of data points for one time period ranged between 71 and 361. The confidence intervals with 95 % and 99 % confidence levels were determined applying Student's t-distribution. They correspond to the intervals having a 95 % or 99 % probability of containing $\bar{X}$ and whose endpoints are $\bar{X} \pm t_{n-1}\frac{\sigma_X}{\sqrt{n}}$, where t_{n-1} is determined using a t-distribution table. The 99 % confidence interval on h_{tube} has a maximum half-width of 32 % and an average half-width of 11 %. The 95 % confidence interval has a maximum half-width of 24 % and an average half-width of 8 %.

All the results presented afterwards in Subsection 2.4.2 are time-averaged values.

2.4.2 Results

2.4.2.1 Global results

h_{tube} is plotted for both experimental campaigns in Figure 2.13 as a function of the solid mass flux G_p with the 95 % confidence intervals. It ranges from 421 W/m^2.K to 1116 W/m^2.K for solid mass flux of 10.2 kg.m^{-2}.s^{-1} and 45.1 kg.m^{-2}.s^{-1}, respectively. It can be noticed that the values of h_{tube} from the first campaign are lower than those from the second campaign. This is due to the lower temperature, as will be explained afterwards. It can also be seen that different values of h_{tube} may be obtained for a given mass flux G_p, varying other experimental parameters: aeration flow rate, DiFB temperature, solar irradiation conditions. However, h_{tube} shows an increasing trend with the solid mass flux. In the following analysis (2.4.2.2), the results are classified into data groups for which only one parameter varies, all others being constant. This will allow focusing on the influence of each parameter on h_{tube} .

2.4.2.2 Influence of solid mass flux, aeration and temperature

To highlight the distinct influences of the solid mass flux, aeration and temperature on h_{tube}, the results have been separated into distinct series where only one parameter varies, while the others are restricted to given ranges that are narrow enough not to influence noticeably the results. The the solar flux density influence could not be analyzed because, as explained before, the different irradiation conditions tested differ not only by the solar flux density impinging on the tube but also by its repartition and the possible hot spots. The reference temperature considered in this analysis is the average suspension temperature in the cavity T_{cav}, defined as the average of the 4 particle temperatures measured in the tube inside the cavity:

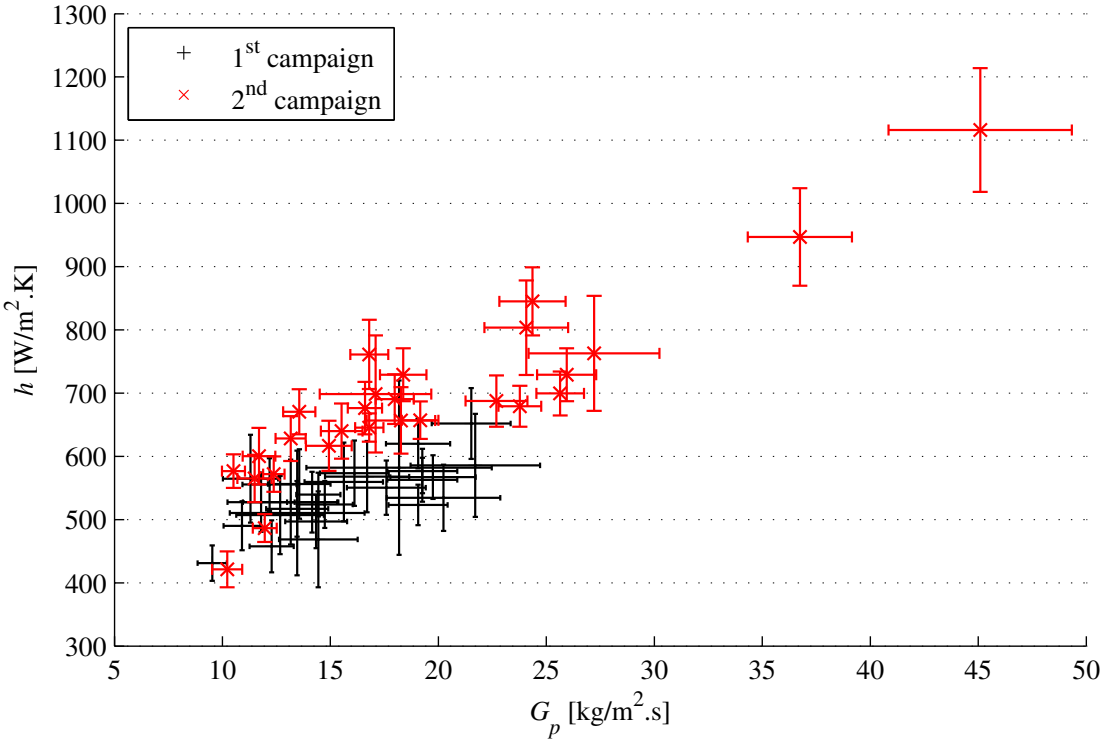

Figure 2.13: Global wall-to-suspension HTC h_{tube} versus solid mass flux G_p, with 95% confidence intervals.

$$T_{cav} = \left(T_{p,i,center} + T_{p,i,5mm} + T_{p,o,center} + T_{p,o,5mm}\right)/4 \tag{2.16}$$

Figure 2.14 plots h_{tube} as a function of the solid mass flux, with the 95 % confidence intervals, for two data series. The high aeration series was obtained with an aeration flux of 0.042 $Nm^3.m^{-2}.s^{-1}$, and the low aeration series with an aeration flux of 0.021 $Nm^3.m^{-2}.s^{-1}$. For both series, the irradiation conditions correspond to such a furnace setting that the normalized solar flux density is 387 kW/m^2, and the average suspension temperatures in the cavity are in the range 380-520 °C. For the high aeration, h_{tube} varies between 630 $W/m^2.K$ for a 13.2 $kg.m^{-2}.s^{-1}$ solid mass flux, and 700 $W/m^2.K$ for a 25.6 $kg.m^{-2}.s^{-1}$ solid mass flux. For the low aeration, h_{tube} varies between 660 $W/m^2.K$ for a 18.3 $kg.m^{-2}.s^{-1}$ solid mass flux, and 1116 $W/m^2.K$ for a 45.1 $kg.m^{-2}.s^{-1}$ solid mass flux. For both series it can be seen that h_{tube} increases with the solid mass flux. This is due to the particle agitation increasing whith the solid mass flux, which improves the particle movement thus the exchange between the wall and the tube center. For the same solid mass flux, the high aeration series presents a lower h_{tube}. This result is analyzed in the next paragraph.

Figure 2.15 plots h_{tube} as a function of the aeration, with the 95 % confidence intervals, for two series of data extracted from the results of the first campaign during which 6 aerations were tested, 5 of them leading to a stable DPS flow (indeed the lowest aeration tested lead to an intermittent suspension flow). The low solid mass flux series was obtained with solid mass fluxes in the range 10.9-13.5 $kg.m^{-2}.s^{-1}$, normalized solar flux density 242 kW/m^2, average suspension temperatures in the cavity in the range 234-253 °C. The medium solid

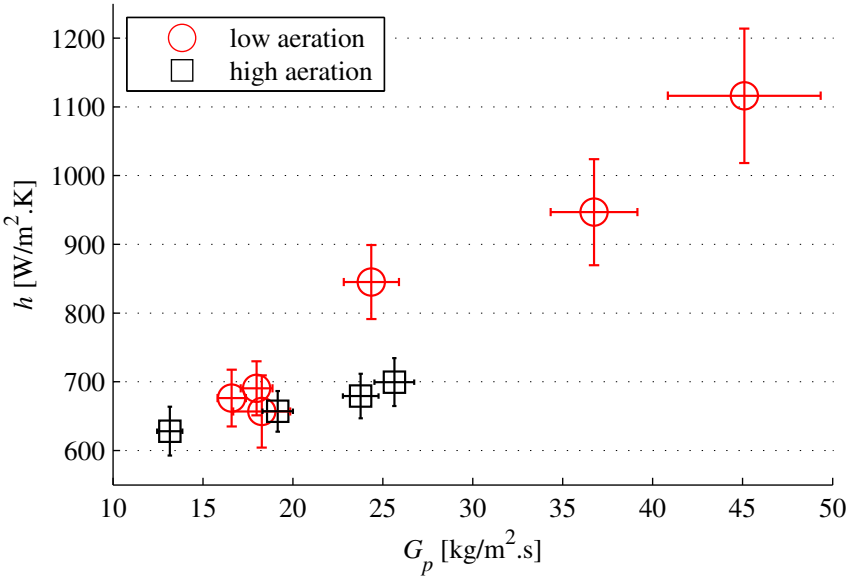

Figure 2.14: Global wall-to-suspension HTC h_{tube} versus solid mass flux G_p, with 95 % confidence intervals for two data series (high aeration series: aeration flux = 0.042 $Nm^3.m^{-2}.s^{-1}$, low aeration series: aeration flux = 0.021 $Nm^3.m^{-2}.s^{-1}$) with normalized solar flux density = 387 kW/m^2 and T_{cav} in the range 380-520 °C.

mass flux series was obtained with solid mass fluxes in the range 16.1-19.3 $kg.m^{-2}.s^{-1}$, normalized solar flux density 221 kW/m^2, average suspension temperatures in the cavity in the range 170-210 °C. For both series, a small decrease of h_{tube} with the aeration is observed. This result differs from what was observed on a single-tube experimental setup with electrical heating tested at the LGC [4]. In this parallel study, it was found that, for a slip velocity $(U_g - U_p)$ between 0.05 and 0.11 m/s, h_{tube} increased with the aeration and finally stabilized above 0.11 m/s.

This behavior was explained by the competition of two phenomena having opposed influences on the heat transfer. On the one hand, the higher the aeration, the lower the solid volume fraction[2] and, therefore, the lower the contact area between wall and particles (less contact leads to less exchange). On the other hand, the higher the aeration, the higher the particle renewal rate at the wall (when particles are in contact with a wall, the wall-to-particle heat transfer rate decreases with time. Therefore, the shorter the contact time, the higher the heat transfer rate).

In the current study, the apparent h_{tube} decrease with the aeration increase was attributed to a calculation error due to the recirculation. As was explained, the recirculation leads to an underestimation of the outlet temperature. Moreover, it was observed that the aeration increases the recirculation (see Chapter 3). Therefore, the higher the aeration mass flow rate, the stronger the recirculation and the higher the temperature underestimation at the

[2]This result was observed on all experimental setups (cold, electrical heating, solar heating). It reproduces the typical behavior of a fluidized bed expanding with the gas mass flow rate increase while maintaning a constant total pressure drop. When the solid mass flow rate remains constant (null in the case of a fluidized bed) so does the force applied by the gas phase on the particles. The drag force depends on the local velocity difference between gas and particles that can only be maintained if the space available for the gas circulation is increased. Therefore, the higher the gas mass flow rate, the lower the solid volume fraction.

outlet.

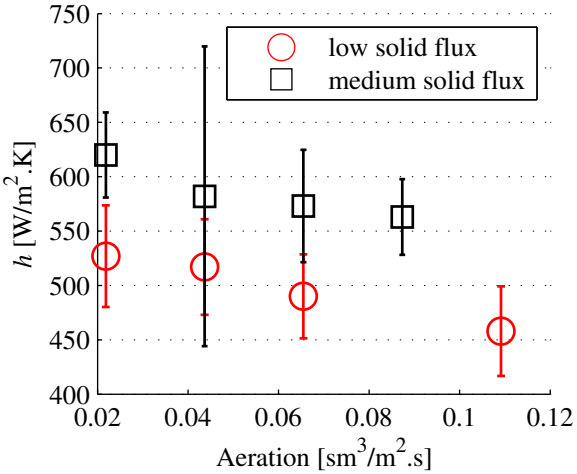

Figure 2.15: Global wall-to-suspension HTC h_{tube} versus aeration, with 95 % confidence intervals for two data series (low solid mass flux: G_p in the range 10.9-13.5 kg.m^{-2}.s^{-1}, normalized solar flux density = 242 kW/m^2, T_{cav} in the range 234-253 °C ; medium solid mass flux: G_p in the range 16.1-19.3 kg.m^{-2}.s^{-1}, normalized solar flux density = 221 kW/m^2, T_{cav} in the range 170-210 °C).

Figure 2.16 plots h_{tube} as a function of the average suspension temperature in the cavity T_{cav}, for the following experimental conditions: aeration flux of 0.021 Nm^3.m^{-2}.s^{-1}, solar flux density at the cavity inlet between 213 and 269 kW/m^2 and solid mass flux between 13.5 and 15.5 kg.m^{-2}.s^{-1}. The temperature has clearly a positive influence on h_{tube}. For the same solid circulation and solar irradiation, h_{tube} increases by almost 30 % when the temperature increases from 220 °C to 580 °C. As underlined by Flamant et al. [13] and Pitié et al. [14] the combination of two factors can explain this: first, the radiation heat contribution, which is negligible at low temperature when the wall temperature is less than 450 °C, becomes important at high temperature when the wall front temperature goes over 800 °C. Second, the air thermal conductivity, which plays an important role in the heat transfer by conduction at the wall, increases by 50 % when the suspension temperature increases from low to high temperature.

We can conclude from this analysis that the facility should be operated at high solid mass flux, at the lowest possible aeration flux and at high temperature to have the highest possible wall-to-suspension HTC. In addition, the solid mass flux can be varied in order to maintain the particle outlet temperature constant when irradiation conditions change.

2.5 Nusselt Correlation for Dense Particle Suspension

2.5.1 Interest of a Nusselt Correlation

Thanks to the results of the experimental campaigns, we were able to analyze the influence of the various parameters on h_{tube} and conclude on how a facility using a DPS receiver

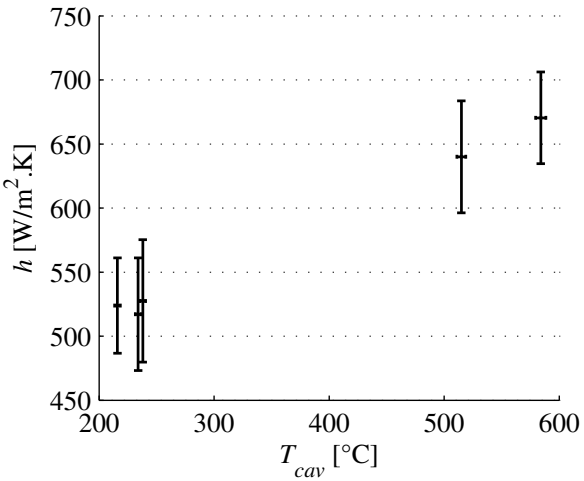

Figure 2.16: Global wall-to-suspension HTC h_{tube} versus average suspension temperature in the cavity T_{cav} (aeration flux = 0.021 $Nm^3.m^{-2}.s^{-1}$, solar flux density at the cavity inlet between 213 and 269 kW/m^2, solid mass flux between 13.5 and 15.5 $kg.m^{-2}.s^{-1}$).

should be operated. But this analysis could only be done for narrow ranges of parameters because they are interconnected. For example, changing the solid mass flux while keeping the aeration and solar irradiation constant changed the DPS temperature. In order to size and operate such an installation, it is necessary to be able to predict precisely h_{tube} for any parameters combination. Therefore, we aimed to establish a correlation applicable to the whole range of tested parameters. As was explained in Chapter 1, the correlations predicting the HTC are based on the Nusselt number Nu that is a function of the Reynolds number Re and Prandtl number Pr. The temperature and aeration cannot be included as such in the correlations. Their influences must be taken into account through their impact on the phases' thermophysical properties (density, conductivity, heat capacity, viscosity) and on the DPS characteristics, the void fraction in particular.

The correlation proposed afterwards did not aim to calculate the Nusselt number on a fundamental basis. It was rather designed with an engineering point of view, the only goal being the prediction of Nu with a reasonable error.

2.5.2 Determination of a Nusselt Correlation

2.5.2.1 Calculation of the Nusselt, Prandtl and Reynolds Numbers for DPS

The Nusselt number is defined as the ratio of convective heat transfer over conductive heat transfer. In the DPS case, it was defined as follows:

$$Nu_{DPS} = h_{tube} D / \lambda_{DPS} \tag{2.17}$$

with D the tube diameter, and λ_{DPS} the DPS effective thermal conductivity.

Since the DPS is not a fluid but a mixture of a gas and solid particles, its effective thermal conductivity depends on the volume fraction and thermal conductivity of both phases.

Different models exist to calculate the effective conductivity of a gas-solid mixture. We chose to apply the same model that was used for the DPS process numerical simulation [15], which is Zehner and Schlünder's model [16]. It was designed for porous media, which does not exactly correspond to a fluidized bed. However it allows to reproduce the influence of the voidage on the suspension conductivity. The model's equation are:

$$\lambda_{mixture} = \lambda_{eff,g} + \lambda_{eff,p} \tag{2.18}$$

with $\lambda_{mixture}$, $\lambda_{eff,g}$ and $\lambda_{eff,p}$ the effective conductivities of the mixture, gas and particles respectively.

$$\lambda_{eff,g} = \left(1 - \sqrt{1-\varepsilon}\right) \lambda_g \tag{2.19}$$

with λ_g the gas conductivity and ε the suspension voidage.

$$\lambda_{eff,p} = \sqrt{1-\varepsilon}\,(\omega Y + (1-\omega)\,\Gamma)\,\lambda_g \tag{2.20}$$

with $\omega = 7.26 \times 10^{-3}$.

$$\Gamma = \frac{2}{1-\frac{Z}{Y}} \left(\frac{Y-1}{\left(1-\frac{Z}{Y}\right)^2} \frac{Z}{Y} \ln \frac{Y}{Z} - \frac{Z-1}{1-\frac{Z}{Y}} - \frac{1}{2}(Z+1) \right) \tag{2.21}$$

$$Z = 1.25 \left(\frac{1-\varepsilon}{\varepsilon} \right)^{10/9} \tag{2.22}$$

$$Y = \lambda_p / \lambda_g \tag{2.23}$$

with λ_p the particle conductivity.

Re and Pr are functions of the fluid viscosity. Hence, the same problem as for conductivity arises: a model must be applied to obtain the viscosity of a gas-particle mixture. Since the objective of this study is not to accurately determine the apparent suspension viscosity, but only to represent how it is impacted by the voidage, a simple model was chosen [17]:

$$\mu_{mixture} = \mu_g \left(1 - \frac{1-\varepsilon}{C_M} \right)^{-2} \tag{2.24}$$

with $\mu_{mixture}$ and μ_g the dynamic viscosity of the mixture and of the gas, respectively, C_M the powder packing concentration.

The particle volume fraction α_p must be known to calculate the DPS density ρ_{DPS}. It was calculated from the measure given by a pressure sensor with its plug placed on the tube

below the irradiated cavity and the atmospheric pressure at the tube's top. As shown by Eq (2.3), the pressure difference is due to the DPS hydrostatic pressure and the friction pressure loss. By neglecting the friction pressure loss in front of the hydrostatic pressure difference, and the air density in front of that of SiC, the formula for α_p becomes:

$$\alpha_p = 1 - \varepsilon = \frac{P_{sensor} - P_{atm}}{\rho_p g \left(z_{top} - z_{sensor}\right)} \tag{2.25}$$

with P_{sensor} the pressure measured, P_{atm} the atmospheric pressure, z_{sensor} the sensor's plug height and z_{top} the tube top height.

Since the air density is neglected, the DPS density ρ_{DPS} is given by:

$$\rho_{DPS} = \alpha_p \rho_p \tag{2.26}$$

The DPS specific heat capacity $c_{p,DPS}$ is equal to that of SiC since the air density is neglected.

The DPS Reynolds number, Re_{DPS} was calculated as follows:

$$Re_{DPS} = \frac{\rho_{DPS} u_p d_{32}}{\mu_{DPS}} \tag{2.27}$$

with u_p the particle average advection velocity in the tube defined as:

$$u_p = G_p / \left(\alpha_p \rho_p\right) \tag{2.28}$$

with S the tube section.

And the DPS Prandtl number was defined as:

$$Pr_{DPS} = \frac{\mu_{DPS} c_{p,DPS}}{\lambda_{DPS}} \tag{2.29}$$

2.5.2.2 Silicon Carbide Particles and Air Properties

The SiC properties needed for calculations are listed in Table 2.3. The SiC density and the packing concentration (determined from the packed powder density) were measured. The other properties are expressed in the form of polynomials that were established with data from the NIST database (source: [12]), as a temperature function (in [K]). The temperature used was T_{cav} since it represents the temperature in the irradiated part of the tube, where the heat exchange occurs.

Table 2.3: SiC particles properties

Properties	**Values/Equations**
Sauter diameter	$d_{32} = 64\ \mu$m
Density	$\rho_p = 3210$ kg/m^3
Packing concentration	$C_M = \frac{\rho_{Packedpowder}}{\rho_{SiC}} = 0.502$
Specific heat	$c_{p,p}(T) = aT^3 + bT^2 + cT + d$ (2.14) in [J/kg.K] with T in [K] and $a = 2.25 \times 10^{-7}$ J.kg^{-1}.K^{-4} , $b = -9.88 \times 10 - 4$ J.kg^{-1}.K^{-3}, $c = 1.62$ J.kg^{-1}.K^{-2}, $d = 320$ J.kg^{-1}.K^{-1}
Thermal conductivity	$\lambda_p(T) = eT^2 + fT + g$ (2.30) in $\left[\text{W.m}^{-1}\text{.K}^{-1}\right]$ with T in [K], and $e = 8.56 \times 10^{-5}$ W.m^{-1}.K^{-3}, $f = -2.14 \times 10^{-1}$ W.m^{-1}.K^{-2}, $g = 169.4$ W.m^{-1}.K^{-1}

As mentioned before, the gas used in the experimental setup is air. The air properties needed for calculations are listed in Table 2.4. They are expressed in the form of equations as a temperature function (in [K]). The temperature used was T_{cav} as for the SiC properties. The properties' equations were defined from the data tables given in Perry's Chemical Engineers' Handbook [18].

Table 2.4: Air properties

Properties	**Values/Equations**
Thermal conductivity	$\lambda_g(T) = iT^3 + jT^2 + kT + l$ (2.31) in $\left[\text{W.m}^{-1}\text{.K}^{-1}\right]$ with T in [K], and $i = 1.52 \times 10^{-11}$ W.m^{-1}.K^{-4}, $j = -4.86 \times 10^{-8}$ W.m^{-1}.K^{-3}, $k = 1.02 \times 10^{-4}$ W.m^{-1}.K^{-2}, $l = 3.93 \times 10^{-3}$ W.m^{-1}.K^{-1}
Dynamic viscosity	$\mu_g(T) = \mu_r \left(\frac{T}{T_r}\right)^m \frac{T_r+B}{T+B}$ (2.32) in [Pa.s] with $\mu_r = 1.716 \times 10^{-5}$ Pa.s, $T_r = 273.15$ K, $m = 1.54$, $B = 110.4$ K

2.5.2.3 Nusselt Correlation Specific to DPS

Currently, the existing Nusselt correlations are not applicable to the case of the DPS flow in vertical tubes. Indeed, Gnielinski's correlation [19], which takes into account all the previous studies on the subject, is only valid when the Prandtl number is larger than 0.5, which is the case for most gases and liquids but not for DPS. The Pr_{DPS} calculated with the method previously detailed are in the range 0.24-0.64, which is partly outside the validity range of Gielinski's equation. This problem is also encountered for liquid metals

due to their very high conductivity that leads to a very low Pr. This is why correlations specific to liquid metals were therefore developed. Sleicher and Rouse's equation [20] only applies to turbulent flows with $Re > 10^4$ and $Pr < 0.1$ so it was not usable for DPS. Lyon-Martinelli [21], as well as Cheng and Tak [22] use the Peclet number, which is the product of Re and Pr, in their equations. They were tested but did not accurately fit the results. Actually, this is not surprising because of the peculiar flow configuration of the DPS that presents a particle reflux close to the wall. This is why we chose to establish a Nusselt correlation specific to DPS flow in vertical tubes. The correlation that gives the best results has the shape of Sleicher and Rouse's equation but it uses the Reynolds and Prandtl numbers calculated at the average DPS temperature in the irradiated part of the tube, instead of the film and wall temperatures, because no significant gain on the coefficient of determination was observed when using the latters. The used correlation is:

$$Nu_{DPS} = 4.5 + 35.4 Re_{DPS}^{0.61} Pr_{DPS}^{0.94} \tag{2.33}$$

Figure 2.17 plots Nu_{DPS} calculated with the correlation in front of the experimental Nu_{DPS}. The determination coefficient is $R^2 = 0.95$, the maximum and average relative errors are 14.7 % and 5.5 %, which is very satisfactory considering the experimental biases (underestimation of the outlet temperature due to the recirculation flux, concentrated solar flux assumed to be uniform, limited number of thermocouples measuring the DPS and wall temperatures, neglected friction pressure loss).

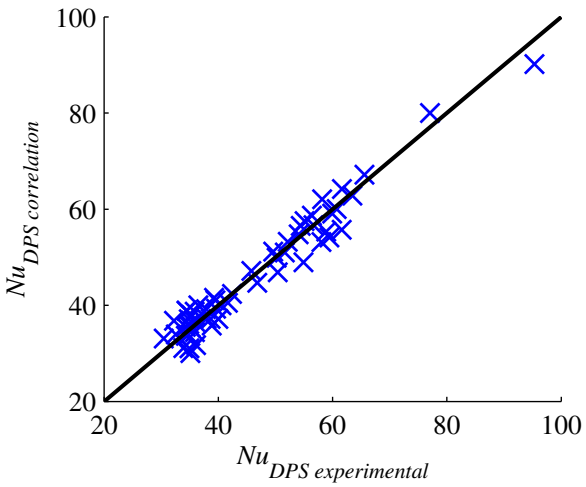

Figure 2.17: Nu_{DPS} from correlation versus experimental Nu_{DPS}.

2.6 Discussion and Conclusion

The aim of the study was to run and exploit a first series of on-sun experiments involving a new type of solar receiver that uses a Dense Particle Suspension (DPS) circulating upward in an opaque tube exposed to the concentrated solar flux. Contrary to Circulating Fluidized Beds (CFB), DPS flows operate at low gas velocity and large solid fraction. Typical air velocity and mean solid fraction in CFBs are respectively 10 m/s and less than 5 %

respectively; these values are typically 0.02 m/s and 30 % in DPS flows, respectively.

It was shown that this innovative process leads to global wall-to-suspension heat transfer coefficients over the receiver tube height exposed to concentrated solar radiation, called h_{tube}, up to 1100 W/m^2.K in the considered conditions, with particle mean advection velocities always less than 6 cm/s. But the solid mass flux for DPS flows can be more than 10 times larger than the maximum tested during our experiments, which would lead to higher h_{tube}. Suspension temperature up to 750 °C was obtained maintaining the absorber wall temperature in its operation limit, thus opening new opportunities for high efficiency thermodynamic cycles. Indeed, Dunham and Iverson [23] showed that using a CO_2 recompression Brayton cycle could lead to whole system efficiencies (solar-to-electricity) of 43 % with a fluid temperature of 746 °C for wet-cooling, and 39 % with a fluid temperature of 766 °C for dry-cooling. Using ceramic tubes might even extend the operating temperature up to more than 1000 °C, which means the thermodynamic cycles would be even more efficient, but it would then require developments to limit the receiver heat losses. More than 200 °C particle temperature elevation was measured in the 50 cm long irradiated part of the receiver tube. A recirculation (downward flow) of particles in the vicinity of the tube wall was observed.

We found that the solid mass flux and the DPS temperature are the main parameters influencing the heat transfer. The higher the solid mass flux, the higher h_{tube}, because when the particle agitation increases, then the particle movement and the exchange between the wall and the tube center are improved. The higher the DPS temperature, the higher h_{tube}, because the air conductivity and radiation exchange increase with temperature.

An apparently detrimental impact of the aeration on h_{tube} was observed. But, by comparison with the LGC results obtained on an electrically heated experimental setting, this effect was finally attributed to a measurement error caused by the particle recirculation. Our partner proved that the aeration positively impacted h_{tube} for a slip velocity between 10 and 22 U_{mf}, due to the particle agitation increasing. Above this range, the opposite effects on the heat transfer of the agitation increase (positive effect) and solid volume fraction decrease (negative effect) compensate and h_{tube} stabilizes.

The system proved to be easily controllable by the pressure imposed in the dispenser fluidized bed, the aeration and the feeding rate from the particle storage. A power plant using this technology should be operated at low aeration, and the solid mass flux modulated to get the desired outlet temperature.

The h_{tube} values, calculated from the results of two experimental campaigns, were successfully fitted with a specific Nusselt correlation that has a determination coefficient $R^2 = 0.95$ and an average relative error of 5 %. This correlation will be a useful tool for sizing and operating future facilities using DPS receivers:

$$Nu_{DPS} = 4.5 + 35.4 Re_{DPS}^{0.61} Pr_{DPS}^{0.94}$$

At this moment, only general trends can be drawn to compare DPSs and molten salts, the more developed HTF technique in central receiver solar power plants. The DPS thermal

capacity (ρc_p) is about half that of molten salts, and, accounting for the measured h_{tube}, the flux limit that the receiver can stand is estimated in the range 300-400 kW/m^2, that-is-to say 1/3 to 1/4 of the flux limit for molten salt receivers. But DPSs extend drastically the operating temperature range of solar heat transfer fluids, currently limited to about 560 °C, they do not suffer any freezing point problem, they are harmless and their cost is low. Moreover, DPSs keep both advantages of being a HTF and a storage medium.

In fact, DPSs appear to open a new domain of applications of concentrated solar energy, compared to existing technologies. Indeed, such a thermal treatment of divided solid in a solar receiver composed of closed and opaque tubes could be implemented for thermochemical particle processing. Applications to concrete industry, to waste and biomass treatment, or to ore processing, can be foreseen.

The next step that consists in testing a multi-tube cavity receiver at pilot scale (150 kW$_{\text{th}}$) will be presented in Chapter 4.

2.7 Nomenclature

Abreviations

CFB	Circulating Fluidized Bed
ColFB	Collector fluidized bed
CSP2	Concentrated Solar Power in Particles (FP7 European Project)
DiFB	Dispenser fluidized bed
DNI	Direct Normal Irradiation
DPS	Dense Particle Suspension
HTC	Heat Transfer Coefficient
HTF	Heat Transfer Fluid
NIST	National Institute of Standards and Technology
PEPT	Positron Emission Particle Tracking
UBFB	Upward Bubbling Fluidized Bed

Latin symbols

A	Internal surface area of the absorber tube [m^2]
a-l	Coefficients in property equations
B	Sutherland's constant for air
C_M	Powder packing concentration
c_p	Specific heat capacity at constant pressure [J/kg/K]
D	Tube diameter [m]
d_{32}	Sauter diameter [μm]
F	Mass flow rate[kg/s]
G	Mass flux [$kg.m^{-2}.s^{-1}$]
g	Gravitational acceleration [m^2/s]
h	Convective heat transfer coefficient [$W.m^{-2}.K^{-1}$]
h_{tube}	Global wall-to-suspension heat transfer coefficient [$W.m^{-2}.K^{-1}$]
$L_{exposed}$	Length of the irradiated part of the tube [m]
m	Exponent in the air dynamic viscosity equation
Nu	Nusselt number
P	Pressure [Pa]
P_{atm}	Atmospheric pressure [Pa]
P_{sensor}	Pressure measured by the sensor set on the tube [Pa]
Pr	Prandtl number
$R_{contact}$	Thermal contact resistance [m^2.K/W]
S	Tube section [m^2]
T	Temperature [K]
t	Time [s]
T_{cav}	Average of the 4 particle temperatures measured in the cavity [K]
T_{side}	Average of the right and left side wall temperatures [K]
Y, Z	Coefficients in Zehner and Schlünder's model [16]
z_{base}	Height of the tube base[m]
z_{top}	Tube top height [m]
z_{sensor}	Pressure sensor's plug height [m]
z_{tube}	Height of the suspension in the tube [m]

Greek symbols

$alpha$	Volume fraction
Γ	Coefficient in Zehner and Schlünder's model [16]
ΔP_{bed}	Hydrostatic pressure of the bed between the freeboard and the tube inlet [Pa]
ΔP_{drive}	Driving pressure (pressure difference between the tube inlet and outlet) [Pa]
$\Delta P_{friction}$	Friction pressure loss inside the tube [Pa]
ΔT_{lm}	Logarithmic-mean temperature difference [K]
ε	Suspension voidage or void fraction
ε_{Nickel}	Emissivity of thermocouple wires
λ	Thermal conductivity [$[W.m^{-1}.K^{-1}]$
μ	Dynamic viscosity [Pa.s]
ρ	Density [kg/m^3]
Φ_{DPS}	Heat transmitted to the DPS [W]
φ	Heat flux density [W/m^2]
φ_{w-HTF}	Heat flux density between the wall and the HTF [W/m^2]
φ_{solar}	Solar flux density reaching the tube [W/m^2]
$\varphi_{wire-tube}$	Heat flux density passing from the wire to the tube wall [W/m^2]
σ	Stefan-Boltzmann constant [W.m^{-2}.K^{-4}]
σ_X	Standard deviation on the parameter X
ω	Coefficient in Zehner and Schlünder's model [16]

Subscripts, Superscripts

$center/5mm$	Thermocouple position inside the tube, at the center/5 mm from the wall
DPS	Refers to properties or dimensionless numbers of the DPS
eff	Refers to the phases effective conductivities
$F/B/W/E$	Front/Back/West/East
$freeDiFB$	Refers to the dispenser fluidized bed freeboard
g	Gas
$iDiFB$	Tube inlet in the dispenser fluidized bed
$i/m/o$	Inlet/Middle/Outlet of the irradiated part of the cavity
int/ext	Internal/External side of the tube wall
$mixture$	Refers to the gas and particle mixture
p	Particles
r	Reference
w	Wall
$wire/tube$	thermocouple wire/tube wall at the front of the tube in the middle of the cavity

Bibliography

[1] G. Flamant, D. Gauthier, H. Benoit, J.-L. Sans, R. Garcia, B. Boissière B., R. Ansart, and M. Hemati. Dense suspension of solid particles as a new heat transfer fluid for concentrated solar thermal applications: On-sun proof of concept. *Chemical Engineering Science*, 102:567–576, 2013.

[2] H. Benoit, I. Pérez López, D. Gauthier, J.-L. Sans, and G. Flamant. On-sun demonstration of a 750 °C heat transfer fluid for concentrating solar systems: Dense particle suspension in tube. *Solar Energy*, 118:622–633, 2015.

[3] H. Benoit, I. Pérez López, D. Gauthier, and G. Flamant. Nusselt correlation for upward bubbling fluidized bed circulating in tube exposed to highly concentrated solar flux. *Chemical Engineering Science*, (Submitted).

[4] B. Boissière. *Étude hydrodynamique et thermique d'un nouveau concept de récepteur solaire à suspensions denses gaz-particules (Hydrodynamic and thermal study of a new concept of solar receiver using dense gas-particle suspensions).* PhD thesis, Institut National Polytechnique de Toulouse (INP Toulouse), 2015.

[5] D. Geldart. Types of gas fluidization. *Powder Technology*, 7:285–292, 1973.

[6] B. Boissière, R. Ansart, D. Gauthier, G. Flamant, and M. Hemati. Experimental hydrodynamic study of gas-particle dense suspension upward flow for applications as new heat transfer and storage fluid. *Canadian Journal of Chemical Engineering*, 93:317–330, 2015.

[7] G. Turzo. *Transport par fluidisation en phase hyperdense : amélioration technologique and modélisation et dimensionnement (in French) (Hyperdense phase transport by fluidization: technological improvement and modeling and design).* PhD thesis, Institut National Polytechnique de Toulouse (INP Toulouse), 2013.

[8] J. Baeyens and W.R.A Goossens. Some aspects of heat transfer between a vertical wall and a gas fluidized bed. *Powder Technology*, 8:91–96, 1973.

[9] T.L. Bergman, A.S. Lavine, F.P. Incropera, and D.P. DeWitt. *Fundamentals of Heat and Mass Transfer.* John Wiley & Sons, 7^{th} edition, 2011. (Chapter 3, Table 3.1, p. 118).

[10] J. Baeyens and D. Geldart. *Gas Fluidization Technology.* (Ed. D. Geldart). John Wiley & Sons, 1986. (Chapter 5: Solids Mixing, pp. 97-122).

[11] P. Garcia-Triñanes, J.P.K. Seville, B. Boissière, R. Ansart, T.W. Leadbeater, and D.J. Parker. Hydrodynamics and particle motion in upward flowing dense particle suspensions: Application in solar receivers. *Chemical Engineering Science*, (submitted).

[12] R.G. Munro. Material Properties of a Sintered alpha-SiC. *Journal of Physical and Chemical Reference Data*, 26:1195–1203, 1997.

[13] G. Flamant and T. Méningault. Combined wall-to-fluidized bed heat transfer. Bubbles and emulsion contributions at high temperature. *International Journal of Heat and Mass Transfer*, 30:1803–1812, 1987.

[14] F. Pitié, C.Y. Zhao, J. Baeyens, J. Degrève, and H.L. Zhang. Circulating Fluidized Bed heat recovery/storage and its potential to use coated phase-change-material (PCM) particles. *Applied Energy*, 109:505–513, 2013.

[15] R.A. Reyes Urrutia, H. Benoit, M. Zambon, D. Gauthier, G. Flamant, and G. Mazza. Simulation of the behavior of a dense SiC particle suspension as an energy transporting vector using computational fluid dynamics (CFD). *Chemical Engineering Research and Design*, (accepted).

[16] P. Zehner and E.U. Schlünder. Thermal conductivity of granular materials at moderate temperatures (in German). *Chemie. Ingr.-Tech.*, 42:933–941, 1970.

[17] D. Quemada. Rheology of concentrated disperse systems and minimum energy dissipation principle. *Rheologica Acta*, 16:82–94, 1977.

[18] D.W. Green and R.H. Perry. *Perry's Chemical Engineers' Handbook*. McGraw-Hill Professional, 8^{th} edition, 2008. (Section 2, Thermodynamic Properties).

[19] V. Gnielinski. On heat transfer in tubes. *International Journal of Heat and Mass Transfer*, 63:134–140, 2013.

[20] C.A. Sleicher and M.W. Rouse. A convenient correlation for heat transfer to constant and variable property fluids in turbulent pipe flow. *International Journal of Heat and Mass Transfer*, 18(5):677–683, 1975.

[21] R.N. Lyon. Liquid metal heat transfer coefficients. *Chemical Engineering Progress*, 47:75–79, 1951.

[22] X. Cheng and N. Tak. Investigation on turbulent heat transfer to lead-bismuth eutectic flows in circular tubes for nuclear applications. *Nuclear Engineering and Design*, 236(4):385–393, 2006.

[23] M.T. Dunham and B.D. Iverson. High-efficiency thermodynamic power cycles for concentrated solar power systems. *Renewable and Sustainable Energy Reviews*, 30:758–770, 2014.

Chapter 3

3D Numerical Simulation of a Dense Particle Suspension Solar Receiver under Uniform Heating

3.1 Introduction

The experimental Dense Particle Suspension (DPS) single-tube receiver described in Chapter 2 was simulated in order to better understand the particle flow and the heat transfer mechanisms inside the absorber tube. Indeed, numerical simulations give access to data impossible to measure without disrupting the observed phenomenon. Specifically, the particular flow pattern that was discovered during the experiments (i.e. the particle reflux in the near wall region) and the particle exchange between the tube wall and the tube center that is responsible for the heat transfer were analyzed through two-phase 3D Computational Fluid Dynamics (CFD) numerical simulations. Previous simulations of a cold mock-up built at the Chemical Engineering Laboratory (in French: Laboratoire de Génie Chimique - LGC) in Toulouse were realized [1] to analyze the hydrodynamics of the Upward Bubbling Fluidized Bed (UBFB) flow in tube. It was observed that modifying the solid flux does not affect the DPS voidage and that the particle volume fraction is higher at the wall than at the tube center. The particle reflux proved by the solar experiments presented in Chapter 2 was reproduced.

Two approaches can be used to simulate fluidized beds: the Eulerian-Lagrangian and Eulerian-Eulerian methods. The Langragian model individually considers each particle and solves the motion equations that include the inter-particle collisions and the force excerced by the fluid. The fluid flow is determined by the Navier-Stokes equation. Therefore, the CFD and the discrete particle method are combined in this model. In the Eulerian-Eulerian approach, all the phases are considered continuous and occupy a fraction of each volume element. This is the concept of phase volume fraction [2]. For each phase, conservation equations are established for the kinetic energy and eventually the heat, and they are coupled. This approach requires to make assumptions on the solid rheology that are not needed with the Lagrangian method. But the latter requires a large computational power because of the great number of equations to solve. Consequently, it can only simulate a small number of particles which limits its use to small-scale fluidized beds. Therefore, the Eulerian-Eulerian model is the most frequently used for studying the hydrodynamics of fluid particle systems [3]. It was used by our CSP2 project partners in 2D simulations to study the heat exchange mechanisms between the tube wall and the DPS [4]. We took part in another study also using the same method that simulated the experiments presented in Chapter 2 and aimed to reproduce the measured heat transfer between the wall and the particles [5].

In our study, the DPS flow simulations were conducted with a uniform heating of the tube. Three cases reproducing steady-state experimental runs were simulated: a medium solid flux-medium temperature case (Ref case), a high solid flux-medium temperature case (HQ case), and a low solid flux-high temperature case (HT case). Section 3.2 presents the simulations parameters that were used. The modeled geometry and the corresponding mesh are described; the two phases' properties and the boundary conditions are indicated; the mathematical models and their equations are given. In Section 3.3, the numerical and experimental results are compared at the level of the pressure drops and temperatures. In Section 3.4, the simulations' results are used to analyze the influence of the solid flux and temperature on the particle reflux in the near wall region. Moreover, the particle exchange between the zone close to the tube wall and the tube center is studied to understand the heat transfer mechanism that takes place in the UBFB flow. To conclude, the results of the model's results are summarized and perspectives are given for future studies.

3.2 Simulation Parameters

3.2.1 Geometry and mesh

Generally, the geometry must be as simple and small as possible to carry out numerical simulations, because the bigger it is, the longer the computation time is. But the previous experimental studies showed that what happens in the tube is highly linked to the Dispenser Fluidized Bed (DiFB). As a consequence, it was necessary to simulate both the DiFB and the absorber tube to have an accurate process representation. The mesh is represented on Figure 3.1. It contains 1,650,000 hexahedral, 1.5 mm high and around 1.2 mm wide cells. The fluidization chamber, corresponding to the DiFB, has a horizontal section area of 0.02 m^2, a height of 0.4 m and is equipped with a lateral solid entrance and a regulation valve at the top. The tube is 2.06 m high and 0.034 m in diameter. Its inlet is set 0.1 m cm above the bottom of the chamber (fluidization plate). A convergent is added at the tube outlet to prevent any backward flow. An aeration injection is set on the tube 0.57 m from its inlet. The geometry dimensions correspond to those of the cold mock-up.

Since the current simulations with heating were conducted after those without heating, we chose to keep the same geometry to be able to compare both numerical studies. It slightly differed from the geometry of the experimental solar receiver. The DiFB section was smaller (0.02 m^2 instead of 0.16 m^2) and its height was greater (0.4 m instead of 0.3 m) but this did not affect the results as long as the fluidized bed state was reproduced (bubbling bed). The tube diameter simulated was 0.034 m whereas that of the experimental absorber tube was 0.036 m. To compensate for this difference, the solid flux was kept constant and the heat flux density imposed during the simulations was adapted to keep the same temperature increase. This is further explained in 3.2.4.2. The tube inlet was set 0.1 m above the fluidization plate whereas it was 0.04 m in the experiments. Finally, the aeration injection was set 0.57 m above the tube inlet in the simulations instead of 0.3 m in the on-sun experiments.

3.2.2 Phases properties

3.2.2.1 Silicon Carbide particles

Figure 3.2 is a Scanning Electron Microscopy (SEM) photograph of the SiC particles used in the experiments. It can be seen that their shapes were very irregular with a high size polydispersion. They had a 63.9 μm mean Sauter diameter (diameter of a sphere that has the same volume to surface area ratio as the particles). Due to the particles' shapes, the bed expansion was under-estimated by the model when the imposed diameter was 64 μm. This result is illustrated in Figure 3.3 that shows the voidage evolution with the particle size, for a fluidization velocity U_f equal to twice the minimum fluidization velocity measured for the particles: $U_{mf} = 5 \times 10^{-3}$ m/s, during a homogeneous bed expansion obtained by reversing the drag equation from the linear momentum equation. The predicted result is a maximum value due to the many collisions occurring in the numerical calculation that tend to reduce this expansion. Therefore, usual drag equations (Wen and Yu drag model [6], Ergun equation [7]) cannot accurately predict the fluidized bed porosity for this highly poly-dispersed distribution of non-spherical particles. The particle diameter was set to 40 μm to obtain the same numerical bed expansion as that measured experimentally,

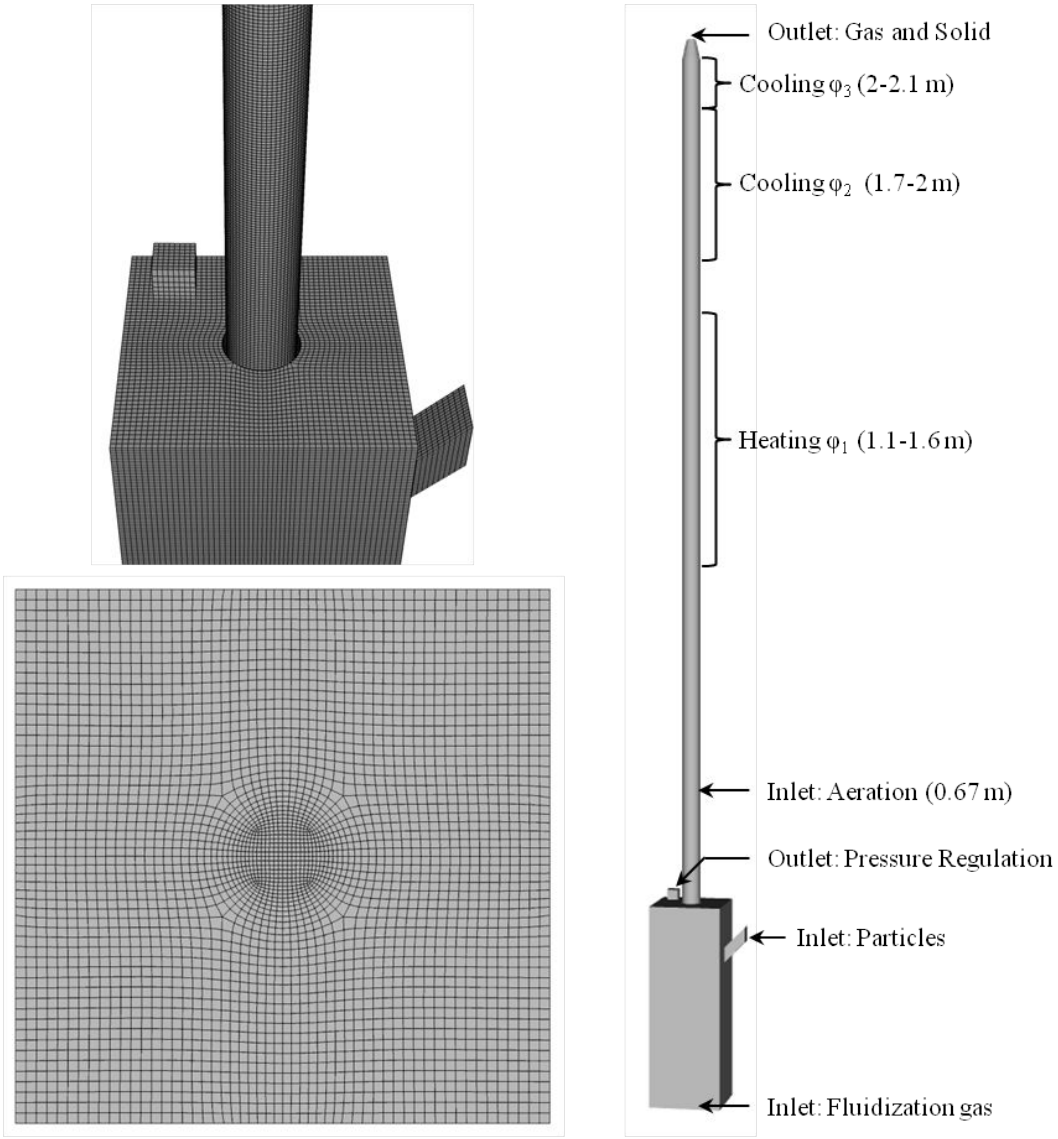

Figure 3.1: 3D Mesh.

while considering perfectly spherical particles. Another option previously considered during ambient temeprature simulations would have been to introduce a shape factor.

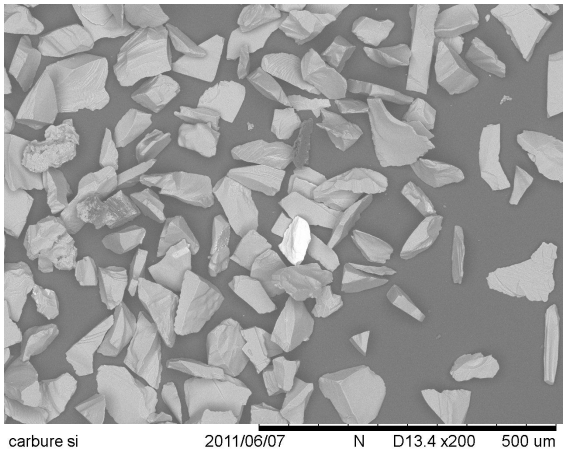

Figure 3.2: SEM photograph of the SiC particles.

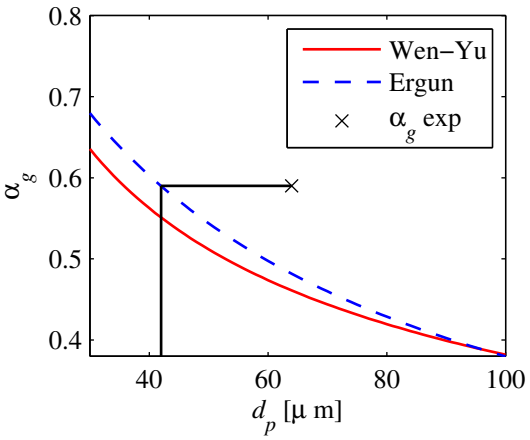

Figure 3.3: Voidage evolution with the particle size for a homogeneous bed expansion with $U_f = 2U_{mf}$.

The SiC particles' properties used in the simulations are indicated in Table 3.1. They were calculated from the data given in [8]. NEPTUNE_CFD equations are written with the enthalpy. It must be noted that the codes' heat transfer equations are written with the phases' specific enthalpies, therefore the variables used in these equations (specific heat capacity and temperature) must be calculated with the specific enthalpy. First, the particles' specific heat capacity $c_{p,p}$ was expressed as a polynomial of the temperature. Then it was integrated to determine the particle's specific enthalpy H_p as a function of the temperature, with the enthalpy reference (0 J/kg) set at 20 °C (=293.15 K). Finally, the temperature and the specific heat capacity were expressed as polynomials of the specific enthalpy in [J/kg].

3.2.2.2 Air

The air properties are indicated in Table 3.1. The density was calculated with the perfect gas law. The polynomials for the specific heat capacity, dynamic viscosity and laminar diffusion coefficient (ratio of the conductivity over the specific heat capacity) were determined from the data tables given in Perry's Chemical Engineers' Handbook [9]. The same treatment as for the particle properties was applied to obtain polynomials of the specific enthalpy in [J/kg].

3.2.3 Mathematical models

The 3D numerical simulations of the experimental DPS solar receiver were carried out using an Eulerian n-fluid modeling approach for turbulent and poly-dispersed fluid-particle flows, which is developed and implemented by the Fluid Mechanics Institute of Toulouse (in French: Institut de Mécanique des Fluides de Toulouse - IMFT) in a specific version of

Table 3.1: Phases' properties

Properties	**Values/Equations**
	SiC particles
Diameter	$d_p = 40\ \mu$m
Density	$\rho_p = 3210\ \text{kg/m}^3$
Specific heat	$c_{p,p} = 8.564 \times 10^{-16} H_p^3 - 1.647 \times 10^{-9} H_p^2 + 1.39 \times 10^{-3} H_p + 717.5$ (3.1) in $\left[\text{J.kg}^{-1}\text{.K}^{-1}\right]$
Temperature	$T_p = 4.01 \times 10^{-16} H_p^3 - 7.35 \times 10^{-10} H_p^2 + 1.33 \times 10^{-3} H_p + 294.2$ (3.2) in [K]
	Air
Density	$\rho_g = \frac{P}{rT_g}$ (3.3) in $\left[\text{kg/m}^3\right]$
Specific heat	$c_{p,g} = -1.346 \times 10^{-11} H_g^2 + 1.793 \times 10^{-4} H_g + 1003$ (3.4) in $\left[\text{J.kg}^{-1}\text{.K}^{-1}\right]$
Temperature	$T_g = -7.457 \times 10^{-11} H_g^2 + 9.931 \times 10^{-4} H_g + 293.3$ (3.5) in [K]
Dynamic viscosity	$\mu_g(T) = \mu_r \left(\frac{T_g}{T_r}\right)^m \frac{T_r+B}{T_g+B}$ (3.6) in [Pa.s] with $\mu_r = 1.716 \times 10^{-5}$ Pa.s, $T_r = 273.15$ K, $m = 1.54$, $B = 110.4$ K
Laminar diffusion coefficient	$LDC = -1.877 \times 10^{-17} H_g^2 + 5.878 \times 10^{-11} H_g + 2.631 \times 10^{-5}$ (3.7) in $\left[\text{kg.m}^{-1}\text{.s}^{-1}\right]$

the NEPTUNE_CFD code. This multiphase flow software uses the finite-volume method, with unstructured meshes, to run parallel calculations [10]. It uses a predictive-corrective method for the equations resolution [11]. It was developed by the consortium Commission for Atomic Energy (in French: Commissariat à l'Énergie Atomique - CEA), Électricité de France (EDF), Radioprotection and Nuclear Safety Institute (in French: Institut de Radioprotection et de Sûreté Nucléaire - IRSN) and AREVA in the frame of the NEPTUNE project.

The proposed modeling uses a hybrid approach [12], to establish the particles' momentum equations from the joint fluid-particle probability density functions. Separate mean transport equations (mass, momentum and fluctuant kinetic energy) are solved for each phase and coupled through inter-phase transfer terms. The transport equations are derived by phase ensemble averaging weighted by the phases' volume fraction and by using kinetic theory of granular flows supplemented by fluid and turbulence effects for the dispersed phase. The drag model used is the Wen and Yu model limited by Ergun equation in the zones of low voidage [13]. The kinetic theory for granular media describes the collisional part of the stress sensor [14]. A frictional model was added to account for the long period interactions in the flow very dense zones [15]. For the continuous gaseous phase, no turbulence model is considered. For the dispersed phase, a transport equation is solved on the particle fluctuating kinetic energy q_p^2.

In this model, the DPS was heated by a heat flux density imposed at the wall. The wall itself was not simulated which means that there was neither a wall temperature nor a wall-to-DPS heat transfer coefficient. This approach was chosen to reproduce the wall-to-DPS heat flux measured during the experiments that includes the radiation contribution. It was preferred to the imposed wall temperature approach because the wall heat transfer models are highly dependent on the thermal boundary layer condition imposed. Therefore, using these models would not have ensured the right value of wall-to-DPS heat flux. On the opposite, by using a heat flux density at the boundary, the wall is not simulated and, logically, no wall heat transfer model is needed. The heat exchanged by contact during the interparticle collisions was neglected. Therefore, the heat exchange modes in the suspension were: the convection/diffusion heat transfer between the gaseous phase and the particles, and the radiative heat transfer between particles. The radiation between the particles in the bed was assumed to take place in the frame of the Rosseland approximation through a diffusion mechanism. The radiative flux was taken proportional to the temperature gradient [16]. Since the wall is not simulated, the radiative transfer between wall and particles is included in the heat flux density boundary condition. Finally, the heat distribution was determined through both phases' enthalpy transport equations.

The models' equations are indicated in Annex: Equations in NEPTUNE_CFD.

3.2.4 Boundary conditions

3.2.4.1 Flow conditions

The geometry comprised 3 inlet boundaries:

- The fluidization grid where the air was injected at a constant mass flow rate. The fluidization air mass flow rate was 0.483 kg/h. The corresponding air superficial velocity was close to 4 U_{mf}. This boundary was seen as a wall by the solid phase. The injected air specific enthalpy corresponded to the DiFB temperature.

- The lateral solid injection where the solid mass flow rate was imposed with an 0.5 particle volume fraction. The imposed air flow rate was 5.2 $\times 10^{-9}$ kg/s. The enthalpies of both phases were calculated to correspond to the measured DiFB temperature (as was mentionned in Chapter 2, the gas and solid temperatures are equal in dense fluidized beds as demonstrated by Baeyens and Goossens [17]).
- The aeration injection, 0.57 m above the tube inlet, where an air flow was injected at a constant mass flow rate. The aeration flow rate was varied to have the same aeration superficial mass flow rate (mass flux) in the tube as in the experiments. The aeration air enthalpy corresponded to 100 °C. This temperature was arbitrarily chosen because it was not measured. The only certainty about the aeration air temperature was that it was comprised between the ambient air temperature and the DiFB temperature since the air pipe passed inside the DiFB insulation. This temperature had a negligible impact since the aeration air heat capacity was extremely low compared to that of the DPS circulating inside the tube.

The geometry had 2 free outlets: one on the DiFB ceiling, through which only air passed (the passing solid fraction was negligible) and the other one at the top of the tube. A pressure loss was imposed on the DiFB outlet to regulate the freeboard pressure rather than imposing pressure or flow rate condition. This choice was made to reproduce to the behavior of the regulation valve used in the experiments. The desired solid flux through the tube was obtained by adjusting the pressure loss coefficient, which is similar to changing the valve's setting.

The reference pressure for the inlet and outlets was the atmospheric pressure at 101325 Pa.

The wall boundary condition was a no-slip condition [18] for both gas and particles. It gave results closer to the cold mock-up experiments than the friction condition and the slip condition that were also tested with cold simulations.

3.2.4.2 Heat conditions

A uniform heat flux density was imposed at the tube wall. On this point, there was a significant difference between experiments and simulations. Indeed, during the experiments, the tube had one side directly exposed to the concentrated solar flux, whereas the opposite side only received the radiation reflected and emitted by the cavity. The approximation of uniform heat flux was used due to the lack of another option, since the reflected and re-emitted fluxes coming from the cavity were not measured. Due to the change in tube diameter (0.036 m inside diameter in solar experiments and 0.034 m in simulations), the heat transferred to the DPS was adapted to keep the same temperature increase for solid flow rates that varied since the solid flux was kept constant.

The ratio of the simulated solid flow rate over the experimental solid flow rate was applied to the heat transferred. It corresponded to the ratio of the simulated tube section over the experimental tube section (square ratio of diameters). The heat flux density to be applied was calculated by dividing the heat by the heat exchange area. Finally, the heat flux densities ratio was equal to the diameters ratio since the heat exchange area was proportional to the diameter.

The heat flux density condition applied was varied along the tube height to be as close as possible to the solar experiments. From the tube inlet (0.1 m) to the cavity inlet (1.1 m), the experimental tube was insulated. Therefore, an adiabatic condition was applied. From the cavity inlet (1.1 m) to its outlet (1.6 m), the tube was exposed to concentrated solar radiation, so a positive heat flux density was applied (φ_1 in Figure 3.1). After the cavity, the tube passed through the cavity insulation. In this zone (1.6 m to 1.7 m) an adiabatic condition was imposed. Above 1.7 m, the tube was not insulated at all, which led to high heat losses. This was represented by a negative heat flux density with a higher loss from 1.7 m to 2 m (φ_2) and a lower one between 2 m and 2.1 m (φ_3) since the heat loss is higher when the temperature is higher.

The heat flux densities were estimated using the experimental DPS temperatures measured (cf. Chapter 2). The temperatures at the tube inlet in the DiFB and at the cavity outlet, at the tube center ($T_{p,iDiFB}$ and $T_{p,o,center}$) were used to determine the heat flux density received between 1.1 m and 1.6 m. These were the same temperatures that were used for the calculation of the heat transferred to the DPS in Chapter 2. $T_{p,o,center}$ and the temperature measured at 2 m ($T_{p,2m}$, not used in Chapter 2) were used to estimate the flux density of the heat loss between 1.7 m and 2 m. It must be noted that, at 2 m, the measured temperatures were the same in the tube center and close to the wall because there was no high flux density heating in this zone. Therefore the upward and downward particle fluxes were at the same temperature. $T_{p,2m}$ and the temperature in the Collector Fluidized Bed (ColFB) were used to determine the flux density of the heat loss between 2 m and 2.1 m.

As will be explained afterwards, the simulations overestimated the particle reflux. This led to the temperature at the cavity outlet being lower than that measured due to the overestimated mixing between the heated particles (in the cavity) and cooled particles (after the cavity). We decided to increase the heat flux in the cavity, with respect to the calculation explained in the previous paragraph, to have matching temperatures at the cavity outlet. The cooling heat flux was increased accordingly to maintain the temperature at the tube outlet.

The boundary conditions of all the simulated cases are given in Table 3.2 (medium solid flux-medium temperature case: Ref; high solid flux-medium temperature case: HQ; low solid flux-high temperature case: HT). F_p is the particle mass flow rate, F_f the fluidization air mass flow rate, F_A the aeration air mass flow rate, $T_{p,iDiFB}$ the DiFB temperature, $\varphi_{1/2/3}$ the wall heat flux densities from 1.1 m to 1.6 m, from 1.7 m to 2 m and from 2 m to 2.1 m, respectively (cf. Figure 3.1).

Table 3.2: Boundary conditions

Case	F_p [kg/h]	F_f [kg/h]	F_A [kg/h]	$T_{p,iDiFB}$ [K]	φ_1 [kW/m^2]	φ_2 [kW/m^2]	φ_3 [kW/m^2]
Ref	59.8	0.483	8.92×10^{-2}	575	128.9	120.9	20
HQ	147.4	0.483	8.92×10^{-2}	601	189.7	172.6	25
HT	32.8	0.483	1.78×10^{-1}	782	107.3	159.7	17

3.2.5 Simulation procedure

The simulations begined by a transitory period during which the pressure loss coefficient at the DiFB outlet and heat flux densities were adapted. They impact the solid flux going up the tube and the solid temperature. On the one hand, increasing the pressure loss coefficient, which corresponded to a valve closing, decreased the air flow rate passing through the regulation valve (outlet of the DiFB) and therefore increased the air flow through the tube. More air passing meant more solid carried up the tube and an increased solid flux. This solid flux modification, for given heat flux densities values, provoked a temperature modification. On the other hand, modifying the heat flux densities modified the temperature distribution along the tube height. Since the temperature affects the air density and velocity, the heat flux densities modifications also impacted the DPS density. The modification of the DPS density meant a hydrostatic pressure variation. Therefore, for a given pressure loss coefficient at the DiFB outlet, modifying the heat flux densities changed the repartition of the air flow between valve and tube, which affected the solid flux going up the tube. This shows that the influences of both the pressure loss coefficient and the heat flux densities on the temperature and the solid flux were intertwined. Therefore, the parameters' adjustment had to be done simultaneously for both, changing one, then correcting the other, to finally obtain the desired conditions that corresponded to the experimental cases.

The pressure loss coefficient was adapted so that the solid flow rate through the tube would be equal to that injected in the DiFB. Therefore, the total mass in the whole geometry remained constant. The heat flux densities were adjusted to reproduce the experimentally measured temperature distribution along the tube height. The transitory regime necessary duration was at least 200 s. The stable state was reached when both conditions were achieved. Since the DPS flow is unsteady, 150 s long time averages were done in order to obtain stable averaged values.

The calculations were conducted with 140 processors on CALMIP's supercalculator EOS. 1 s was simulated in 1.2 to 1.5 hour, which gives a totat computational time of approximately 200 hours. Close to 7×10^4 s were necessary to simulate the 350 s minimum duration for one case, sometimes more when the transitory regime was longer.

To illustrate the unsteady flow, Figure 3.4a shows an instantaneous solid velocity field in the tube, for the ref case, at a height comprised between 1.3 and 1.4 m, at 720 s after the beginning of the simulation. The tube vertical slice is colored by the magnitude of the velocity. It can be seen that the particles are going in some zones, down in some others, and that their velocities range from 0 to 0.5 m/s. Figure 3.4b illustrates the result obtained after a 150 s long time average. The average solid velocity is positive in the center and negative close to the wall. This phenomenon is the particle recirculation that was previously outlined in Chapter 2.

3.3 Comparison between simulations and experiments

3.3.1 Pressure drop

The first element of comparison between experiments and simulations must be the pressure drop through the suspension. If the simulations are not able to reproduce the measured

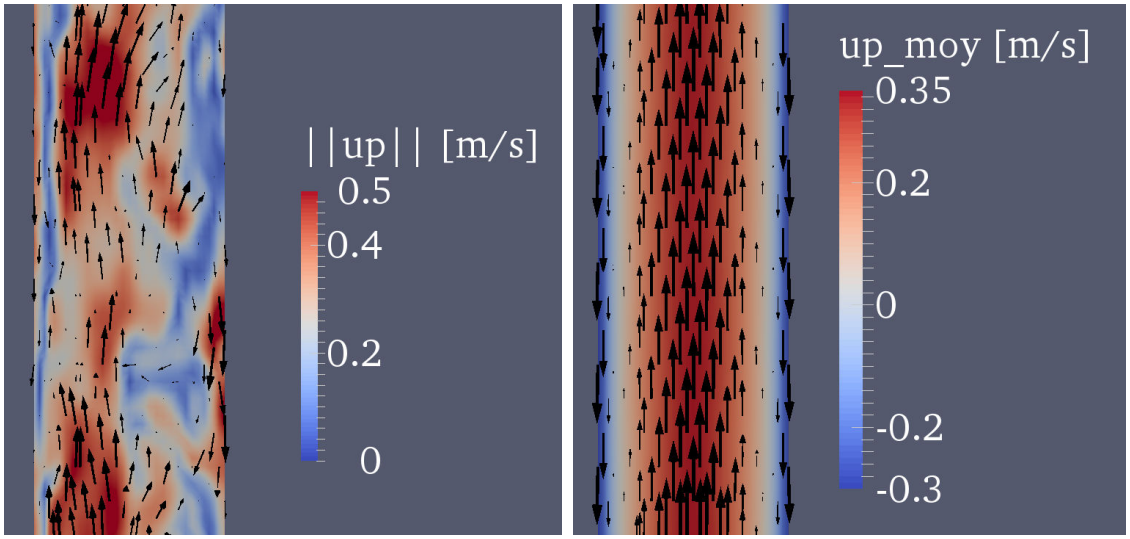

(a) Instantaneous. (b) Time averaged.

Figure 3.4: Solid velocity fields in the tube, for the ref case, at a height comprised between 1.3 and 1.4 m, at 720 s after the beginning of the simulation.

pressure drop, then none of the other numerical results can be validated. As explained in Subsection 3.2.2.1, the particle size was decreased to compensate for the model's voidage understimation that corresponds to a pressure drop overestimation. Thanks to this adaptation, the experimental and simulated pressure drops were identical for the case without heating on the cold mock-up (115 mbar/m) [19]. Therefore we have confidence that, at this level, the model is able to reproduce the experiments.

The measured and simulated pressure drops must be considered in the same conditions to be comparable. In particular, the aeration plays an essential role on the suspension voidage. Since the aeration position differs between the model and the experiments, the locations at which the pressure is considered must be adapted. In the experiments, the pressure drop was measured between a pressure sensor whose plug was set on the tube 0.2 m above the aeration (0.5 m above the tube inlet) and the tube's top at atmospheric pressure. The simulated pressure drop was considered between 0.2 m above the aeration and the tube's top. In the Ref and HQ cases, the simulated pressure drops were close to the measured ones, with a 4.6 % underestimation for the Ref case (8340 Pa/m instead of 8750 Pa/m obtained experimentally) and a 2.6% overestimation for the HQ case (9120 Pa/m instead of 8880 Pa/m obtained experimentally). The HT case was not satisfactorily reproduced with a pressure drop underestimation as high as 27 %(4510 Pa/m instead of 6180 Pa/m obtained experimentally). Table 3.3 below shows the compared linear pressure drops.

The linear pressure drops differences are due to the variation of the air density that impacts its velocity. The air velocity affects the DPS voidage that sets the DPS density, and the pressure drop is directly linked to the DPS density. The air density depends on the absolute pressure and on the temperature.

- Two parameters impact the absolute pressure: the tube height and the ambient pressure. The tube was 2.65 m high on the experimental receiver while it was 2.06 m high in the model's geometry that reproduces the dimensions of the cold mock-up.

Therefore, the hydrostatic pressure for a given vertical position differed between the experiments and the simulations. For the Ref and HT cases, the height difference (= 0.59 m) corresponds to an approximately 5000 Pa absolute pressure underestimation in the simulations. The absolute pressure underestimation is about 2500 Pa for the HT case that presents a lower linear pressure drop. The experimental solar receiver was tested at Odeillo, 1600 m above sea level, where the ambient pressure is around 84000 Pa. In the model, the ambient pressure corresponds to the pressure imposed at the outlets that was 101325 Pa. This parameter was not modified to remain in the same conditions than in the simulations without heating. Therefore the imposed ambient pressure led to an absolute pressure overestimation of about 17000 in the simulations. The effect of the tube height and that of the ambient pressure were opposed and resulted in a 12000 Pa total absolute pressure overestimation that increased the air density in simulations.

- On the opposite, when the DPS was heated, the voidage increased because of the air expansion with temperature. As a consequence, the pressure drops were lower when the DPS was heated than when it was at ambient temperature. As will be seen in the next subsection, the model overestimated the temperature in the lower part of the tube. Therefore the air density was underestimated.

To summarize, the effect on the air density of the absolute pressure overestimation and that of the temperature overestimation were opposed. In the Ref and HQ cases, they compensated each other and the linear pressure drop $\Delta P/L$ was reproduced with a difference lower than 5 %. As will be showed in the next subsection, the lower the solid flux, the higher the temperature overestimation. Therefore, in the HQ case with the highest solid flux, the temperature was less overestimated by the simulation than in the other cases and the resulting linear pressure was higher than the experimental one by 2.6 %. In the Ref case, the numerical temperature overestimation was higher and the linear pressure drop was underestimated by 4.6 %. In the HT case with the lowest solid flux, the temperature was greatly overestimated by the simulation and the resulting linear pressure drop was lower than in the experiment by 27 %.

The experimental and simulated linear pressure drops of all cases are shown in Table 3.3.

3.3.2 Temperature

The second element of comparison between simulations and experiments is the repartition of temperature along the tube height. The inlet temperature was imposed (the initial DiFB temperature, the fluidization air temperature and the solid feeding temperature are all equal). The temperature at 2 m was the same as long as the solid flux was reproduced, due to the heat flux condition that was calculated to respect the enthalpy balance between inlet and outlet. As explained in 3.2.4.1, the solid flux through the tube was controlled by adjusting the pressure loss coefficient at the DiFB outlet. This iterative process allowed reaching the desired solid flux with a difference between simulations and experiments inferior to 2 %. The first simulations showed that, while the solid flux was accurately reproduced and the outlet temperature respected. The temperature at the cavity inlet was overestimated and that at the cavity outlet was underestimated. This was due to the particle recirculation being overestimated. As a consequence, the particles heated in the cavity and going down were heating the DPS before the cavity more than what

was observed experimentally, and the particles cooled after the cavity were cooling those at the cavity outlet. To correct this phenomenon, the solid volume fraction at which the frictional viscosity model is triggered, initially set at 0.5, was lowered to the solid volume fraction at the minimum fluidization (0.43), which remained in the model's validity range. The recirculation decreased by about 10 % but it was not sufficient. It would have been possible to further lower the trigger value but we decided not to get out of the model's validity range. Another available option would have been to increase the particle size but this would also have modified the pressure drop. Consequently, we chose to keep working with the overestimated recirculation.

To obtain the right temperatures at the cavity outlet, the heat flux in the cavity was increased, as well as the heat loss between 1.7 m and 2 m, while the mass flow rate was maintained, to keep the right temperature after the cavity, at 2 m. This increase is partly justified because the method used to calculate the heat flux transferred did not account for the recirculation at the cavity outlet. Therefore, the heat flux absorbed by the particles in the cavity was slightly underestimated since the outlet temperature considered - $T_{p,o,center}$ - was affected by the downward particle flow cooled above the cavity due to the tube not being insulated. However, the increased heat flux was higher than the actual, unknown heat flux, otherwise the temperature at the cavity outlet would still have been underestimated due to the recirculation overestimation. The heat flux densities previously indicated in Table 3.2 correspond to the increased values.

Figure 3.5 presents the simulated temperature profiles at the center of the tube and 5 mm from the tube wall along the tube height and the experimental temperatures for the three cases. The HT case did not reach the right temperature at the cavity outlet even though the heat flux in the cavity and heat loss between 1.7 m and 2 m was tripled. As was said, this is due to the recirculation being the strongest since the solid flux is the lowest. For the Ref case, the heat flux was increased by 44.5 % with respect to the value calculated by enthalpy balance, while the mass flow rate was maintained. The experimental temperature at the cavity outlet is 842 K whereas the simulated temperature is 820 K. But the maximum simulated temperature at the tube center reaches 842 K, 0.15 m before the cavity outlet. For the HQ case, the heat flux was increased by 16.3 %. It allowed reaching the right temperature at the cavity outlet at the tube center. The simulated temperature was 800 K and the experimental one was 804 K. The 4 K difference was inferior to the measure accuracy. It also is the the case that less overestimates the temperature at the cavity inlet because the recirculation was the least overestimated due to the solid flux being the highest. The temperatures at 2 m are well reproduced by the simulations, with a small underestimation in the Ref case.

Figure 3.6 plots the simulated radial temperature profiles and the experimental temperatures for the Ref case and the HT case. Once again, it can be seen that the temperature at the cavity inlet (1.1 m) is greatly overestimated due to the exagerated recirculation. In the Ref case, the difference is 157 K (25 %) at the center and 170 K (27%) 5 mm from the wall. In the HQ case, the difference is 53 K (8%) at the center and 73 K (12 %) 5 mm from the wall. The temperature at the cavity outlet (1.6 m) at the center is well reproduced in the HQ case, with a difference inferior to the measure accuracy, and underestimated by 23 K (3 %) in the Ref case. The profile's shape varies along the tube height. At the inlet of the cavity, the DPS is hotter 5 mm from the wall than in the center because the downward flux comes from the heated zone. On the contrary, at the cavity outlet, it is hotter at the center because the upward flux comes from the heated zone while the downward flux comes from the zone with heat losses. This experimental observation is reproduced but

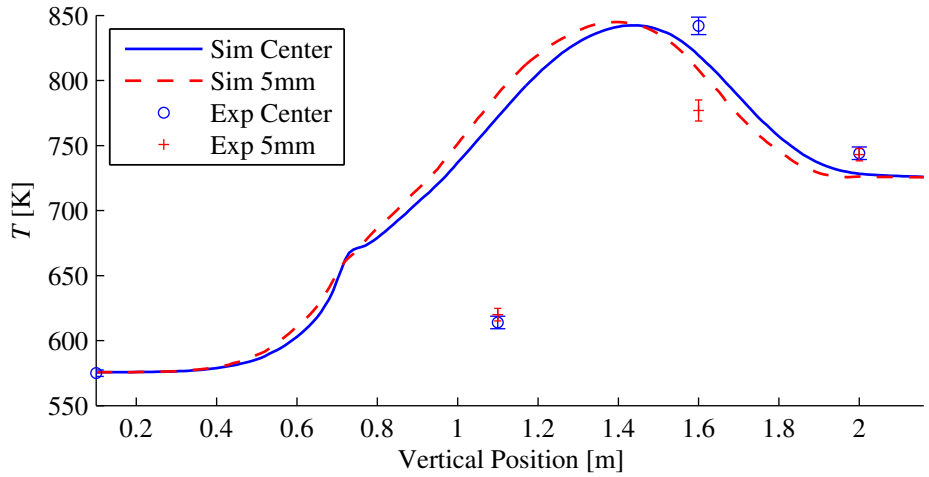

(a) Ref case.

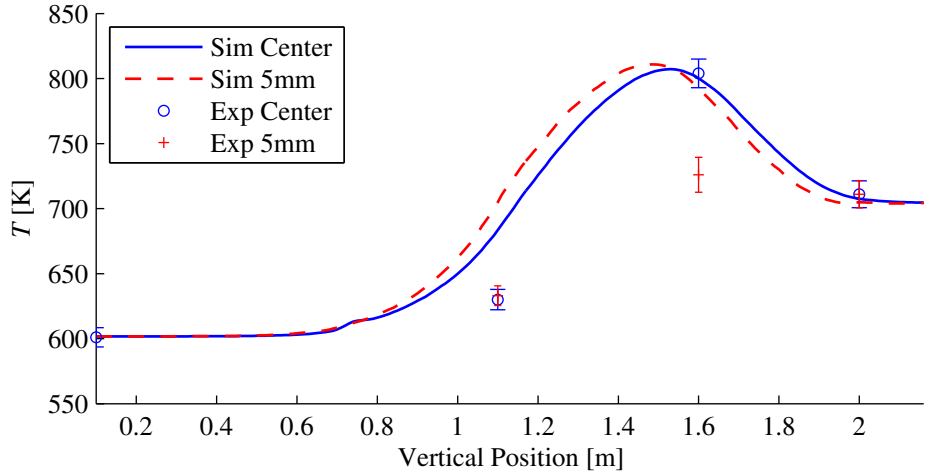

(b) HQ case.

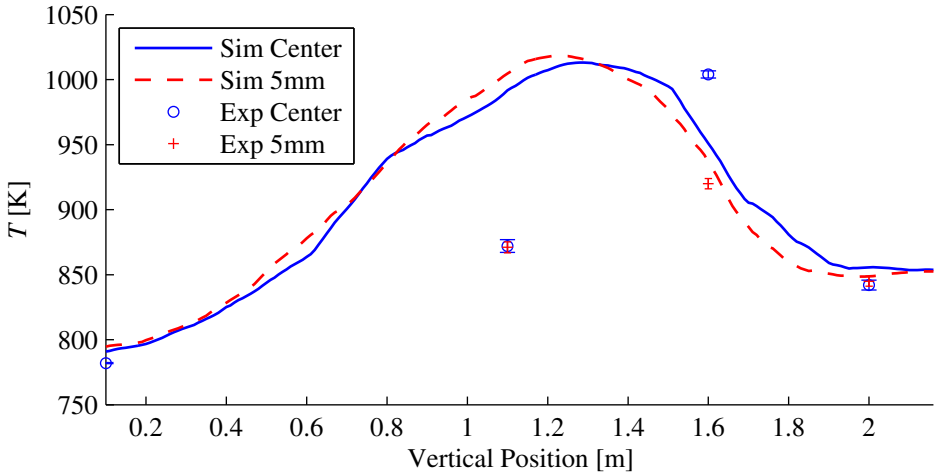

(c) HT case.

Figure 3.5: Simulated axial temperature profiles and experimental temperatures at the center of the tube and 5 mm from the tube wall.

the simulations overestimates the difference between the temperature at tube center and 5 mm from the wall at the cavity inlet and underestimates it at the cavity outlet. These differences are once again due to the overestimated recirculation. The upward flux at the center at the inlet and downward flux close to the wall at the oulet are heated too much by the mixing with the overestimated hot fluxes coming from the heated zone. At 2 m, the temperature is the same at the center and 5 mm from the wall for both experiments and simulations, in both cases, because the heat flux density transferred at the wall (heat loss) is lower in this region.

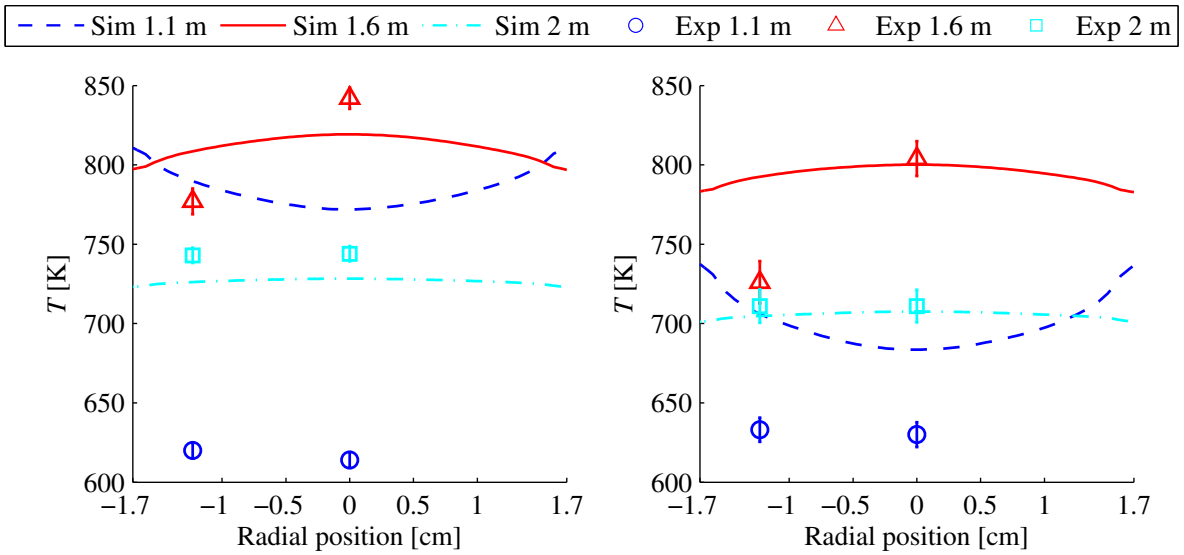

(a) Ref case.

(b) HQ case.

Figure 3.6: Simulated radial temperature profiles and experimental temperatures.

Table 3.3 presents the results of the simulations alongside the experimental values. The solid flux, the linear pressure drop and the temperatures are indicated. The errors are given.

Table 3.3: Parameters comparison between experiments and simulations

Parameter	**Ref case**			**HQ case**			**HT case**		
	Exp	**Sim**	**Error**	**Exp**	**Sim**	**Error**	**Exp**	**Sim**	**Error**
G_p [kg.m^{-2}.s^{-1}]	18.3	18	- 1.8 %	45.1	44.7	- 0.7 %	10	10.1	1 %
Linear pressure drop [Pa/m]	8750	8340	- 4.6 %	8880	9120	2.6 %	6180	4510	- 27 %
$T_{p,i,center}$ [K]	614	772	26 %	630	684	9 %	872	992	14 %
$T_{p,o,center}$ [K]	842	819	- 2.7 %	802	804	0.2 %	1004	951	- 5.3 %
$T_{p,2m,center}$ [K]	743	728	- 2 %	711	708	- 0.4 %	842	856	1.7 %

3.3.3 Model validation

As was shown in this section, discrenpacies remained between the numerical and experimental results. In spite of our efforts to correct the recirculation, it was still overestimated. The highly poly-dispersed distribution of non-spherical particles prevented the calculation from reproducing both the right linear pressure drop and the right temperature ditribution. The HT case numerical results were so different from the experimental ones, for both temperature and pressure loss, that it was discarded for the rest of the study. The Ref case simulation differed from the experiment at the temperature level but it reproduced the linear pressure drop with a difference lower than 5 %. The HQ case simulation was the most satisfactory thanks to the recirculation having less impact at high solid flux. It matched the experimental results at the linear pressure drop level with a difference of only 2.6 % and well reproduced the temperature at the cavity outlet while overestimating it by less than 10 % at the cavity inlet at the tube center. Consequently, the Ref and HQ cases simulations were usable to analyze the DPS hydrodynamics and the heat transfer mechanisms.

3.4 Numerical results

3.4.1 Gas vertical velocity

Figure 3.7 presents the gas vertical velocity u_g, z radial profiles for the Ref and HQ cases at 4 positions along the tube height: 0.5 m, 1.1 m, 1.6 m and 2 m. The first element to notice is that the velocity is positive in the center and negative at the wall. This is due to the particle recirculation. The velocity is lower before the aeration than it is after because the air mass flow rate is increased by the aeration. Moreover, we can see that the velocity is lower at 1.1 than above, at 1.6 m and 2 m due to the air density decreasing when the pressure decreases. The velocity increases in spite of the pressure decrease between 1.6 m and 2 m because of the temperature that is higher at 1.6 m, making the air density lower.

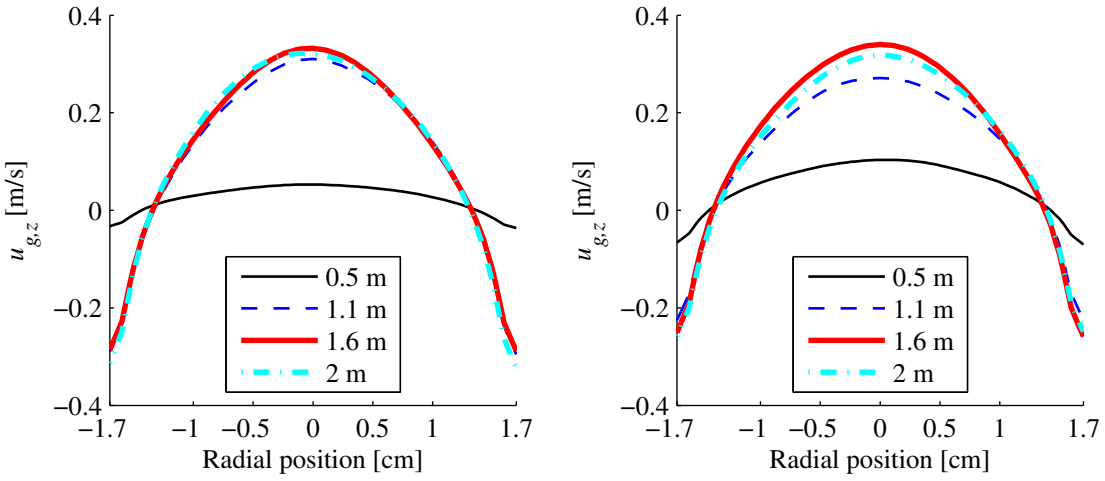

(a) Ref case.

(b) HQ case.

Figure 3.7: Gas vertical velocity radial profiles.

3.4.2 Solid Volume fraction α_p and bubbles influence

Figure 3.8 presents the solid volume fraction α_p radial profiles for the Ref and HQ cases at 4 positions along the tube height: 0.5 m, 1.1 m, 1.6 m and 2 m. It can be seen that α_p is higher at 0.5 m, below the aeration located at 0.67 m. The aeration purpose was to help the solid circulation, and α_p was lowered as a consequence of the air flow increase. This effect is well reproduced by the simulations. The profiles show that the volume fraction is higher close to the tube wall than at the center. This difference increases after the aeration. This is due to the bubbles circulating in the tube cntral zone. At 2 m, α_p is equal to 0.23 and 0.26 at the tube center for the Ref case and HQ case respecively, and it is 38 % higher at the wall. We can also observe that it is higher at 1.1 m than above because the pressure is higher and, therefore the air velocity is lower. In the HQ case the difference between 1.1 m and above is increased because the temperature at this position is lower, which combines with the higher pressure to decrease the air density and increase its velocity (see Figure 3.5).

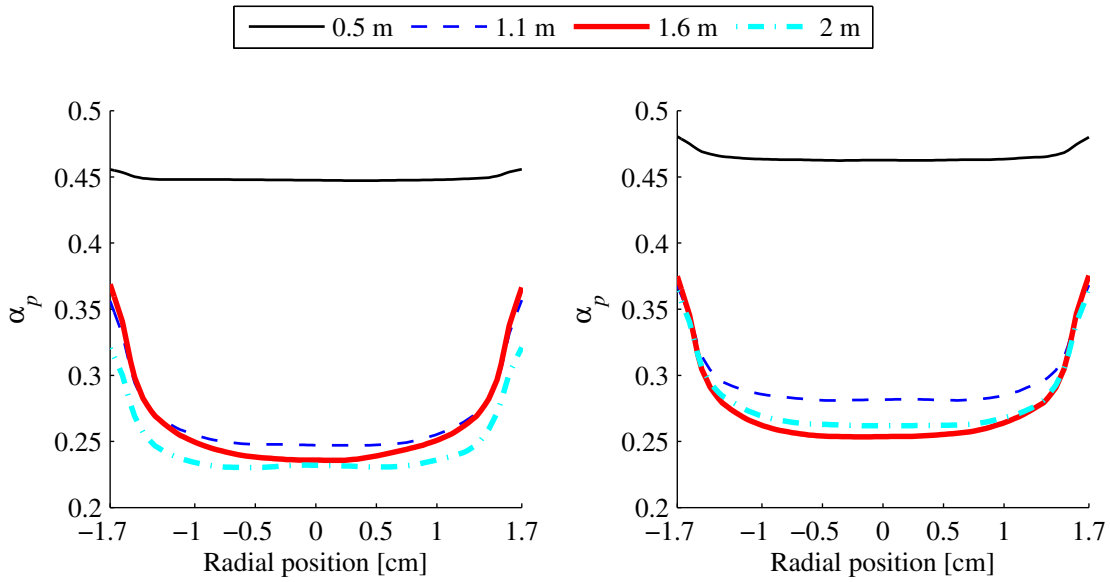

(a) Ref case.

(b) HQ case.

Figure 3.8: Solid volume fraction radial profiles.

Figure 3.9 presents the solid volume fraction time-variance radial profiles for the Ref and HQ cases. This parameter characterizes the gas bubbles in the suspension that provoke great variations of the solid volume fraction. The time-variance of α_p is much lower at 0.5 m than above due to the aeration (at 0.67 m) that increases the air flow rate and therefore increases the bubble size and frequency. The variance is the highest at 1.6 m, same as the air velocity. This indicates a direct link between the air velocity and the bubbles size and frequency. Above the aeration, the time-variance of α_p increases from the tube center to 3 mm from the wall and then decreases to reach its minimum at the wall. This profile shape can be explained by the combination of the bubbles' passage and of the α_p profile shape. There is practically no solid in the bubbles. As a consequence, their passage creates lower variations of α_p in the zones were it is lower than in the zones of higher solid volume fraction. Therefore, from the center to 3 mm from the wall, the time-variance of α_p increases as does α_p. The bubbles circulate in the tube center. Hence, in the zone close

to the wall, their influence decreases and the time-variance of α_p decreases.

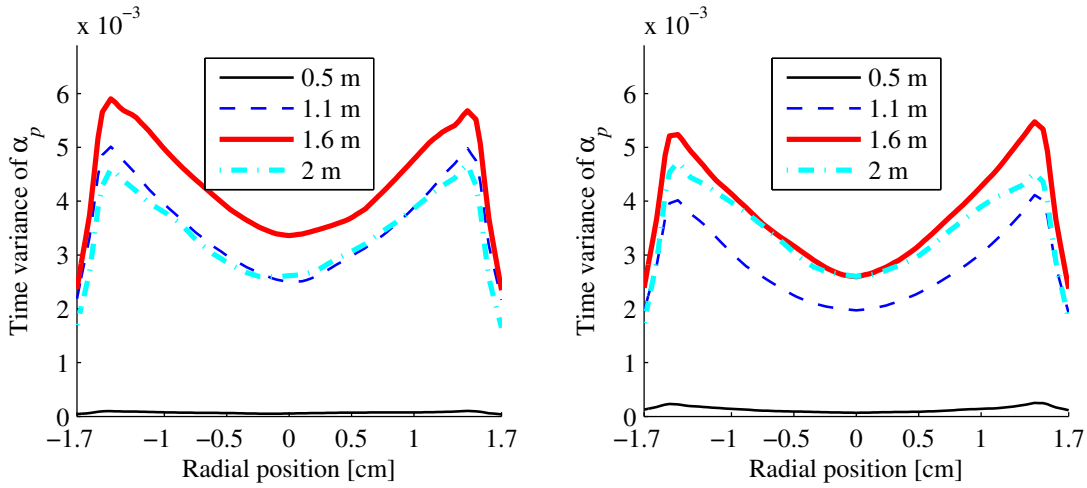

(a) Ref case. (b) HQ case.

Figure 3.9: Solid volume fraction time-variance radial profiles.

3.4.3 Solid flux

Figure 3.10 presents the solid flux G_p radial profiles for the Ref and HQ cases. The recirculation is clearly visible with G_p being positive in the center and negative close to the wall. The recirculation ratio, defined as the ratio of ascending solid flux over descending solid flux, is much higher above the aeration where the air flow rate is increased than below. It is the highest at 1.6 m where the air velocity is the highest due to the temperature influence. This is easier to see for the HQ case. Therefore it can be said that there is a direct link between the air velocity and the solid recirculation. For a given solid flux, the higher the air velocity, the higher the recirculation. At 1.6 m, the recirculation ratio is 83 % in the Ref case and 64 % in the HQ case. It is reminded that these values are overestimated as showed by the comparison between experimental and simulationed temperatures. However, it is confirmed that, as was deduced from the temperatures comparison, the higher the solid flux, the lower the recirculation. Moreover we can see that the recicrulation zone (zone with a negative solid mass flux) is 4 mm thick for the entire tube height. Therefore, the solid mass flux close to the wall should remain constant even for an industrial facility with higher tubes.

3.4.4 Particle velocity time-variance and random kinetic energy

Figure 3.11 presents the particle vertical velocity time-variance radial profiles, and Figure 3.12 those of the particle radial velocity time-variance, for the Ref and HQ cases. The variance is higher above the aeration than below. The profiles have a shape similar to those of the solid volume fraction time-variance with higher values in the center than at the wall. It was explained that the α_p time-variance profiles' shape is caused by the bubbles' passing. Therefore, it can be said the bubbles are also resposible for the variations of the solid vertical and radial velocity. The $u_{p,r}$ time-variance fall occurs closer to the tube center, and the values at the wall are lower relatively to the values at the center. This

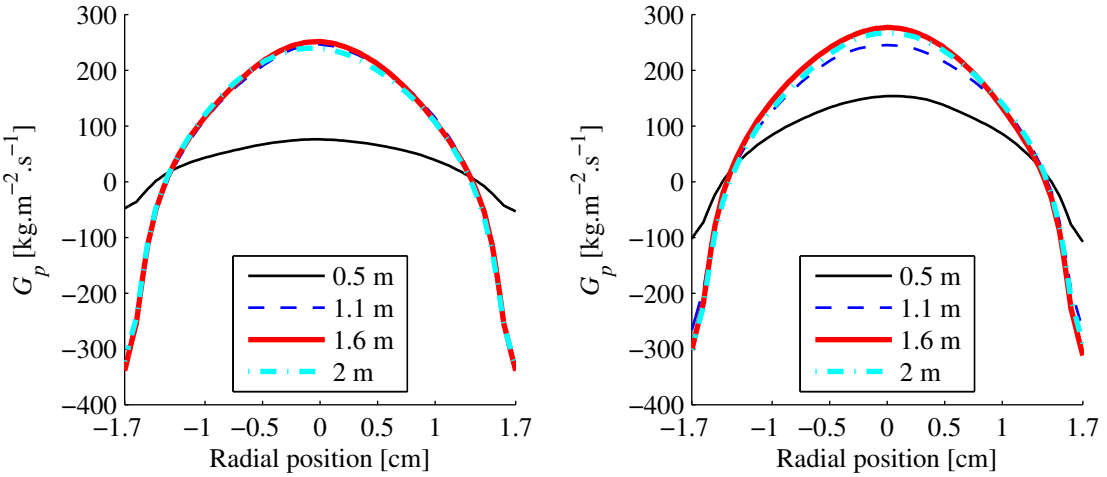

(a) Ref case. (b) HQ case.

Figure 3.10: Solid flux radial profiles.

is due to the wall that hinders the horizontal movement of the particles. For both $u_{p,z}$ and $u_{p,r}$ time-variances, it is observed that they are higher at 1.1 m than at 2 m in the Ref case, and lower in the HQ case. Moreover, the highest values are reached at 1.6 m and the difference between the values at 1.1 m and 1.6 m are greater in the HQ case than in the Ref case. This is linked to the temperature overestimation at the cavity inlet (1.1 m) which is greater in the Ref case than in the HQ case. For the Ref case, the temperature is higher at 1.1 m than at 2 m, and the temperature difference between 1.1 m and 1.6 m is lower than for the HQ case (see Figures 3.5 and 3.6). When the temperature rises, the air velocity increases, the bubbles circulate faster and the axial and radial particle mixings intensify.

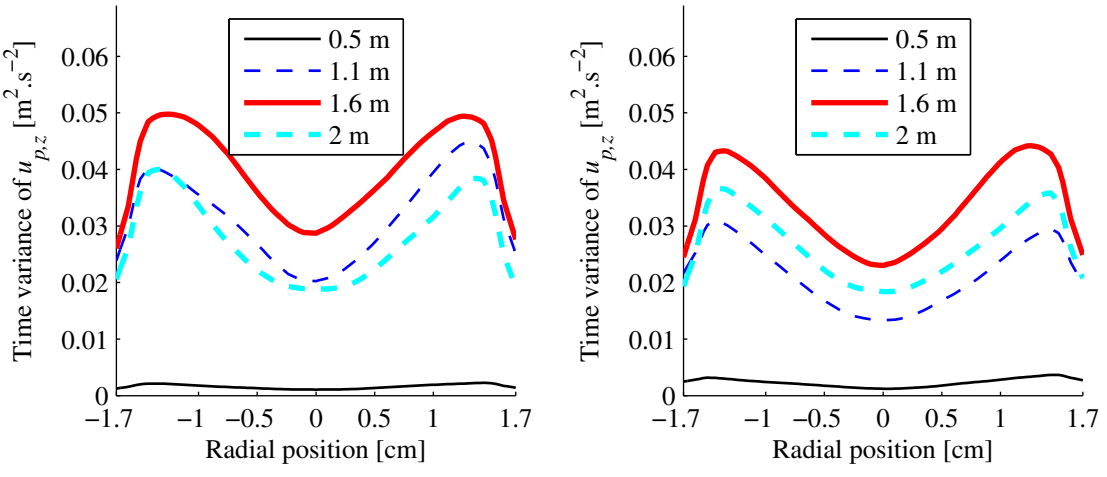

(a) Ref case. (b) HQ case.

Figure 3.11: Solid vertical velocity variance radial profiles.

The random kinetic energy of particles q_p^2 $(= \frac{1}{2}\left\langle u'_{p,i}u'_{p,i}\right\rangle)$ represents the particle agitation at the microscopic level. Figure 3.13 presents the q_p^2 radial profiles for the Ref and HQ cases. It shows that the agitation is higher close to the wall than in the central zone of

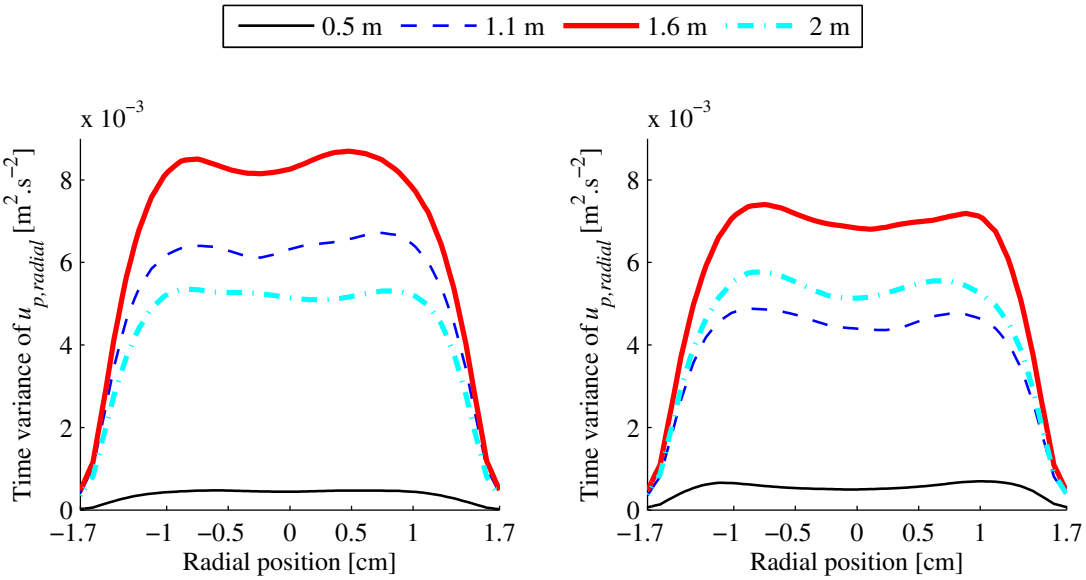

(a) Ref case. (b) HQ case.

Figure 3.12: Solid radial velocity variance radial profiles.

the tube. The heat transfer inside the suspension is due to two mechanisms: the particle diffusion linked to q_p^2, and the collective particle movement related to $u'^2_{p,r}$. $u'^2_{p,r}$ is more than 10 times higher than q_p^2 at the wall and 10^4 times higher in the central zone. Therefore, for the DPS flow in tube, the heat transfer from the wall to the center is due to the particles' collective movement.

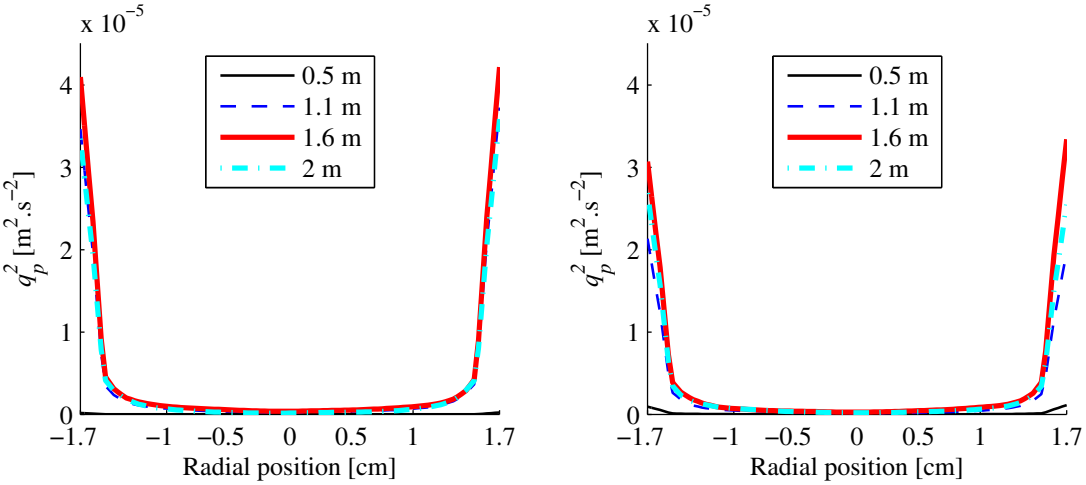

(a) Ref case. (b) HQ case.

Figure 3.13: Random kinetic energy of particles radial profiles.

3.5 Conclusion

The 3D numerical study of the experimental DPS solar receiver was realized with the NEPTUNE_CFD code. The simulations' geometry comprised the Dispenser Fluidized Bed (DiFB) and the vertical tube. Its dimensions corresponded to those of the cold mock-up tested at the LGC so that the simulations would be realized in the same conditions as the previously done simulations at ambient temperature. The tube diameter was 0.034 m in the model instead of 0.036 m for the experimental solar receiver and the its lenghth was 2.06 m instead of 2.64 m. The solid flux and aeration flux were kept and the tube wall-to-DPS heat flux was adapted to maintain the DPS temperature increase through the tube. During the experiments, the heat flux density was higher at the front where the concentrated solar radiation directly hit the tube than at the back where there was only radiation reflected and re-emitted by the cavity, but the distribution could not be precisely measured. Therefore, a uniform over the tube circumference heat flux density condition was applied in the model. The highly poly-dispersed distribution of non-spherical particles could not be precisely modeled. Instead, a uniform particle diameter was imposed. The boundary conditions were defined to reproduce three experimental cases: a case with medium solid flux and medium temperature (Ref case), a case with high solid and medium temperature (HQ case), and a case with low solid flux and high temperature (HT case). After a transitory period during which the simulation parameters were varied, a stable state was reached for which the solid flux and temperature remained constant. Time averages were done over 150 s to obtain stable averaged values.

The model was able to reproduce the experimental results to some extent but differences remained. The particle size had to be adapted to obtain the right pressure drop at ambient temperature. The particle diameter was set to 40 μm, instead of the actual 64 μm average Sauter diameter. The modification of the particle size affected the hydrodynamics of the DPS flow. The particle recirculation that had been noticed during the experiments was reproduced but the comparison between experimental and simulated temperatures showed that it was overestimated. This overestimation could be reduced but it remained significant. As a consequence, we chose to increase the imposed wall heat flux densities, in comparison to the the values determined by enthalpy balance, to obtain the right temperature in the tube at a 1.6 m height, which corresponded to the outlet of the irradiated cavity. The HT case was discarded because the simulation greatly diverged from the experiment at both the pressure drop and temperature level. In the Ref and HQ cases, the linear pressure drop and the temperature at 1.6 m could be reproduced with errors below 5 %, while the temperature at 1.1 m (cavity inlet) remained overestimated.

The numerical results put in evidence the aeration effects. The air velocity increase induced by increasing the air mass flow rate provoked a bubbles' influence increase. Moreover, the pressure decrease going up the tube provoked an air velocity increase that emphasized the bubbles' effects. The temperature also affected the air velocity and made the bubbles effects stronger where the temperature was higher.

The solid volume fraction inside the tube was found to be higher close to the wall than at the tube center, and it decreased with the tube height and the temperature. It is directly linked with the air velocity: the higher the air velocity, the lower the solid flux. Moreover, the solid volume fraction variance was higher in the tube central zone than close to the wall. It was due to the bubbles circulating in the central zone.

The solid flux radial profiles clearly showed the recirculation with positive values in the tube central zone and negative values close to the wall. For a given total solid flux on the

tube section, it was noticed that the higher the air velocity, the higher the recirculation. Moreover, the higher the total solid flux, the lower the recirculation. At 1.6 m, the ratio of descending solid flux over ascending solid flux was as high as 83 % in the Ref case and 64 % in the HQ case. These values were overestimated but it still shows that the particle recirculation is significant for the DPS flow in tube.

The particle vertical and radial velocities time-variances were found to be provoked by the bubbles and directly related to the air velocity. The higher the air velocity, the higher the bubble's influence and the higher the time-variances. The particle radial velocity variance represents the particles' collective movement while the random kinetic energy of particles characterizes the particle diffusion at the microscopic level. The simulations showed that the particle radial velocity time-variance was far greater than the random kinetic energy of particles, which indicates that the heat transfer from the tube wall to the tube center is due to the particles' collective movement.

There are several possibilities that could be explored to improve the fit between simulations and experiments. The mesh could be further refined in the radial direction which could lead to a recirculation zone thickness different from that obtained with the current mesh. The particle size distribution could be modeled as well as the non-sphericity. Lastly, the inhomogeneous heat flux could be accounted for by coupling NEPTUNE_CFD with the SYRTHES code that would allow computing the heat flux through the tube wall.

The model at ambient temeprature is currently being compared to positron emission particle tracking measurements by the CSP2 projects partners. This will tell us at which levels the model without heating is valid and what are the elements that must be improved. Future solar experiments will be conducted with different particles. In particular, Cristobalite particles are very interesting because, apart from their low cost and good thermal properties, they have a high sphericity factor and a narrow diameter distribution that will make them much easier to simulate than the SiC particles of this study.

3.6 Nomenclature

Abreviations

CFD	Computational Fluid Dynamics
ColFB	Collector fluidized bed
DiFB	Dispenser fluidized bed
DPS	Dense Particle Suspension
HTF	Heat Transfer Fluid
IMFT	Institut de Mécanique des Fluides de Toulouse
PEPT	Positron Emission Particle Tracking
SEM	Scanning Electron Microscopy
UBFB	Upward Bubbling Fluidized Bed

Latin symbols

B	Sutherland's constant for air
c_p	Specific heat capacity at constant pressure [J/kg/K]
d_p	Particle diameter [μm]
F	Mass flow rate[kg/s]
G	Mass flux [kg.m^{-2}.s^{-1}]
H	Specific enthalpy [J.kg^{-1}]
LDC	Laminar diffucion coefficient [kg.m^{-1}.s^{-1}]
m	Exponent in the air dynamic viscosity equation
q_p^2	Random kinetic energy of particles [m^2.s^{-2}]
r	Specific gas constant [J.kg^{-1}.K^{-1}]
T	Temperature [K]
t	Time [s]
U	Superficial velocity [m/s]
U_f	Fluidization velocity [m/s]
U_mf	Minimum fluidization velocity [m/s]
u	Velocity [m/s]
z	Vertical coordinate [m]

Greek symbols

α	Volume fraction
ε	Suspension voidage or void fraction
μ	Dynamic viscosity [Pa.s]
ρ	Density [kg/m^3]
φ	Heat flux density [W/m^2]

Subscripts, Superscripts

1/2/3	Refers to the zones where the wall heat flux density is applied
$2m$	Position 2 m above the fluidization plate
$center$	Thermocouple position at the tube center
g	Gas
$iDiFB$	Tube inlet in the dispenser fluidized bed
o	Outlet of the cavity
p	Particles

r	Reference
radial	Radial component
z	Vertical component

Bibliography

[1] B. Boissière. *Étude hydrodynamique et thermique d'un nouveau concept de récepteur solaire à suspensions denses gaz-particules (Hydrodynamic and thermal study of a new concept of solar receiver using dense gas-particle suspensions).* PhD thesis, Institut National Polytechnique de Toulouse (INP Toulouse), 2015.

[2] A. Abbasi, P.E. Ege, and H.I. de Lasa. CPFD simulation of a fast fluidized bed steam coal gasifier feeding section. *Chemical Engineering Journal*, 174(1):341–350., 2011.

[3] F. Fotovat, R. Ansart, M. Hemati, O. Simonin, and J. Chaouki. Sand-assisted fluidization of large cylindrical and spherical biomass particles: Experiments and simulation. *Chemical Engineering Science*, 126:543–559, 2015.

[4] J. Marti, A. Haselbacher, and A. Steinfeld. A numerical investigation of gas-particle suspensions as heat transfer media for high-temperature concentrated solar power. *International Journal of Heat and Mass Transfer*, 90:1056–1070, 2015.

[5] R.A. Reyes Urrutia, H. Benoit, M. Zambon, D. Gauthier, G. Flamant, and G. Mazza. Simulation of the behavior of a dense SiC particle suspension as an energy transporting vector using computational fluid dynamics (CFD). *Chemical Engineering Research and Design*, (accepted).

[6] C. Wen and Y. Yu. Mechanics of fluidization. *Chemical Engineering Progress Symposium Series*, 62:100–111, 1966.

[7] S. Ergun. Fluid flow through packed columns. *Chemical Engineering Progress*, 48, 1952.

[8] R.G. Munro. Material Properties of a Sintered alpha-SiC. *Journal of Physical and Chemical Reference Data*, 26:1195–1203, 1997.

[9] D.W. Green and R.H. Perry. *Perry's Chemical Engineers' Handbook.* McGraw-Hill Professional, 8^{th} edition, 2008. (Section 2, Thermodynamic Properties).

[10] H. Neau, P. Fede, J. Laviéville, and O. Simonin. High performance computing (HPC) for the fluidization of particle-laden reactive flows. *Proceedings of Fluidization XIV, Noordwijkerhout, The Netherlands*, 2013.

[11] N. Méchitoua, M. Boucker, J. Laviéville, S. Pigny, and G. Serre. An unstructured finite volume solver for two phase water/vapour flows based on an elliptic oriented fractional step method. *Proceedings of NURETH 10, Seoul, South Korea*, 2003.

[12] S. Morioka and T. Nakajima. Modeling of gas and solid particles two-phase flow and application to fluidized bed. *Journal of Theoretical and Applied Mechanics*, 6(1):77–88, 1987.

[13] A. Gobin, H. Neau, O. Simonin, J.-R. Llinas, V. Reiling, and J.-L. Sélo. Fluid dynamic numerical simulation of a gas phase polymerization reactor. *International Journal for Numerical Methods in Fluids*, 43:1199–1220, 2003.

[14] G. Balzer, O. Simonin, A. Boelle, and J. Lavieville. A unifying modelling approach for numerical prediction of dilute and dense two-phase flows. *Proceedings of Circulating Fluidized Bed Technology V, Beijing, May 28-June 1*, 1996.

[15] A. Srivastava and S. Sundaresan. Analysis of a frictional kinetic model for gas/particle flows. *Powder Technology*, 129:72–85, 2003.

[16] N. A. Konan, H. Neau, O. Simonin, M. Dupoizat, and T. Le Goaziou. CFD prediction of uranium tetrafluoride particle fluorination in fluidized bed pilot. *AIChE Annual Meeting, Nashville, TN, USA, November 8-13*, 2009.

[17] J. Baeyens and W.R.A Goossens. Some aspects of heat transfer between a vertical wall and a gas fluidized bed. *Powder Technology*, 8:91–96, 1973.

[18] P. Fede, G. Moula, T. Ingram, and O. Simonin. 3D numerical simulation and PEPT experimental investigation of pressurized gas-solid fluidized bed hydrodynamic. *Proceedings of* 12^th *Int. Symp. on Gas-Particle Flows, 2009 ASME Fluids Engineering Summer Conference, Vail (USA), FEDSM2009-78048*, 2009.

[19] B. Boissière, R. Ansart, D. Gauthier, G. Flamant, and M. Hemati. Experimental hydrodynamic study of gas-particle dense suspension upward flow for applications as new heat transfer and storage fluid. *Canadian Journal of Chemical Engineering*, 93:317–330, 2015.

Chapter 4

Study of a 150 kW_{th} 16-tube experimental solar receiver

4.1 Introduction

In order to confirm that the process of Dense Particle Suspension (DPS) circulating upward in vertical tubes was applicable at industrial scale, a 16-tube 150 kWth experimental receiver was built by our project partners to be tested at the PROMES-CNRS solar furnace in Odeillo. It worked following the same principles as the single-tube experimental receiver presented in Chapter 2. The improved, larger-scale installation could be operated continuously instead of the batch operation of the previous single-tube receiver. Two test campaigns took place. The first one, in July 2014, was the commissioning and it allowed checking that the experimental installation was operational. Several necessary modifications to be made were discovered. The receiver was equipped with more than a hundred sensors measuring the air and particle mass flow rates, the pressures and the temperatures in all parts of the installation. During the on-sun operation, the installation was exposed to high solar flux densities. Therefore, it was critical to quickly detect any malfunction to prevent the receiver from being damaged. The essential measurements to follow were put in evidence during the commissioning and the software specifically implemented for the data acquisition was optimized so that the operators would easily access these important measures.

After the modifications underlined by the commissioning were implemented, the second test campaign took place. It spanned over 2 month, between the end of March and the end of May 2015. It was preceded and followed by solar flux measurements campaigns that were used to define the solar facility settings and precisely characterized the solar power reaching the receiver during its operation. The 16-tube receiver was operated on-sun during close to 80 hours, with several full days of operation. The solid flow rate, the solar flux entering the receiver cavity, and the DPS temperature at the inlet of the irradiated cavity were varied. The variable weather conditions influence was observed. States of stable temperatures and flow rates lasting several hours were reached. The heat flux absorbed by the DPS was estimated. Thanks to the precise solar flux measurements, the receiver efficiency, also called cavity thermal efficiency, could be calculated.

This chapter first describes the set-up of the pilot receiver, its functioning principle and the experimental procedure that was applied during its operation. The measurements that were performed in order to characterize the solar facility are presented. In the second section, the system's transient behavior is observed in the case of changing weather conditions and in the case of controlled parameters' variations. The third section focuses on the experimental results during stable periods. The operating parameters are indicated and the resulting DPS temperatures obtained after the passage through the irradiated cavity are observed. The power transferred to the DPS is determined for the different conditions tested and it is compared to the results of the single-tube pilot plant. The thermal efficiency of the receiver is estimated and its dependence on the solid mass flux is analyzed. Finally these results are used to conclude on the applicability of the DPS process at large scale.

4.2 Experimental set up and procedure

4.2.1 Pilot solar receiver loop

The pilot solar loop is schemed in Figure 4.1. The COMESSA company managed the precise engineering arrangement and built the installation. It was operated continuously,

in closed loop. An Archimedes screw conveyor feeds SiC particles of 64 μm average Sauter diameter, the same as those used in the single-tube experiments, from the bottom of the storage tank (hopper) to the Dispenser Fluidized Bed (DiFB), where they are fluidized. Because of the overpressure in the DiFB, the dense particle suspension (DPS) rises up the 16 identical vertical absorber tubes (29.7 mm inside diameter, 2 mm thickness) set inside the solar receiver cavity. The sun heated tubes transmit their absorbed energy to the particles. A gas injection nozzle is set on each tube for aeration 53 cm from the tube bottom. Particles leaving the tubes at their upper section are all collected in the collector fluidized bed (ColFB), where their temperature is homogenized. Then, the DPS can be water-cooled in the cooling fluidized bed (CoolFB) to adjust its temperature. At the outlet of the CoolFB, the particles are fed up to the storage tank by a recycling screw conveyor. The solid circulation in loop is closed when particles fall into the DiFB feeding screw through a rotary valve set at the storage hopper outlet that controls their flow rate. The tank inlet and outlet valves allow the pressure to be increased from the outlet of the recycling screw conveyor, at ambient pressure, to the inlet of the feeding screw, at the DiFB pressure, with an intermediate pressure in the tank. During the on-sun experiments, the complete load of the rig was 900 kg of SiC particles. Figure 4.2 displays a 3D view of the main equipments of the CSP2 pilot unit.

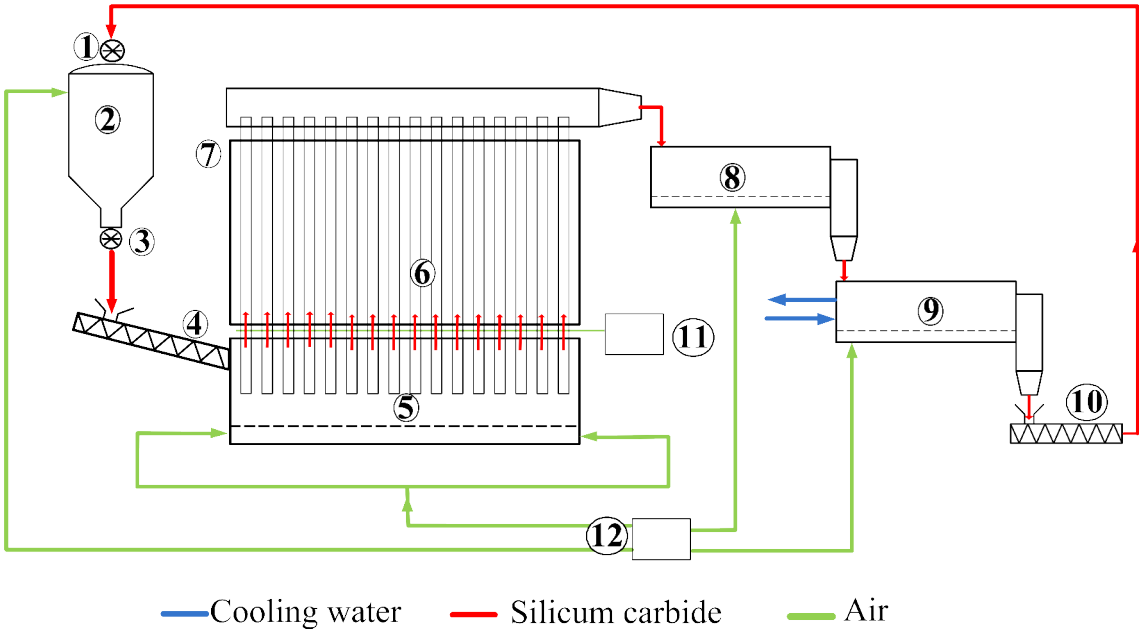

Figure 4.1: Schematic view of the pilot solar receiver loop: 1 Rotary valve 1, 2 Storage tank, 3 rotary valve 2, 4 feeding screw conveyor, 5 dispenser fluidized bed, 6 irradiated tubes, 7 receiver cavity, 8 collector fluidized bed, 9 cooling fluidized bed, 10 recycling screw conveyor, 11 aeration, 12 compressed air supply.

4.3 Instrumentation

The pilot rig instrumentation comprised 126 instruments: pressure indicators, pressure and differential pressure sensors, thermocouples, gas and solid mass flow meters, valves and security switches.

Each fluidized bed was equipped with a differential pressure sensor whose plugs were located

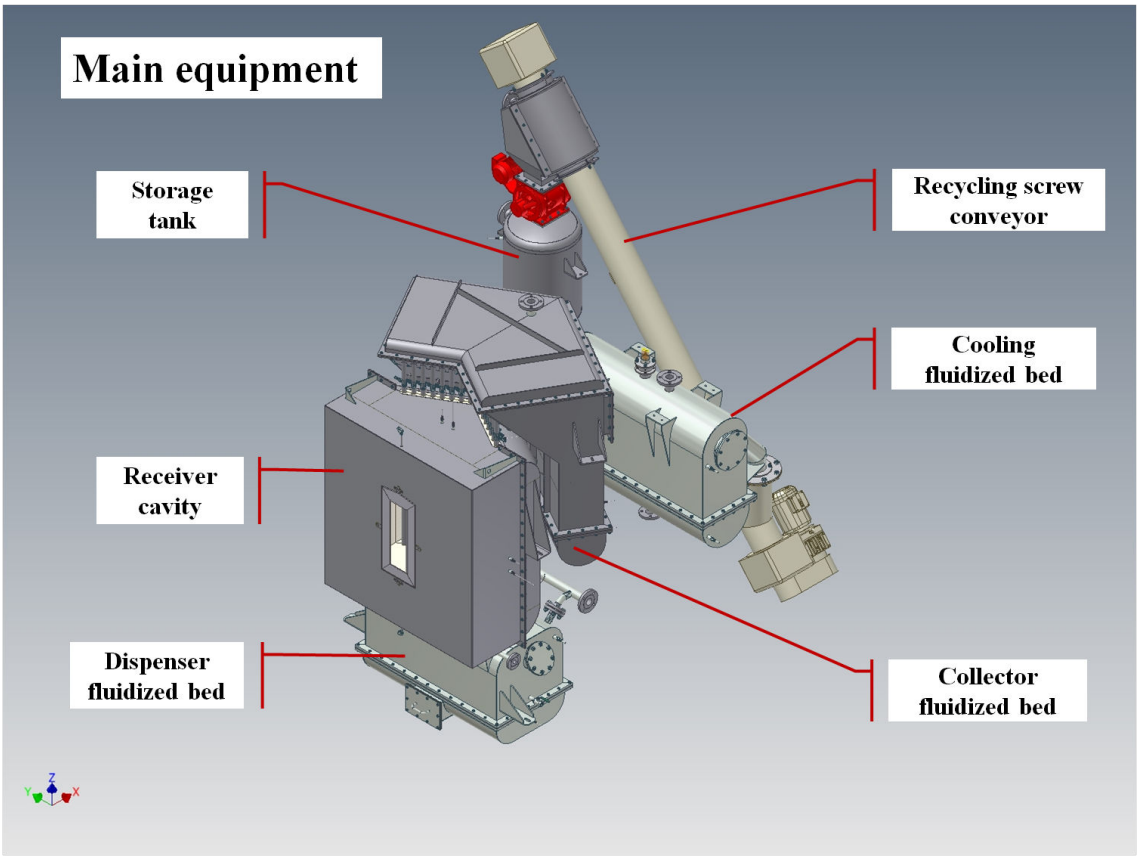

Figure 4.2: 3D view of the pilot solar receiver rig (source: COMESSA).

in the fluidized bed for the lower one and in the freeboard for the upper one, and two pressure sensors located in the freeboard and in the plenum, respectively.

The particle temperature in the DiFB was measured with four K thermocouples placed at the bottom and at middle height of the bed, at both sides (East and West). There were two K thermocouples in the lower part of the ColFB, at both sides. The CoolFB was equipped with one K thermocouple for particle temperature measurement. It must be noted that, as mentioned in Chapter 2, the gas and particle temperatures in dense suspensions are equal.

The solar receiver cavity was inside-insulated by high temperature resistant micro-porous modules. For each of the 16 absorber tubes, a differential pressure sensor measured the pressure drop. The tube wall temperatures at the rear, at the cavity middle height, and the DPS outlet temperatures were measured with K thermocouples for all tubes. In addition, for six selected tubes, the rear wall temperature and the DPS temperature were also measured at the irradiated cavity inlet.

Figure 4.3 displays the main measure instruments and their locations. On this screen printing of the pilot rig flow sheet, white squares correspond to the DPS temperature measurements, red squares to the rear wall and front wall temperature measurements, and green and blue squares display the absolute and differential pressure measurements, respectively. The red line and arrows represent the particle flow.

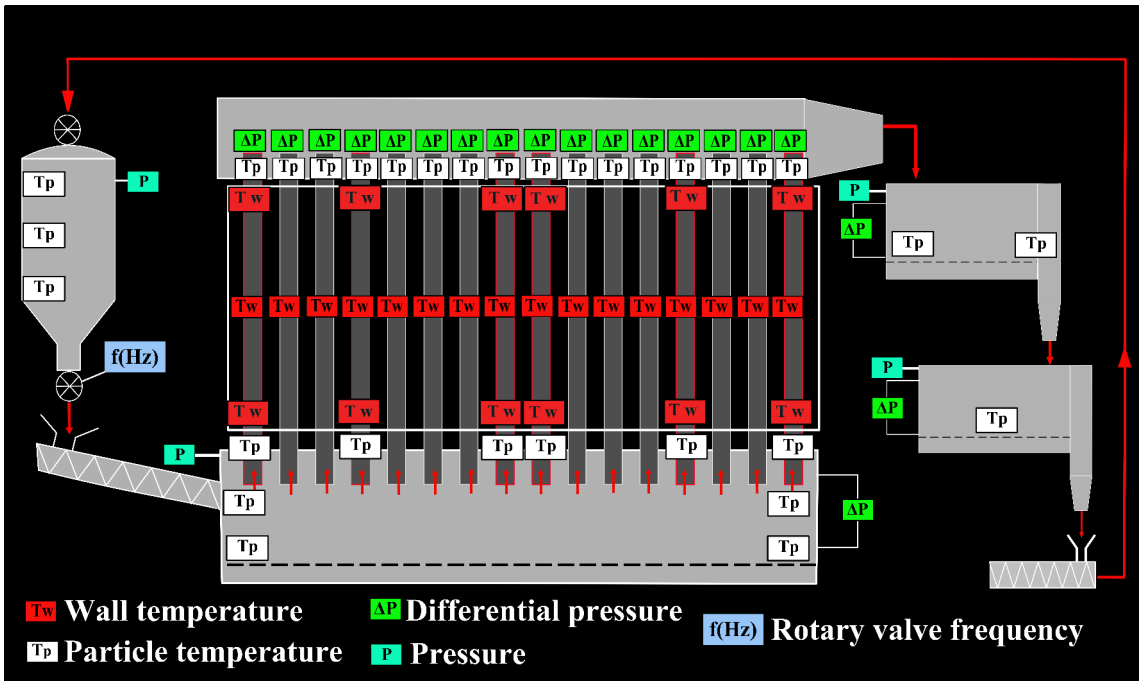

Figure 4.3: Main instrumentation of the pilot plant.

4.3.1 Solar flux qualification

4.3.1.1 Solar facility settings

The experiments were carried out at the CNRS 1 MW solar furnace in Odeillo. Before operating the pilot receiver, it was necessary to define the solar facility settings. The solar

furnace was composed of a 63 heliostats solar field, a parabola and a receiver building. The heliostats, facing south, reflected the solar radiation parallel to the optical axis of the parabola, facing north, that concentrated the radiation toward its focus. The receiver was set at the last floor of the receiver tower, with the center of its cavity aperture located at the position of the focus.

The solar flux at the focus can be modulated by selecting the shooting heliostats and by changing the opening of the receiver building doors to intercept a fraction of the incoming concentrated solar flux. It must be noted that the solar furnace was conceived to obtain a maximum solar flux concentration at the focus. On the opposite, the pilot receiver needed a uniform flux density hitting the tubes. The solar flux distribution can be made uniform in a vertical plane by setting the heliostats to shoot with an offset. The solar flux uniformity is checked with a CCD camera filming a flat Lambertian surface receiving the concentrated radiation. However, determining the right heliostats shooting, doors' opening and heliostat offsets to obtain a given uniform flux value is complicated and can only be achieved through succesive trials. Moreover, the weather conditions to conduct these trials need to be excellent without any wind our clouds.

In the specific case of the multitube solar receiver, the tubes are inside a cavity with a small opening (0.5 m high, 0.15 m wide). To measure the solar flux and check its uniformity on two planes corresponding to the tube bundles (two 8-tube bundles with a 120 ° angle between them), set behind a small aperture, more equipment is needed. The biggest obstacle resides in obtaining a uniform flux density while shooting through the cavity aperture. Indeed, it is not known in advance if moving one heliostat to shoot in one direction will increase the solar flux density in this direction or if it will be intercepted by the limits of the cavity aperture. Therefore, it was decided to limit ourselves to having a uniform solar flux density at the cavity aperture, which at least allowed knowing the solar power entering the cavity. But this method, which was the best available option, did not ensure a uniform flux distribution at the back of the cavity where the tubes were set.

In order to test the pilot receiver under various solar heat flux conditions, three heliostat field and furnace doors' opening were defined. For each configuration, the number of heliostats shooting, their offsets and the doors' opening were different.

4.3.1.2 Flux density measurement at the cavity aperture

For each of the three furnace configurations, the solar flux density was measured in the focal plane of the parabola, where the receiver cavity aperture was located, using a calorimeter with a 24.7 mm aperture diameter. Each measurement was realized over at least a hundred seconds, with one value taken every second. The values presented here are the time average of all the instantaneous values. The variations of instantaneous values due to wind or partial shadows because of a cloud cover on the heliostat field were less than 8 %. The solar flux density was obtained by dividing the power measured by the calorimeter by its aperture area.

The measurements were carried out at 33 different positions that were included in the area corresponding to the cavity aperture. 11 vertical positions were covered with a 5 cm calorimeter shifting between two consecutive positions. The horizontal positions corresponded to the middle width of the cavity aperture, 5 cm to the east and 5 cm to the west. Figure 4.4 displays the distribution of the calorimeter positions over the cavity aperture.

Figure 4.5 displays flux density maps at the cavity aperture that were obtained by interpolating the calorimeter measurements. The values are normalized for a 1 kW/m^2 Direct Normal Irradiation (DNI), which means that the measured values were divided by the actual DNI and multiplied by 1 kW/m^2. It can be seen that the solar flux distribution is quite uniform for all the settings, except at the bottom where the flux density is lower. But the solar flux uniformity was not ensured at the back of the cavity where the absorber tubes are located. Indeed, the solar radiation coming from different heliostats went in different directions when getting out of the parabola focal plane. Flux measurements carried out at the back wall of the cavity showed that there were some hot spots and cold zones. These measurements will be detailed in Chapter 5.

The average solar flux density of each furnace configuration was calculated as the average of the 33 measured values with half the weight applied to the six higher and lower measures because, for these, half the calorimeter aperture was out of the cavity aperture. It ranged from 1 MW/m^2 to 1.8 MW/m^2 (values normalized for a 1 kW/m^2 Direct Normal Irradiation (DNI)). A coefficient of solar flux density variation was defined to characterize the uniformity. It corresponded to the solar flux density standard deviation divided by the average solar flux density. It was 13 % for the lowest flux density setting, 2 % for the intermediate flux density and 1% for the highest flux density, which showed that the solar flux uniformity at the cavity aperture is better when the solar flux density is higher. This was due to more heliostats being used to increase the solar flux density, which increased the heliostats arrangement possibilities.

The aperture through which the solar flux entered the cavity was 0.15 m wide and 0.5 m high. The power that entered the cavity during the experiments, called inlet power (Φ_{in}), depended on the furnace configuration and on the weather conditions (DNI). It ranged between 63 and 142 kW over the whole experimental campaign.

For each furnace configuration, the number of heliostats shooting, the normalized average solar flux density at the cavity aperture, the coefficient of solar flux density variation and the normalized solar heat flux entering the cavity are indicated in Table 4.1.

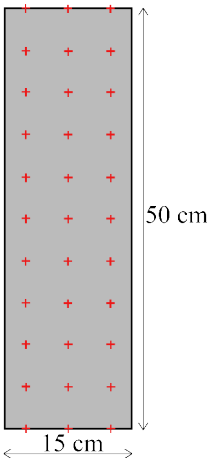

Figure 4.4: Calorimeter positions distributed over the cavity aperture.

4.3.2 Experimental procedure

The procedure applied for the on sun-tests of the pilot receiver is described here. First, compressed air was injected to fluidize the particles in all the beds and aeration air was

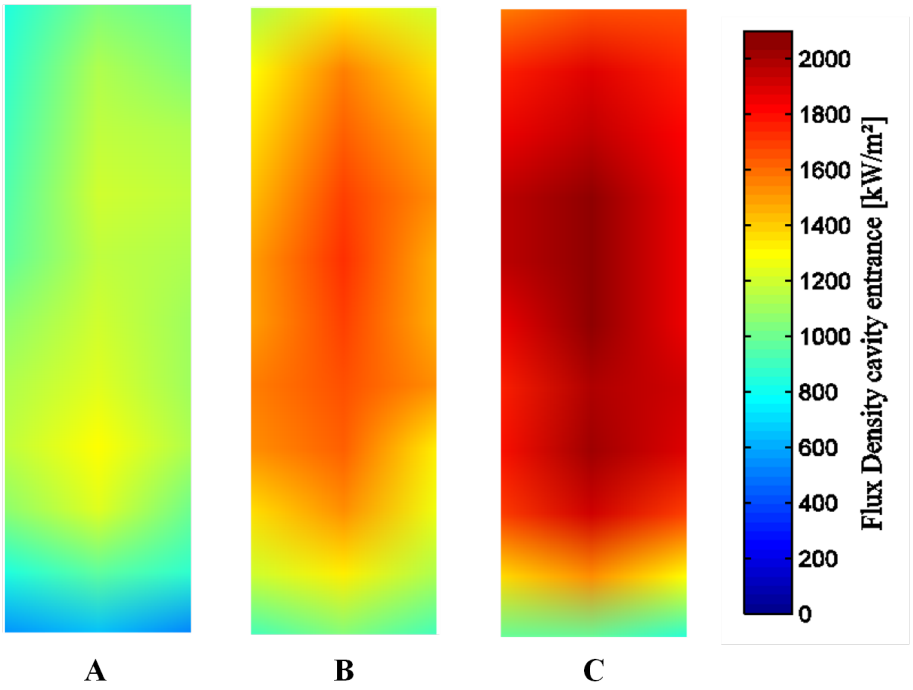

Figure 4.5: Flux density distribution at the cavity entrance for the three furnace settings.

Table 4.1: Solar furnace settings' characteristics.

Setting	Number of heliostats	Normalized inlet flux density [kW/m^2]	Coefficient of solar flux density variation	Normalized inlet power [kW]
A	19	1048	13 %	78.6
B	27	1429	2 %	107.2
C	32	1772	1 %	132.9

injected in the tubes. Then, the regulation valve that controlled the DiFB freeboard pressure was progressively closed to make the DPS rise in the vertical absorber tubes. When the DPS reached the tubes' top and started flowing out in the ColFB, which was indicated by the differential pressure in the DiFB starting to decrease, the screw conveyors and the rotary valves at the inlet and outlet of the storage tank were activated. The rotation speed of the outlet valve was set to get the desired mass flow rate (the rotary valve was previously calibrated). By adjusting the DiFB freeboard pressure a stable circulation was established, with the same solid flow rate entering and exiting the DiFB.

When the circulation was established, the heliostats were put in shooting position and the furnace doors' were opened. Under the effect of concentrated solar radiation, the cavity got progressively heated. The temperature increase provoked the expansion of the air flowing in the absorber tubes which increased the air velocity and the DPS voidage. Since the voidage is inversely proportional to the DPS density, the hydrostatic pressure of the DPS in the tubes decreased. Consequently, the regulation valve was progressively opened to equilibrate the pressure and maintain the solid flow rate that would have increased otherwise. The heated particles circulated through all equipments, heating the whole experimental installation.

The fluidized beds needed to be in bubbling regime to have a good temperature homogenization. The minimum bubbling velocity and the air density decreased with the temperature. Therefore, the fluidization mass flow rates were also decreased along with the temperature increase.

The operator could choose to cool the particles in the CoolFB, which limited their return temperature, or to let them get hotter, which progressively increased the DiFB temperature.

Finally, when all the components were heated and their heat losses became equal to the solar power entering the cavity, the temperature stopped increasing and the system reached a stable state with constant solid flow rate and temperature. The stable state was maintained during a long enough time period to confirm that the system was indeed stable. After a reasonable time at stable state, the operator could change the solid flow rate or the furnace configuration to modify the incoming solar flux in order to shift toward another stable state for different conditions.

More than 100 hours of on-sun experiments were performed. Several runs did not reached the stable state because of varying weather conditions. Twenty-nine experiments reached stable states that were maintained during periods lasting from 16 and 110 minutes.

4.4 Transient periods

4.4.1 Particle temperature

Figure 4.6 shows the particle temperature distribution at the tubes' outlets and the average tube outlet temperature for an experimental run with a 30 $kg.m^{-2}.s^{-1}$ mass flux, and an 83 kW average solar power at the cavity entrance. The particle temperature reaches 755 °C at the outlet of the hottest tube and the average tube outlet temperature reaches 590 °C. Due to the particularity of the solar furnace that was conceived to obtain the maximum

concentration at the focus, the solar flux distribution on the tubes was not uniform. This is why the particle temperature overpasses 700 °C only at the outlet of tubes 5 and 12, and it overpasses 600 °C in only five out of sixteen tubes. The greatest DPS outlet temperature difference between tubes is as high as 246 °C.

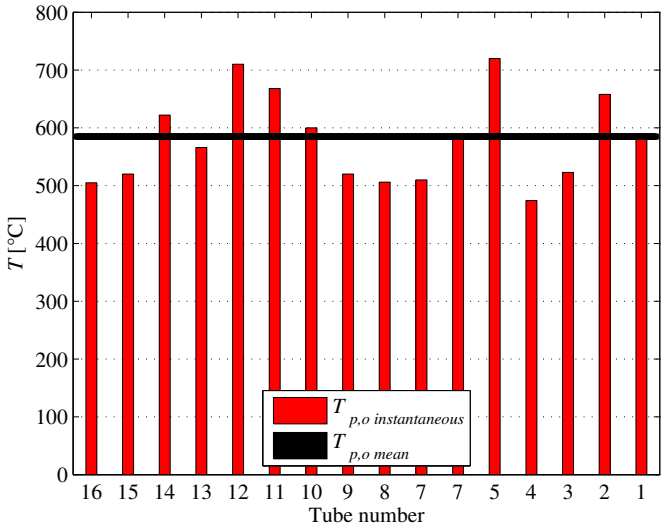

Figure 4.6: Instantaneous DPS temperatures at the tubes' outlets and instantaneous DPS outlet temperature averaged on all tubes during a transient period (mass flux = 30 kg.m^{-2}.s^{-1}, aeration = 0.09 Nm^3.m^{-2}.s^{-1}, inlet power = 76 kW.

4.4.2 System self-regulation

The system response to the DNI variations was studied when irradiation conditions changed quickly with a cloud passage. Figure 4.7 displays the DNI and the DPS and wall temperatures as a function of time for an experiment run under variable irradiation conditions. The purple line represents the average of all the tube wall temperatures measured.

Between 12:48 and 12:53, the DNI drops under 150 W/m^2. Under these conditions, the tubes' surface temperature falls from 397 °C to 232 °C (ΔT= 165 °C), while the DPS temperature at the tubes outlet drops down from 257 °C at 12:48 to 200 °C at 12:53 (ΔT=57 °C). The particle temperature in the ColFB varies from 245 °C to 226 °C (ΔT= 19 °C).

This phenomenon can be explained by two factors: on the one hand, the receiver cavity has a good thermal inertia, and on the other hand, the system is able to self-regulate. When the DNI drops, the solid mass flow rate decreases from 1.25 T/h to 0.96 T/h without any intervention of the operators. The reason is that the temperature drop provokes an air density increase. Consequently, the air velocity decreases, the voidage decreases and the DPS hydrostatic pressure in the tube increases. The pressure drop on the tubes comprises the hydrostatic pressure, which is its main component, and the friction pressure loss. To maintain the pressure equilibrium, the pressure loss must decrease when the hydrostatic pressure increases. A friction pressure loss decrease means a velocity decrease and a mass flow rate decrease. When the sky clears, the solid flow rate rises from 0.96 T/h to 1.2 T/h. The system well stands quick irradiation fluctuations; small clouds have very little impact on the particle temperature at the tubes' outlet and in the ColFB.

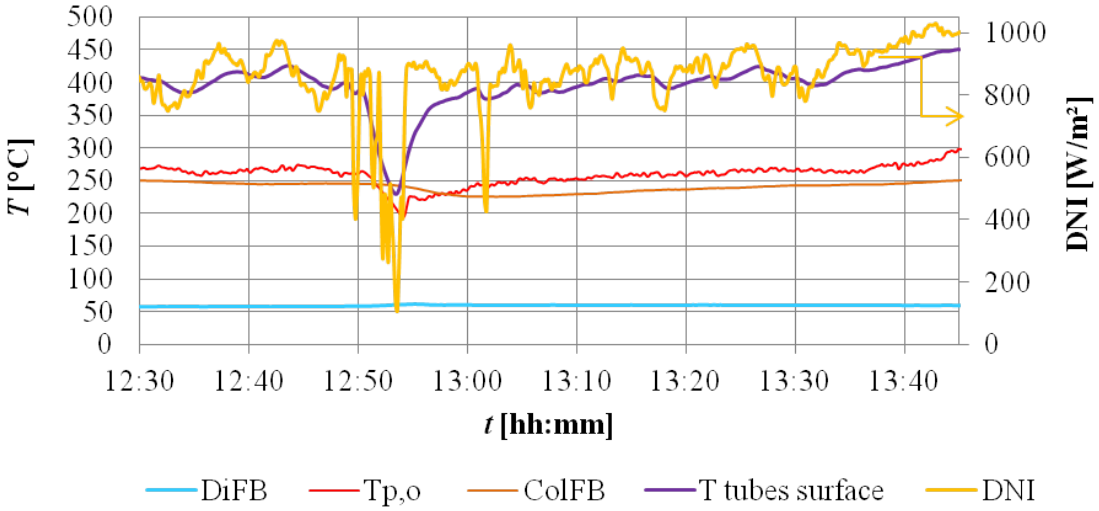

Figure 4.7: DNI and temperatures versus time (operating parameters: solid mass-flow rates = 1.25; 0.96; 1.2 T/h; mass fluxes = 31; 24; 30 kg.m^{-2}.s^{-1}; average inlet power = 77 kW).

4.4.3 System response to controlled mass flow rate variations

Figure 4.8 shows the system response when the mass flow rate is changed voluntarily by the operator. The DNI, the tube wall surface average temperature, the solid average temperature at the sixteen tube outlets and the temperature increase between DiFB and ColFB are plotted. During the first stable state period, a mass flux of 36 kg.m^{-2}.s^{-1} leads to a $\Delta T_{DiFB-ColFB}$ of 216 °C. When the operator changes the rotary valve setting to decrease the mass flux, from 36 to 31 kg.m^{-2}.s^{-1} (14 % decrease), $\Delta T_{DiFB-ColFB}$ increases from 216 to 228 °C (6 % increase). When the mass flux goes down to 21 kg.m^{-2}.s^{-1}, the temperature increase goes up to 269 °C, which means a 23 % $\Delta T_{DiFB-ColFB}$ increase, for a 48 % solid mass flux decrease, relatively to first stable state period.

4.5 Stable states

4.5.1 Steady state periods selection

The first criteria to select the stable state experiments were the stability of the solid mass in the DiFB, which reflected the solid flow rate stability, and the temperature stability, evaluated through the stability of the particle temperature increase between the DiFB and the ColFB. Specifically, the variation over time of this difference was considered. In total, 29 experimental runs were stable at the level of these criteria. The highest variation of particle temperature increase on all the stable states was less than 1.6 °C/min, and for 76 % of the experimental runs it was less than 0.5 °C/min.

4.5.2 Operating parameters

The main system's operating parameters were the solar power at the cavity entrance, the particle flow rate and the particle temperature in the DiFB. The aeration flow rate was

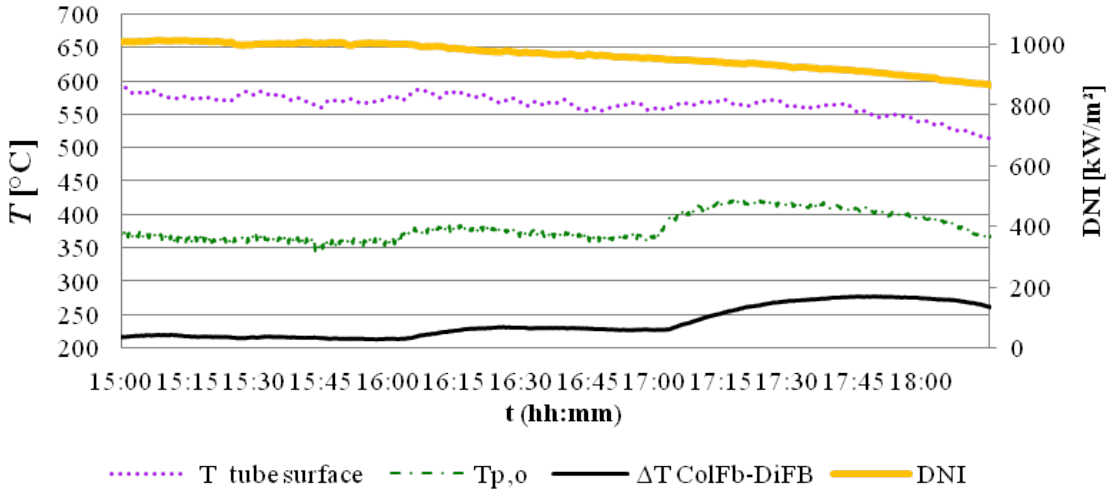

Figure 4.8: Solid outlet temperature averaged on the 16 tubes, wall mean temperature, DPS temperature increase between the DiFB and the ColFB and DNI as a function of time (operating parameters: solid mass-flow rates = 36, 21, 31 kg.m^{-2}.s^{-1}; inlet power = 108, 104, 98 kW; $\Delta T_{DiFB-ColFB}$ = 216, 228, 269 °C; $T_{p,o}$ = 359, 369, 403 °C).

evenly distributed between all tubes thanks to sonic nozzle installed on the injectors. The aeration in each tube was 0.09 Nm^3.m−2.s−1 for all experiments. Three solar furnace configurations were tested, providing solar flux densities at the receiver entrance in the range 1-1.8 MW/m^2, which corresponded to inlet powers ranging from 63 to 142 kW. The solid mass flow rate was varied from 600 to 1800 kg/h, which corresponded to solid mass fluxes between 17 and 44 kg.m−2.s−1. It was limited by the capacity of the rotary valve and not by the process itself. As mentioned in Chapter 2, solid mass fluxes as high as 700 kg.m−2.s−1 can be achieved with the DPS upward flow in tube technology. The particle temperature in the DiFB varied from 43 to 184 °C. The return particle temperature was regulated through a water cooling coil submerged in the CoolFB. Table 4.2 displays the ranges of operating parameters and of experimental results.

Table 4.2: Ranges of operating parameters and corresponding experimental results.

Parameter ranges				**Experimental results ranges**					
Φ_{in}	F_p	G_p	T_{DiFB}	ΔT^1	$T_{w,tubes}$	$T_{p,i}$	$T_{p,o}$	T_{ColFB}	$\Delta P/L$
[kW]	[kg/h]	[kg/m^2.s]	[°C]	[°C]	[°C]	[°C]	[°C]	[°C]	[Pa/m]
63-142	662-1759	17-44	43-184	137-335	366-625	69-251	217-495	188-433	11340-11780

4.5.3 DPS temperature during stable periods

4.5.3.1 DPS temperature inside the tubes

As mentioned in Chapter 2, a 750 °C stable DPS temperature was reached at the outlet of the single-tube experimental receiver, with particles electrically preheated up to 503 °C in the lack of closed loop circulation. In the present study, a 693 °C stable temperature was reached at the outlet of at least one of the tubes, and the mean temperature of the 16 tubes reached 495 °C, with solar heating only.

As explained in Section 4.3.1, the flux distribution at the location of the tubes in the cavity

example of the particle temperatures at all tubes' outlets during a stable experimental run lasting 55 minutes, and the particle temperature distribution at the tubes' outlets at the hottest moment of this experiment. The mean particle temperature over the 16 tube outlets is 442 °C.

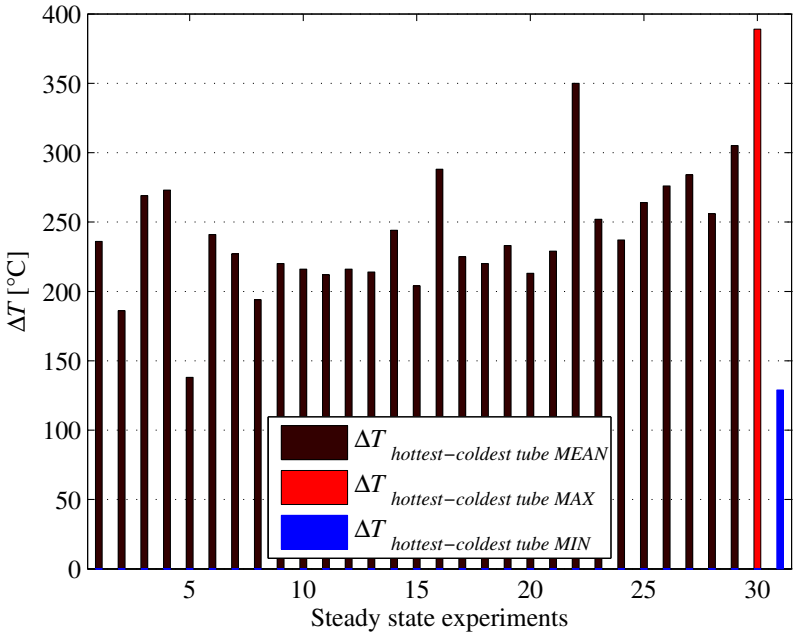

Figure 4.9: DPS mean temperature difference between the hottest tube and the coldest tube for all stable states, and minimal and maximal temperature differences.

4.5.4 DPS temperature increase and solid flow rate

The total solid mass flow rate is known thanks to the storage tank outlet rotary valve calibration, but the individual solid mass flow rate in each tube was not measured. Several factors can create an uneven solid mass flow rate distribution between tubes.

First, the tube inlet position in the DiFB must be considered. Indeed, the solid mass flow rate entering the tube might be impacted by the proximity of the particle injection (fluidization affected by the powder falling down from the screw conveyor), by the presence of the DiFB wall or by the behavior of the neighboring tubes.

Second, the differences at the level of the tubes' temperatures provoked variation of the air density between the tubes, and thus variations of the air velocity. As was explained in 4.4.2, the air velocity impacts the solid mass flow rate.

Due to this unequal solid mass flow rate distribution between tubes, the average of the DPS temperatures at the tubes' outlets did not represent the actual outlet temperature. It gave too much weight to the temperature of tubes with low solid flow rate, and too little to those of tubes with high solid flow rates.

If the tube outlet temperature had been the only factor impacting the solid mass flow rate, it could have been said with certainty that the average of the tubes' outlets temperatures

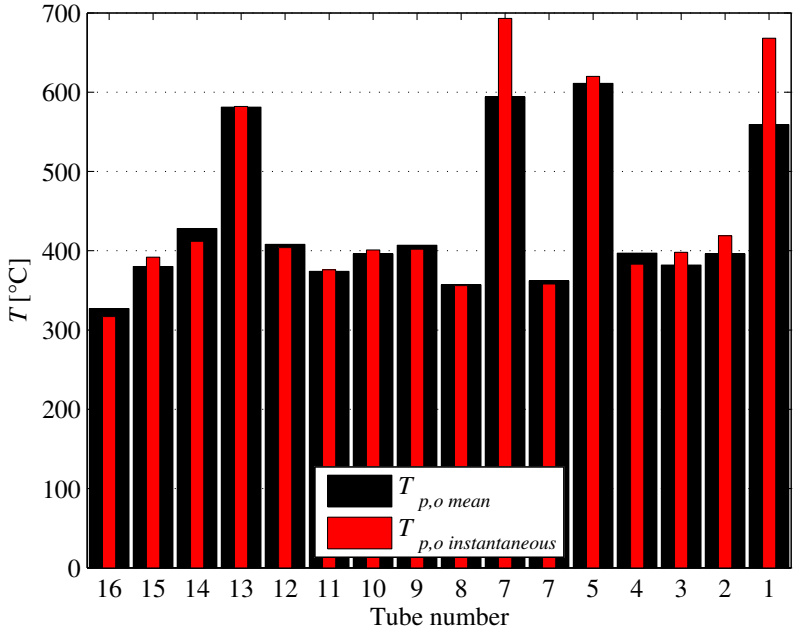

Figure 4.10: Particle temperature at the hottest moment and particle temperatures at the tubes' outlets during a 55-minute stable experimental run (aeration = 0.09 $Nm^3.m^{-2}.s^{-1}$, mass flux = 35 $kg.m^{-2}.s^{-1}$, inlet power = 142 kW).

underestimated the actual outlet temperature. Indeed, the higher the temperature, the lower the air density, the higher the air velocity and the higher the solid mass flow rate. So, in this case, the tubes at high temperature would have had too little weight in the average, hence a temperature underestimation. But due to the solid mass flow rate also being impacted by each tube's individual temperature distribution (a tube might show a continuous DPS temperature increase, or an increase followed by a stabilization, depending on its exposition to the solar flux) and by geometrical factors, the above reasoning was incomplete. Therefore, it was not possible to estimate if the average of the DPS temperature at the tubes' outlets overestimated or underestimated the outlet temperature.

When focusing on the total solid flow rate influence on the DPS temperature increase through the cavity, the uncertainty was avoided by considering as outlet temperature the temperature in the ColFB since it collected the solid flow rates coming from all tubes and homogenized the temperature. Due to the ColFB heat losses, the temperature is necessarily underestimated but only to a limited extent because it was well insulated. Thus, the temperature increase between the DiFB and the ColFB ($\Delta T_{ColFB-DiFB}$) was considered as the reference temperature increase.

Figure 4.11 plots $\Delta T_{ColFB-DiFB}$ as a function of the average solid mass flux on all the tubes G_p for all steady state periods. G_p is the total solid flow rate divided by the total tube section area (tube section area × 16). $\Delta T_{ColFB-DiFB}$ ranges between 137 and 335 °C for a 1 m irradiated tube length. The 335 °C maximum corresponds to an experimental run with a 21 $kg.m^{-2}.s^{-1}$ mass flux and a 105 kW solar flux entering the cavity. The 137 °C minimum corresponds to an experimental run with a 37 $kg.m^{-2}.s^{-1}$ mass flux and a 63 kW inlet power. For the three ranges of inlet solar powers, it can be seen that the $\Delta T_{ColFB-DiFB}$ decreases with the solid mass flux. Moreover, for a given solid mass flux, the higher the solar power at the cavity inlet, the higher the temperature increase. These

results are logical and were expected.

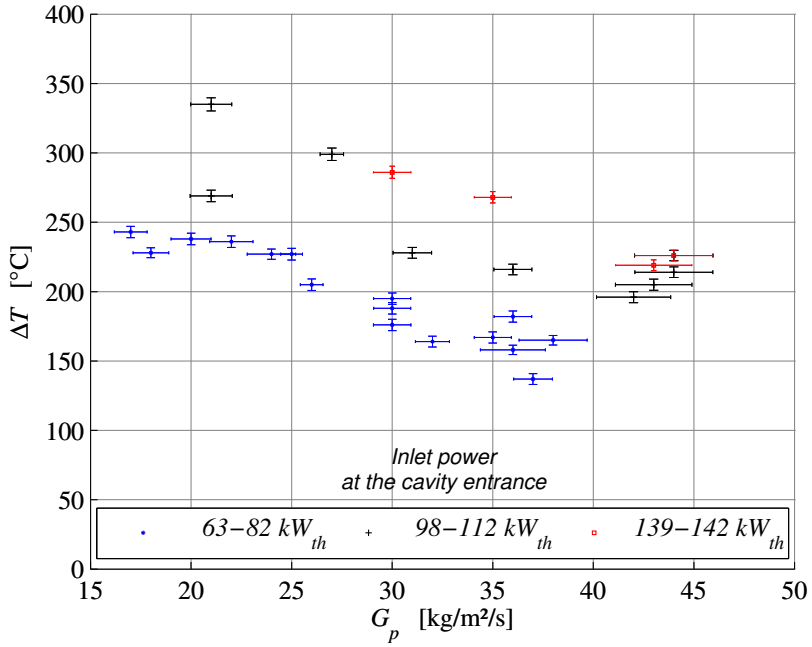

Figure 4.11: Temperature increase between the DiFB and the ColFB as a function of the solid mass flux at the cavity entrance.

4.5.5 Heat flux: multi-tube and single-tube experiments comparison

In order to show the coherence between the single-tube and the multi-tube setups, the heat fluxes absorbed by the DPS in both experiments were calculated. The calculation of the heat flux transferred to the DPS was already detailed in Chapter 2.

In the multi-tube solar receiver experiments, the heat flux distribution in the cavity was uneven and not all tubes received enough solar flux to work in the same conditions as the tube of the single-tube rig. The tubes receiving solar fluxes comparable to those of the single-tube experiment were not the same for all the stable runs because of the different solar furnace configurations. The hottest tube was the one that received the highest solar flux. Therefore, in order to compare the heat extraction capacity of both solar rigs, for each experimental run on the multi-tube solar rig, the tube with the hottest outlet temperature was selected for the calculation of the power transferred to the DPS.

The inlet temperature was the DiFB temperature.

As explained in the previous section, the distribution of the solid flow rate between the tubes was unknown. Due to the lack of another option, the average solid flow rate for one tube was used (total flow rate divided by the number of tubes).

Due to the tube external diameters and irradiated height that differed between the experiments, the tube surface irradiated was not the same. Therefore, the power absorbed by the DPS was divided by the irradiated area and the obtained heat flux densities absorbed by the DPS (φ_{DPS}) were compared.

Figure 4.12 displays the heat flux density extracted by the hottest tube as a function of the average solid mass flux. Contrarily to $\Delta T_{ColFB-DiFB}$ that increases with the solar flux entering the cavity, no clear influence of the inlet power on the heat flux density extracted by the DPS can be noticed. This is due to the fact that the heat flux absorbed by the DPS was calculated with the hottest outlet temperature, which corresponds to the tube receiving the highest solar flux. Even if the total solar heat flux entering the cavity varies with the furnace configuration, the solar flux received by the hottest tube does not vary much.

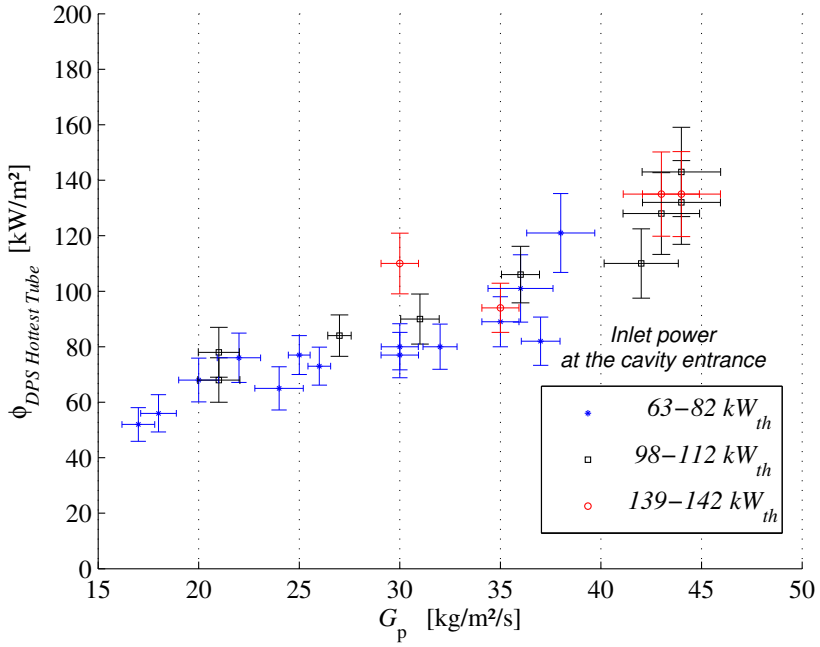

Figure 4.12: Heat flux density extracted by the hottest tube as a function of the solid mass flux.

Figure 4.13 plots the heat flux densities absorbed by the DPS in both experiments as a function of the solid mass flux. The two data series show a strong coherence. The maximum extracted flux density is 160 kW/m^2 for a 45 kg/m^2 mass flux for the single-tube setup and 143 kW/m^2 for a 44 kg/m^2 mass flux for the multi-tube solar rig. Some single-tube experimental runs present higher heat flux densities absorbed because they were carried out with aeration fluxes lower than the aeration flux used for the multi-tube experiment.

4.6 Receiver thermal efficiency

4.6.1 Importance of the thermal efficiency

The receiver thermal efficiency corresponds to the ratio of the thermal power exiting the receiver over the solar power reflected by the heliostat field that reaches the receiver. Therefore, a better thermal efficiency means a smaller heliostat field for a same thermal power output. In Concentrating Solar Power (CSP) plants, the heliostat field represents one of the main capital costs. By reducing the size of the solar field for a given electricity

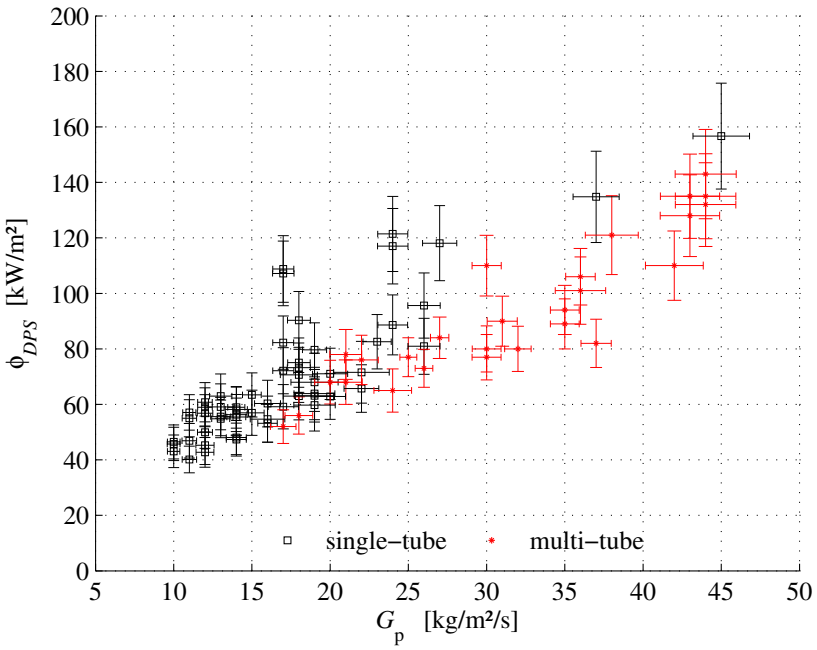

Figure 4.13: Heat flux densities absorbed by the DPS in both experiments as a function of the solid mass flux.

production capacity, the capital cost will be reduced and so will be the levelized electricity cost. Thus, the thermal efficiency clearly plays an important role in the improvement of CSP plants performance. The DPS multi-tube receiver thermal efficiency determination was one of the main objectives of this experiment.

4.6.2 Thermal efficiency calculation

To calculate the receiver thermal efficiency, the solar flux entering the cavity needed to be precisely known. Therefore, the stability of the DNI was added two the two criteria previously applied for the stable state periods selection. Among the 29 periods stable at the level of the solid mass flux and the temperature, the twenty periods with the most stable irradiation conditions were selected for calculating the thermal efficiency. Figure 4.14 plots an example of stable state period that is unusable for the thermal efficiency calculation due to its DNI variations.

In the study of the multi-tube experimental solar receiver, the thermal efficiency η_{th} was defined as the ratio of the power absorbed by the DPS over the solar flux entering the cavity.

$$\eta_{th} = \frac{\Phi_{DPS}}{\Phi_{in}} \tag{4.1}$$

where Φ_{DPS} represents the power transmitted to the DPS and Φ_{in} represents the solar power at the cavity entrance.

The heat flux transferred to the DPS was calculated using the total solid flow rate, the DiFB temperature as inlet temperature and the ColFB temperature as outlet temperature. As was explained the ColFB temperature underestimated the outlet temperature due to the ColFB heat losses.

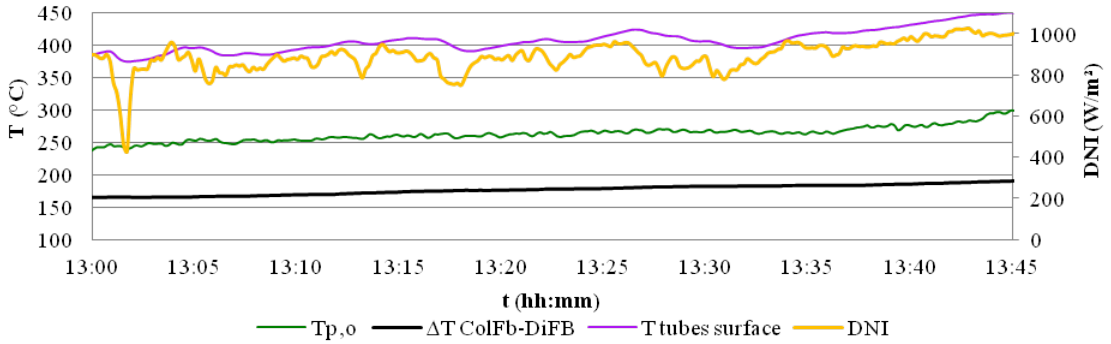

Figure 4.14: Particle temperature averaged on all tubes' outlets, temperature increase between ColFB and DiFB and direct normal irradiation as a function of time.

The thermal efficiency average over each stable state period was determined in two different ways: by averaging all instantaneous thermal efficiency values, and by calculating the thermal efficiency with the time averages of the solid flow rate, of the temperatures and of the DNI. The difference between the two averaging methods was less than 0.05 %, with a mean value of 0.01 %. It shows the consistency of the stable states and validates the selection criteria.

Figure 4.15 plots the thermal efficiency η_{th} as a function of the solid mass flux for all the stable state periods selected. η_{th} ranges from 50 to 90 % for solid mass fluxes in the range 17-44 kg.m^{-2}.s^{-1}. It increases with the solid mass flux. No clear difference can be seen between the low and average solar fluxes but it appears that the high solar flux leads to lower efficiencies. This is due to the increase of the heat losses (radiation, convection, conduction through insulating material) with the temperature increase provoked by the greater solar power entering the cavity.

4.7 Conclusion

A series of on-sun tests of a 50-150 kW_{th} multi-tube solar receiver with dense particle suspension as HTF were performed. Several full days of on-sun operation of the pilot rig were achieved, with continuous particle circulation in closed loop and more than 30 h of stable state in total. The rig was steadily operated with particle temperature increases through the receiver cavity in the range 137-335 °C for a 1 m irradiated tube height.

The solar furnace in which the experiments were carried out could not irradiate the pilot receiver tubes uniformly which put a limit on the maximum temperature that was reached at the outlet of the receivers' 16 tubes. However, the temperature of the ColFB, which was an underestimation of the actual receiver outlet temperature, reached 490 °C during a stable state period and went up to 590 °C during a transient period. The particle temperature was even higher than 700 °C in some tubes.

During transient periods, the system showed a self-regulation capacity, decreasing and increasing the solid flow rate when the DNI dropped or rose. This is a very interesting advantage for power plant operation.

The experimental results obtained on the single-tube and on the multi-tube solar receiver showed a strong coherence at the level of the heat flux density absorbed by the DPS.

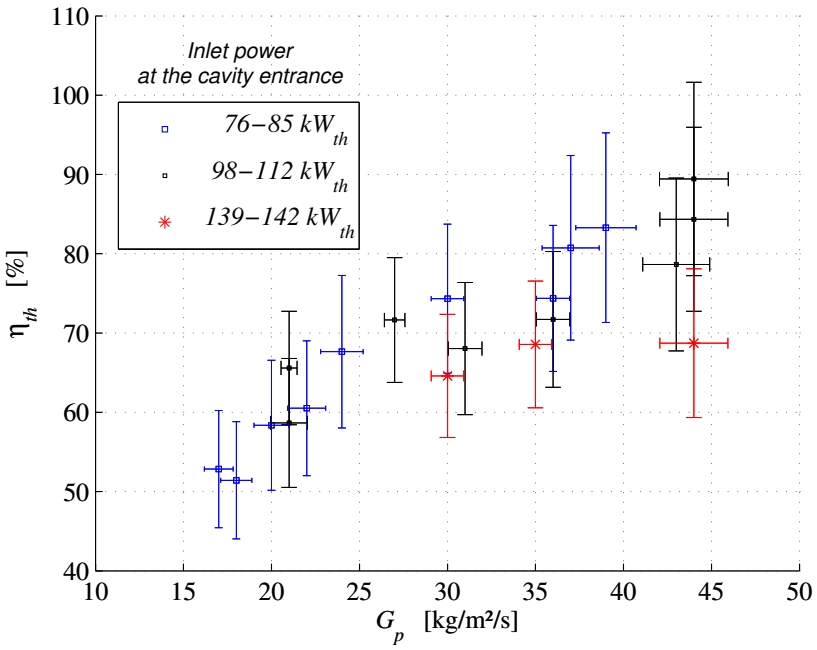

Figure 4.15: Cavity thermal efficiency as a function of the solid mass flux.

The experimental results proved the feasibility of the multitube DPS receiver concept and its capacity to operate at high temperature in realistic conditions.

The receiver thermal efficiency is a key factor for decreasing the capital cost of a CSP plant. In this study that used a cavity receiver, it reached 90 % for a solid mass flux of 44 $kg.m^{-2}.s^{-1}$.

In the case of an industrial solar tower power plant, the heliostat field efficiency is better when there is no cavity. It also makes the shooting strategy easier. To be usable in such conditions, the DPS concept will need to achieve high heat transfer coefficients, otherwise the high temperature of the receiver tubes will lead to very high radiation losses. Moreover, to limit the temperature increase while receiving more power, higher solid mass flow rates will be needed. Previous tests on the DPS upward flow in tubes proved that much higher solid mass fluxes can be achieved. We have shown with the experiments on the one-tube receiver rig presented in Chapter 2 that the higher the solid mass flux, the higher the DPS heat transfer coefficient. This behaviour is beneficial but more tests are needed to determine if the heat transfer coefficient will keep increasing with solid fluxes above the maximum value that was tested. Other improvements should be considered such as the use of finned tubes.

4.8 Nomenclature

Abreviations

ColFB	Collector Fluidized Bed
CoolFB	Cooling Fluidized Bed
DiFB	Dispenser Fluidized Bed
DNI	Direct Normal Irradiation
DPS	Dense Particle Suspension

Latin symbols

F	Mass flow rate [kg/s]
G	Mass flux [kg.m^{-2}.s^{-1}
T	Temperature [°C]
$T_{w,tubes}$	Average tube wall temperature [°C]

Greek symbols

$\Delta P/L$	Linear pressure drop [Pa/m]
ΔT	Temperature difference [°C]
$\Delta T_{DiFB-ColFB}$	Temperature increase between DiFB and ColFB [K]
$\Delta T_{hottest-coldest}$	DPS temperature difference between the hottest tube and the coldest tube [°C]
η_{th}	Receiver thermal yield
φ	Heat flux density [W/m^2]
φ_{DPS}	Heat flux density transferred to the DPS [W/m^2]
Φ_{DPS}	Heat flux transferred to the DPS [W]
Φ_{in}	Inlet power [W]

Subscripts, Superscripts

i/o	Cavity inlet/outlet
p	Particle temperature
w	Wall

Chapter 5

Modeling of a Multi-Tube Receiver Cavity

5.1 Introduction

Computational models are used to describe the complex heat transfers occurring inside cavity receivers that combine solar and infrared radiation with convection, conduction, and possibly chemical reactions. Several methods are available to study the radiative heat transfer. The Discrete Ordinates (DO) method, initially developed for astrophysical and atmospheric radiation [1], was implemented for the radiative heat transfer analysis [2, 3]. This method uses a set of discrete directions spanning the total solid angle range to represent the directional distribution of the intensity. The method accuracy strongly depends on the quadrature scheme used for the integrals over solid angles. The DO method errors are false scattering caused by the spatial discretization and ray effect due to angular discretization. Its main drawback is that it does not ensure the conservation of radiant energy. The Finite Volume (FV) method, thanks to finite solid angles, respects the energy conservation and is compatible with fluid flow solvers [4]. Both methods can be used when modeling absorbing media. Indeed, the radiation intensity along its path can be calculated since the radiation propagation directions are computed. Therefore, these methods were applied in several cases of receivers working with methane and particle-loaded gas [5–10]. The radiosity model only considers surface-to-surface radiation exchanges [11, 12]. Radiosity corresponds to the radiation leaving a surface per unit surface area. This method works by determining view factors between all surfaces in the geometry to calculate the radiation they exchange. It initially worked with diffuse surfaces only since the radiation directions are not computed, but extensions have been developped [13]. The radiosity model allows calculation in any enclosure configuration, with any surface temperature distribution, whereas the previous methods cannot be applied to complex geometries or highly inhomogeneous surface temperature distributions, because it would require the computation of a too high number of radiation propagation directions. Solar thermal chemical reactors [14, 15] and cavity receivers [16] were modeled using this method. Monte-Carlo Ray Tracing (MCRT) techniques are used to compute estimates of quantities expressed with high-dimensional integrals [17]. Due to the geometry complexity as well as multiple reflections, this technique is well suited for flux map computations in solar facilities [18]. These algorithms were applied for solar facilities [18–22] and solar thermal chemical reactors [23–26].

In this chapter, a model of the the multi-tube receiver cavity installed at the focus of the 1 MW solar furnace (cf. Chapter 4) is described. It had to take into account the concentrated solar radiation, the radiation and convection exchanges inside the receiver cavity, and the heat absorbed by the Dense Particle Suspension (DPS) circulating inside the tubes. Therefore, both the specular reflectivity that occurs due the solar concentrator and the complex geometry with highly inhomogeneous surface temperature distributions were considered. This complex problem was divided into two parts. First, a model of the solar furnace used to concentrate the solar radiation onto the receiver was realized using a MCRT method with the software Solfast-4D [18, 20, 21]. It gave the solar flux condition for the cavity model computed using the radiosity method with the commercial code ANSYS FLUENT version 15.0 [27]. This coupled method is interesting because it combines the advantages of each method to produce a model that is precise and does not require a very important computational capacity. It is a variant from a coupled method used for modeling a solar reactor cavity that combined the MCRT with the finite volume method [28, 29].

The MCRT model of the solar furnace and its validation with experimental measurements

are detailed in Section 1. In Section 2, the receiver cavity radiosity model is characterized and its results are compared with those from the experimental campaign. Finally, the validated model is used to get complementary information on heat fluxes inside the receiver cavity that will be useful for a more precise analysis of the experimental results. The solar furnace model results were part of a publication on the specific MCRT formulation encoded in the Solfast-4D code [18].

5.2 Solar furnace model

5.2.1 Methodology

The solar furnace was modeled using the MCRT method with the software Solfast-4D. The facility parameters were encoded. It comprises 63 heliostats, a parabolic concentrator and a focal tower, which is located at the focus of the parabola, where experiments are conducted. In the Solfast-4D, the specularly reflective surfaces are characterized by two parameters: the reflectivity and the optical error σ_{HP}. The optical error corresponds to half the opening angle of the reflected beam spread that is due to the mirrors' surface roughness. To take this effect into account, Solfast-4D uses the microfacet model of Torrance and Sparrow [30] in which the surface is decomposed in a distribution of specular microfacets whose normal can differ from the surface normal. For this model, a Gaussian form of the microfacet slope distribution is used. In order to determine the best set of parameters for our model, three types of experimental solar flux density measurements were conducted in order to be compared with the model results: 1) measurements in the parabola focal plane for heliostats shooting one at a time; 2) measurements in the focal plane for groups of heliostats shooting each with a specific offset (in the experimental campaign on the solar receiver, the heliostats did not shoot at the focus to get a more uniform flux density distribution at the cavity entrance, cf. Chapter 3); 3) measurements at the back wall of a mock-up cavity (with the same geometry as that of the experimental receiver) for heliostats shooting in the same configurations as those tested at the cavity opening (focal plane). Each heliostat's parameters were then optimized to fit the results of the single heliostat measurements. Then the configurations of multiple heliostats shooting with their own offsets were reproduced. The results were compared to the second type of measurements and the model's parameters were globally adjusted to get the same solar flux at the cavity opening as for the measurements. Finally, the mock-up cavity was inserted in the model and the experimental and numerical flux densities at the back wall were compared.

5.2.2 Geometry

The 1 MW CNRS solar furnace located at Odeillo is a double reflection facility. It involves 63 heliostats with flat mirrors (6 m high and 7.5 m wide, composed of 180 elementary mirrors 0.5 m $\times$ 0.5 m, 45 m^2 area each, 2835 m^2 total area), facing south, positioned on 8 terraces (5 m between two terraces) to reflect the solar rays parallel to the optical axis of the parabola (40 m high, 55 m wide, 18 m focal length) facing north. Thanks to this double reflection, the solar rays are concentrated at the parabola focus, located at 18 m from the ground, in the focal tower where experimental setups are installed. Figure 5.1 is a schematic view of the heliostat field that indicates the heliostats' positions relative to the

parabola. Figure 5.2 is a schematic view of the parabola where the portions corresponding to each heliostat are indicated. Figure 5.3 shows a photograph of the solar furnace and Figure 5.4 presents a 3D-rendering of this facility in Solfast-4D with samples of ray paths.

5.2.3 Individual heliostats' parameters optimization

5.2.3.1 Experimental measurements

As mentioned above, measurements of solar flux densities in the focal plane obtained for heliostats shooting one by one were conducted. There were two steps for these measurements. First, we took pictures with a CCD camera of the heliostats shooting on a Lambertian reflectiveplane surface located in the focal plane. They indicated the shape of each heliostat's spot using a grey scale imaging. Pictures were taken for 36 heliostats. By themselves, they are enough to optimize the heliostats optical errors, since the beam spread resulting from this parameter sets the spot shape. The second step consisted in measuring the experimental solar flux density at the center of the spot with a fluxmeter (Vatell® model TG 1000-1). It gave the value of the solar flux density in W/m^2 at this position and allowed the whole pictures conversion from pixels to W/m^2. By knowing the actual value of the solar flux density, we were able to determine the reflectivities for each heliostat and its associated part of the parabola (they are considered to be equal). The flux density at the center of the spot was measured for only 17 heliostats due to the facility limited availability and the difficulty to combine the weather conditions necessary for this kind of measurement that are a completely clear sky (no cloud veil) and no wind. Indeed, a cloud veil could create Direct Normal Irradiation (DNI) discrepancies between the heliostats and the DNI measurement equipment, while wind makes the heliostats move around their shooting position. Figure 5.5 shows the flux density maps in the focal plane for two heliostats. It can be seen that when the heliostat is located further away from the parabola's axis, its spot is larger and the maximum solar flux density is lower.

5.2.3.2 Optimization

The goal of the reflectors' parameters optimization was to determine the set of parameters for each heliostat and its corresponding portion of the parabola that better fitted the experimental measures. This was realized thanks to the solar flux density sensitivities that were computed by Solfast-4D. The used algorithm only allowed the calculation of sensitivities when all reflections occur on the same material. Therefore, each parabola portion was made of the same material as its corresponding heliostat. The reflectivity only impacted the value of the solar flux density and not its distribution shape. Hence, the first step was to find the optical error value for each heliostat-portion of parabola couple that produced a simulated flux map best matching the experimental flux map in the same configuration. Since the reflectivity was not optimized yet at this point, the flux densities were normalized. To solve this nonlinear least-square problem, a trust-region-reflective algorithm was used [31] with a Jacobian matrix comprising the sensitivities computed by Solfast-4D to minimize the cost function $\chi^2(\sigma_{HP})$ defined by:

$$\chi^2(\sigma_{HP}) = \sum_{i=1}^{N_p} [\varphi_{N,i}(\sigma_{HP}) - \hat{\varphi}_{N,i}]^2 \tag{5.1}$$

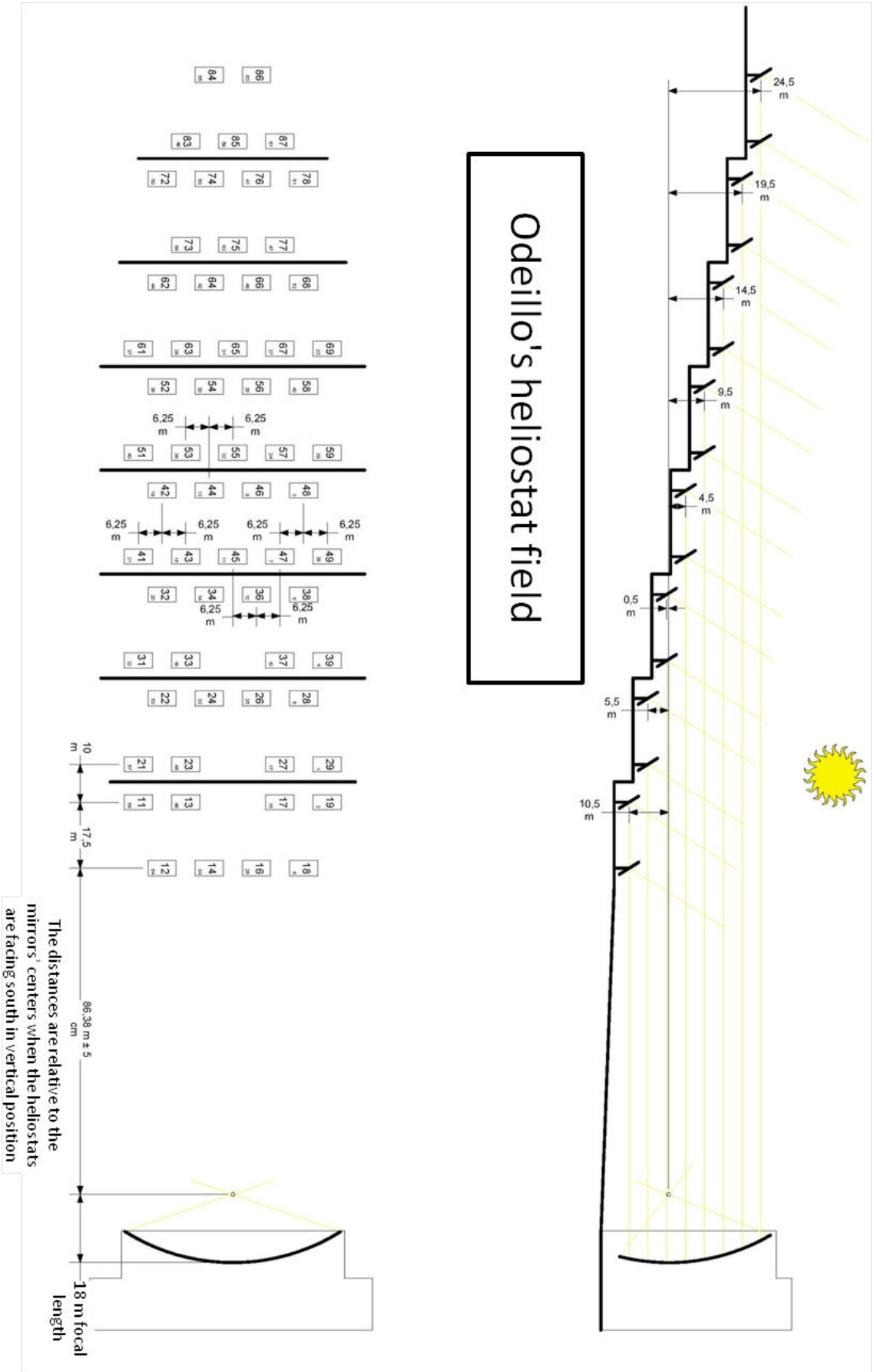

Figure 5.1: Schematic view of the heliostat field.

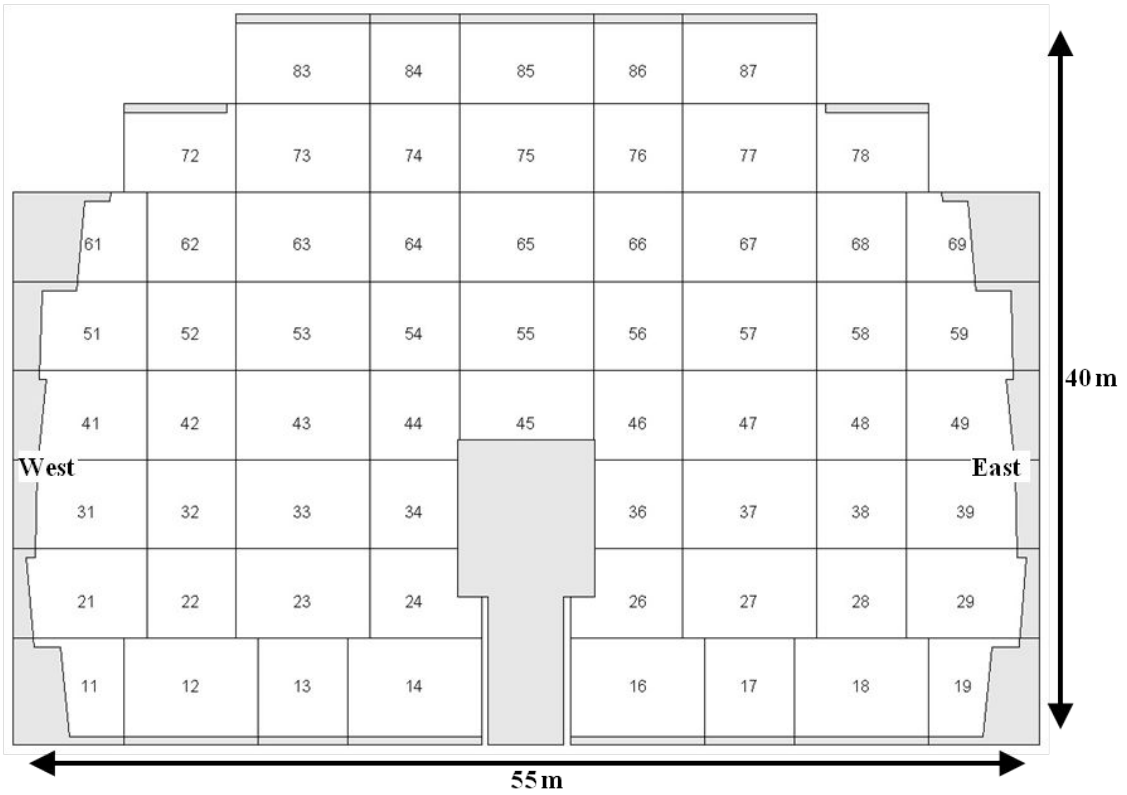

Figure 5.2: Schematic back view (looking north) of the parabola.

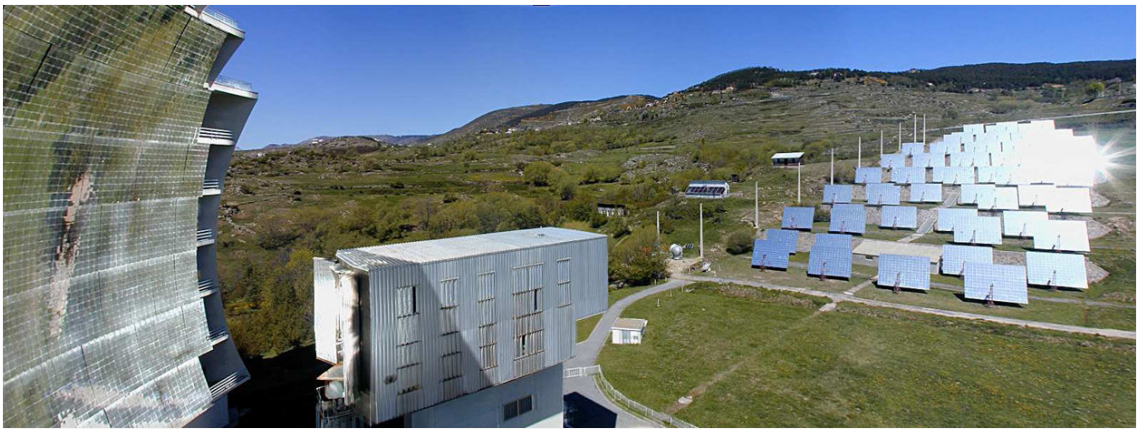

Figure 5.3: Photograph of Odeillo's 1 MW solar furnace.

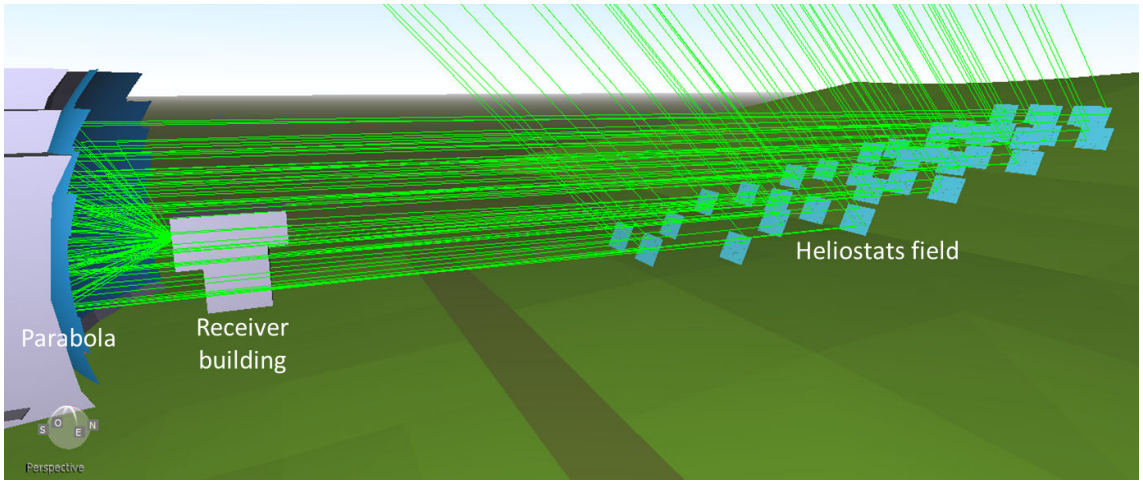

Figure 5.4: 3D-rendering of the solar furnace in Solfast-4D with samples of ray paths.

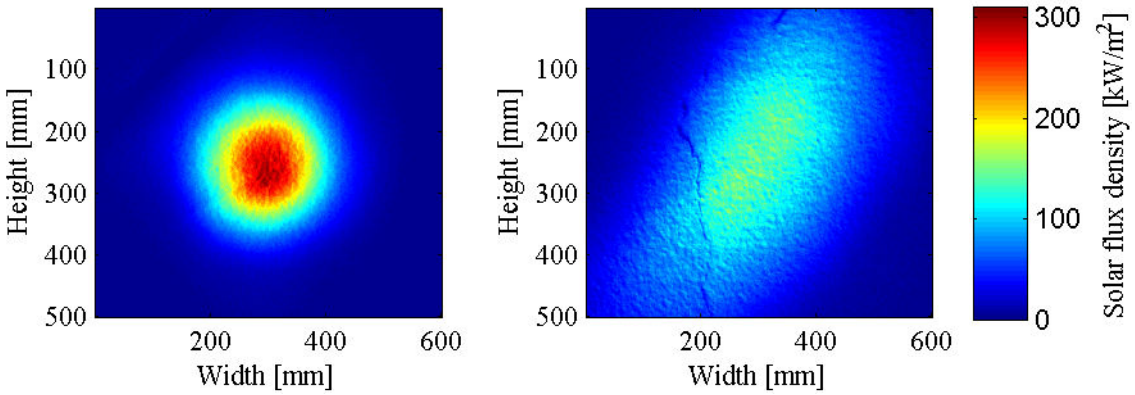

(a) H34. (b) H67.

Figure 5.5: Experimental flux density maps in the focal plane for two heliostats.

where N_p is the number of points in the matrix, $\hat{\varphi}_{N,i}$ the normalized measured flux density of the pixel number i for the considered heliostat and $\varphi_{N,i}(\sigma_{HP})$ the simulated flux density of the corresponding pixel.

The simulated flux map was obtained with 20×10^6 rays bundle. The flux map was measured on a 50 × 60 cm target surface and simulated on a similar target with square pixels of 0.5 × 0.5 cm. The identification of σ_{HP} was iteratively determined with MATLAB software using the "lsqnonlin" function in the optimization toolbox. An initial value $\sigma_{HP,0}$ was set to 0.1 mrad and the modeled flux map with its sensitivities $\partial_{\sigma_{HP,0}}\varphi_{N,i}$ were computed at each iteration of the optimization method. The results were obtained after less than 20 iterations for each heliostat and σ_{HP} ranged between 0.88 to 1.72 mrad with an average of 1.32 mrad. A comparison of the measured flux distribution with the simulated one obtained for one heliostat (H13) with the optimized σ_{HP} is given in Figure 5.6. The mean relative difference between the measured and simulated flux densities on the 400 central pixels (it is not interesting to consider pixels where the flux density is close to 0) is inferior to 5 %. Then, for the 17 heliostats that had their flux density at the center of the measured spot, the pixel values were converted to W/m^2, and the reflectivities r_{HP} were calculated to respect the power balance on the whole target surface. They ranged between 0.48 and 0.73 with an average of 0.64. These values were very low but this can be explained by several factors. First, the mirrors' interspaces of the heliostats and parabola were not considered in the model. Second, several heliostats had mirrors that were broken or removed (in particular, heliostat H45 that had the lowest estimated reflectivity of 0.48 had approximately 10 % of its mirrors removed). Third, the solar furnace mirrors were covered with dust since they are not regularly cleaned. All these factors combined together explain how with a local reflectivity superior to 0.8 at clean positions on the mirrors the average reflectivity on the whole surface came to be only 0.64. This average 0.64 reflectivity was applied to the heliostats for which we did not measure the flux density at the spot center and the average 1.32 mrad optical error was applied to the heliostats that did not have their spot shape measured (this only concerned one of the 35 heliostats used for the highest flux density setting).

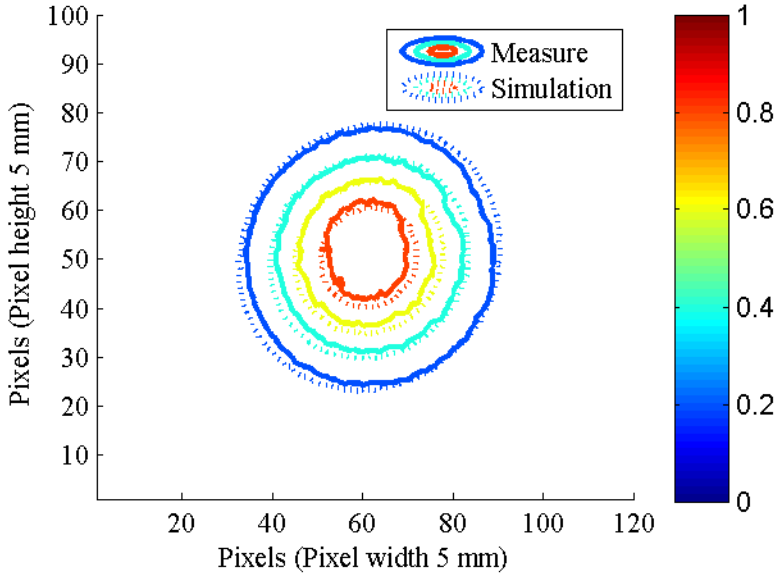

Figure 5.6: Contours of normalized flux density for heliosat H34 with $\sigma_{HP} = 1.315$ mrad.

5.2.4 Multiple heliostats shooting configurations

5.2.4.1 Experimental measurements

Two kinds of measurements were conducted for 4 multiple heliostats shooting configurations close to the ones used during the 16-tube pilot receiver experimental campaigns. Unlike, the configurations used during the experimental campaign that used a different number of heliostats for each setting, these 4 configurations used the same 33 heliostats. It must be noted that a shooting direction offset was imposed, specific to each heliostat, so that the flux density was alsmost uniform in the parabola's focal plane. Moreover, each configuration had a specific opening of the furnace focus's doors that set the acceptance angle for the incoming concentrated solar radiation. The configurations acceptance angles were 50.1 °, 60.3 °, 71.8 ° and 87.3 °. For the small doors' openings, the flux coming from the heliostats located further away from the parabola's axis and having the highest incidence angles was intercepted by the doors. When the opening was increased, so was the acceptance angle and, therefore, more flux reached the focus. The average measured heat flux densities for the 4 doors' opening were 0.93, 1.3, 1.61 and 1.97 MW/m^2 by increasing order of acceptance angle.

First, the flux density was measured with a fluxmeter (Vatell® model TG 1000-1) at 11 positions (5 cm between 2 consecutive positions) along the 50 cm height of the cavity opening (in the parabola's focal plane), in the middle of the opening width (15 cm). The profiles obtained for the 4 tested configurations are plotted in Figure 5.7. It can be seen that, as desired, the flux density is homogeneous except for the highest and lowest parts of the cavity opening where it is lower.

The second kind of measurement was done with the fluxmeter inserted in the back wall of a mock-up cavity (without tubes) at 41 positions. It gave flux density maps at the cavity back wall for the 4 configurations tested. Figure 5.8 is a photograph of the mock-up cavity back, installed behind a protective shield at the focus of the solar furnace. These maps, with interpolated values between the fluxmeter positions, are presented in Figure 5.9. We can observe that the flux density was far from homogeneous when considered out of the focal plane. Hot spots can be seen. The reversed shadow of the focal tower led to a cold spot in the middle of the back wall upper part. For the smallest focus's doors opening, the flux density reaching the sides was very low. As the opening was increased and the beam angle got larger, more flux reached the sides.

5.2.4.2 Model results

The multiple heliostats shooting configurations were reproduced in Solfast-4D model, with the corresponding heliostats' offsets and focus's doors openings. The previously optimized heliostats' properties were used. The first simulated results were good but did not perfectly fit the experimental measurements. This was due to two factors: the delay between the measurements campaigns and the flux density measurement of only 17 heliostats. The delay between measurements campaigns allowed for meteorological events to alter the state of the reflectors' surfaces, changing their properties; and the use of the average optimized reflectivity value for 16 heliostats did not exactly correspond to reality. Therefore, the modeled heliostats' reflectivities were adapted to fit the measured flux density profile at

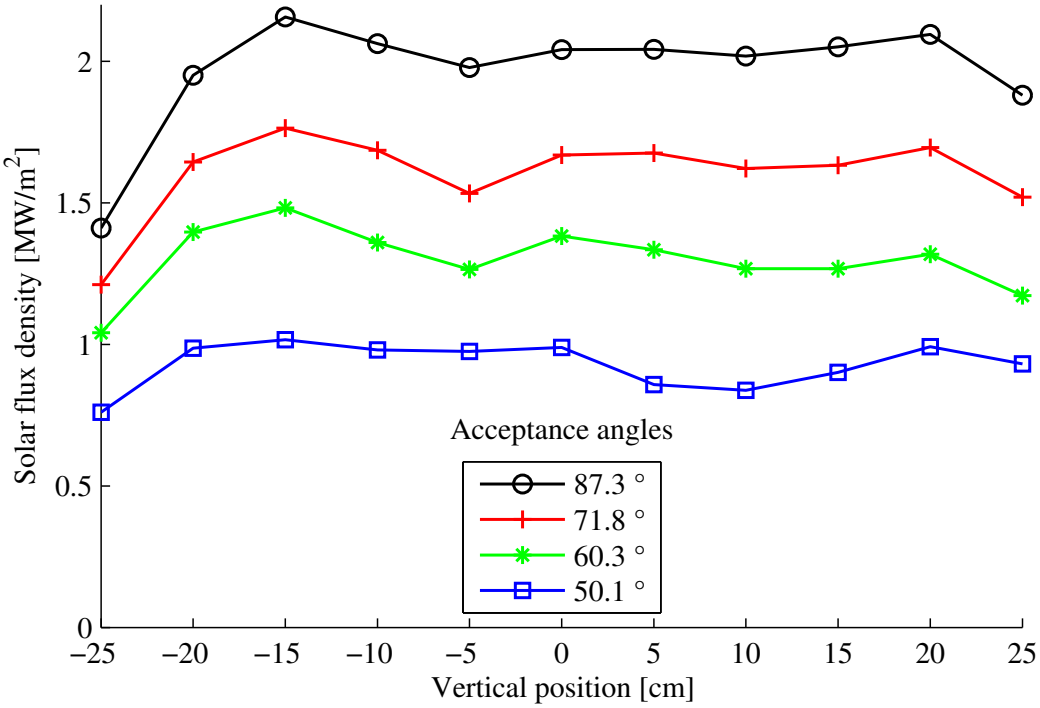

Figure 5.7: Vertical profiles of solar flux density in the middle of the cavity aperture for 4 acceptance angles.

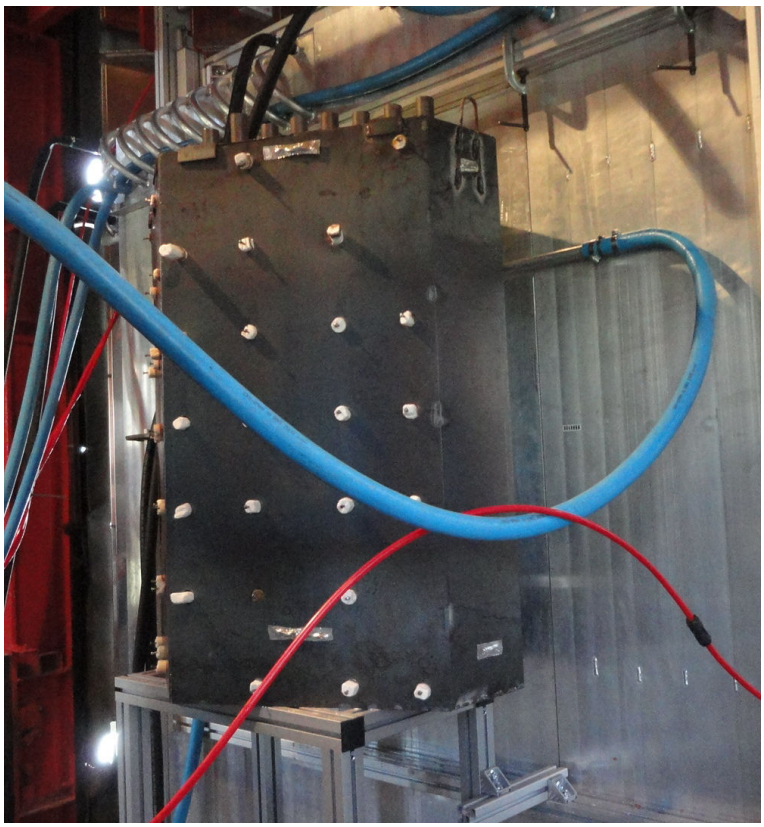

Figure 5.8: Solar flux density maps at the back wall of the mock-up cavity.

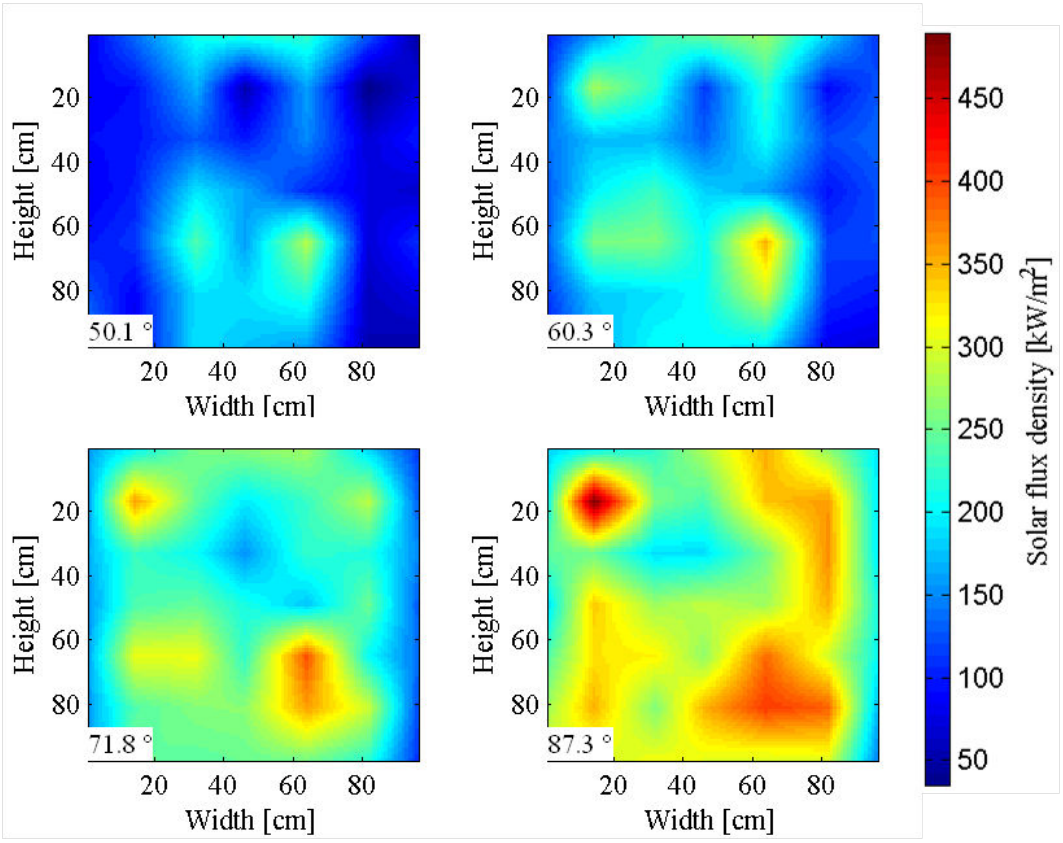

Figure 5.9: Solar flux density maps at the back wall of the mock-up cavity.

the cavity inlet. The comparison between the measured and the simulated flux density profiles at the cavity aperture for the 50.1 ° acceptance angle case is shown in Figure 5.10. The correspondence is good, with a maximum error of 10 % and an average error of 5 %.

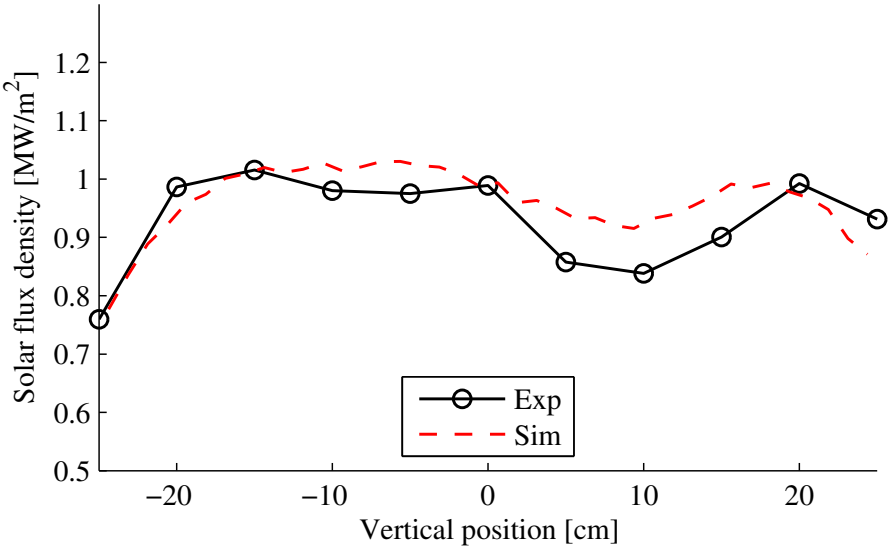

Figure 5.10: Experimental and numerical vertical flux density profiles in the middle of the cavity for the 50.1 ° acceptance angle configuration.

5.2.5 Complete solar furnace model

The model was applied with the heliostats configuration used during the 16-tube pilot receiver experimental campaigns. The flux density resulting from the new heliostats configurations applied during the campaign was once again measured, this time with a calorimeter at 11 positions along the height of the cavity opening, at 3 distinct horizontal positions (middle of the opening width, 5 cm to the east and 5 cm to the west), which gave a total of 33 measures. The model's reflectivities were adjusted to have the same inlet power (average flux density × cavity entrance area) as that obtained with the calorimeter measurements (2.4 % reflectivity increase with respect to the previous case). The simulated and measured flux density profiles are shown in Figure 5.11 for the configuration corresponding to an average normalized flux density of 1 MW/m^2 (flux density for a DNI of 1 kW/m^2)[1]. They did not match perfectly but the general tendencies were reproduced: highest flux in the center, lowest flux 5 cm to the east, lower flux at the top and bottom positions. A more accurate model would have required adjusting once again the heliostats' reflectivities (another significant time period passed between the previous measurements at the cavity inlet and the experimental campaign on the pilot receiver). But since the most important parameter - the inlet power - was respected, the model was used as it was.

The receiver cavity geometry was added to the model with the center of its aperture at the focal point of the parabola. The cavity opening is 15 cm wide and 50 cm high,

[1] It must be noted that this configuration is not the same as the one that gave the profile of Figure 5.10. Both configuration give an average solar flux density at the aperture close to 1 MW/m^2 but they were obtained with different heliostats and doors settings. This is why some local differences can be seen such as the different flux densities in the low part of the aperture.

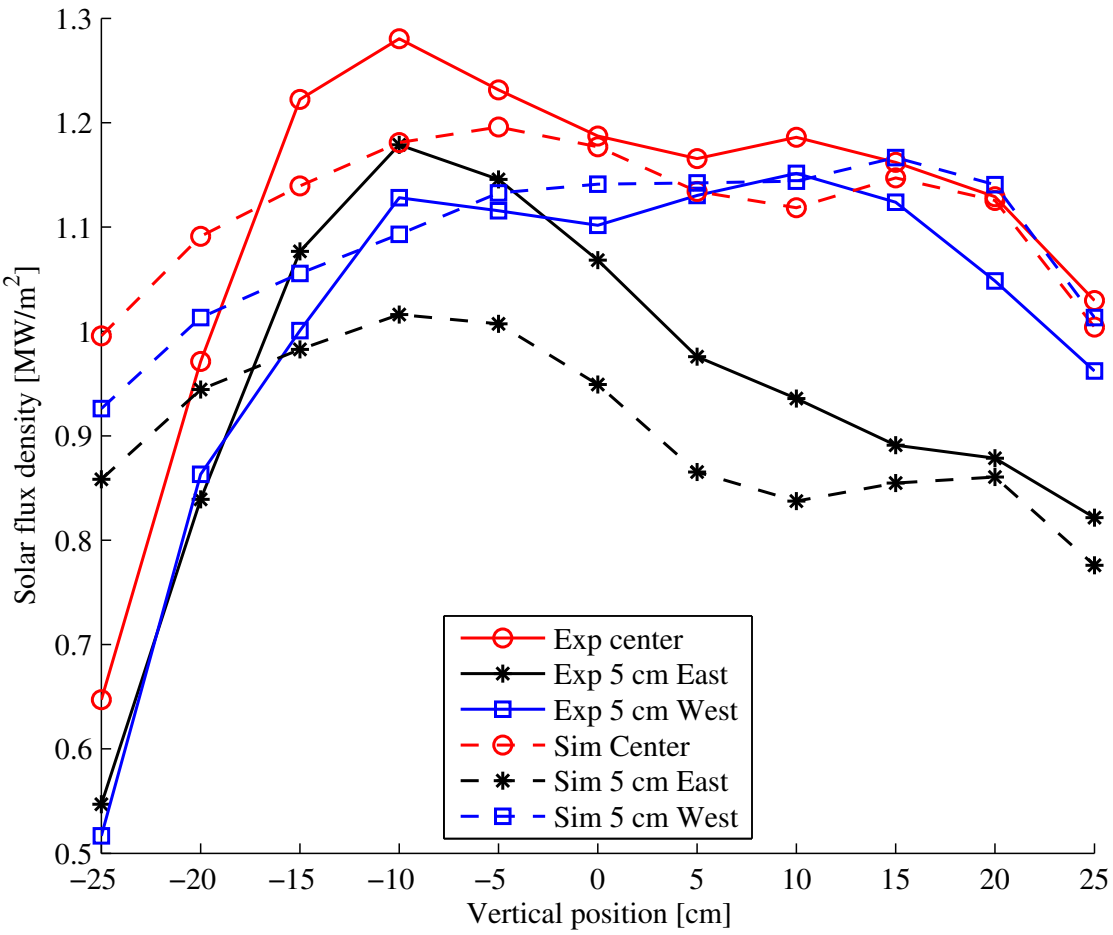

Figure 5.11: Vertical profiles of solar flux density at the cavity inlet for the configuration giving an average normalized flux density of 1 MW/m^2 at the cavity aperture. (configuration different from that of Figure 5.10, see previous footnote)

the cavity height is 1 m. A horizontal cross-sectional view of the cavity with the tubes (exterior diameter 33.7 mm) is shown in Figure 5.12. The cavity and tubes' materials were specified. They were approximated as diffuse materials, which was close to reality according to reflectivity measurements that were conducted. The reflectivities were 0.66 for the insulating material and 0.05 for the Pyromark® coated tubes. Finally, the flux density maps for all surfaces inside the receiver cavity were computed. The applied cell size was 1 cm × 1 cm.

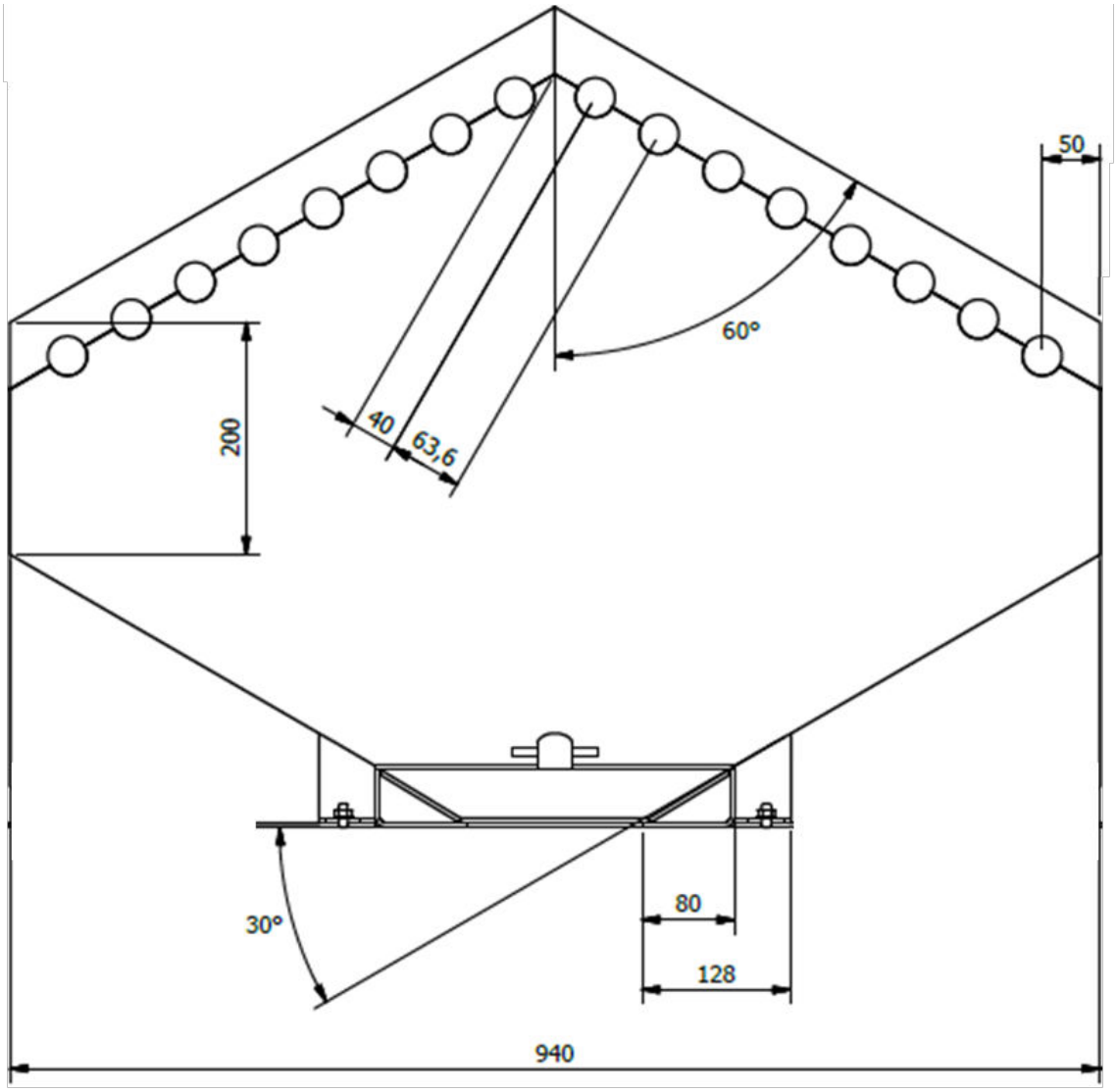

Figure 5.12: Horizontal cross-sectional view of the cavity.

5.3 Receiver cavity radiosity model

5.3.1 Simulation Parameters

As mentioned above, the radiosity method was used to model the receiver cavity. The method was computed in the commercial code ANSYS FLUENT version 15.0 [27] under

the name of Surface-to-Surface (S2S). The surfaces view factors were computed by the software. For the flow, the laminar model was used. The study was conducted in steady-state.

The model considered that air was transparent to radiation and that all surfaces were diffuse grey bodies. The insulating material and Pyromark® paint emissivities in the infrared region differed from their emissivities in the solar spectrum. The insulating material emissivity was taken as an average of those of silica and calcium carbonate that are its main components and it was set to 0.2. The Pyromark®'s emissivity was 0.88.

The used geometry was the same as that used in Solfast-4D model (cf. Figure 5.12). The mesh was created using ANSYS Design Modeler. It comprised 2 334 000 tetrahedral cells with 1 cm edges. The tubes inside was not modeled and, therefore, not meshed. The tubes and insulating material thickness were not simulated and appropriate boundary conditions were set instead, as explained in the next subsubsection. Polynomial functions of the temperature were computed to determine the air properties. They were the same as those used in Chapter 2, except for the dynamic viscosity that was approximated by:

$$\mu_g = -6.11 \times 10{-}12T^2 + 4.23 \times 10{-}8T + 7.03 \times 10{-}6 \tag{5.2}$$

5.3.2 Boundary conditions

The difficult part of this modeling was to set boundary conditions able to reproduce the physical phenomena occurring inside the receiver cavity.

The cavity aperture was set as free surface (pressure inlet in FUENT) at atmospheric pressure (101325 Pa) and 10 °C. This boundary was not only an inlet but also an outlet since the air could enter and exit freely, following the convection created by its heating inside the cavity. The fact that an inlet condition was imposed did not prevent the air exiting. The modeled system was limited to the cavity volume, thus no wind velocity could be imposed. But given the small size of the opening (15 cm × 50 cm), we believe that wind effect was very limited. This entrance was set as a blackbody at 10 °C for the radiation exchange.

A no-slip condition was imposed to all the walls inside the cavity (the term "wall" applies to the insulating material as well as to the tubes).

The solar flux density impacting the walls that was previously determined with Solfast-4D was interpolated for each face of the mesh thanks to User Defined Functions (UDFs). Each surface had its specific UDF. The solar flux density could not be computed as a wall heat flux because it would have prevented adding the other heat exchanges through the walls that are the conduction heat loss through the insulating material and the heat transfer to the DPS circulating inside the tubes. Thus, the solar flux density was transformed into an equivalent heat generation rate inside the walls. A virtual wall thickness of 1 m was imposed and therefore the value of the heat generation rate in W/m^3 was equal to

the solar flux density in W/m^2. Note that any virtual wall thickness could have been chosen as long as the product thickness $\times$ heat generation rate remained equal to the solar flux density. The absurdity of having a tube thickness larger than the diameter was not a problem since this thickness was virtual. The heat loss by conduction through the insulating material was modeled by an equivalent convection heat transfer with the environment at 10 °C (thermal resistance equal to the sum of the conduction resistance and convection resistance). The heat transfer with the DPS circulating inside the tubes was also modeled by a convection heat transfer, but since the DPS temperature increased along the tubes' height, a temperature profile was imposed thanks to a UDF instead of a constant temperature.

5.3.3 Model validation method

Two comparison elements between the model and the experiments were used: one for the insulating materials, to validate the convection heat transfer coefficient applied as boundary condition, and the other one for the tubes, to validate the convection heat transfer coefficient as well as the temperature profile.

During the experiments, thermocouples were inserted in the insulating material in the east and west cavity walls. On each side, one was close to the cavity interior wall, the other was located 7.5 cm from the cavity. These thermocouples allowed estimating the conduction heat loss density passing through those walls. The convection heat transfer coefficient set at the boundary was validated when the same heat loss density was observed in the model.

For the tubes, the comparison between the model and the experiments could be done at two levels: the heat flux transmitted to the DPS and the temperatures inside the cavity. But actually, the value of the heat flux calculated from the experimental measurements was unsure. The power gained by the particle was calculated by an enthalpy balance. But a question remained concerning the outlet power to choose: the ColFB temperature or the average of the DPS temperatures measured in the tubes at the cavity outlet (cf. Chapter 4). The problem of using the ColFB temperature was that it included the heat losses that occurred between the cavity outlet and the ColFB, as well as the ColFB losses, thus underestimating the heat flux received by the DPS. In the other case, the problem was that the solid flow repartition between the 16 tubes was not known. Therefore using the average of the DPS temperatures measured in the tubes would give too much weight to tubes with low solid flow rate and too little weight to those with high solid flow rate if significant differences existed. It was not unknown if the second calculation option led to an overestimation or an underestimation of the power absorbed by the DPS.

Due to this uncertainty, the comparison between the model and the experiments was done with the temperatures measured inside the cavity, and more specifically, those measured at the back of the tubes. Indeed, these measurements were not affected by direct solar irradiation, contrarily to those at the tubes' front.

5.3.4 Case study

5.3.4.1 Case characteristics

One experimental run was selected to be modeled among the experimental runs performed that led to steady conditions. It was performed with a normalized average solar flux density of 1 MW/m^2 at the cavity inlet, corresponding to an actual 83.9 kW solar power entering the cavity. The corresponding maps of solar flux density on the cavity walls were computed with the solar furnace model. The total solid flow rate was 974 kg/h. The heat flux transferred to the DPS estimated with the ColFB temperature was 56.7 kW and that estimated with the average tube outlet temperature was 72.7 kW. The temperatures in the Dispenser Fluidized Bed (DiFB) and Collector Fluidized Bed (ColFB) were 132 °C and 359 °C respectively. The average DPS temperature in the tubes at the cavity inlet and outlet were 197 °C and 421 °C, respectively. The average tube back temperatures at the inlet and outlet were 488 °C and 512 °C, respectively. The heat loss density through the insulating material at the thermocouples' locations on the east and west sides were 555 W/m^2 and 589 W/m^2, respectively.

5.3.4.2 Boundary conditions' parameters tuning

Insulating material The initial value of the insulating material heat transfer coefficient was set to 0.43 W.m^{-2}.K^{-1}, which corresponds to a conductivity of 0.09 W.m^{-1}.K^{-1}, a wall thickness of 20 cm and an external convection coefficient of 10 W.m^{-2}.K^{-1}. With this value, the heat loss density at the thermocouples' locations was underestimated by half. The heat transfer coefficient was increased to 1 W.m^{-2}.K^{-1} to obtain a heat loss flux density of about 600 W/m^2 on both sides. We chose to overestimate this value by about $\tilde{5}$ % (600 W/m^2 instead of 555 W/m^2 at the east wall and 589 W/m^2 at the west wall) rather than risking overestimating the heat flux transferred to the DPS.

Tubes The initial temperature profile was linear with the inlet (bottom) and outlet (top) temperatures equal to the average of the temperatures measured during the experiments at the corresponding locations. It was applied to all 16 tubes. The initial value of convection heat transfer coefficient applied to all 16 tubes was calculated by dividing the power transmitted to the DPS, calculated with the enthalpy balance between the Dispenser Fluidized Bed (DiFB) and Collector Fluidized Bed (ColFB), by the tubes' surface area and ΔT_{lm}, calculated with the temperature profile imposed and the average wall temperatures measured at the tubes rear at the top and bottom of the cavity during the experiments. The resulting heat transfer coefficient value was 266 W.m^{-2}.K^{-1}. The simulated temperatures obtained at the tubes rear with these settings were overestimated for some tubes, and underestimated for others. Actually, this result was expected since we knew that the flow and temperature conditions were different for each tube. Consequently, the heat transfer coefficients and temperature profiles were adapted with values specific to each tube. The outlet temperature was measured for the 16 tubes. For the 6 tubes that had the temperature measured at the inlet, the temperature profile was modified by using these measured values. For the other tubes, the inlet temperature was adapted according to the simulation results. At the same time, the heat transfer coefficient applied to each tube was either increased if the simulated temperature was too high, or decreased in the other case. By an iterative process, the simulated tubes' temperatures were adjusted to those measured. In the end, the heat transfer coefficients ranged from 100 to 450 W.m^{-2}.K^{-1}.

5.3.4.3 Model validation

The model was validated when the simulated temperatures satisfactorily matched the temperatures measured at the tubes rear, in the middle, at the bottom and at the top of the cavity. The results can be seen in Figures 5.13, 5.14 and 5.15 for the middle, bottom and top, respectively. The largest errors produced by the model at this tuning stage were an overestimation of 63 °C in the middle, and underestimations of 79 °C at the bottom and 127 °C at the top. The average simulated temperature was underestimated by 15 °C in the middle and overestimated by 33 °C at the bottom and 31 °C at the top. The model did not match the results perfectly, a finer tuning would be required to improve the fit, but it was close enough to draw conclusions from these results.

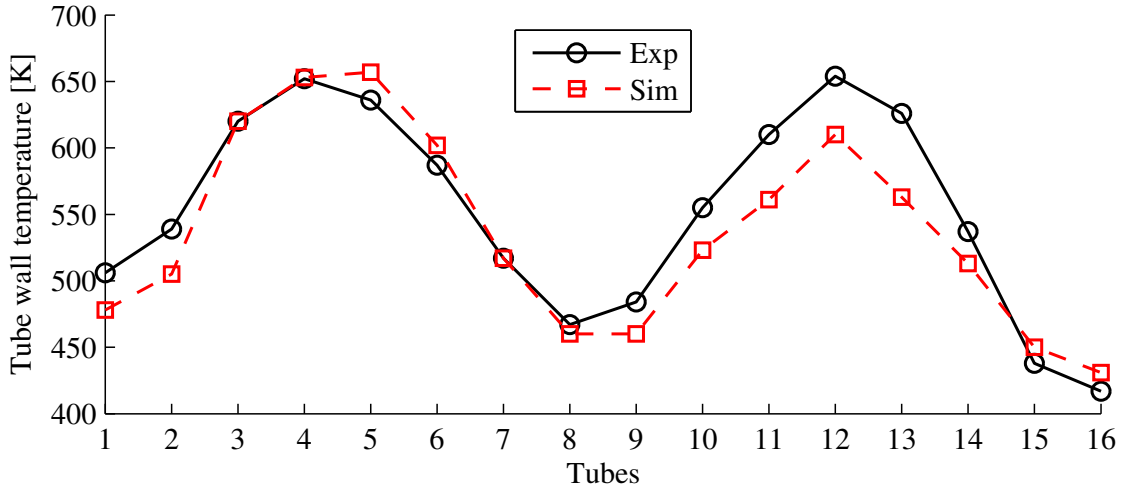

Figure 5.13: Comparison of measured and simulated temperatures measured at the tubes rear in the middle of the cavity.

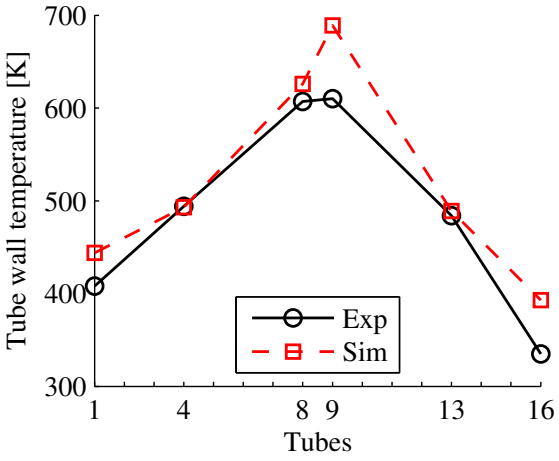

Figure 5.14: Comparison of measured and simulated temperatures measured at the tubes rear at the bottom of the cavity.

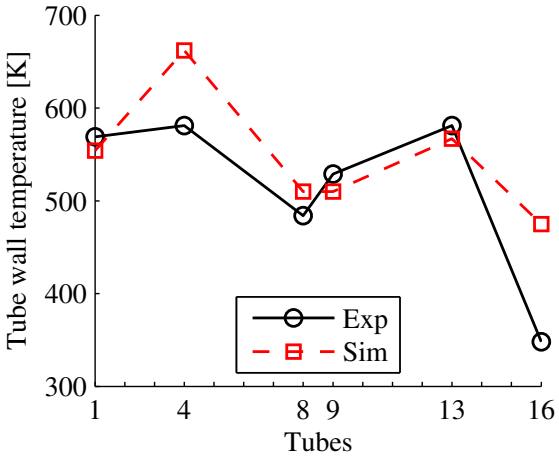

Figure 5.15: Comparison of measured and simulated temperatures measured at the tubes rear at the top of the cavity.

5.3.4.4 Results

The results presented here focus specifically on the distribution of the incoming solar power between reflection losses, convection and radiation losses through the cavity aperture, heat loss through the insulating material and heat transferred to the DPS inside the tube. The Solfast-4D model showed that 1.3 kW of the 83.9 kW solar heat flux entering the cavity exited the system after multiple reflections without being absorbed. The total heat loss through the cavity opening was 13.9 kW, with 10.9 kW due to convection and 2.9 kW due to radiation. The heat loss through the insulating material was 2.3 kW. The remaining 66.6 kW were absorbed by the tubes, which corresponds to being transferred to the DPS.

These results show that the receiver cavity was well designed with only 1.6 % of the incoming solar energy lost without being absorbed. In spite of its compact conception, the receiver is well insulated with 2.8 % heat loss through the insulating material. The cavity shape limits the radiation heat loss through the opening to 3.5 %. The main heat loss comes from the air circulation generated by its heating when it comes into contact with the cavity walls. This convection heat loss through the cavity opening is as high as 13 %. The reason for this result is that, the other losses being limited by the cavity shape and insulation, the convection is the only remaining heat exchange mode to evacuate the power unabsorbed by the DPS. The simulations showed that a natural convection flow was created. The air is motionless in the top half of the cavity volume. A cold air flow is progressively heated while it enters through the low part of the aperture, flows along the bottom of the cavity, goes up at the back and then flows toward the aperture at the cavity middle height to exit in the middle of the aperture. Finally, 79 % of the incoming solar energy is transferred to the DPS. The repartition of the solar power entering the cavity is displayed on Figure 5.16.

The heat flux transferred to the DPS estimated by enthalpy balance with the Collector FB temperature was underestimated by 15 % since it was 56.7 kW instead of the 66.6 kW given by the model. The estimation using the average DPS temperature at the tubess outlets at the outlet overestimated the results since it gave 72.7 kW, but it was closer than the other option with only 9 % overestimation.

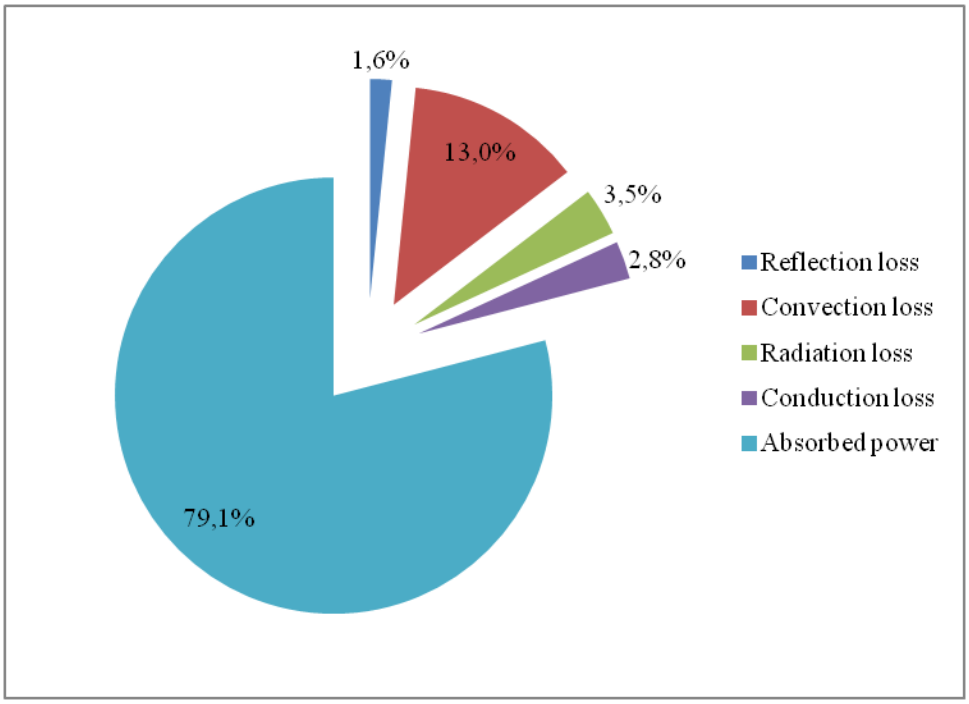

Figure 5.16: Repartition of the solar power entering the cavity.

5.4 Conclusion and perspectives

The MCRT model of the 1 MW CNRS solar furnace developed with Solfast-4D was able to accurately reproduce the flux distribution produced by individual heliostats at the solar furnace focus, both at the level solar spot shape and total power. Measurements showed that, in the experimental conditions of the 16-tube pilot receiver testing, the solar flux density was homogeneous when considered in the focal plane of the parabola but not at the back wall of the cavity where hot and cold spots were observed. When modeling multiple heliostats shooting configurations, discrepancies from the measurements appeared. They were due to several used heliostats that were not individually optimized and to modifications of the reflectors' surfaces optical properties linked to meteorological events that occurred during the time period between the measurements campaigns. This underlines the need to conduct the measurements campaigns in time frames as reduced as possible. Moreover, it shows that the impact of meteorological events on the reflectors' surfaces optical properties is not negligible and that, ideally, these surfaces should be cleaned before any measurement to keep the optical properties constant. In spite of the problems mentioned, the adaptation of the reflectivities allowed Solfast-4D to reproduce the solar flux density at the cavity opening with the exact value of the received solar power, and it produced the solar flux density maps of all the cavity walls necessary for defining of the boundary conditions of the receiver cavity radiosity model.

The receiver cavity was modeled with ANSYS FLUENT version 15.0 [27] using the radiosity method. It used the solar flux density maps of the previous MCRT model as boundary conditions. The tuning of the model's parameters was complex because specific temperature and in-tube convection conditions had to be estimated for each of the 16 tubes due to the inhomogeneous distribution of the solar flux and the uneven repartition of the solid flow rate during the experiments. The model was validated for one steady-state case by comparing the heat loss density through the insulating material and the tubes' wall temperature obtained experimentally and numerically. It showed that the main source of heat loss is the convection heat loss through the cavity opening that was as high as 13 % of the solar power input. The reflection, radiation and conduction through insulating material losses altogether amount to less than 8 %. 79 % of the solar power was transmitted to the DPS.

For the experimental case studied, the model results showed that the power transferred to the DPS calculated by enthalpy balance on the particles between the inlet and outlet of the tubes was either underestimated by 15 % when using the collector fluidized bed temperature as outlet temperature, or overestimated by 9 % when using the average DPS temperature in tubes at the cavity outlet.

The tuning of the studied case will be refined even more and the model will be applied to other experimental cases. This will allow determining the actual power transferred to the DPS for each case. A relation between the actual power transferred and estimations by enthalpy balance will be established that will allow determining the exact power absorbed by the DPS without having to model every case.

5.5 Nomenclature

Abreviations

ColFB	Collector Fluidized Bed
DiFB	Dispenser Fluidized Bed
DNI	Direct Normal Irradiation
DO	Discrete Ordinates
DPS	Dense Particle Suspension
FV	Finite Volume
MCRT	Monte-Carlo Ray Tracing
UDF	User Defined Function

Latin symbols

N_p	Number of points
r	Reflectivity

Greek symbols

ΔT_{lm}	Logarithmic mean temperature difference [K]
σ	Optical error [mrad]
φ	Simulated flux density [W/m^2]
$\hat{\varphi}$	Measured flux density [W/m^2]
χ^2	Cost function

Subscripts, Superscripts

i	Pixel number
HP	Heliostat and parabola portion couple
N	Normalized for a DNI of 1 kW/m^2

Bibliography

[1] S. Chandrasekhar. *Radiative Transfer*. Dover Publications, 1960.

[2] W.A. Fiveland. Discrete-Ordinates Solutions of the Radiative Transport Equation for Rectangular Enclosures. *ASME Journal of Heat Transfer*, 106(4):699–706, 1984.

[3] J.S. Truelove. Discrete-Ordinate Solutions of the Radiation Transport Equation. *ASME Journal of Heat Transfer*, 109(4):1048–1051, 1987.

[4] G.D. Raithby and E.H. Chui. A Finite-Volume Method for Predicting a Radiant HeatTransfer in Enclosures with Participating Media. *ASME Journal of Heat Transfer*, 112(2):415–423, 1990.

[5] S. Abanades and G. Flamant. Experimental study and modeling of a high-temperature solar chemical reactor for hydrogen production from methane cracking. *International Journal of Hydrogen Energy*, 32:1508–1515, 2007.

[6] S. Abanades, P. Charvin, and G. Flamant. Design and simulation of a solar chemical reactor for the thermal reduction of metal oxides: Case study of zinc oxide dissociation. *Chemical Engineering Science*, 62:6323–6333, 2007.

[7] S. Rodat, S. Abanades, J.-L. Sans, and G. Flamant. Hydrogen production from solar thermal dissociation of natural gas: Development of a 10 kW solar chemical reactor prototype. *Solar Energy*, 83:1599–1610, 2009.

[8] S. Haussener, D. Hirsch, C. Perkins, A. Weimer, A. Lewandowski, and A. Steinfeld. Modeling of a Multitube High-Temperature Solar Thermochemical Reactor for Hydrogen Production. *ASME Journal of Solar Energy Engineering*, 131(2):024503, 2009.

[9] C.K. Ho, S.S. Khalsa, and N.P. Siegel. Modeling on-sun tests of a prototype solid particle receiver for concentrating solar power processes and storage. *Proceedings of ES2009, San Francisco, California USA, July 19-23*, 2009.

[10] N.P. Siegel, C.K. Ho, S.S. Khalsa, and G.J. Kolb. Development and Evaluation of a Prototype Solid Particle Receiver: On-Sun Testing and Model Validation. *ASME Journal of Solar Energy Engineering*, 132(2):021008, 2010.

[11] M.F. Modest. *Radiative Heat Transfer*. Academic Press, Waltham, MA, 2^{nd} edition, 2003.

[12] J.R. Howell, R. Siegel, and M. Pinar Mengüç. *Thermal Radiation Heat Transfer*. CRC Press, 2011.

[13] H.E. Rushmeier. Extending the radiosity method to transmitting and specularly reflecting surfaces. M.S. Thesis, Sibley School of Mechanical and Aerospace Engineering, Cornell Univ., Ithaca, N.Y., 1986.

[14] R. Palumbo, M. Keunecke, Möller, and A. Steinfeld. Reflections on the design of solar thermal chemical reactors: thoughts in transformation. *Energy*, 29:727–744, 2004.

[15] C. Wieckert, R. Palumbo, and U. Frommherz. A two-cavity reactor for solar chemical processes: heat transfer model and application to carbothermic reduction of ZnO. *Energy*, 29:771–787, 2004.

[16] K.S. Reddy and N. Sendhil Kumar. Combined laminar natural convection and surface radiation heat transfer in a modified cavity receiver of solar parabolic dish. *International Journal of Thermal Sciences*, 47:1647–1657, 2008.

[17] L. Dunn and J. Shultis. *Exploring Monte Carlo Methods*. Academic Press, Waltham, MA, 2012.

[18] C. Caliot, H. Benoit, E. Guillot, J.L. Sans, A. Ferriere, G. Flamant, C. Coustet, and B. Piaud. Validation of a Monte Carlo Integral Formulation Applied to Solar Facility Simulations and Use of Sensitivities. *ASME Journal of Solar Energy Engineering*, 137(2):021019, 2015.

[19] J. Delatorre. *Calculs de sensibilites par la methode de monte-carlo pour la conception de procédés à énergie solaire concentré (in French) (Calculation of sensitivities by the monte-carlo method for concentrating solar energy processes conception)*. PhD thesis, Institut National Polytechnique de Toulouse, 2011.

[20] B. Piaud, C. Coustet, C. Caliot, E. Guillot, and G. Flamant. Application of Monte-Carlo sensitivities estimation in Solfast-4D. *Proceedings of 18 th SolarPaces Conference, Marrakech, Morocco, September 11-14*, 2012.

[21] J.P. Roccia, B. Piaud, C. Coustet, C. Caliot, E. Guillot, G. Flamant, and J. Delatorre. SOLFAST, a Ray-Tracing Monte-Carlo software for solar concentrating facilities. *Journal of Physics: Conference Series*, 369(1):012029, 2012.

[22] J. Delatorre, G. Baud, J. Bézian, S. Blanco, C. Caliot, J. Cornet, C. Coustet, J. Dauchet, M.E. Hafi, V. Eymet, R. Fournier, J. Gautrais, O. Gourmel, D. Joseph, N. Meilhac, A. Pajot, M. Paulin, P. Perez, B. Piaud, M. Roger, J. Rolland, F. Veynandt, and S. Weitz. Monte-carlo advances and concentrated solar applications. *Solar Energy*, 103:653–681, 2014.

[23] D. Hirsch and A. Steinfeld. Radiative transfer in a solar chemical reactor for the co-production of hydrogen and carbon by thermal decomposition of methane. *Chemical Engineering Science*, 59:5771–5778, 2004.

[24] T. Melchior, C. Perkins, A.W. Weimer, and A. Steinfeld. A cavity-receiver containing a tubular absorber for high-temperature thermochemical processing using concentrated solar energy. *International Journal of Thermal Sciences*, 47:1496–1503, 2008.

[25] A. Z'Graggen and A. Steinfeld. Hydrogen production by steam-gasification of carbonaceous materials using concentrated solar energy - V. Reactor modeling, optimization, and scale-up. *International Journal of Hydrogen Energy*, 33:5484–5492, 2008.

[26] A. Z'Graggen and A. Steinfeld. A two-phase reactor model for the steam-gasification of carbonaceous materials under concentrated thermal radiation. *Chemical Engineering and Processing*, 47:655–662, 2008.

[27] http://www.ansys.com/Products/Simulation+Technology/Fluid+Dynamics/Fluid+Dynamics+Products/ANSYS+Fluent.

[28] J. Martinek and A.W. Weimer. Evaluation of finite volume solutions for radiative heat transfer in a closed cavity solar receiver for high temperature solar thermal processes. *International Journal of Heat and Mass Transfer*, 58:585–596, 2012.

[29] J. Martinek, C. Bingham, and A.W. Weimer. Computational modeling and on-sun model validation for a multiple tube solar reactor with specularly reflective cavity walls. part1:heat transfer model. *Chemical EngineeringScience*, 81:298–310, 2012.

[30] K.E. Torrance and E.M. Sparrow. Theory for off-specular reflection from roughened surfaces. *Journal of the Optical Society of America*, 57(9):1105–1112, 1967.

[31] T. Coleman and Y. Li. An Interior, Trust Region Approach for Nonlinear Minimization Subject to Bounds. *SIAM Journal of Optimization*, 6(2):418–445, 1996.

Conclusion

In this study, it was seen that, among the various concentrated solar thermal technologies, solar tower power plants have the greatest improvement potential. Many studies are focused on the development of new solar heat transfer fluids that can stand the high temperatures needed to power Brayton or combined cycles that can attain efficiencies higher than 50 % while the current steam Rankine cycles are limited to a maximum 42 % efficiency. New molten salts, liquid metals, supercritical water and carbon dioxide, pressurized gases and particles are possible candidates for reaching this aim.

The coupling between heat transfer fluid characteristics and storage performances is of prime importance for plant design and cost. Obviously, the best solution consists in using the same fluid for HTF and storage medium.

The solution we proposed and studied in the frame of the CSP2 project was to use a dense suspension of solid particles transported by an upward air flow through vertical tubes as heat transfer fluid. Particles can stand high temperatures and can be used as a direct heat storage medium. The circulation in tubes allows a precise control of the HTF mass flow rate, unlike the systems using directly irradiated particles that can reach higher temperature to the detriment of the solid flow rate stability.

Contrary to circulating fluidized beds, Dense Particle Suspension (DPS) flows operate at low gas velocity and large solid fraction. Typical air velocity and mean solid fraction in circulating fluidized beds are respectively 10 m/s and less than 5 % respectively; these values are typically 0.02 m/s and 30 % in DPS flows, respectively.

On-sun tests of a single-tube DPS receiver were carried out at the 1 MW solar furnace of the PROMES-CNRS laboratory with 64 μm Sauter diameter SiC particles.

It was shown that this innovative process leads to global wall-to-suspension heat transfer coefficients over the receiver tube height exposed to concentrated solar radiation, called h_{tube}, up to 1100 W/m^2.K in the considered conditions, with particle mean advection velocities always less than 6 cm/s.

Suspension temperature up to 750 °C was obtained maintaining the absorber wall temperature in its operation limit. This temperature allows the use of high efficiency thermodynamic cycles. Using ceramic tubes might even extend the operating temperature up to more than 1000 °C, which means the thermodynamic cycles would be even more efficient, but it would then require developments to limit the receiver heat losses. More than 200 °C particle temperature elevation was measured in the 50 cm long irradiated part of the receiver tube. A recirculation (downward flow) of particles in the vicinity of the tube wall was observed.

We found that the solid mass flux, and the DPS temperature are the main parameters influencing the heat transfer. In the explored parameters ranges, the higher the solid mass flux, the higher h_{tube}, because when the particle agitation increases, then the particle movement and the exchange between the wall and the tube center are improved. The higher the DPS temperature, the higher h_{tube}, because the air conductivity and radiation exchange increase with temperature.

The system proved to be easily controllable by the pressure imposed in the bottom fluidized bed, the aeration and the feeding rate from the particle storage. In a power plant using this technology the solid mass flux should be modulated to get the desired outlet temperature.

The h_{tube} values, calculated from the results of two experimental campaigns, were successfully fitted with a specific Nusselt correlation that has a determination coefficient $R^2 = 0.95$ and an average relative error of 5 %. This correlation will be a useful tool for sizing and operating future facilities using DPS receivers:

$$Nu_{DPS} = 4.5 + 35.4 Re_{DPS}^{0.61} Pr_{DPS}^{0.94}$$

At this moment, only general trends can be drawn to compare DPSs and molten salts, the more developed HTF technique in central receiver solar power plants. The DPS thermal capacity (ρc_p) is about half that of molten salts, and, accounting for the measured h_{tube}, the flux limit that the receiver can stand is estimated in the range 300-400 kW/m^2, that-is-to say 1/3 to 1/4 of the flux limit for molten salt receivers. But DPSs extend drastically the operating temperature range of solar heat transfer fluids, currently limited to about 560 °C, they do not suffer any freezing point problem, they are harmless and their cost is low. Moreover, DPSs keep both advantages of being a heat transfer fluid and a storage medium.

A 3D numerical study of the experimental single-tube DPS solar receiver was realized with the NEPTUNE_CFD code. The experimental flow conditions were reproduced except for two significant elements. A uniform over the tube circumference heat flux density condition was applied in the model because the experimental heat flux distribution was not measured. The highly poly-dispersed distribution of non-spherical particles could not be precisely modeled. Instead, a uniform particle diameter was imposed. The boundary conditions were defined to reproduce three experimental cases.

The model was able to reproduce the experimental results to some extent but differences remained. The particle size was adapted to obtain the right pressure drop at ambient temperature. The particle recirculation was overestimated which affected the temperature distribution. However, the simulated case with the highest solid mass flux well fitted the experimental results because at high solid mass flux the recirculation had less influence. It must be noted that in an industrial application of the DPS receiver process, the solid flux will be at least double the maximum value tested during the experimental tests in order to maintain a reasonable outlet temperature for longer tubes. Therefore the numerical model is pertinent for industrial application studies.

The numerical results put in evidence the aeration effects. The air velocity increase induced by increasing the air mass flow rate provoked a bubbles' influence increase. Moreover, the pressure decrease going up the tube provoked an air velocity increase that emphasized the bubbles' effects. The temperature also affected the air velocity and made the bubbles effects stronger where the temperature was higher.

The solid volume fraction inside the tube was found to be higher close to the wall than at the tube center, and it decreased with the tube height and the temperature. It is directly linked with the air velocity: the higher the air velocity, the lower the solid flux. Moreover, the solid volume fraction variance was higher in the tube central zone than close to the wall. It was due to the bubbles circulating in the central zone.

The particle vertical and radial velocities variances were found to be provoked by the bubbles and directly related to the air velocity and, thus, to the temperature. The higher the temperature, the higher the air velocity, the higher the bubble's influence and the

higher the variances. The simulations showed that the particle radial velocity variance was far greater than the random kinetic energy of particles, which indicates that the heat transfer from the tube wall to the tube center is due to the particles' collective movement.

The model could be improved by refining the mesh over the tube radius and by a better taking into account the particle shape and size with an enhanced frictional viscosity model and a numerical polydisperse particle distribution. It could be coupled with the SYRTHES code that computes thermal conduction in solids in order to simulate the tube wall and better define the heat flux condition.

The model at ambient temeprature is currently being compared to positron emission particle tracking measurements by the CSP2 projects partners. This will tell us at which levels the model without heating is valid and what are the elements that must be improved. Future solar experiments will be conducted with different particles. In particular, Cristobalite particles are very interesting because, apart from their low cost and good thermal properties, they have a high sphericity factor and a narrow diameter distribution that will make them much easier to simulate than the SiC particles.

A series of on-sun tests of a 50-150 kW_{th} 16-tube DPS solar receiver were performed. Several full days of on-sun operation of the pilot rig were achieved, with continuous particle circulation in closed loop and more than 30 h of stable state in total. The rig was steadily operated with particle temperature increases through the receiver cavity in the range 137-335 °C for a 1 m irradiated tube height.

The average outlet temperature was limited due to the specificity solar facility but, nevertheless, it reached 490 °C during a stable state period and went up to 590 °C during a transient period. The particle temperature was even higher than 700 °C in some tubes.

During transient periods, the system showed a self-regulation capacity, decreasing and increasing the solid flow rate when the DNI dropped or rose. This is a very interesting advantage for power plant operation.

The experimental results obtained on the single-tube and on the multi-tube solar receivers showed a strong coherence at the level of the heat flux density absorbed by the DPS.

The thermal yield calculated for this cavity receiver was as high as 90 % for a solid mass flux of 44 $kg.m^{-2}.s^{-1}$. However, the open receiver configuration with higher tubes and higher solar flux densities needs to be considered for industrial applications. This will require strategies to increase the wall-to-DPS heat transfer coefficient in order to limit the tubes' temperature and the radiation losses. The increase of the solid flux, also necessary to limit the temperature increase when using longer tubes, should improve the heat transfer and finned tubes are being considered.

The results analysis still needs to be refined. In particular, a better understanding of the solid flow rate distribution between the tubes will allow a more precise calculation of the thermal yield.

The modeling of the multi-tube receiver cavity with a coupled Monte Carlo Ray Tracing (MCRT)-radiosity method can help improving the experimental results analysis.

The MCRT model of the 1 MW CNRS solar furnace developed with Solfast-4D was able to accurately reproduce the flux distribution produced by individual heliostats at the solar

furnace focus. Difficulties were encountered when extending the model to the whole set of heliostats used during the on-sun tests of the multi-tube receiver but it did not prevent Solfast-4D to reproduce the solar flux density at the cavity opening with the exact value of the received solar power.

The receiver cavity modeled with ANSYS FLUENT version 15.0 used the solar flux density maps of the previous MCRT model as boundary conditions. The tuning of the model's parameters was complex and in the available time, the model could only be validated for one steady-state case. For the studied case, it showed that the receiver cavity main source of heat loss was the convection loss through the cavity opening that was as high as 13 % of the solar power input. The reflection, radiation and conduction through insulating material losses altogether amount to less than 8 %. 79 % of the solar power was transmitted to the DPS.

The power transferred to the DPS calculated by enthalpy balance on the particles between the inlet and outlet of the tubes was either underestimated by 15 % when using the collector fluidized bed temperature as outlet temperature, or overestimated by 9 % when using the average DPS temperature in tubes at the cavity outlet.

The model will be applied to other experimental cases to determine the actual power transferred to the DPS for each case. A relation between the actual power transferred and estimations by enthalpy balance will be established and will help improving the experimental results analysis. Moreover, the model could be applied to the single-tube receiver to determine the heat flux distribution around the tube that could then be used as boundary condition in an improved version of the 3D DPS flow simulations.

The DPS solar receiver study is far from complete. More information can still be obtained from the experimental results. The numerical models can be further refined, their application will lead to more precise experimental data exploitation. The heat transfer should be studied with higher tubes, at higher solid mass fluxes and higher solar fluxes to be closer to the conditions of industrial power plants.

However, significant progress were made on the DPS solar receiver process undertanding. Moreover, the feasibility of the concept and its capacity to operate at high temperature in realistic conditions were proven. It is a promising technology that could be used in solar tower power plants in combination with high efficiency thermodynamic cycles. Pre-industrial scale applications are already being considered.

DPSs also open a new domain of applications of concentrated solar energy. Applications to concrete industry, to waste and biomass treatment, or to ore processing, can be foreseen. In fact, the SOLPART european project that will try the DPS process for lime production will start in January 2016.

Annex:

Equations in NEPTUNE_CFD

In the follwing equations the subscript $k = g$ refers to the gas phase and the subscipt $k = p$ to the particle phase. $\alpha_p \rho_p$ in the particle transport equation represents $n_p m_p$ where n_p is the number density of particle center and m_p is the mass of a single particle: $\alpha_p = \frac{n_p m_p}{\rho_p}$ is an approximation of the local particle volume fraction. Hence, gas and particle volume fractions, α_g and α_p have to satisfy:

$$\alpha_g + \alpha_p = 1 \tag{1}$$

Mass transport equation:

$$\frac{\partial}{\partial t}\alpha_k \rho_k + \frac{\partial}{\partial x_j}\alpha_k \rho_k U_{k,j} = 0 \tag{2}$$

where ρ_k is the density of k-phase and $U_{k,i}$ is the $i-$component of its velocity.

Momentum transport equation

$$\alpha_k \rho_k \left[\frac{\partial U_{k,i}}{\partial t} + U_{k,j}\frac{\partial U_{k,i}}{\partial x_j}\right] = -\alpha_k \frac{\partial P_g}{\partial x_i} + \alpha_k \rho_k g_i + \sum_{q=g,p} I_{q\to k,i} - \frac{\partial \Sigma_{k,ij}}{\partial x_j} \tag{3}$$

where P_g is the mean gas pressure, g_i is the gravity $i-$component. $I_{g\to p}$ are the interphase momentum transfer between particle and gas without the mean gas pressure contribution and $\Sigma_{k,ij}$ is the effective stress tensor of phase k.

Interphase transfer modeling:

According to the particle to gas density ratio, the dominant forces between the gas phase and particles are the drag and Archimede's force, so the mean momentum gas-particle transfer term may be written:

$$I_{g\to p,i} = -\frac{\alpha_p \rho_p}{\tau_{gp}^F} V_{rp,i} \tag{4}$$

$$\frac{1}{\tau_{gp}^F} = \frac{3}{4}\frac{\rho_g}{\rho_p}\frac{\langle|\vec{v}_r|\rangle_p}{d_p} C_d(Re_p) \tag{5}$$

$$C_d(Re_p) = \begin{cases} C_{d,WY} & \text{if} \quad \alpha_g \geq 0.7 \\ \min\left[C_{d,WY}, C_{d,Erg}\right] & \text{else} \quad \alpha_g < 0.7 \end{cases} \tag{6}$$

$$C_{d,WY} = \begin{cases} \frac{24}{Re_p}\left(1 + 0.15 Re_p^{0.687}\right)\alpha_g^{-1.7} & Re_p < 1000 \\ 0.44\alpha_g^{-1.7} & Re_p \geq 1000 \end{cases} \tag{7}$$

$$C_{d,Erg} = 200\frac{(1-\alpha_g)}{Re_p} + \frac{7}{3} \tag{8}$$

$$Re_p = \alpha_g \frac{\rho_g \langle|\vec{v}_r|\rangle_p d_p}{\mu_g} \tag{9}$$

$$V_{rp,i} = < v_{r,i} >_p = U_{p,i} - U_{g,i} - V_{dp,i} \tag{10}$$

$V_{dp,i}$ is the drift velocity which can appear due to turbulence [1] or sub-grid effect [2].

Particle stress modeling:

$$\Sigma_{p,ij} = \Sigma_{p,ij}^{kin} + \Sigma_{p,ij}^{col} + \Sigma_{p,ij}^{fric} \tag{11}$$

$$\Sigma_{p,ij}^{kin} + \Sigma_{p,ij}^{col} = \left[P_p - \lambda_p \frac{\partial U_{p,n}}{\partial x_n}\right]\delta_{ij} - \mu_p\left[\frac{\partial U_{p,i}}{\partial x_j} + \frac{\partial U_{p,j}}{\partial x_i} - \frac{2}{3}\frac{\partial U_{p,n}}{\partial x_n}\delta_{ij}\right] \tag{12}$$

$$P_p = \alpha_p \rho_p \left[1 + 2\alpha_p g_0 (1+e_c)\right]\frac{2}{3}q_p^2 \tag{13}$$

$$g_0 = \left[1 - \frac{\alpha_s}{\alpha_{s,max}}\right]^{-2.5\alpha_{s,max}}, \qquad e_c = 0.9 \tag{14}$$

$$\mu_p = \alpha_p \rho_p \left(\nu_p^{kin} + \nu_p^{col}\right) \tag{15}$$

$$\nu_p^{kin} = \left[\frac{1}{2}\tau_{gp}^F \frac{2}{3} q_p^2 \left(1 + \alpha_p g_0 \Phi_c\right)\right] \times \left[1 + \frac{\tau_{gp}^F}{2}\frac{\sigma_c}{\tau_p^c}\right]^{-1} \tag{16}$$

$$\Phi_c = \frac{2}{5}(1+e_c)(3e_c - 1), \quad \sigma_c = \frac{1}{5}(1+e_c)(3-e_c) \tag{17}$$

$$\nu_p^{col} = \frac{4}{5}\alpha_p g_0 (1+e_c)\left[\nu_p^{kin} + d_p\sqrt{\frac{2}{3}\frac{q_p^2}{\pi}}\right] \tag{18}$$

$$\lambda_p = \alpha_p \rho_p \frac{4}{3}\alpha_p g_0 (1+e_c) d_p \sqrt{\frac{2}{3}\frac{q_p^2}{\pi}} \tag{19}$$

$$\frac{1}{\tau_p^c} = 24\frac{\alpha_p g_0}{d_p}\sqrt{\frac{2}{3}\frac{q_p^2}{\pi}} \tag{20}$$

$$\Sigma_{p,ij}^{fric} = \left[P_p - \lambda_p \frac{\partial U_{p,n}}{\partial x_n}\right]\delta_{ij} - \alpha_p \rho_p \nu_p^{fric}\left[\frac{\partial U_{p,i}}{\partial x_j} + \frac{\partial U_{p,j}}{\partial x_i} - \frac{2}{3}\frac{\partial U_{p,n}}{\partial x_n}\delta_{ij}\right] \tag{21}$$

$$\nu_p^{fric} = \frac{P_f \ sin\ \phi}{2(1-\alpha_g)\rho_p\sqrt{I_{2D} + 2/3\frac{q_p^2}{d_p^2}}} \tag{22}$$

$$P_f = Fr\frac{\left[(1-\alpha_g) - \alpha_{s,min}\right]^n}{\left[\alpha_{s,max} - (1-\alpha_g)\right]^m} \tag{23}$$

$$Fr = 0.05,\ \phi = \pi/4,\ n = 2,\ m = 5,\ \alpha_{s,min} = 1 - \alpha_{g,mf} \tag{24}$$

$$I_{2D} = \left[\frac{\partial U_{p,i}}{\partial x_j} + \frac{\partial U_{p,j}}{\partial x_i}\right]\frac{\partial U_{p,i}}{\partial x_j} - \frac{2}{3}\left[\frac{\partial U_{p,i}}{\partial x_i}\right]^2 \tag{25}$$

Particle random kinetic energy transport equation:

$$\begin{aligned}\alpha_p \rho_p \left[\frac{\partial q_p^2}{\partial t} + U_{p,j}\frac{\partial q_p^2}{\partial x_j}\right] &= \frac{\partial}{\partial x_j}\left[\alpha_p \rho_p \left(K_p^{kin} + K_p^{col}\right)\frac{\partial q_p^2}{\partial x_j}\right] \\ &\quad - \left[\Sigma_{p,ij}^{kin} + \Sigma_{p,ij}^{coll}\right]\frac{\partial U_{p,i}}{\partial x_j} - \frac{\alpha_p \rho_p}{\tau_{gp}^F} 2q_p^2 - \frac{1}{2}\left(1 - e_c^2\right)\frac{\alpha_p \rho_p}{\tau_c}\frac{2}{3}q_p^2\end{aligned} \tag{26}$$

$$K_p^{kin} = \frac{2}{3} q_p^2 \frac{5}{9} \tau_{gp}^F \left(1 + \alpha_p g_0 \phi_c\right) \left[1 + \frac{5}{9} \tau_{gp}^F \frac{\xi_c}{\tau_p^c}\right]^{-1} \tag{27}$$

$$\phi_c = \frac{3}{5} \left(1 + e_c\right)^2 \left(2e_c - 1\right), \quad \xi_c = \frac{(1 + e_c)(49 - 33e_c)}{100} \tag{28}$$

$$K_p^{col} = \alpha_p g_0 (1 + e_c) \left[\frac{6}{5} K_p^{kin} + \frac{4}{3} d_p \sqrt{\frac{2}{3} \frac{q_p^2}{\pi}}\right] \tag{29}$$

Phase enthalpy and heat transfer equations

The heat exchanged by contact during the interparticle collisions is neglected. Therefore, the main heat exchange modes in the bed are summarized by:

The convection/diffusion heat transfer Π_{g-p} between the gaseous phase and the particles occurring with a characteristic time scale τ_{gp}^T such that

$$\Pi_{g-p} = -\Pi_{g-p} = \frac{\alpha_p \rho_p c_{pp}}{\tau_{gp}^T} \left(T_p - T_g\right) \tag{30}$$

with

$$\frac{1}{\tau_{gp}} = \frac{6\lambda_g}{\rho_p c_{pp}} \frac{\langle Nu_p \rangle}{d_p^2} \tag{31}$$

where λ_g is the thermal conductivity of the gaseous phase. $\langle Nu_p \rangle = 2 + 0.55 Re_p^0.5 Pr^(1/3)$ is the Nusselt number of the particle phase and $Pr = \rho_p \nu_g c_{pg})/\lambda_g$ is the Prandtl number. c_p is the specific heat of the gas/particle phase.

The radiative heat transfer between particles of the dense phase. Assuming that the radiation between the particles in the bed takes place in the frame of the Rosseland approximation through a diffusion mechanism, Konan et al. [3] write the radiative flux in the alumina particle enthalpy equation as proportional to the temperature gradient with a radiative thermal diffusion coefficient given by:

$$K_p^r = \frac{32\sigma}{9\alpha_p} \frac{d_p T_p^3}{\rho_p c_{pp}} \tag{32}$$

in which σ is the Stefan-Boltzmann constant and T_p the particle temperature.

Then the distribution of the each phase's enthalpy satisfies the transport equation:

$$\alpha_k \rho_k \frac{\partial H_k}{\partial t} + \alpha_k \rho_k U_{k,j} \frac{\partial H_k}{\partial x_j} = \frac{\partial}{\partial x_j} \left(\alpha_k \rho_k K_k\right) + \sum_{m \neq k} \Pi_{m-k} + \varphi_{wall} \tag{33}$$

with φ_{wall} the heat transfer received from external sources (heated tube wall).

The cells at the wall in the heated part of the tube receive the heat transfer $\varphi_w all = \frac{(\Phi/S)_{wall}}{\Delta_r}$, where Δ_r is the radial thickness of the cells and $(\Phi/S)_{wall}$ is the condition of heat flux density imposed at the wall. The first term on the right-hand side is a transport term written in the frame of the gradient approximation with an effective phase diffusivity coefficient $K_{g/p}$.

For the particle phase:

$$K_p = K_p^t + K_p^r \tag{34}$$

where K_p^t and K_p^r are the contributions due to the transport of the enthalpy by the velocity fluctuations and the radiative heat transfer between the particles, respectively.

For the gas:

$$K_g = K_g^t + K_g^l \tag{35}$$

where K_g^t and K_g^l are the contributions to the transport of the enthalpy due to the gas turbulence and the laminar diffusivity, respectively.

There is no heat exchange with the wall.

Bibliography

[1] O. Simonin, E. Deutsch, and J.P. Minier. Eulerian prediction of the fluid/particle correlated motion in turbulent two-phase flows. *Applied Scientific Research*, 1993.

[2] J.-F. Parmentier, O. Simonin, and O.Delsart. A functional subgrid drift velocity model for filtered drag prediction in dense fluidized bed. *AIChe Journal*, 58(4):1084–1098, 2011.

[3] N. A. Konan, H. Neau, O. Simonin, M. Dupoizat, and T. Le Goaziou. CFD prediction of uranium tetrafluoride particle fluorination in fluidized bed pilot. *AIChE Annual Meeting, Nashville, TN, USA, November 8-13*, 2009.

List of Figures

List of Tables

Publications

Published articles

G. Flamant, D. Gauthier, H. Benoit, J.-L. Sans, R. Garcia, B. Boissière, R. Ansart, and M. Hemati. Dense suspension of solid particles as a new heat transfer fluid for concentrated solar thermal applications: On-sun proof of concept. Chemical Engineering Science, 102:567-576, 2013.

H. Benoit, I. Pérez López, D. Gauthier, J.-L. Sans, and G. Flamant. On-sun demonstration of a 750 °C heat transfer fluid for concentrating solar systems: Dense particle suspension in tube. Solar Energy, 118:622-633, 2015.

C. Caliot, H. Benoit, E. Guillot, J.L. Sans, A. Ferrière, G. Flamant, C. Coustet, and B. Piaud. Validation of a Monte Carlo Integral Formulation Applied to Solar Facility Simulations and Use of Sensitivities. ASME Journal of Solar Energy Engineering, 137(2):021019, 2015.

H.L. Zhang, H. Benoit, D. Gauthier, J. Degrève, J. Baeyens, I. Pérez López, M. Hemati, and G. Flamant. Particle circulation loops in solar energy capture and storage: gas-solid flow and heat transfer considerations. Applied Energy, 161:206-224, 2016.

H. Benoit, L. Spreafico, D. Gauthier, and G. Flamant. Review of heat transfer fluids in tube-receivers used in concentrating solar thermal systems: Properties and heat transfer coefficients. Renewable and Sustainable Energy Reviews, 55:298-315 2016.

R.A. Reyes Urrutia, H. Benoit, M. Zambon, D. Gauthier, G. amant, and G. Mazza. Simulation of the behavior of a dense SiC particle suspension as an energy transporting vector using computational fluid dynamics (CFD). Chemical Engineering Research and Design, 106:141-154, 2016.

Articles submitted or in preparation

P. Garcia-Triñanes, R. Ansart, H. Benoit, O. Simonin, J.P.K. Seville. Dense gas-particle suspension upward flow used as heat transfer fluid in solar receiver: PEPT experiments and 3D numerical simulations. Chemical Engineering Journal, submitted.

I. Pérez López, H. Benoit, D. Gauthier, J.-L. Sans, E. Guillot, G. Mazza, G. Flamant. On-sun operation of a 150 kWth pilot solar receiver using dense particle suspension as heat transfer fluid. Solar Energy, submitted.

H. Benoit, R. Ansart, G. Flamant, O. Simonin. 3D Numerical Simulation of a Dense Particle Suspension Solar Receiver under Uniform Heating, in preparation.

Conference articles

D. Gauthier, J.-L. Sans, G. Flamant, A. Reyes, G. Mazza, B. Boissière, R. Ansart, M. Hemati, H. Benoit. Une suspension dense de particules utilisée comme fluide de transfert pour les centrales solaires thermiques á concentration (in French) (A dense particle suspension used as heat transfer fluid for concentrating solar power plants). Conference SFGP 2013.

G. Flamant, D. Gauthier, H. Benoit, J.-L. Sans, B. Boissière, R. Ansart, M. Hemati. A New Heat Transfer Fluid for Concentrating Solar Systems: Particle Flow in Tubes. Proceedings of the SolarPACES 2013 International Conference. Energy Procedia 49: 617-626, 2014.

H. Benoit, I. Pérez López, D. Gauthier, G. Flamant. Temperature Influence on Wall-to-Particle Suspension Heat Transfer in a Solar Tubular Receiver. SolarPACES 2015 International Conference.

I. Pérez López, H. Benoit, D. Gauthier, J.-L. Sans, E. Guillot, R. Cavaillé, G. Mazza, G. Flamant. On-sun first operation of a 100 kWth pilot solar receiver using dense particle suspension as heat transfer fluid. SolarPACES 2015 International Conference.

G. Flamant, J. Degrève, J. Baeyens, J. Marti, A. Steinfeld, D. Gauthier, M. Romero, J. Gonzalez-Aguilar, H. Benoit, H.L. Zhang. High-Temperature Solar Heat Collection and Storage in Circulating or Dense Upflow Fluidized Beds. SolarPACES 2015 International Conference.

Résumé

Cette thèse, financée dans le cadre du projet européen CSP2, porte sur l'étude d'un nouveau type de récepteur solaire thermique à concentration utilisant comme fluide caloporteur une suspension dense de fines particules en circulation ascendante dans des tubes verticaux. Ladite suspension est obtenue par fluidisation de particules de classe A. Le principe consiste à créer un écoulement ascendant de la suspension dans un tube vertical exposé au rayonnement solaire concentré qui chauffe la paroi du tube, qui transmet ensuite cette chaleur aux particules, qui la transportent jusqu'à un cycle de conversion d'énergie pour la production d'électricité. Au contraire des fluides solaires classiques, les particules peuvent atteindre les hautes températures ($>$ 700 °C) permettant l'utilisation de cycles à haut rendement de conversion (Brayton, cycles combinés), tout en permettant un stockage direct de la pour une production continue. Au cours de la thèse, un récepteur à un tube a été testé avec succès au grand four solaire du laboratoire PROMES-CNRS à Odeillo, les particules en sortie atteignant 750 °C, ce qui a prouvé la faisabilité du concept et permis la détermination des premières valeurs de coefficient d'échange de chaleur tube-suspension. L'hydrodynamique de l'écoulement et les mécanismes d'échange de chaleur ont été observés grâce à des simulations numériques 3D. Un récepteur de 150 kW_{th} à 16 tubes a ensuite été testé et modélisé, validant l'utilisation du procédé à plus grande échelle.

Abstract

This thesis, financed in the frame of the CSP2 European project, concerns the study of a new kind of thermal concentrating solar receiver using a dense suspension of solid particles circulating upward in vertical tubes. The suspension is obtained by fluidizing Geldart A-type particles. The principle consists in creating an upward flow of the suspension in a vertical tube exposed to the concentrated solar radiation that heats the tube wall. The heat is then transmitted to the particles circulating inside that transport it to a conversion cycle for electricity production. Contrarily to usual solar heat transfer fluids, particles can reach high temperatures ($>$ 700 °C) that permit to power high efficiency thermodynamic cycles such as Brayton or combined cycles. Moreover they can be used as a direct heat storage medium for continuous electricity production. During this thesis, a one-tube solar receiver was successfully tested at the PROMES-CNRS solar furnace in Odeillo, with particle outlet temperatures of 750 °C reached. The first values of wall-to-suspension heat transfer coefficient were calculated and a Nusselt correlation was determined. A specific flow pattern with a particle downward flux close to the wall and upward flux in the tube center was underlined. The flow hydrodynamics and the heat transfer mechanisms were studied thanks to 3D numerical simulations. A 16-tube 150 kWth receiver was finally tested and modeled, proving the process applicability at larger scale.